Title
CELLULAR AND MOLECULAR RESPONSES TO MECHANICAL CUES: FROM THE EXTRACELLULAR MATRIX TO THE NUCLEUS

Permalink
https://escholarship.org/uc/item/3hp2h9p9

Author
Jahed Motlagh, Zeinab

Publication Date
2018

Peer reviewed|Thesis/dissertation

CELLULAR AND MOLECULAR RESPONSES TO MECHANICAL CUES:

FROM THE EXTRACELLULAR MATRIX TO THE NUCLEUS

By
Zeinab Jahed Motlagh

A dissertation submitted in partial satisfaction of the
requirement for the degree of
Doctor of Philosophy

in

Applied Science and Technology
and the Designated Emphasis

in

Nanoscale Science and Engineering

in the

Graduate Division

of the

University of California Berkeley

Committee in charge:

Professor Mohammad R. K. Mofrad, Chair
Professor Lydia Sohn
Professor Seung-Wuk Lee

Spring 2018

Abstract

Cellular and Molecular Responses to Mechanical Cues:
From Extracellular Matrix to the Nucleus

by
Zeinab Jahed Motlagh

Doctor of Philosophy in Applied Science and Technology
With Designated Emphasis on
Nanoscale Science and Engineering
University of California, Berkeley

Professor Mohammad R.K. Mofrad, Chair

Mechanical signals affect virtually every fundamental single- and multi-cellular process in biology. The local responses of individual molecules to mechanical stimuli at the interface of cell with its adjacent microenvironment (extracellular matrix or material) elicit global responses at the cell and tissue scales. Understanding and manipulating the cell-material interaction can be leveraged to design biomaterials with unique characteristics tailored towards a wide variety of biological applications such as platforms that direct stem cell differentiation for tissue engineering, sensors that can record accurate electrical signals in single cells for neuroscience, and implants that are susceptible to cell adhesion for biomedical applications. In this thesis I present work characterizing the response of cells to mechanical stimuli at the single cell and single molecule scales. At the single cell scale, we provide insights into how mechanical signals such as micro- and nano-topography of metallic and metallic surfaces affect cell adhesion, both in mammalian and bacterial cells. Next we characterize the mechanical response of protein complexes involved in the transmission of mechanical signals across the cytoskeleton to the nucleus.

The four main contributions of the work presented in this thesis are as follows: 1) We used high resolution scanning electron microscopy to characterize the cell-nanostructure interface and provide insights into the response of individual mammalian cells to nanostructures with complex geometries. 2) We provide a first look at how individual bacterial cells adhere to metallic nanostructures, which could lead to new techniques to thwart infections. 3) We proposed a novel technique to control the growth and arrangements of bacterial cell communities. This method will allow precise small-scale mechanical manipulation of bacterial cells and could be utilized for unraveling the understudied mechanisms of bacterial mechanosensitivity. 4) We performed the first molecular dynamics study on the mechanisms of force transmission to the nucleus of eukaryotic cells through protein complexes known as linkers of the nucleoskeleton and cytoskeleton (LINC complexes). We showed that LINC complexes are highly stable under tensile forces, and that the transmission of force across the complex depends highly on the unique intermolecular covalent bonds formed between the two proteins that construct the complex. Finally, we presented a model for the molecular mechanisms of LINC complex activation and regulation at the nuclear envelope.

Dedicated to *Maman* and *Baba*

For inspiring me to think and question, and to never stop learning.

Acknowledgements

First and foremost, I would like to express my gratitude towards my advisor Prof. Mofrad for his mentorship, and the numerous opportunities he has given me in the past 5 years. I am forever grateful to him for taking a chance on me, and drawing the confidence in me. Under his mentorship I have learned that confidence and humility are not mutually exclusive, and I have grown personally and academically. Besides my advisor, I would like to thank my committee members Prof. Lydia Sohn and Prof. Seung-wuk Lee for their support and encouragement. I would also like to thank all members of Mofrad lab, and the people with whom I collaborated, especially Ting Tsui, Frank Gu, Maud Gorbet, Hengameh, Brandon, Mohit, Sara and Hamed. The work presented in this thesis would not have been possible without their contributions.

I could not have powered through these five years without the support of my family. Nima, you have been my greatest supporter throughout my PhD years, and stood by me through thick and thin. Your level of kindness and intellect is exemplary and I am extremely proud and grateful for having you as my partner in life. Berkeley will always be the most special place to me because it is where our paths crossed. Being 2500 miles away from my family was the most difficult aspect of my PhD years and it would not have been possible without your love and support. I missed the birth of my niece Noora, as well as many birthdays, graduations and other special occasions. However, I'm thankful to my mom and dad and my siblings for making me feel closer to home by virtually including me in the celebrations and gatherings whenever possible. Thank you to my favorite little people: Noora, who successfully graduated from kindergarten this year, and Mahdiar who is on his way to finish grade 3. You made my days brighter with your occasional Facetime calls.

Maman and baba, thank you for giving me the gift of life. I would not be here if it weren't for all the sacrifices you made along the way; from your sleepless nights, to the thousands of miles you have travelled for us. Thank you for giving me the most wonderful brothers and sisters: Zahra, who always has the wisest and most encouraging words to say; Fatemeh and Andische, for suggesting the best documentaries to watch when I needed a distraction from working on my thesis; Maryam, for making me feel less homesick with her occasional surprise visits; Ali, for encouraging me to work hard to finish my PhD by constantly reminding me that I am too old to be a student and need to find a "real" job; my youngest brother, Hossein, who makes me proud every day by being intelligent, strong and wise beyond his years; and my best friend and fourth sister Jash, for caring, listening, and always knowing when something was wrong with me even though we were so far apart. I love you all and I am grateful for your love and support throughout these years.

Thank you to the wonderful friends I met at Berkeley: Hengameh, for always listening to me rant about queue wait times on NERSC supercomputers, rejected papers, and refused scholarships; And Mona, for encouraging me to be healthier by trying new fitness classes with me and for giving me the look every time I went for something sugary.

Finally, I have to thank my favorite instructors at Berkeley: Shane and Shola. I learned the most valuable lessons of endurance and passion in your classes. There was absolutely no better way to spend TTh evenings than being "tough never tired" in Shola's Stronger classes, and MF mornings in Shane's HIIT classes. You helped me stay motivated during the most difficult times of my PhD. My experience at Berkeley would not have been the same without you. I will miss your classes dearly when I leave Berkeley.

Preface

**The emerging fields of Mechanobiology and Mechanomicrobiology**

Mechanobiology is an emerging discipline with dramatic growth in the past decade. Over a decade of research in this field has lead to the discovery that mechanical phenomena affect virtually every fundamental eukaryotic cellular process, including adhesion, proliferation, polarization, migration, and differentiation (Panciera et al. 2017; Ladoux & Mège 2017; Uhler & Shivashankar 2017; Vining & Mooney 2017). More recently, nuclear mechanobiology research has shown that even the organization of the genome and gene expression can be altered in response to mechanical stimulation (Uhler & Shivashankar 2017). The transduction of extracellular mechanical signals into biochemical activity is termed mechanotransduction, and the further transduction of intra- and extra- cellular forces to the nucleus is often referred to as nuclear mechanotransduction.
Cell sensitivity to mechanical cues is not limited to eukaryotes. Many recent studies have shown that bacterial cells can also respond to mechanical stimuli (Cox et al. 2018; Seo et al. 2016; Z. Jahed, Lin, Seo, et al. 2014; Persat et al. 2015). Although expanding, the field of "mechanomicrobiology" is much younger and remains much smaller than the field of mechanobiology. One reason for the slower progress is this field is that bacterial cells are orders of magnitude smaller in size and their mechanical manipulation is significantly more challenging than that of mammalian cells. Therefore the mechanisms of bacterial cell responses remain largely unexplored and there is a strong need for designing tools that can mechanically manipulate these cells at the single cell level.

Mechanical manipulation: cells respond to stiffness and surface geometry

Advancements in micro- and nano- technologies have resulted in the development of several platforms to mechanically manipulate mammalian cells at the single cell level (D. H. Kim et al. 2012). Using various methods of manipulation, it is now widely accepted that cells respond to the stiffness and shape of the surfaces they come in contact with. In order to characterize these cellular responses in the context of various cellular functions, micro-patterned surfaces of various materials have been used to manipulate cell morphology and function (Fig. 1). For example, soft micro-patterned polymeric platforms coated with extracellular matrix (ECM) molecules are now established tools for characterizing cellular responses to substrate stiffness (Fig. 1A) (Kilian et al. 2010). Arrays of elastomeric micropillars are commonly used on these platforms due to the ease of controlling the mechanical stiffness of the micropillars by changing theirs diameters or heights. Once attracted to the micropillars, cells exert mechanical forces and elastically bend them during cell spreading and migration (Fig. 1A). On such soft polymeric micropillar platforms, both the stiffness and geometry of the micropillar arrays affect cell morphology, which ultimately affects several cellular functions. To eliminate the effect of surface stiffness, rigid 3D metallic nano- and micro-pillars have alternatively been used to characterize the response of cells to surface geometry (Fig. 1B). These platforms are usually coated

uniformly with a layer of ECM molecules and since cells are unable to deform the micropillars, they must conform to the 3D geometry of their surrounding environment during cell adhesion and spreading (Fig. 1B). Finally, pattered 2D islands of ECM proteins can be deposited onto rigid surfaces to control the 2D shape of cells (Fig. 1C). On these platforms, cells must conform to the shape of the ECM islands due to lack of adhesion molecules in other regions (Fig. 1C). With a precise control of cells shape, the effect of cell shape on the localization of various adhesion molecules can be determined.
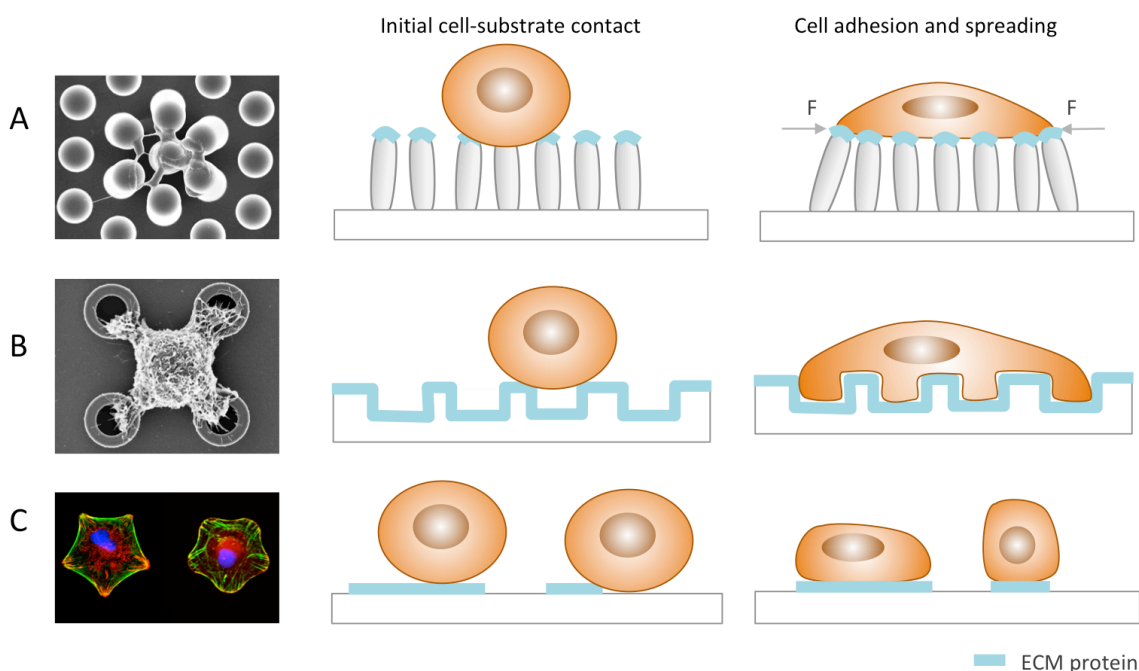
Figure 1. Nano- and micro-pattered substrates for mechanical regulation of cell morphology. A) Elastomeric micropillars (also called micropost) platforms are typically used to characterize cellular responses to substrate rigidity. The micropillars are deformed as cells adhere and spread on them. The scanning electron microscope (SEM) image on the left shows cells on top of deformed elastomeric microposts. B) Rigid pillars on which cells must conform to the 3D geometry of the substrate. These platforms have been used to characterize cellular responses to substrate geometry. The SEM image on the left shows a cell spreading on top of rigid Si micropillars and conforming to the shape of these micropillars. C) Islands of ECM molecules with specific shapes on which cells much conform to the 2D geometry of the islands. These platforms are generally used to test the effect of cell shape on the arrangement of cellular components. The image on the left (Kilian et al. 2010) shows cells conforming to the shape of 2D star-shaped ECM islands. These cells are fluorescently labeled for various proteins and the organization of these proteins are compared in various cellular shapes.

The methods mentioned above are only a few examples of platforms that have led to the discovery that cell shape affects cellular function, and that cells can sense and respond to the stiffness and geometry of their environments. Taking advantage of these properties, vertically aligned micropillars are now used for a variety of biological applications. To name a few examples, nano- and micro- pillars of various cross sectional geometries are used for applications such as tumor cell capture (Wang et al. 2010; S. Wang et al. 2009), drug delivery into cells (VanDersarl et al. 2012; Xie, Alexander M. Xu, et al. 2013) and recording neuronal activities (Hai et al. 2010; Robinson et al. 2013; Xie et al. 2010; Robinson et al. 2012). The first two chapters of this thesis focus on the characterization of the cell-micropillar interface using high-resolution electron microscopy and fluorescent

techniques. Subsequent chapters discuss the molecular mechanisms of cellular mechanotransduction.

Molecular mechanisms of force transmission and mechanotransduction

The response of cells to mechanical cues at the cellular level emanates from several local changes in the composition of molecules at the interface between the cell and its environment. Of course, these features are not observable in electron microscope images such as the ones shown in Fig 1. However, it is well established that cells separate their constituents from the environment through a lipid bilayer known as the cell membrane (Fig 2). Additionally, the genetic material is isolated from other cellular components through a double-layered nuclear envelope (NE) consisting of an inner and outer nuclear membrane (INM and ONM) (Fig 2). Large protein complexes known as nuclear pore complexes (NPC) perforate the NE at several locations and control the bidirectional transport of molecules between the nucleus and cytoplasm.

Figure 2. Formation of *S. aureus* colonies on hydrophobic PDMS micropillars. A) Representative scanning electron micrograph and optical images of *S. aureus* cells at the interface between PDMS micropillars and their adjacent smooth surfaces. The top row shows a side view SEM image of PDMS micropillars after 1hr, 4hr, and 24hr bacteria incubation times at a 70 degree SEM stage tilt. The second row represents top view SEM images of PDMS micropillar arrays. Note that the side and top views are not from the same PDMS micropillar arrays. These images indicate that bacterial cells adhere preferentially to the smooth surface as well as pillar tops after 1-4hr incubation times but penetrate in between micropillars and cover the platforms fully after 24 hours. Low magnification top view optical microscope images on the third row also show the absence of bacterial cells in between micropillars after 1-4hr incubation times but a full coverage of the platform after 24 hours of incubation. The white dotted lines indicate the interface between micropillars arrays and the adjacent smooth surfaces. Cracking of the bacteria film and clustering of micropillars seen for 24hr incubations times are likely caused while drying the samples for imaging. B) Schematic representation of the interfaces between the micropillar platform and the solution containing *S. aureus* bacterial cells. The air pockets trapped in between PDMS micropillars inhibit the *S. aureus* solution from penetrating in between the micropillars. After 24 hours the solution penetrates in between micropillars resulting in cell attachment to the micropillar sidewalls as well as the smooth surface in between micropillars. Scale bars shown on SEM images represent 20 µm.

3

To transfer mechanical signals across the cell membrane and the NE, cells contain several mechao-sensing components. During cell-ECM adhesion, a complex network of molecules mechanically couples the ECM, cytoskeleton and nucleoskeleton. Mechanical signals are transmitted between the ECM and cytoskeleton through integrin-mediated focal adhesions (Fig. 2), and a percentage of these adhesions are directly linked to the nucleus through bundles of actin filaments. Large KASH (Klarsicht, ANC1 and Syne Homology) proteins that are anchored to the outer nuclear membrane (ONM) bind to these actin filaments at their cytoplasmic domain, and to INM (inner nuclear membrane) anchored SUN (Sad1p/UNC (uncoordinated)-84) proteins at their luminal domains (Fig 2). SUN proteins can also bind to nucleoskeletal elements through their nucleoplasmic domains. SUN-KASH complexes are therefore known as the linkers of the nucleoskeleton and cytoskeleton (LINC). Through the SUN-KASH interaction, a direct physical linkage is formed between the ECM and the nucleus rendering the LINC complex a likely and important candidate for cell mechanotransduction. In agreement with this, recent studies suggest that mechanotransduction on stiff substrates is dominated by focal adhesions that are directly linked to the nucleus (Dong-Hwee Kim et al. 2012). Numerous studies have focused on the molecular mechanisms of force transmission and transduction through integrin-mediated focal adhesions at the cell-ECM interface, thereby the proteins involved in cell-ECM adhesion are well characterized (Z. Jahed, Shams, Mehrbod, et al. 2014). On the other hand, the molecular mechanisms of force transmission across the nuclear envelope through SUN-KASH complexes are mainly unknown. The final chapter of this thesis discusses the molecular mechanisms of force transmission across the nuclear envelope.

Thesis content

Chapters 1-2 of this thesis present my studies on the responses of cells to mechanical manipulations at the cellular level, whereas Chapter 3 discusses how mechanical forces are transferred to the nucleus at the molecular level. Specifically, Chapter 1 examines the response of mammalian cells to micro- and nano-pattered surfaces. In Chapter 2 we show that bacterial attachment also depends on the micro-topography of surfaces they attach to. Furthermore, in Chapter 2 we present a tool for patterning bacterial cells at the nano- and micro-scales that allows the control of bacterial cell arrangements and growth. This tool can be used to mechanically manipulate bacterial colonies to explore the particularly understudied molecular mechanisms of bacterial mecha-nosensitivity. Finally, in Chapter 3, we discuss the molecular mechanisms of force transmission to the nucleus. We first discuss the roles of the only two known protein complexes that span the nuclear envelope, namely the LINC complex and the NPCs. Next we present molecular mechanisms of force transmission across the SUN-KASH complex and show that a covalent bond between SUN and KASH is essential for forces transmission across the NE. Finally, we present our findings on the molecular mechanisms of the activation and oligomerization of members of the SUN domain protein family.

Chapter 1

CELLULAR RESPONSES TO MICRO- AND NANO-TROPOGRAPHY

1.1 CELL RESPONSES TO METALLIC NANOSTRUCTURE ARRAYS WITH COMPLEX GEOMETRIES

Introduction

Metallic nanopillar/nanowire arrays are becoming widely recognized as promising platforms for characterizing and regulating cell functions (Mcguire et al. 2018). For example, nanowire arrays are used as a high-throughput method for direct cytosolic biomolecule delivery with a wide range of potential applications such as drug delivery, gene transfection and immunofluorescent staining (Shalek et al. 2010; Kim et al. 2007). Furthermore, nanowires have been used for stimulation and recording of single neural activities (Robinson et al. 2013; Robinson et al. 2012), localized fluorescent imaging (Xie et al. 2011), neuron pinning (Xie et al. 2010), and most recently, exploring mechanisms of cell nanotopography sensing (Albuschies & Vogel 2013). Nanowires of complex geometries have occasionally been used for specific cellular applications; hollow 100nm alumina nanowires were able to pierce cells, and form fluidic pipelines efficiently delivering ions directly into the cytosol (VanDersarl et al. 2012). Mushroom shaped gold electrodes were used to activate cell phagocytic-engulfment mechanisms, and form strongly sealed membrane-electrode interfaces for detection of subthreshold synaptic and action potentials (Hai et al. 2010).

Over the past two years, numerous studies have investigated cell-nanowire interactions with a focus on the plasma membrane-nanopillar interactions, at their interface, examining the ability of nanowires to penetrate cells (Hanson et al. 2012; Berthing et al. 2012; Wierzbicki et al. 2013; Xie, Alexander M Xu, et al. 2013). However, with the exception of long nanowires (diameter to height ratios greater than 10) which have shown to impair cell function (Persson et al. 2013) , in most cases, nanopillars do not penetrate cells but form adhesions on the nanopillar surfaces (Berthing et al. 2012; Hanson et al. 2012). Moreover, when penetration does occur, it is likely mediated by adhesion dependent forces (Xie, Alexander M Xu, et al. 2013). Herein, we investigate the interactions of 3T3 Swiss Albino fibroblast cells with arrays of metallic nanopillars of various shape, size and spacing. Nickel nanopillars of various geometries were fabricated on a single platform allowing the direct assessment and comparison of single nanopillar-cell interactions. Hollow, x-shaped, c-shaped and mushroom-shaped nanopillars were also fabricated to study the response of cells to nanostructural features of naopillars. Finally, we assessed the response of cells to palladium nanopillars of similar geometries which were weakly bonded to the flat substrate underneath, allowing the inspection of another potential effector of cell-nanopillar interaction. We propose

Methods

Nanopillar fabrication. Nickel and palladium nanopillars were fabricated using ebeam lithography and electroplating techniques (Seo et al. 2013; Jahed, Jin, et al. 2012). Silicon substrates were coated with a ~20nm adhesive layer of titanium and ~30-100nm gold using electron beam evaporation. A layer of Poly methyl methacrylate (PMMA) photoresist was then spin coated on the substrate with various speeds to obtain desired thicknesses.

Following PMMA coating, a variety of hole diameters and cross sectional geometries were patterned on the resists by an electron beam with a 100kv acceleration voltage using a Leica EBPG 5000+ electron beam lithography system. Nickel and palladium metals were electroplated into the patterned arrays using Galvanostatic electroplating techniques. Watts-type nickel electroplating solution was made in-house, containing 300 g/l of nickel (II) sulfate hexahydrate (99%, Sigma Aldrich), 30 g/l nickel (II) chloride (98%, Sigma Aldrich), and 30 g/l of boric acid (BX0865, EMD Millipore)(Rashidi & Amadeh 2010) . A commercially available palladium tetrammine (II) chloride based electroplating solution (Technology Without Limits, Inc.) was used for fabricating palladium nanopillars. Electroplating duration and current densities were adjusted to obtain desired nanopillar heights. Mushroom shaped nanopillars were fabricated by extending the electroplating duration and allowing the growth of metals above the photoresist thickness. The photoresist films were removed by submerging samples into a bath of acetone and samples were further cleaned with a final rinse of acetone and isopropanol.

Cell culture. 3T3 Swiss Albino fibroblasts were maintained in Dulbecco's Modified Eagle Medium (DMEM; Lonza, USA) supplemented with Fetal Bovine Serum (FBS; Lonza, USA) and penstrep (Invitrogen, NY, USA) at 37 0C, 5% CO2 and 95% humidity. Cell culture medium was replaced every 2 to 3 days. Samples were sterilized using UV light for 20 minutes. Following sample sterilization, 4×104 cells were seeded on the samples and incubated for 24, 48, and 72 hours.

SEM sample preparation. Interactions of fibroblasts with metallic nanostructures were characterized by scanning electron microscopy. To prepare for microscopy, samples were first rinsed with 0.2mM sodium phosphate buffer (v/v: 36 ml Na2HPO4/14 ml NaH2PO4) and then fixed with 2.5% glutaraldehyde at 40°C overnight. Samples were then dehydrated using a graded series of ethanol dilutions (10% to 100%) and dried for two hours prior to microscopy. All images were taken at a 70° SEM stage tilt.

Results and Discussion

Size, shape and spacing of nanopillars. Arrays of ~220nm solid nickel nanopillars with heights of ~1.25μm, and 10 μm spacing (Figure 1a,b), were fabricated to assess cell interactions with small diameter, and high aspect ratio nanopillars. The effect of nanopillar spacing was also studied by fabricating arrays of solid nickel nanopillars (600nm in diameter) in clusters of 13 nanopillars spaced 500nm apart, alongside 10μm spaced individual nanopillars (Figure 1c). 1 μm outer diameter nickel nanopillars with various cross sectional geometries and 10μm spacing (Figure 1d-h) were also fabricated to explore the adhesion of cells to nanostructural features. Mushroom shaped nickel nanopillars of various sizes and 10μm spacing (Figure 1i-k, S1) allowed the study of more complex geometries, while activating cell-nanopillar engulfment mechanisms. Palladium nanopillars of 1 μm outer diameter with various cross sectional geometries and 10μm spacing (similar to nickel structures in Figure 1f) were also fabricated. SEM micrographs (Figure 1m) revealed that a significant fraction of palladium nanopillars were washed off the substrate during the fabrication process leaving a non-uniform array of nanopillars prior to cell culture. This showed poor bonding and low interfacial strength between palladium

nanopillars and the gold substrate, allowing these structures to be suitable for studying the effects of nanopillar-substrate interfacial strengths on nanopillar-cell interactions.
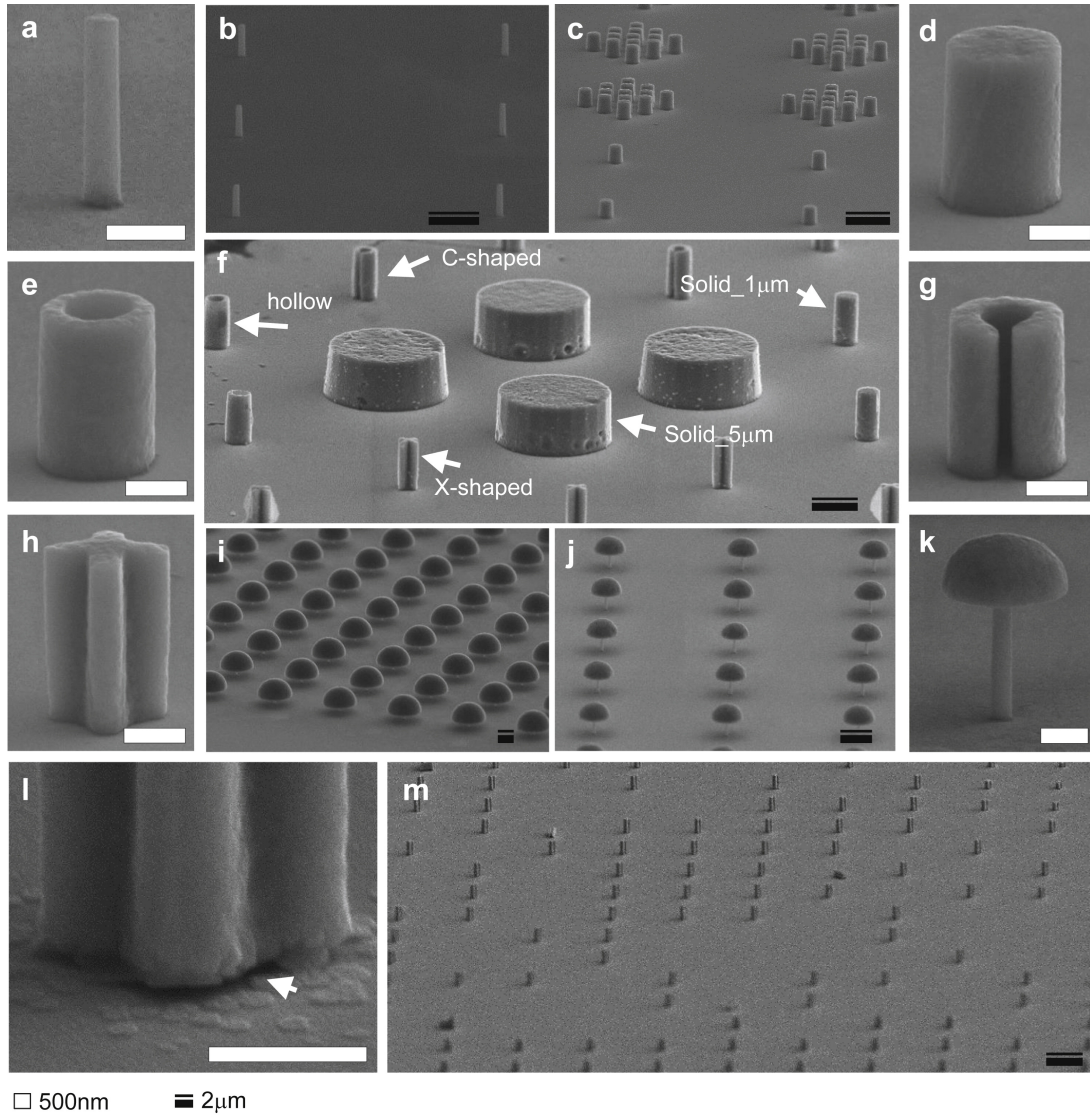
Figure 1: SEM micrographs of nanopillars of various size, shape and materials. (a) a representative image of ~220 nm diameter, high aspect ratio nickel nanopillar, (b) array of 220 nm nickel nanopillars with 10μm spacing, (c) arrays of clustered and individual 600nm nanopillars on a single substrate, (d) a representative image of 1μm solid nanopillar, (e) representative image of 1μm outer diameter hollow nanopillar, (f) arrays of solid, hollow, c-shaped and x-shaped nanopillars with 1μm outer diameters and 10μm spacing, and solid 5 μm disk shapes, (g) representative image of c-shaped nanopillar with 1 μm outer diameter, (h) representative image of x-shaped nanopillar with 1μm outer diameter, (i),(j) arrays of mushroom-shaped pillars with various mushroom top sizes and 10 μm spacing (k) representative image of a mushroom shaped nanopillar with a ~220nm stem, (l) image of palladium cross shaped nanopillar showing a small gap at the interface of the nanopillar with the gold substrate underneath (arrow), (m) arrays of palladium nanopillars, several pillars were detached from the substrate during fabrication, indicating weak bonds between nanopillars and the gold substrate. All white scale bars represent 500nm and black scale bars represent 2μm.

Basic cellular functions on nanopillar arrays. Fibroblasts were able to adhere and spread on the metallic platforms without any special treatment of the metal surface with extracellular matrix (ECM) molecules prior to the cell culture (Figure 2a-c). Several finger-

8

like membrane protrusions (filopodia) were extended from cells that were not fully spread (Figure 2a,b). Additionally, a few retraction fibers remained attached to distant nanopillars in cells that were fully spread (Figure 2 c-e). Filopodia are known to be highly involved in nanotopography sensing in initial stages of cell-substrate contact (Dalby, Gadegaard, et al. 2004; Albuschies & Vogel 2013; Bornschlögl et al. 2013). Albuschies et al. (Albuschies & Vogel 2013) showed that fibroblast filopodia quickly retracted from the flat substrate but maintained contact with silicon nanowire bundles. Our results show that each fully spread cell interacted with at least 6 nanopillars spaced 10μm apart. To observe cell growth on the nanopillar arrays, cells were incubated on three different substrates for 24, 48 and 72 hours (Figure 3a-c, S2). Almost full confluency was reached on patterns after 72 hours of incubation (Figure 3c, S2). To analyze single cell-nanostructure interactions as opposed to cell-cell interactions, 24-hour incubation was chosen to achieve an optimum cell density on each array. Cell division was also seen in several cases where cells were fixed during division, and before respreading on the substrates (Figure 4a,b). Finally, several cell-cell connections were formed in areas with higher density of cells (Figure 4c,d, S2). These junctions are conceivably maintaining connections between filopodia-like protrusions of each cell, after cell spreading. Hoelzle et al. (Hoelzle & Svitkina 2012) observed similar results where cells initially interacted with neighboring cells through protruding lamellipodia, and maintained filopodia-like contact bridges after cell retraction. Our results show that cells maintain regular basic functions despite interactions with the metallic nanopillar arrays.
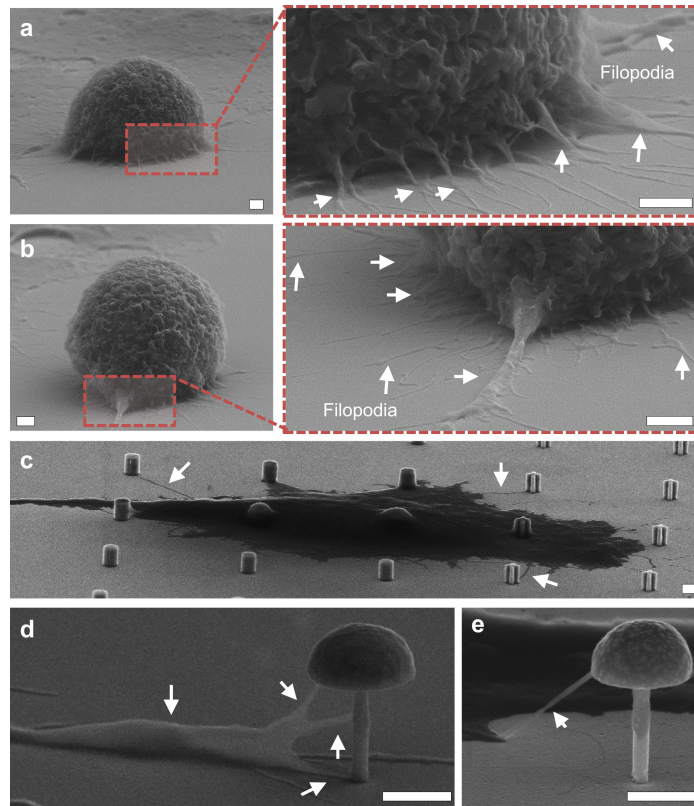
Figure 2: (a),(b) figure of fibroblasts adhering to the substrate, several long filopodia extended from the cell to sense the environment. (c) Image of a single spread cell where most of the filopodia has retracted with few remaining attached to nanopillars. (d),(e) finger -like filopodia sensing mushroom shaped nano-pillars. All scale bars represent 1μm.
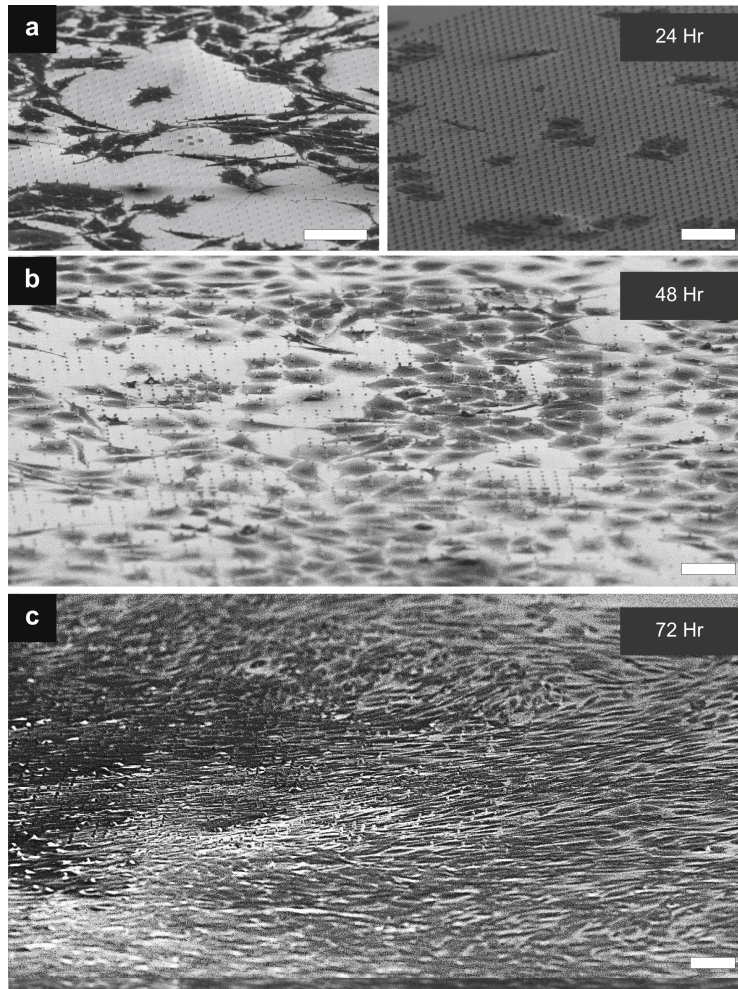
Figure 3. SEM Images of nanopillar substrate after (a) 24, (b) 48 and (c) 72 hours of incubation, cells reached full confluency on top of the nanopillar arrays after 72 hours. All scale bars represent 40μm.
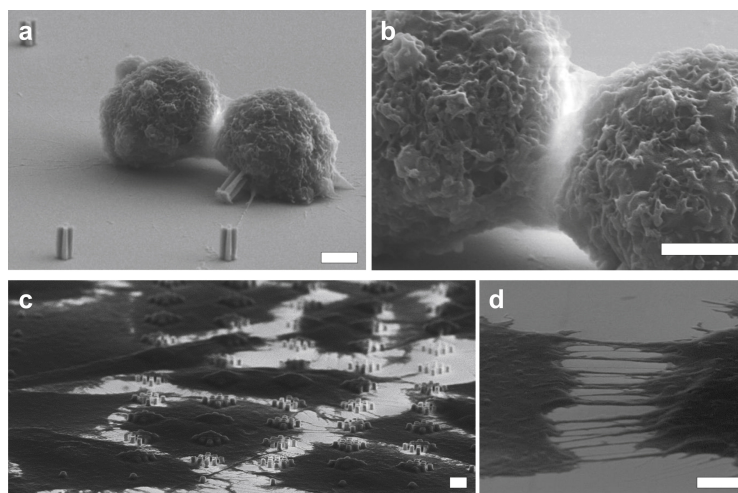
Figure 4. (a),(b) Images of fibroblasts dividing on the nanopillars, cells were fixed at the time of division , and before re-spreading on the substrate. (c), (d) cell-cell junctions were formed by connections between filopodia like membrane protrusions of two cells. All scale bars represent 2μm.

Cell interactions with nickel nanopillar arrays. Cells fully spread on top of the 220nm nanopillars. In some cases, the tips of the 220nm nanopillars were visible, suggesting possible membrane penetration and rupture by these small and high aspect ratio nanopillars (Figure 5a). Such cell-nanopillar interactions have been proven suitable for molecule delivery to the cytosol (Shalek et al. 2010; Kim et al. 2007). Conversely, in most cases, 1μm outer diameter nanopillars of various cross sectional geometries, and lower aspect ratios were buried underneath the cell, where the cell membrane appears to engulf the nanopillars. For example, 1μm solid core nanopillars were fully buried under the cell (Figure 5b). Similarly, the cell membrane conformed to the shapes of hollow, c-shaped, and cross-shaped nanopillars (Figure 5c-f). The cell membrane appears to form contacts within the hollow nanopillars (Figure 5c), and on the groves of x-shaped and c-shaped nanopillars (Figure 5d, e). s
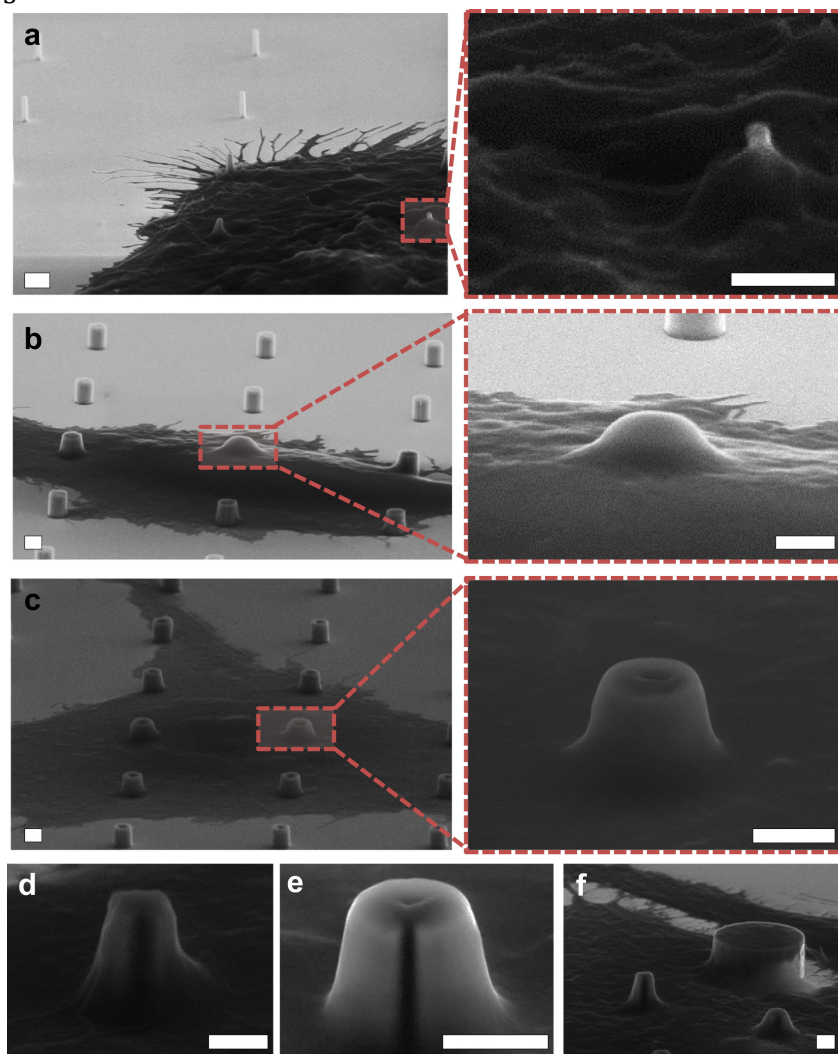
Figure 5. A variety of nanopillar-cell interactions , (a) fibroblasts fully spread on top of ~220 nm nanopillars, some nanopillars tips were visible in SEM images, suggesting full nanopillar penetration through the cell, (b) a fibroblast fully spread on 1μm diameter solid nanopillars, where most pillars were buried under the cell body, (c) fibroblast spread on top of hollow shaped array of nanopillars, the membrane conformed to the shaped of these nanostructures and appears to adhere to the inside of the hollow nanopillars. (d)-(f) membrane conformed to the shape of x-shaped and c-shaped nanopillars forming contacts on the sidewall grooves. All scale bars represent 1μm.

The response of cells to clustered arrays of 600nm diameter nanopillars was highly dependent on the location of cell-nanopillar interaction. Our results suggest a disturbed sensing and retraction of filopodia on these nanopillars. At the edge of the cells, several membrane protrusions remained on the clustered arrays with signs of membrane rupture at these locations (Figure 6a). Contrarily, at the center of cells, all 600nm nanopillars were buried under the cells with no signs of membrane rupture (Figure 6a,b). Similar results have been observed for bundles of silicon nanowires where cells retracted all protrusions but ones attached to the bundles, and eventually all nanowires were realigned in the direction of the retraction fibers (Albuschies & Vogel 2013).
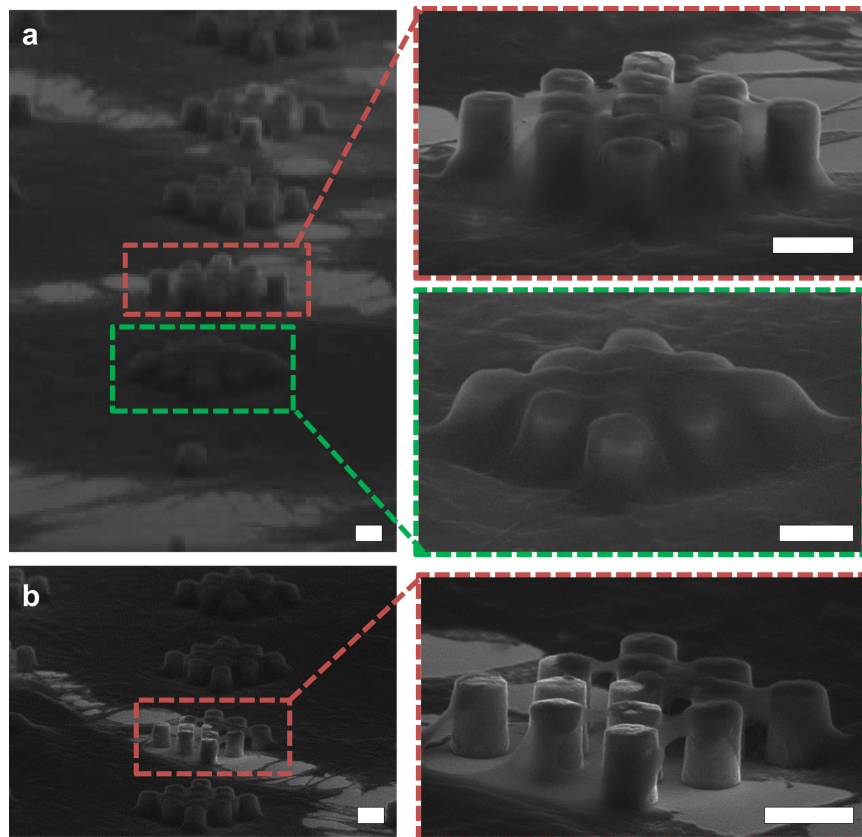
Figure 6. Fully spread fibroblast on clustered nanopillars resulting in two types of cell-naopillar interactions at the cell center and edges. (a) two locations of cell-nanopillar interactions are shown where nanopillars are buried under the cell in the cell center (top image) and membrane protrusions remain on the nanopillars with signs of membrane rupture at the cell edges (bottom image). (b) image of cell edge where several membrane protrusions are trapped on clustered nanopillars. All scale bars represent 1μm.

Cells responded uniquely to the mushroom shaped nanopillars. In most cases, cells were able to tilt the ~220 nm mushroom shaped nanopillars towards the cell body (Figure 7a,b, S3). In some cases, pillars at distances greater than 5 μm from the cell edge were detected and pulled towards the cell with a single filopodium contacting the nanopillar (Figure 7a). Strong propulsive traction forces were previously seen at small (nascent) adhesions, which decreased as mature focal adhesions were formed (Beningo et al. 2001). Mushroom shaped nanopillars in direct contact with the cell body are also tilted likely due to traction forces, and all seem to be pulled towards a center (Figure 7b, S3). Micro-post arrays and

elastomeric pillars have been used extensively for cell traction force measurements (Tan et al. 2003; Wang & Lin 2007). However, due to their rigidity and plasticity, metallic nanopillars have not been a suitable candidate for cell traction force assessments. On the other hand, nanopillars with lower stiffness (smaller diameters) do not allow the formation of mature focal adhesions; due to small areas at the top of these pillars, adhesions can not mature and thereby measurement of forces generated by mature focal adhesions are not possible. However, the unique geometry of mushroom shaped nanopillars provide enough surface area (>1 µm) for mature focal adhesions to form at the large mushroom caps, while the small stems allow pillar deflection with forces in the ranges exerted by cells. This method can be used to determine 3D vectors of cell force generation; to determine the direction of spatially localized single filopodia forces at various stages of sensing, adhesion and spreading. The other advantage of these metallic nanopillars over polymeric micro-post arrays is that cells are able to attach to these surfaces without surface functionalization with ECM molecules.
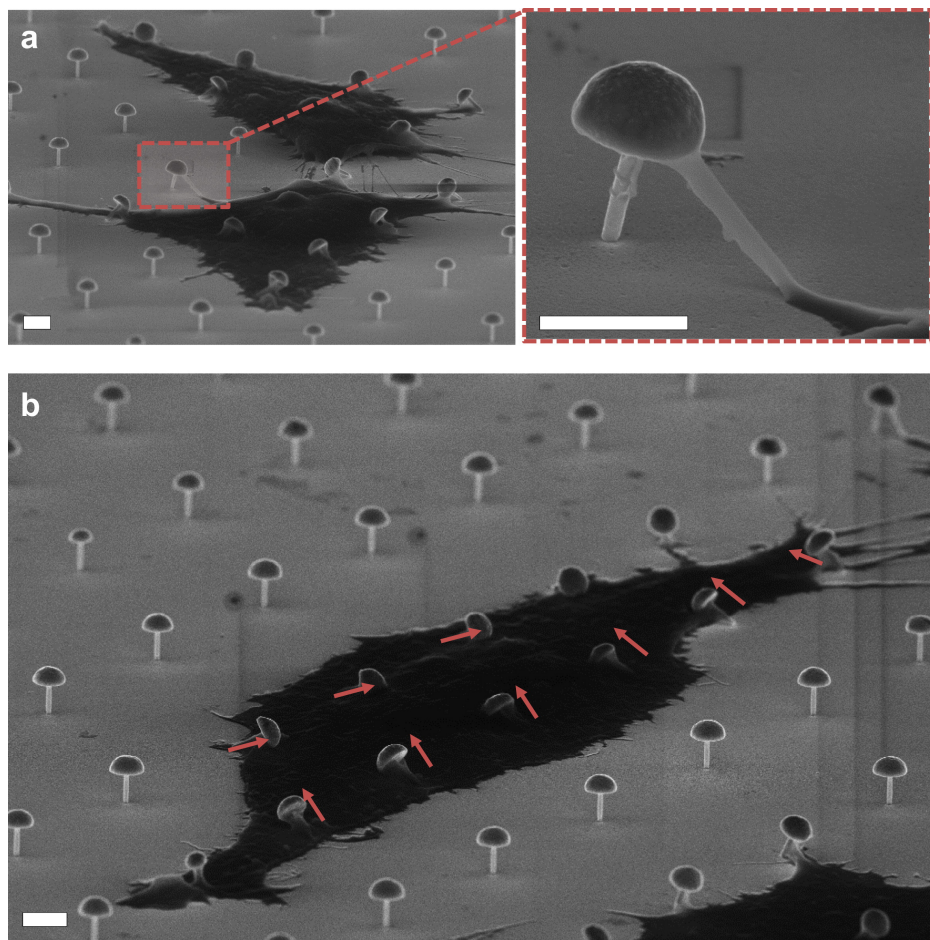
Figure 7. Mushroom shaped nanopillars were pulled towards the cell body, (a) a fully spread fibroblast pulling on a distant mushroom shaped nanopillar by a single filopodium (b) Localized force directions can bee determined from nanopillar tilt directions (red arrows). Scale bars represent 2µm.

Cell interactions with palladium nanopillar arrays. Fibroblasts were also seeded on palladium nanopillars with similar geometries to assess cell responses to other metals. Palladium nanopillars appear to have weaker interfacial strengths with the substrate than nickel nanopillars as several pillars were detached from the surface, prior to cell culture (Figure 1l,m). This detachment is conceivably caused by the turbulent flow stresses incurred by fluids used to rinse the substrate during the fabrication process, as previously discussed. Consequently, these nanopillars were not able to withstand forces exerted by the retracting protruded cell membrane, and were detached from the substrate, lifted by single filopodia and transported towards the cell body (Figure 8a,b). Bornschlögl et al. (Bornschlögl et al. 2013) showed the displacement of an optically trapped bead by a single fibroblast filopodium. We observed such behaviors in both unspread (Figure 8a) cells and fully spread (Figure 8b) cells. Figure 8b shows the lifting of two nanopillars by a fully spread cell; in both figures the protruded membrane wraps around the round nanopillar sidewalls, creating a larger contact area. Such nanopillar-cell interactions can possibly be the cause of nanopillar uptake for small nanopillars seen previously in some studies (Wierzbicki et al. 2013; Safi et al. 2011; Song et al. 2010).
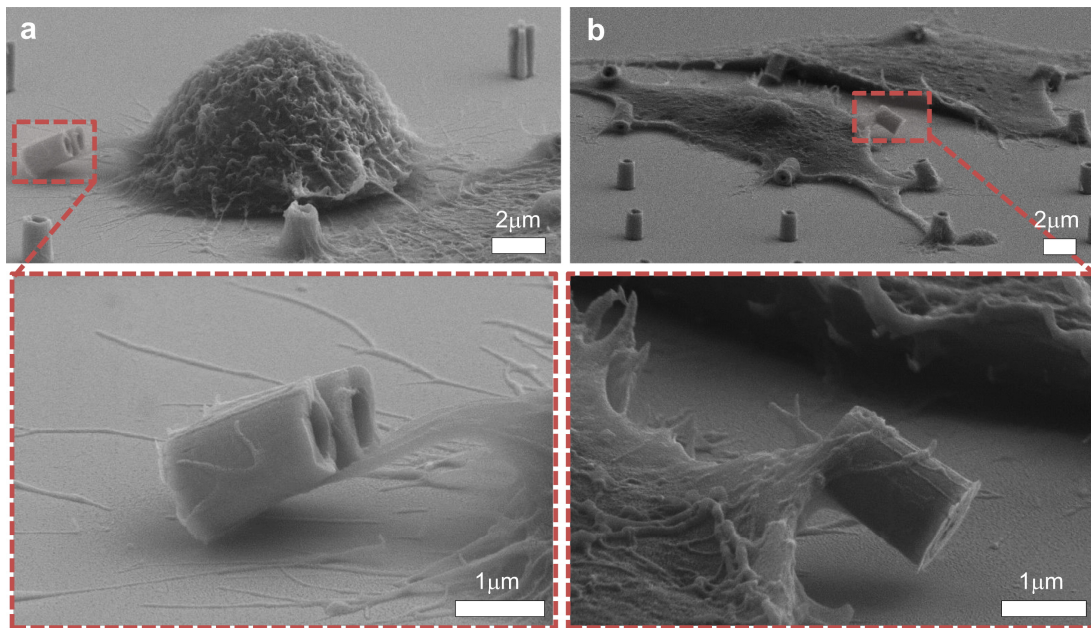
Figure 8. Fibroblasts lifting palladium nanopillars off the substrate possibly during filopodia retraction, (a) an unspread cell lifting two hollow nanopillars with membrane protrusions wrapped around the nanopillars, (b) a fully spread cell lifting a single hollow nanopillar by wrapping several membrane protrusions around its sidewalls.

Membrane thinning. Mushroom shaped nanopillars with 500nm diameter stems, and large mushroom caps (~2.75 μm diameter) exhibited penetration through the cell, regardless of their interaction location with the cell (Figure 9a, S4). Hanson et al. (Hanson et al. 2012) show that cortical neurons maintained their membrane integrity on 500nm in diameter nanopillars and up to 2μm tall, suggesting that the nanopillars are not able to penetrate the cell membrane. However, our results show localized thinning and possible rupture of the plasma membrane on the mushroom shaped nanopillars (Figure 9a, S4). The observed membrane thinning can be caused by an "adhesion mediated" process similar to

14

recent mechanical models of nanowire penetration into cells proposed by Xie et al (Xie, Alexander M Xu, et al. 2013). Upon landing on these nanopillars, cells form adhesions with the large pillar mushroom tops (see Figure 9b-1). At the same time, cells possibly deform around the nanopillar and ultimately form strong integrin mediated focal adhesions at the flat substrates (see Figure 9b-2) and subsequent adhesions are formed at the pillar base (see Figure 9b-3) as the cell attempts to engulf the nanopillar in an phagocyte-like mechanism. Consequently, the membrane withstands high tensile forces between the mushroom top and stems ultimately resulting in membrane thinning and potential rupture in these areas. Hai et al. (Hai et al. 2010) also observed tight adhesions formed around mushroom shaped gold electrodes. However, Hanson et al. (Hanson et al. 2012) observed close membrane-nanopillar contacts at the bottom of cylindrical nanopillars, whereas cavities were formed at the top of pillars, suggesting that the mushroom tops are favorable for cell adhesion.
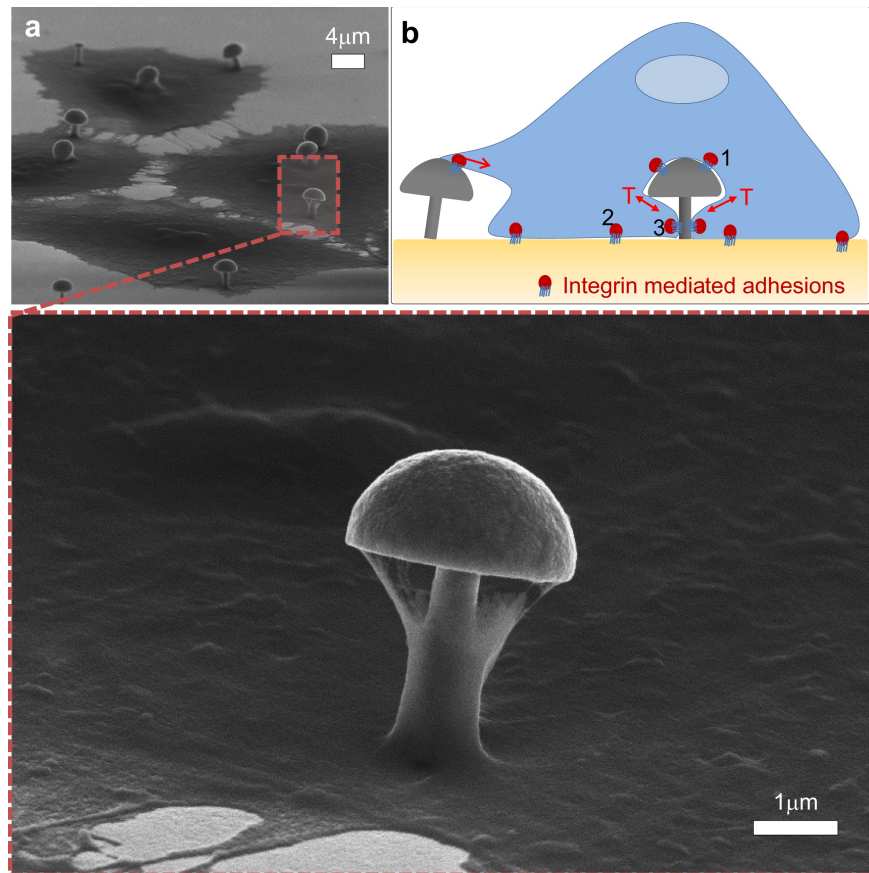
Figure 9. (a) Large mushroom shaped nanopillars of 500nm diameter penetrating a fibroblast. Membrane stays intact at the bottom of the nanopillar and membrane rupture is observed at the mushroom-stem interface. (b) Schematic of proposed mechanisms of membrane rupture based on previously observed "adhesion mediated" nanopillar penetration. 1- Cells initially form adhesions on the mushroom shape tops of each nanopillar as they land on top of a nanopillar, 2- they continue to deform around the nanopillar until they sense the substrate, where they form strong focal adhesions. 3- subsequently, adhesions begin to form at the pillar base while the cell attempts to engulf the nanopillar (a phagocytotosis-like mechanism), resulting in tensile forces (T) on the cell membrane at the mushroom top-stem interface , and ultimate membrane rupture during cell spreading.

Conclusions

Cell-nanopillar interactions have been shown to depend on several factors, such as cell membrane properties (cell type), and nanopillar size and spacing; our results show dependencies on location of cell interaction with nanopillar (i.e. edges vs. cell center), and nanopillar geometry, in addition to their size and spacing. We also show that interfacial strengths between the nanopillar and flat substrate play an important role in cell-nanopillar interactions where weaker interfacial bonds can lead to nanopillar detachment from the surface. Based on our results, various types of cell-nanopillar interaction can be achieved, regulating cell function on a single platform consisting of different nanopillar geometries. To better understand the mechanisms of interaction, small diameter nanopillars which penetrate cells can be added to the platform and utilized to deliver biological effectors into cells. Consequently, responses of cells to all other nanostructures can be assessed on the same platform, upon disturbing various regulators of nanostructure sensing with the delivered biological effectors. Combining various cell-nanopillar interactions on a single platform with methods presented here will allow the direct assessment of different cell sensing and adhesion mechanisms upon cell transfection with effectors tethered to membrane-penetrating nanopillars.

1.2 DIFFERENTIAL COLLECTIVE AND SINGLE CELL BEHAVIORS ON SILICON MICROPILLAR ARRAYS

Introduction

Cells have the ability to sense and respond to the micro- and nano scale topography of their environment (D. H. Kim et al. 2012). Studies on micro- and nano-patterned engineered surfaces have demonstrated the influence of topography on a variety of cellular functions including the directed migration of endothelial cells and fibroblasts (Jiang et al. 2005; Mahmud et al. 2009), osteogenic differentiation of stem cells (McBeath et al. 2004; Avizienyte & Frame 2005; Popat et al. 2007; Gittens et al. 2012), altered mechano-sensitive gene expressions in fibroblasts (McNamara et al. 2012; Dalby, Gadegaard, et al. 2004; Dalby, Riehle, et al. 2004; Dalby 2005), directional polarization of neurons (Rajnicek et al. 1997; Fozdar et al. 2011; Gomez, Lee, et al. 2007; Gomez, Chen, et al. 2007; Gomez, Lu, et al. 2007; Ferrari et al. 2010) and immobilization of tumor cells (Wang et al. 2014; Wang et al. 2010) .

Researchers have taken advantage of these cellular responses and utilized micro and nanostructured surfaces and in particular, vertically aligned three-dimensional (3D) pillar structures, for a wide range of biological applications. Small-diameter nanowires with high aspect ratios are known to penetrate the cell membrane and are therefore most commonly used for applications requiring intracellular access such as drug delivery (Xie, Alexander M. Xu, et al. 2013; Chiappini et al. 2015; Shalek et al. 2012; Persson et al. 2013; Shalek et al. 2010; VanDersarl et al. 2012). On the other hand, larger pillar structures are engulfed by the cell without membrane rupture and are more commonly used in applications requiring an intact cell membrane. For example, nanopillar arrays have been used for noninvasive immobilization of neurons to obtain long periods of activity measurements from the same neuron (Xie et al. 2010). Furthermore, silicon micropillar arrays have been utilized for efficient isolation and capture of circulating tumor cells, possibly through enhanced local topographic interactions of cells with the micropillars (Wang et al. 2014; Wang et al. 2010; Zhang et al. 2016; Nagrath et al. 2007).

A great number of experimental and computational studies have examined the mechanisms of small-diameter nanowire penetration into cells showing that penetration depends on several parameters including the nanowire diameter, height to diameter aspect ratio, and spacing (Xie, Alexander M Xu, et al. 2013; Xie et al. 2015; Aalipour et al. 2014; Persson et al. 2013; Berthing et al. 2012). However, a limited number of studies have looked at cell interactions with larger pillar structures where penetration is unlikely to occur (Hanson et al. 2012; Wang et al. 2014; Zeinab Jahed, Molladavoodi, et al. 2014). Wang et al. examined the role of spacing and diameter on the capture rates of circulating tumor cells and showed that higher capture rates were achievable on pillar arrays of smaller diameters compared with larger pillars or a flat silicon wafer (Wang et al. 2014). Hanson et al. characterized the cell-nanopillar interface using transmission electron microscopy and showed that cortical Neurons preferentially sit on top of nanopillars with 500nm diameters and 1μm center-to-center spacing, but engulf nanopillars with 200nm diameters and similar center-to-center spacing (Hanson et al. 2012). Finally, Xie developed a continuum mechanical model to quantify the cell-pillar interactions and showed that this interaction is not only dependent

on the pillar geometry, but also the flat surface or gap available between the nanopillars, which is a function of nanopillars spacing. Their results suggest that decreased nanopillar spacing can lift the cells away from the flat silicon surface. Despite great advancements in understanding cell-pillar interactions, the effects of these rigid structures on intracellular components such as the nucleus and cytoskeleton remains understudied. Additionally, the collective behaviors of cells on pillar arrays are poorly understood. In this study, we fabricated vertically aligned arrays of micropillar structures side by side on a silicon platform. These micropillar arrays consisted of micropillars of identical heights and side-to-side spacings, but with varying geometries allowing us to explore single and collective cell behaviors at array interfaces. Using high resolution scanning electron microscopy and fluorescent microscopy techniques we show that cells on the same platform interact distinctly with micropillars of varying sizes. Interestingly, aggregation and branching of cells was observed on specific micropillar arrays but restrained on neighboring arrays with different micropillar geometries. Cells interacted with the top surfaces of larger micropillar arrays and conversely with the sidewalls and flat areas between smaller diameter micropillars. Furthermore, cell protrusions conformed to the shape of micropillars and local cytoskeletal rearrangements were observed on micropillar arrays.

Results

Fabrication of Silicon platform. Arrays of rigid silicon micropillars of various geometries were successfully fabricated side by side on a silicon platform (Figure 1A). This platform was used to assess glioma cell responses to vertically aligned 3D micropillars of varying geometry and configuration. Fabricated micropillars were characterized using scanning electron microscopy (SEM) as shown in Figure 1B-D. The outer diameters of the fabricated micro-pillars were measured to range from 0.7-5.5µm. Each silicon platform consisted of two arrays of the same micropillar geometry, one with a square configuration (Figure 1C-i) and another with a hexagonal configuration (Figure 1C-ii). In all arrays, a constant 5µm side-to-side spacing was maintained between neighboring micropillars resulting in comparable free flat areas between the micropillars irrespective of their sizes. Furthermore, the heights of all micropillars were maintained at 2µm. The designed platform allowed for characterizing single glioma interactions with the distinct topographic features of each micropillar array, comparing cell behaviors at array interfaces, and assessing the collective behaviors of cells on the entire silicon platform.

Preferential aggregation of cells on large micropillar arrays. U87 glioma cells were plated on the silicon platforms uniformly covering all micropillar arrays. After 24 hours, cells showed a slightly higher concentration on small sized micropillars (Figure S1). Interestingly, after 68 hours, glioma cells exhibited distinctive arrangements on various micropillar arrays. Cells formed aggregates on micropillars with outer diameters larger than 2mm, whereas cells on micropillars smaller than 2mm were evenly distributed on the platform leaving small voids. This was evident from dark field microscope images of the interfaces between small (<2mm) and large (>2mm) micropillar arrays on both square (Figure2A-1) and hexagonal (Figure 2A-2) array configurations on the silicon platforms. Magnified images indicated larger voids (areas with no cells), and longer branch like connections between cell aggregates on larger micropillar arrays as shown in Figure2B.

These results were observed on several silicon platforms and to quantify this collective cell behavior, we measured the cell coverage area, defined as the ratio between the area covered by cells and the total imaged area (see methods), for each micropillar array on two identical silicon platforms as shown in Figure 2C (blue and red curves). Both platforms showed similar trends in coverage area as a function of micropillar diameter. In both cases, micropillars with diameters <2mm showed the highest cell coverage and a decrease in cell coverage area for larger micropillars (Figure 2C). The lowest coverage areas were observed for cells on a smooth flat silicon substrate (Figure 2C). As shown in Figure 3, although Platform 1 (blue) and Platform 2 (red) show the same trends, Platform 1 (blue curve) exhibited overall higher cell coverages on all micropillar arrays despite identical cell seeding and growth conditions. Therefore, for better control, in this study we only compare cell behaviors on the different micropillar arrays of the same silicon platform.
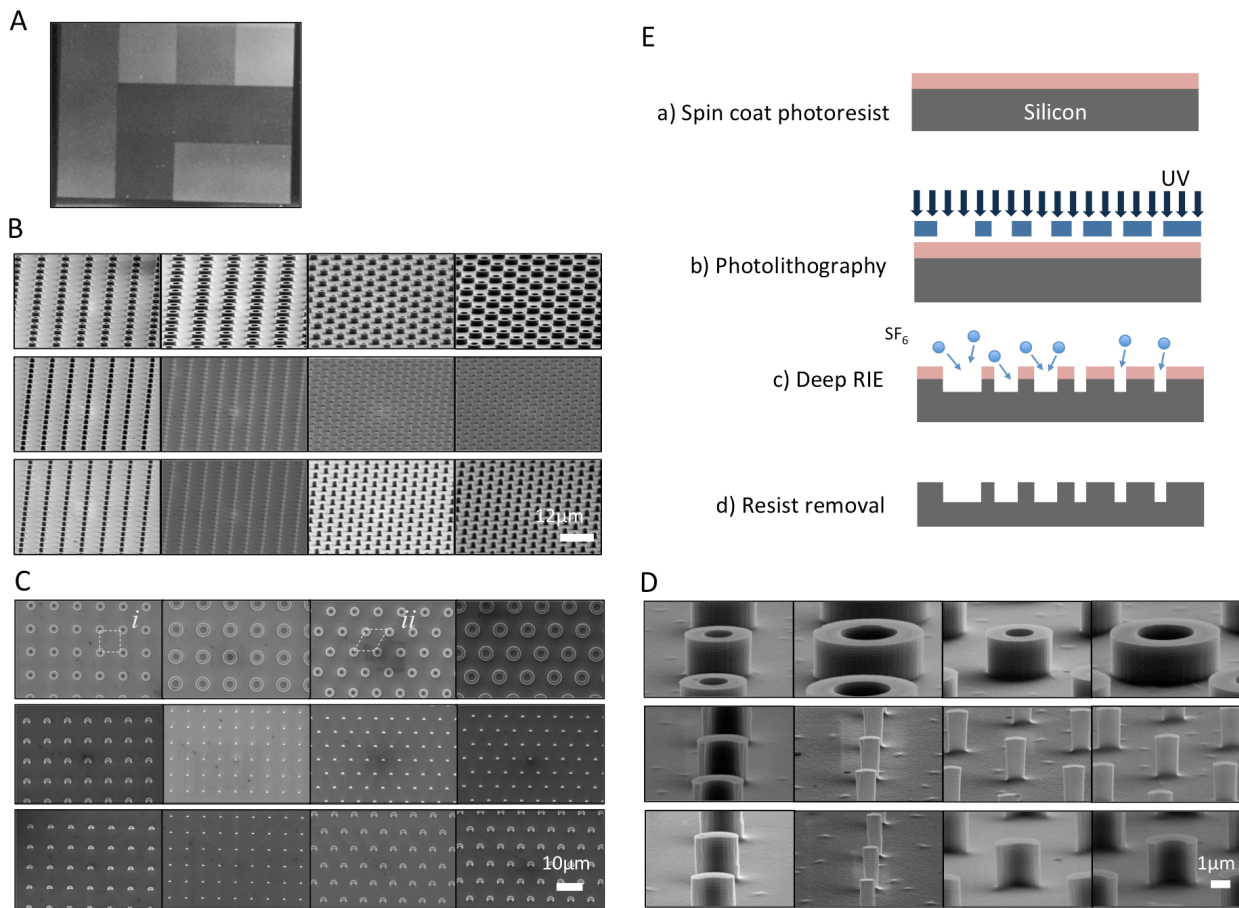
Figure 1: Fabricated Silicon platform consisting of micropillar arrays of various shape, sizes and configurations. A) Digital camera image of the Silicon platform showing 12 different micropillar arrays fabricated on a single device. B) Scanning electron micrograph of each array observed at 70° and C) 0°stage tilt angles. D) High magnification Scanning electron micrograph of each micropillar in the arrays. E) Fabrication process of Si micropillar platform including the spin coating of a photoresist onto silicon substrates (a), performing photolithography to achieve the desired patterns on the resists (b), followed by a deep reactive ion etching process in which the silicon micropillars are fabricated (c), and a final removal of the photoresist (d).

The highest cell coverage areas were observed within the smaller silicon micropillar dimensions with outer diameters of <2mm, and were statistically significant from all other micropillars with outer diameters >2mm, and from a control flat silicon substrate. However, the differences between the measured coverage areas of micropillars arrays with outer diameters ranging from 2.5-5.5mm was not statistically significant.

We also compared the cell coverage areas for square vs. hexagonal configurations of each micropillar size for both platforms as shown in figure S2. However, the coverage areas seem to be independent of the micropillar configurations tested in this study.

In order to observe cells-micropillar interactions in 3D, the silicon platforms were inspected using high resolution scanning electron microscopy at a 70 degree° stage tilt at the mircopillar array interfaces. On larger structures, glioma cells formed large cell aggregates with long branches consisting of few elongated cells connecting neighboring cell aggregates both in the hexagonal (Figure 3A) and square (Figure 3B) array configurations. These SEM images also confirmed the presence of larger voids between cell aggregates on large micropillar arrays.
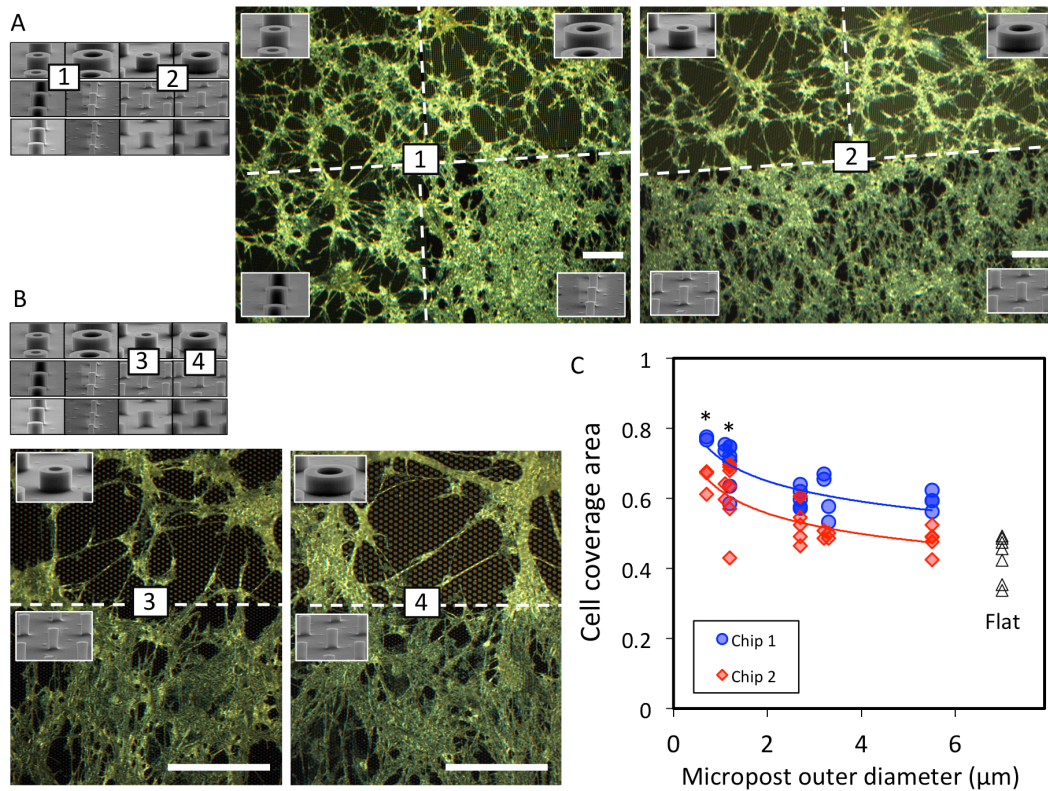
Figure 2: Dark field microscopy images of U87 glioma cells on a Si micropillar platform showing the interfaces between the smallest and largest micropillars, cell arrangements and branching are evidently different between the various regions. B) High magnification dark field microscope image of U87 cells spreading differentially on various regions of the micropillar platform. C) Cell coverage area as a function of micropillar size, * symbol represent the difference compared with all other micropillars with outer diameters greater than 2 μm and the control flat silicon substrate (Mann–Whitney U test, p <0.01). Scale bars represent 200μm.
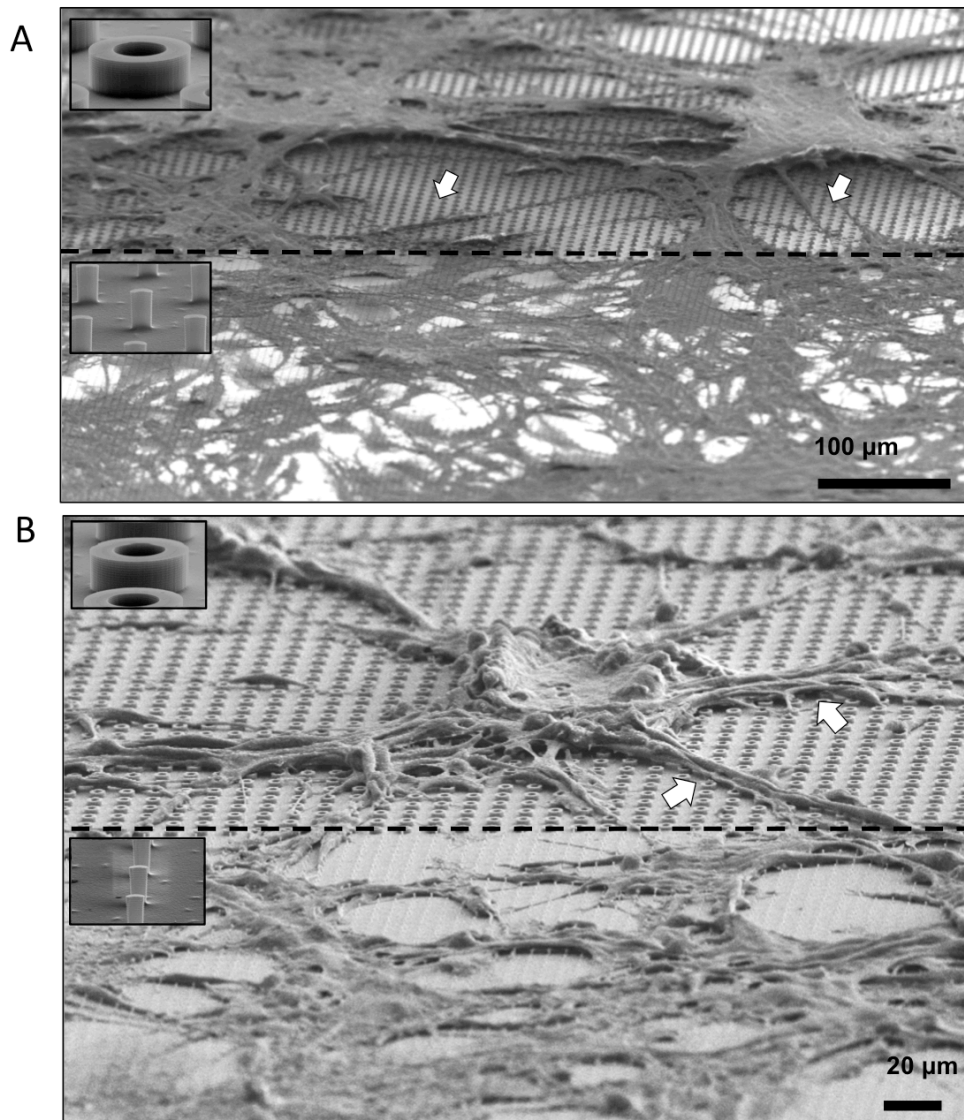
Figure 3: A) SEM micrograph of U87 glioma cells on the interface of two micropillar arrays with different sizes, with A) hexagonal or B) square configurations. Cells show a tendency to form tumor-like aggregates on larger structures (top) whereas fewer clusters are seen on small micropillars (bottom). These aggregates are connected via long branches consisting of one or several cells (white arrows).
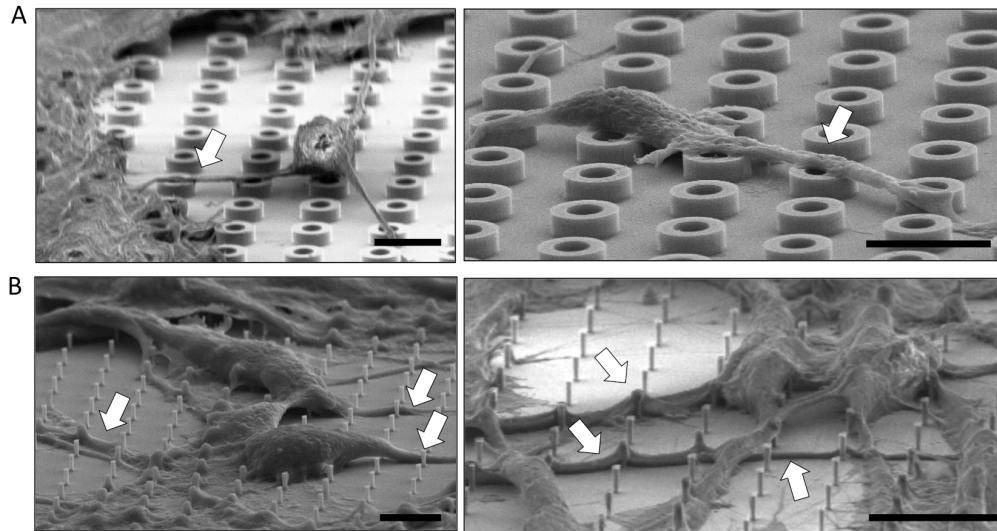
Figure 4: Representative images of U87 glioma-micropillar interactions. A) U87 cells sit on top of micropillars with outer diameters >2µm while cell protrusions (white arrows) interact with pillar tops rather than the flat area in the gap between micropillars B) U87 glioma cells and their protrusions (white arrows) interact with small micropillars (outer diameters <2µm) as well as the flat silicon area in between micropillars. All scale bars correspond to 10µm.

F-actin rich cell protrusions interact distinctly with small vs. large micropillars. High resolution SEM inspections of single cell-micropillar interactions showed that despite similar side-to-side spacing between micropillars of all sizes, on large micropillars (>2mm), the cell body is lifted away from the flat silicon substrate and cells preferentially anchored onto micropillar tops as opposed to the flat silicon regions in between the micropillars (Figure 4A). Contrarily, on smaller micropillars (<2mm) the cell body was close to the flat silicon substrate and cell protrusions extended in between these micropillars (Figure 4B).

We next used 3D confocal z-stacks to compare F-actin and DAPI expressions at various focal planes above the silicon platform at interfaces between small (Figure 5A-ROI1) and large (Figure 5A-ROI2) micropillars. To analyze single cell-micropillar interactions and avoid cell aggregation, cells used for confocal microscopy were plated on the silicon substrate for 3 hrs. A representative Z slice near the top of the micropillars is shown in Figure 5B,5C,5D. A higher number of f-actin rich protrusions with high-intensity f-actin expressions are observable on micropillar tops in ROI2, as compared to ROI1 in the shown z-slice (Figure 5C). Conversely, cells in ROI1 show higher F-actin rich protrusions at a lower z-slice as shown in Figure 5E. Normalized mean fluorescent intensities (MFI) for f-actin in ROI1 peaked at a slice ~1.8mm lower than ROI2 (Figure 5G). This difference is approximately equivalent to the height of the micropillars suggesting that cells in ROI2 interact and explore the micropillar tops with actin rich extensions, whereas cells in ROI1 interact mostly with the bottom of the micropillars and the flat regions between the micropillars. Instead, normalized MFIs for DAPI showed peaks at a distance several microns above the micropillars on both ROIs (Figure 5C,5G) suggesting that cell nuclei are positioned above the micropillars in both ROIs. The z-slice with maximum normalized MFI for DAPI is shown in Figure 5F.
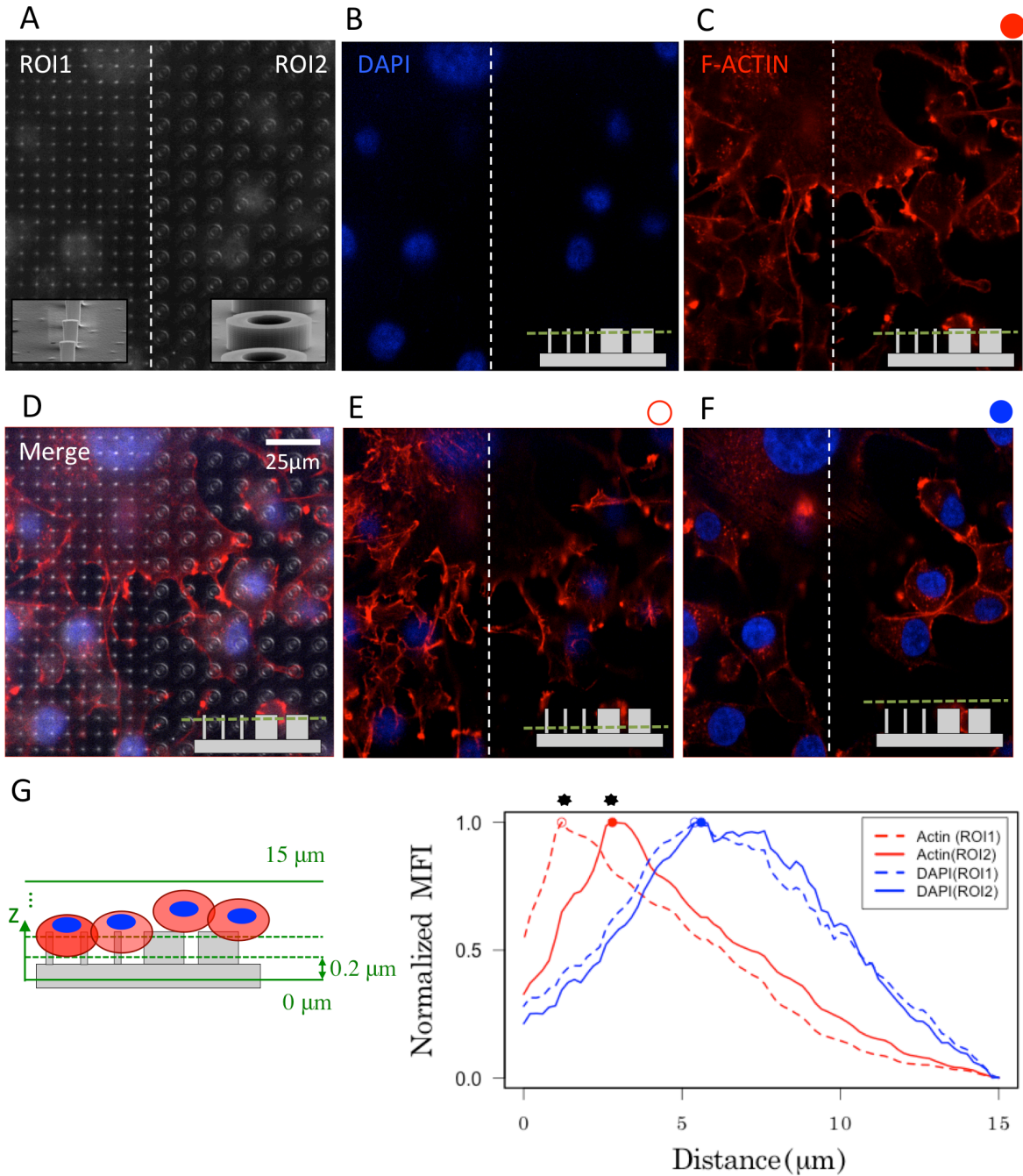
Figure 5: A) Confocal images of U87 cells on interfaces between small (ROI1) and large (ROI2) micropillars, B) cell nuclei stained with blue (DAPI) and B) the actin cytoskeleton with red (F-Actin). C) Overlay of optical image with DAPI and F-actin to show the relative position of cells on the two ROIs E) Confocal plane with maximum DAPI fluorescent intensity for ROI2 F) confocal plane with maximum F-Actin fluorescent intensity for ROI 1 G) Normalized mean fluorescent intensity of F-actin and DAPI for ROI1 and ROI2 as a function of the distance from the initial confocal plane on the flat surface. Schematic on left shows the confocal z-slices from 0-15 μm at 0.2 μm intervals. The z-slice with maximum F-actin intensity is shown with a hollow and red circle for ROI1 and with a filled red circle for ROI 2.

Local cytoskeletal re-arrangements in response to micropillar geometry. Cytoskeletal arrangements of fully spread glioma cells on various micropillar arrays were also examined through confocal microscopy. On 5.5μm hollow shaped micropillars with square

configurations, cells exhibited remarkable localized stress fibers aligned along free spaces between micropillars. The cell shown in Figure 6A exhibited localized, elongated and aligned vertical and horizontal stress fibers in response to spatial limitations formed between the micropillars; whereas, stress fibers were arranged randomly on parts of the cell that rested on the free space between two arrays lacking spatial cues. Orthogonal views of the z-stacks also indicate the nuclei positioned on top of the micropillars in these cells. These elongated and aligned actin stress fibers were also observable on 3.2μm hollow micropillar arrays with square configurations, as shown in Figure 6B. The dark areas free of F-actin in between the elongated stress fibers correspond to the location of micropillars as evident from the merged images in Figures 6A and 6B. The F-actin fluorescent intensity profiles along lines crossing these micropillars also show that the drops in intensity correspond to the location of the micropillars. A similar phenomenon was observed on hexagonal array configurations; however, the actin stress fibers of cells on these arrays were aligned diagonally at random orientations (Figure S3) suggesting that these cells rearrange their cytoskeleton to conform to the micropillar array shape.

F-actin rich cell protrusions also traveled inside the openings of hollow micropillars as evident from SEM images shown in Figure 7A. Confocal microscopy revealed circular and high intensity F-actin expressions on hollow micropillars with hole diameters of 1.8-5 mm. Furthermore, actin-rich filopodia conformed to the sharp edges on top of hollow micropillars (Figure 7C) where high expressions of F-actin is observable at filopodia tips.
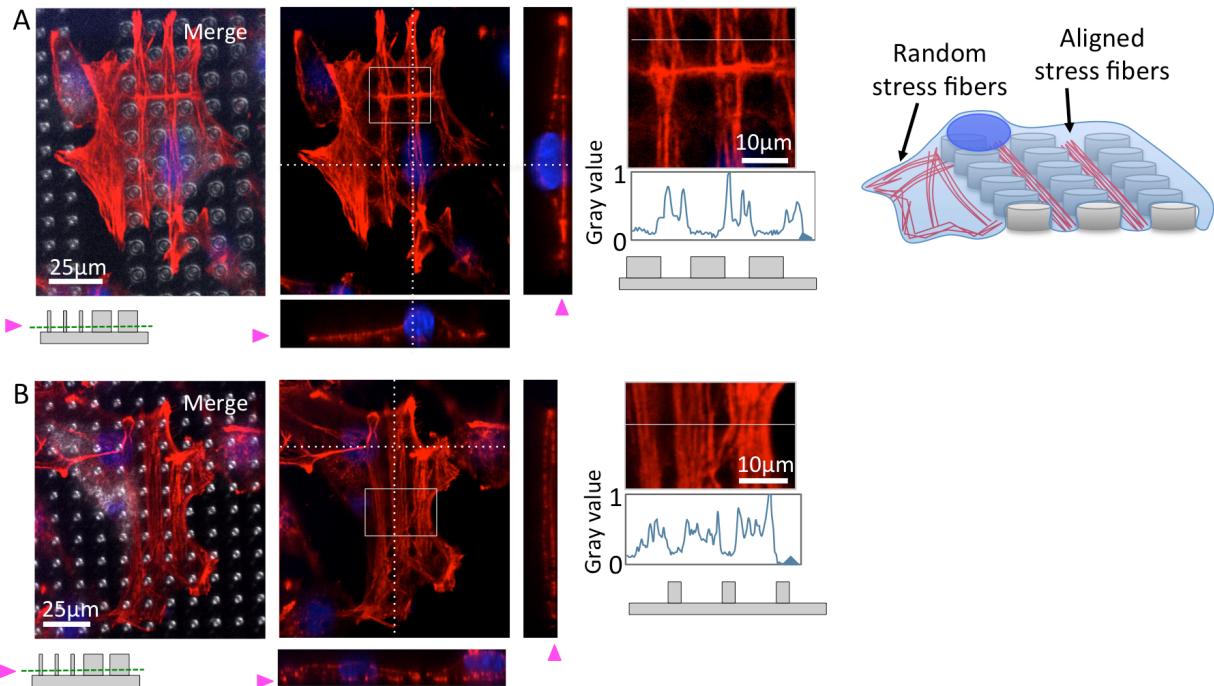
Figure 6: A) Confocal z-stacks show localized, elongated and aligned vertical and horizontal stress fibers in response to spatial limitations formed in the gaps between the micropillars on 5.5 μm hollow shaped micropillars with square configurations, B) elongated and aligned actin stress fibers on 3.2 μm hollow micropillars arrays with square configurations
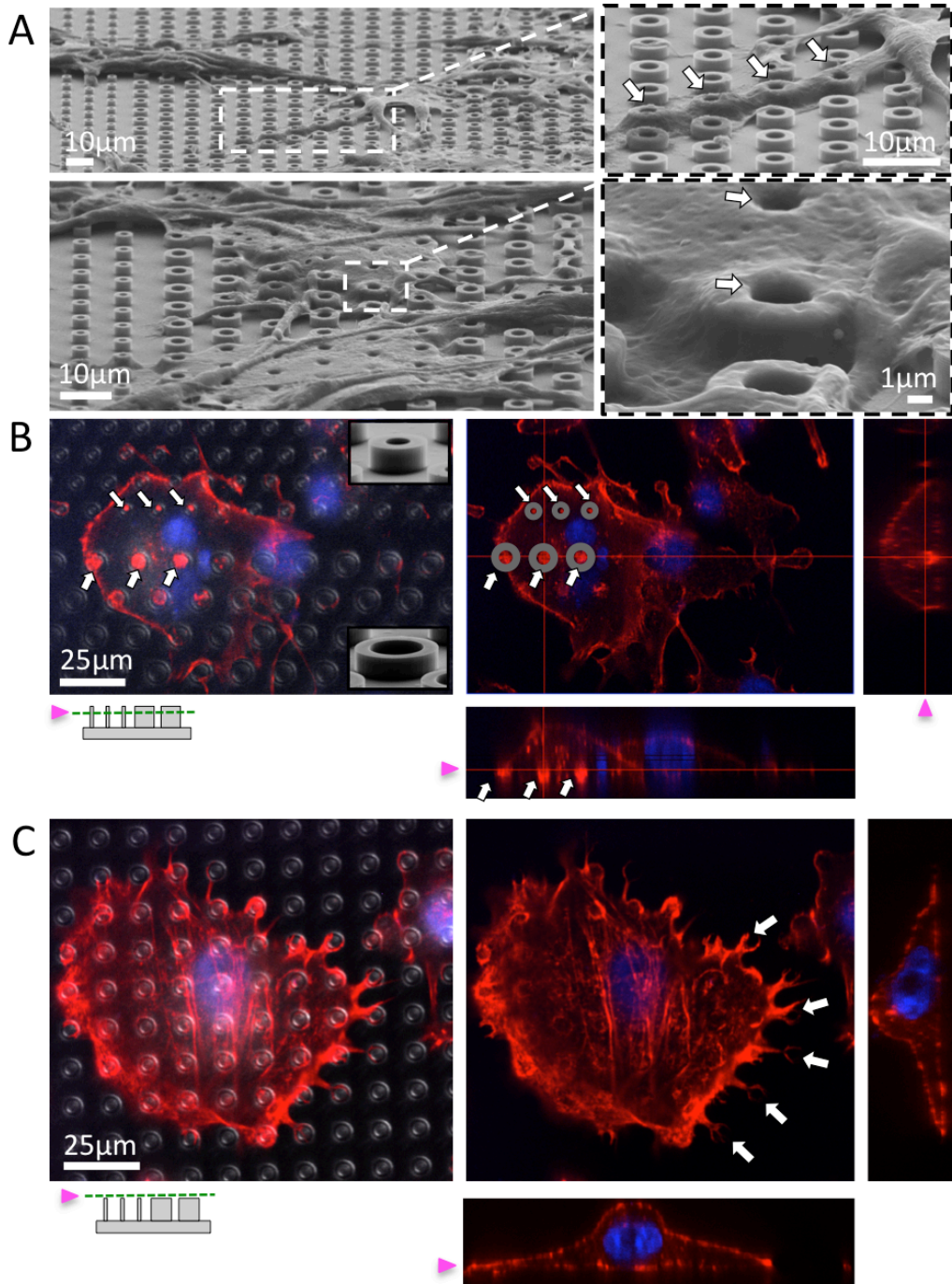
Figure 7: A) SEM micrograph of U87 cells protruding into hollow shaped micropillars B) Confocal images indicating the high expression of F-actin within the openings of hollow micropillars (arrows) C) confocal z-stack of cell on top of micropillars showing actin rich protrusions conformed to the shape of hollow micropillars, with high F-actin expressions on sharp edges

Discussion

Vertically aligned micropillars of solid and hollow cross sections are used for a variety of biological applications including tumor cell capture (Wang et al. 2010; S. Wang et al. 2009), drug delivery into cells (VanDersarl et al. 2012; Xie, Alexander M. Xu, et al. 2013) and recording neuronal activities (Hai et al. 2010; Robinson et al. 2013; Xie et al. 2010; Robinson et al. 2012). In this study, a silicon platform was developed and used to explore the responses of glioma cells to silicon micropillar arrays of various sizes. The Si micropillars used in this study were rigid: i.e. cells were not able to deform these micropillars. Therefore we assume a constant stiffness for all micropillars arrays, eliminating the role of stiffness in the differential responses we observed. Indeed, glioma cells also show sensitivity to substrate stiffness and their response has been characterized by several groups (Wong et al. 2015; Umesh et al. 2014; Ulrich et al. 2009) . Furthermore, micropillars of various sizes were fabricated side-by-side on silicon platforms providing identical chemical environments for the cells. Thereby, the distinguishable collective and single behaviors exhibited by glioma cells on various micropillar arrays were attributed to their differential responses to the size of the micropillars.

Previous studies have looked at the effect of pillar size and spacing on the cell-pillar interfaces by using the same center-to-center spacing but varying pillar sizes. However, using the same center-to-center spacing results in smaller flat surfaces available to the cells between larger pillars compared with smaller pillars. Hence, in this study, instead of center-to-center distances, we kept the side-to-side spacing (i.e. gap) of pillars constant while changing the pillar sizes. Xie et al observed that Chinese hamster ovary cells were able to deform and wrap around pillars of 5μm spacing and made contact with the flat substrate in between the pillars. On the other hand, these cells were lifted away from the substrate on pillars with the same size but with a reduced spacing of 2μm (Xie, Alexander M Xu, et al. 2013). Here, we show that despite the 5μm side-to-side spacing of all arrays, whether glial cells make contact with the flat substrate depends highly on the pillar size (Figure 8). Even with similar flat surface areas available to the cell in between micropillars of different sizes, glioma cells preferentially interacted with the tops and sides of large micropillars rather than the flat surface in between pillars. This was evident both from high-resolution SEM inspections (Figure 4A and 4B), as well as confocal z-stacks showing F-actin expressions at different planes at micropillar array interfaces (Figure 7).

The preferential interactions of cells with the micropillar tops for larger arrays (>2 μm) may be attributed to the higher surface area provided by these structures for cells to anchor onto. After landing on these pillars cells can form adhesions on the micropillar tops as depicted in Figure 8A. Subsequently, in order to strengthen their anchorage, glioma cells explore the nearby microenvironment through actin rich protrusions (as seen in Figure 7C) and spread on top of multiple micropillars while forming adhesions on the top and sidewalls of these micropillars (Figure 8A). Conversely, smaller (<2 μm) micropillars do not provide enough anchorage area for the cells on their top surfaces resulting in cells deforming around these pillars to anchor onto the flat silicon area (Figure 8B). Therefore, cells form strong adhesions on the flat areas as well as the micropillar sidewalls and tightly wrap around these micropillars. Note that the same flat area is available to cells in the gaps between large micropillar arrays but cells do not deform around the pillars to reach this

flat gap area on large micropillars. The deformation of cells around small micropillars to form 2D adhesions on both the flat silicon surface and the sidewalls of small micropillars could lead to the trapping and immobilization of cells on these surfaces. Immobilization of cells on nanopillar arrays was demonstrated previously for CTCs (Wang et al. 2010; Wang et al. 2014), neurons (Xie et al. 2010) and mouse fibroblasts (Persson et al. 2015). Glioma cells with reduced motility may be unable to form aggregates on the small micropillar arrays used in this study, which would explain their differential arrangements on top of small micropillar arrays; however, further live cell imaging would be required to verify a reduction in cell motility on small micropillar arrays. Our future studies will aim at conducting live cell imaging and comparing cell migration speeds on various micropillar arrays. We also showed that the stresses induced in the cell body to conform to the shape of its underlying substrate also resulted in local changes in cytoskeletal organization and F-actin expression for the glial cells on our silicon platforms (Figure 6,7). The long-term effects of such changes on cell behaviors remain unknown.
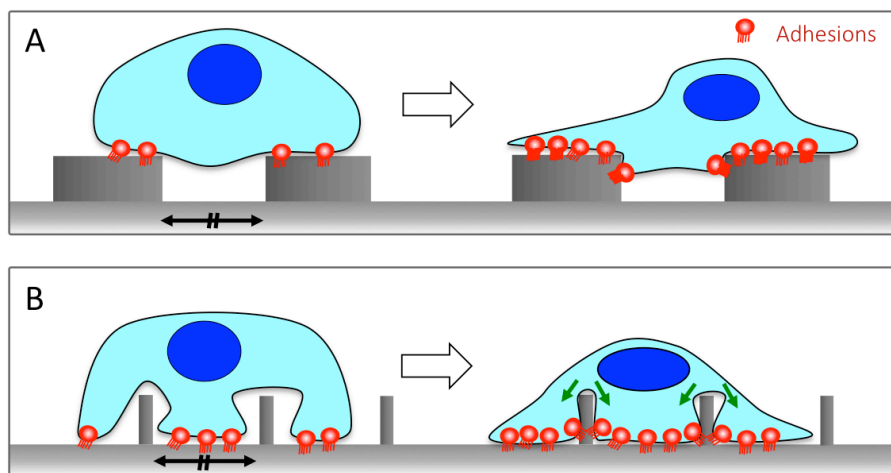
Figure 8: Hypothetical model of cell-micropillar interactions A) micropillars with outer diameters greater than 2 μm, with a side to side spacing of 5μm provide enough anchorage area for glioma cells to form adhesions on top of these pillars. Subsequent to initial attachments, cells spread on top of these pillars and away from the flat silicon substrate between pillars while anchoring to the pillar top and sides. B) Micropillars with outer diameters less than 2 μm, and side-to-side spacing of 5μm do not provide enough anchorage area for cells resulting in cell deformation around these pillars and interaction with the available flat space between micropillars. Subsequently, cells spread on these micropillars wrapping tightly around the micropillars and forming strong adhesions on the flat silicon substrate as well as micropillar sidewalls. Black arrows indicate the equal side-to-side spacing between micropillars of different sizes.

Conclusions and future perspectives

Our results demonstrated the significance of micropillar size on collective and single glioma behaviors. The size of the silicon micropillars determined the arrangement of glioma cells on these structure: cells formed small tumor like clusters on larger micropillars, but were evenly spread out on small micropillars. Interestingly, we did not observe such distinct cell arrangements for PC3 cancer cells or 3T3 mouse fibroblast on the same silicon substrate (unpublished work); this is not unexpected as the response of cells to the size of the micropillars and spacing is in part dependent on the cell size, shape and stiffness (Xie, Alexander M Xu, et al. 2013). Other cell types may show similar behaviors on

smaller or larger micropillars than the ones used in this study depending on their cell shape and properties such as stiffness. Additionally, glioma cells are specifically known to be sensitive to the shape of their microenvironment in the brain. In fact, brain tumor progression is regulated by the transduction of particular physical and chemical signals in the brain extracellular environment (Louis 2006). Specifically, glioma cell growth and invasion relies on the detection of specific topographic patterns in brain tissue (Bellail et al. 2004; Agudelo-Garcia et al. 2011; Deok-Ho Kim et al. 2012; Louis 2006). Further studies aimed at understanding the mechanisms of cell sensitivity to micropillar shape and size will not only allow the design and tuning of micropillar platforms based on their desired applications, but may additionally provide insights into the *in vivo* shape sensing mechanisms of glioma cells.

Methods

Silicon Micropillar platform fabrication process. 12 different arrays of silicon micropillars were fabricated side by side. These arrays consisted of large micropillars with hollow cross-sectional geometries or small c-shaped micropillars. Hollow micropillars were fabricated with inner diameters of 1.5μm, 2μm, 3μm and 5μm, all with a wall thickness of 1.5μm, and side-to-side spacing of 5 μm, arranged in both square and hexagonal configurations. For the smaller C-shaped micropillars, the final measured circle diameters are 1.5 μm and 3μm, with openings of 0.5μm and 0.75μm on the edges of the micropillars, with side-to-side spacing of 5 μm, arranged in both square and hexagonal configurations. Each micropillar array covered an area of approximately 3.5x3.5 mm.
After soft-baking a clean silicon wafer coated with photoresist (AZ 7908), it underwent UV exposure in ASML Stepper 5000 (PHT-S1), after developing the patterns, followed by hard-baking, we used deep reactive ion etching (Surface Technology Systems, ICP DRIE) to render micropillars with heights of 2 μm. The undulating sidewalls were created by pulsed etching in a typical Bosch process. C4F8 of 15Sccm, Sf6 of 45Sccm 5 Sccm were used during etching and 75Sccm of C4F8 was used in the passivation process.

Cell culture. U-87 cells (Human Primary Glioblastoma cell line) were provided from Department of Molecular and Cell Biology (MCB) at UC Berkeley, California. Cells were cultured in cell DMEM 1X - Dulbecco's Modified Eagle Medium (with 4.5 g/L glucose, L-glutamine & sodium pyruvate, Corning Cellgro). The cell DMEM 1X was enriched with 10 % Fetal Bovine Serum (FBS, Corning Cellgro), 1% Penicillin- Streptomycin (Corning Cellgro) and 1% non-essential amino acid (Gibco, Life Technologies). Cells were cultured and kept in an incubator which was set to 5% CO_2 and 37 °C temperature. In this study, cells were passaged every week with a passage number between 15 and 30 for all experiments. For each experiment, cells were washed one time by PBS 1X (Phosphate-Buffered Saline, Corning) and trypsinized by 0.05% pre-heated Trypsin (0.53 mM EDTA, 1X without sodium bicarbonate, Corning) for 5 minutes in a laminar hood and incubator. Then, cells were collected in 15 ml centrifuge tubes and were centrifuged at 850 rpm for 5 minutes. At the end of preparing the cell solution, the cell concentration was adjusted to 16 X 10^4 cells/ml for all experiments in this study.

Seeding U-87 cells on silicon platforms. All silicon micropillar platforms were placed into sterile 6-well cell culture plates (flat bottom with Lid, Corning) and were submerged in 70% Ethanol for 5 minutes in a laminar hood. After treating with Ethanol, all platforms were washed 3 times by PBS 1X and once more using the enriched cell culture DMEM 1X. Then, cells were seeded on the sterilized micropillar platforms at a concentration of 16 X 10^4 cells/ml. Silicon platforms were then placed in new 6-well culture plates and 3 ml of the prepared cell solution (16 X 10^4 cells/ml) was added to each well and kept in an incubator. Every 24 hours, cells were fed by fresh, enriched cell culture DMEM throughout the experiments.

Cell imaging and analysis: confocal microscopy. Cells were washed and fixed with 4% parafalmadehyde. Membranes were permeabilized with 5% goat serum and 1% triton-X in PBS. Cells were then stained for F-actin and DNA with Phalloidin and DAPI respectively. Swept field confocal microscopy was conducted using a Bruker/Prairie Aurora launch microscope system. Confocal z-stacks were taken using a 60x water-dipping objective (LUMPlan Fl, NA = XX, Olympus) at either 200 or 300 nm Z-steps using a 35µm pinhole aperture setting. Images (512x512) were taken using an EM-CCD camera. Images were additionally taken using transmitted light to superimpose on the fluorescent images.

Cell imaging and analysis: SEM procedure. To prepare cells for electron microscopy, samples were rinsed with 0.2mM sodium phosphate buffer (v/v: 36 ml Na_2HPO_4/14 ml NaH_2PO_4) and then fixed with 2.5% glutaraldehyde at 4°C overnight. Samples were then dehydrated using a graded series of ethanol dilutions (10% to 100%) and dried, and coated with a ~10nm layer of gold prior to microscopy.

Coverage area calculations. Cell coverage area was simply defined as the ratio between the area covered by cells or its protrusions and the bare silicon area. In order to measure the cell coverage area of each array, micrographs were converted to binary images and were quantified using ImageJ. For each measured cell coverage area value, two-tailed Mann-Whitney test was performed to conclude that the difference observed between the groups for measured cell coverage area is unlikely to have occurred by chance at both 0.05 and 0.01 significance level.

Supporting Information. Cell coverage after 24 hours (Figure S1), Cell coverage data for hexagonal *vs.* square micropillar configurations (Figure S2), and stress fiber orientation on hexagonal micropillars (Figure S3).

Chapter 2

BACTERIAL RESPONSES TO MICRO- AND NANO-TROPOGRAPHY

2.1 Responses of Staphylococcus aureus bacterial cells to nanocrystalline nickel nanostructures

Introduction

Staphylococcus aureus (*S. aureus*) is a grape-like shaped bacterium that can adhere to organic (Gristina et al. 1987; Oga et al. 1988; Francois et al. 2000) and metal (Gristina et al. 1987; Oga et al. 1988; Barth et al. 1989; Cordero et al. 1994; Melcher et al. 1994; Arenas et al. 2013; Harris et al. 2007; X. Wang et al. 2009; Teterycz et al. 2010) surfaces. The overall geometry of *S. aureus* is round ("coccus") with diameters approximately ~ 0.5 μm. This bacterium is a common source of nosocomial infections especially after implant associated surgeries (Melcher et al. 1994; Harris et al. 2002), such as prosthetic joint implants (Moran et al. 2010), and heart valves (Renzulli et al. 2000). In addition, they are a common cause of food borne illnesses by adhering to food service surfaces and contaminating food supplies (da Silva Meira et al. 2012).

Moreover, the recent discovery of drug resistance strains of *S. aureus* (Karska-Wysocki et al. 2010; Chiu et al. 2012; Williamson et al. 2000), such as methicillin-resistant and oxacillin-resistance *S. aureus*, has led to an emergence of research on bacterial adhesion and survival mechanisms on various surfaces. Several experimental surface coatings and treatment techniques on implant surfaces have been developed (X. Wang et al. 2009; Campoccia et al. 2008; Arenas et al. 2013; Huo et al. 2013; Rochford et al. 2013; Hu et al. 2010; Papa et al. 2013) with the goal of enhancing osseointegration and reducing bacterial cell adhesion capabilities. Recent studies have suggested a sensitivity of bacteria to nanoscale topographical properties of implant substrates. Wu et al. (Wu et al. 2011) performed an *in vitro* study on the effects of titanium surface roughness on *Staphylococcus epidermidis* and human osteoblast behavior. These surfaces were prepared with polished, satin, grit-blasted and plasma-sprayed surface finishes. Their results indicated that not only the vertical roughness is important but also the lateral roughness parameters of these small surface features play a role in bacteria attachment. Furthermore, their results showed a preferential colonization of bacteria on micro-rough surfaces, whereas the osteoblasts favored interaction with smooth plasma-sprayed surfaces than with rough satin treated titanium substrates. In a different study, Truong *et al.* (Truong et al. 2010) highlighted the effects of nanoscale surface roughness on the adhesion of *S. aureus* and *Pseudomonas aeruginosa* bacteria. Bacteria attachment densities were compared on substrates with different topographical features, but with identical surface chemistry and wettability. Their experiments demonstrated altered bacteria adhesion merely due to surface nano-topography. Specifically, they showed that *S. aureus* tend to attach at significantly higher densities to treated ultrafine-grained titanium substrates as compared to untreated bulk substrates. Truong *et al.* (Truong et al. 2010) hypothesized that surface nano-topography is a leading factor in controlling bacterial attachment. The effects of nanorough, nanotubular, and nanotextured titanium surfaces on *S. aureus* adhesion were also investigated by Puckett *et al.* (Puckett et al. 2010). They demonstrated that bacteria are less likely to adhere to the nanorough Ti surfaces prepared with electron beam evaporation but prefer to attach to nanotubular surfaces.

Despite the industrial and clinical importance of the bacterial surface adhesion, there is no in-depth study on single *S. aureus* cell interactions with well-defined nanometer scale three-dimensional structures. Herein, we preset a detailed investigation aimed at understanding how *S. aureus* cells attach to nanocrystalline (nc) nickel columnar nanostructures with various 3D nano-topographical features. These nanostructures include pillars of various cross-sectional geometries, namely solid core, hollow, c-shaped, and x-shaped pillars. These features have outer diameters as small as 220 nm.

Three-dimensional mushroom shaped nanostructures were also prepared to understand how these cells interact with overhang topographies. These complex nanostructures were fabricated with electronic beam lithographic techniques and electroplating methods (see Experimental Methods). It is observed that *S. aureus* cells exhibit interesting and unexpected behaviors. High resolution scanning electron microscopy inspections show that not only do they adhere to horizontal smooth surfaces as expected but also to highly curved features, such as the side walls of nickel pillars with diameters in the range of ~220 nm - 1000 nm. In addition, these microorganisms attach like free-standing membranes at the top of the hollow and c-shaped pillars with adhesion contact points only along the rims. Finally, *S. aureus* cells are able to uniquely suspend from the overhangs of the mushroom shaped nanostructures with stem diameters as small as 220 nm.

Experimental Methods

Nanometer scale nanocrystalline nickel columns pillars were prepared by using state-of-the-art electronic beam lithographic (EBL) methods and electroplating techniques (Burek & Greer 2010; Jahed, Evans, et al. 2012; Jin, Xie, et al. 2012; Jin, Burek, et al. 2012; Seo et al. 2013). Figure 1 illustrates the fabrication steps for these nanostructures. Thin titanium (~20 nm) and gold (~ 100 nm) films were first deposited on bare silicon substrates using the electron beam deposition methods. They are then spin coated with Poly (methyl methacrylate) (PMMA) EBL resists. Complex geometric via-hole patterns were produced on these silicon wafers by exposing these thermal plastic films to an electron beam. Nanocrystalline nickel was deposited in these hole patterns with an electrolyte that contains nickel (II) sulfate hexahydrate (99%, Sigma Aldrich), nickel (II) chloride (98%, Sigma Aldrich), and boric acid (BX0865, EMD Millipore) with concentrations of 300 g/L, 30 g/L, and 30 g/L, respectively. A small amount of saccharine (1.9 g/L) was also added in the plating solution in order to reduce the nickel crystalline size while the current density was maintained at 11.5 +/- 2 mA/cm^2 during the plating process. The excess PMMA film was dissolved in acetone after the nickel deposition processes. Detailed transmission electron microscopy analyses revealed a grain size in the range of 9.4 and 13.2 nm for these nickel nanostructures(Seo et al. 2013).

S. aureus (ATCC 6538) bacteria were generously provided by Dr. Lyndon Jones' laboratory at the University of Waterloo. *S. aureus* bacteria were cultured on trypticase soy agar (TSA) plates by using alginate swabs and incubating the plates at 37 °C overnight. A 2.55% saline solution was prepared and sterilized by using Nalgene filters and ~0.006% of nutrient broth was added to the saline to preserve *S. aureus* during tests. *S. aureus* cells were transferred to saline solution by adding 5 mL of saline to the TSA plate and using alginate

swabs to dislodge the bacteria from the plates. *S. aureus* cells were washed with saline solution seven times by centrifugation at 4,000 rpm for 10 minutes. The stock solution of *S. aureus* cells was diluted 10-fold in saline before testing. During a typical test, a drop of diluted *S. aureus* solution was placed on the silicon substrate containing nc-nickel shaped pillars. The specimens were left in the incubator with constant temperatures of ~37 °C. After 6 hours, the samples were rinsed with deionized water to remove cells that are not well adhered to the surfaces and air dried in fume hood for 12 hours. Field emission scanning electron beam microscope (Zeiss LEO 1550) was used to inspect how these *S. aureus* cells interact with nickel nanostructures.
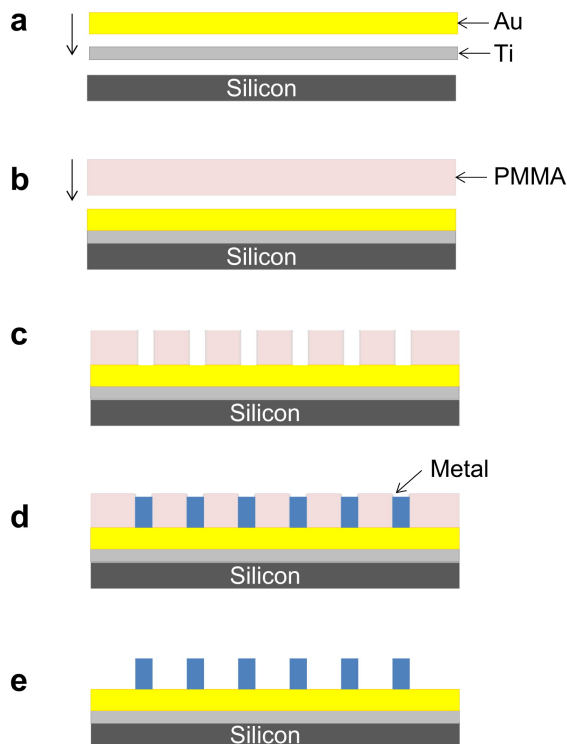
Figure 1: nanostructure fabrication process a) electron beam evaporation of 20 nm titanium and 30 nm gold on silicon substrate, b) spin coating of PMMA resist, c) patterning of PMMA resist with ebeam lithography, d) electroplating of desired metal into patterned holes, e) PMMA resist removal via acetone

Results and Discussions

Representative 70 degree tilted scanning electron microscopy (SEM) images of as-fabricated nc-nickel nanostructures with solid core, hollow, c-shaped, and x-shaped pillars are shown in Figures 2 (a) – (d), respectively. The outer diameter of these vertical pillars is ~1000 nm with a height to diameter aspect ratio of approximately 1.5. Figure 2 (b) shows a representative image of the hollow pillars with average inner diameters of ~ 840 nm. The c-shaped pillars have an inner diameter of ~ 760 nm (see Figure 2 (c)). The small openings along the edges of c-shaped pillars allow inspections of the interiors of these nanostructures. Careful SEM inspections of the fabricated pillars with different shapes reveal the pillar exterior sidewalls are extremely smooth and aligned nearly perfectly vertical from the substrate surface. Furthermore, the top surfaces of these nanostructures

are flat and slightly rougher than the sidewalls but the roughness still remains in the nanometer scale.
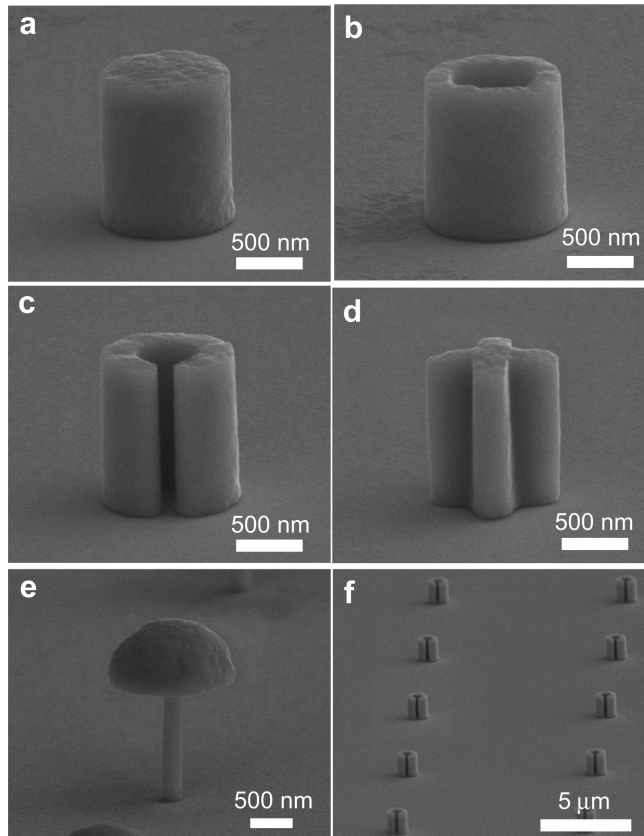
Figure 2. Representative SEM micrographs revealing pillars with different cross-sectional geometries – (a) solid; (b) hollow (c) c-shaped (d) x-shaped pillars, (e) mushroom shaped nanostructures. An array of c-shaped pillars are shown in (f).

All the nanostructures shown in Figure 2 were fabricated simultaneously on a single silicon substrate, and are thereby expected to have similar surface chemical compositions and wettability, and differ only in nanometer scale morphology. Furthermore, cell plating was carried out on a single substrate containing all pillar shapes under identical environmental treatments. These nanocrystalline nickel pillars are regularly spaced at a 10 μm center to center distance as shown in Figure 2 (f). In order to better examine how an individual *S. aureus* cell interacts with overhang nano topography, mushroom shaped nc-nickel nanostructures with stem diameter of 220 nm were fabricated as displayed in Figure 2 (e). The micrographs clearly reveal the smooth nickel pillar sidewalls. However, the mushroom caps are fairly rough compared to other parts of these nanostructures.

All nanostructures were fabricated in large arrays allowing for the inspection of multiple samples for each cell culture experiment. A representative micrograph revealing a section of the array containing c-shaped pillars is shown in Figure 2 (f). Overall, the dimensions of all fabricated nanostructures were comparable to that of a single *S. aureus* bacterium, allowing for detailed studies on single bacterium responses to the topographical cues of each nanostructure.

Several *S. aureus* cells rested on top of c-shpaed pillars, covering the top opening of these pillars as shown in tilted (figure 3(a)) and top-down (figure 3(b)) SEM micrographs of c-shaped pillars which were exposed to saline solution containing *S. aureus* cells. These microorganisms have diameters of ~500 nm. Other cells adhered to the pillar interface with the substrate below that was coated with a thin layer of gold. As implied by Figure 3 (a), the micro-organism appears to be partially embedded inside the opening but not fallen into the hollow center, likely because it is adhered to the pillar rim. This indicates that this *S. aureus* cell is in fact suspended like a free-standing object with only the edges attached to the nanostructure. In some rare occasions, small bacterial colonies were formed on the top surfaces of a single c-shaped pillar as show in figure 3(c) and (d) where two or three cells cluster on the top of the pillar, likely impeding bacteria from entering the opening. This demonstrates that *S. aureus* cells can attach securely with little contact surfaces, such as the top rim of c-shaped pillars. The bacterial adhesion area to the pillar is estimated to be 0.074 μm^2 (see Figures 3(a) and (b)) Another interesting observation is that a considerable number of *S. aureus* bacteria were able to attach to the vertical, highly curved sidewalls and withstand the DI water rinse process (see Figures 3(c) and (d)). These results demonstrate a strong and adhesion of *S. aureus* on nickel surfaces. Some *S. aureus* cells were also able to enter and fall into the opening instead of residing at the top of the pillars. Figure 3(e) shows a micrograph of a c-shaped pillarwhere no bacterium is located at the top opening. However, top-down images revealed that a cell is within the hole and partially adhered to the interior sidewall. In addition, it is possible that no cell is deposited within these holes, such as the pillar shown in Figure 3 (g) and (h). The top-down image clearly shows no *S. aureus* cells are in the pillar center.

Figure 3. (a),(b) Tilted and top-down SEM micrographs of the same c-shaped pillar that has been exposed to the *S. aureus* cells, a single *S. aureus* cell is attached to the rim of the c-shaped pillar opening. (c),(d) Tilted SEM micrographs of c-shaped pillars on which small bacteria colonies have formed. (e),(f) Tilted and top-down SEM micrographs of the same c-shaped pillar where an *S. aureus* cell has penetrated into the c-shaped hole. (g), (h) Tilted and top-down SEM micrographs of the same c-shaped pillar where no *S. aureus* cells have penetrated inside the c-shaped hole. (i). SEM micrographs of c-shaped pillar array with eleven of fifteen covered with *S. aureus* cells at the top surface.
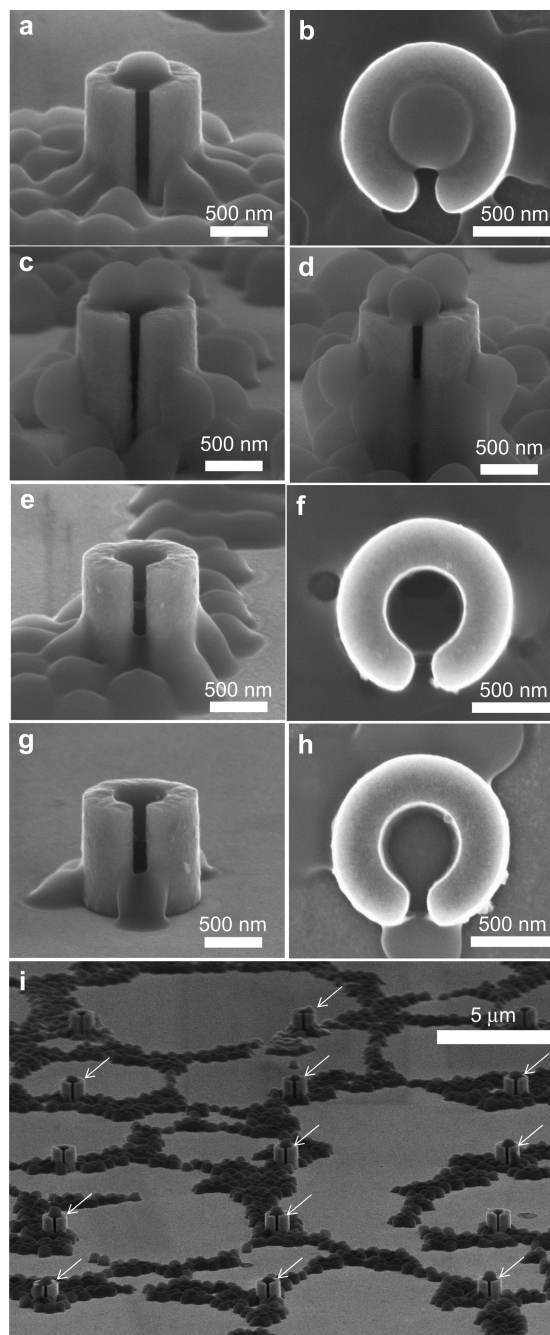
However, a majority of cells attach and remain on the top of c-shaped pillars rather than within, as shown in the SEM micrograph with the view of 15 pillars in Figure 3(i). The image clearly shows eleven out of fifteen pillars inspected contain cells attached on the top surface which are highlighted with arrows. This demonstrates that c-shaped pillars with proper inner and outer diameter can be an efficient method to capture individual cells.

In addition to the c-shaped pillars, *S. aureus* cells were also deposited on hollow pillars with the same outer diameters of ~ 1 μm. SEM inspections of these specimens reveal that some of the bacterial cells were successfully attached to the rim of the pillars as shown in Figure 4.
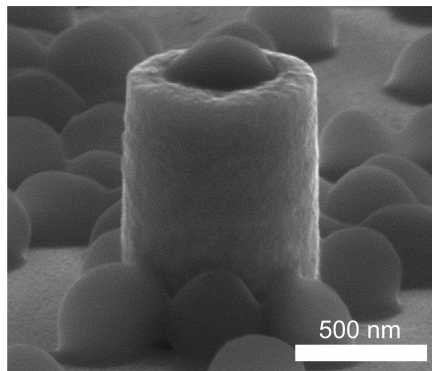
Figure 4. 70º tilted SEM micrograph revealing a *S. aureus* cell embedded at the top of a hollow pillar.

This micrograph shows that the *S. aureus* cell attachment mechanism to the pillars appears to be similar to those observed in the c-shaped pillars shown in Figure 3 (a). In addition to adhesion at the top of the hollow pillars, SEM inspections show cells can penetrate deep into the openings due to the slight larger inner diameter of the hollow pillars when compared to the c-shaped cross-sectional geometries. Cells were located inside the hollow pillar holes as shown in tilted (figures 5 (a)) and top-down (figures 5 (b)) SEM micrographs. Cells are clearly not residing at the top of pillar but have penetrated inside the hole (figures 5 (a)). This penetration was not visible with a 70 degree tilt view, however, when inspecting the same pillar with a top-down view, a cell can be observed resting at the interior of the hole (figures 5 (b)) with the cell partially attached to the interior wall of the column. However, it is unclear if the cell is located mid-point or at the bottom of the pillar. Since the cell is constrained within a hollow pillar, it is not certain if it can grow or divide due to the space confinement. As a comparison, the tilted and top-down view of another pillar without a *S. aureus* cell inside the pillar is shown in Figures 5(c) and (d). The grain microstructure of the gold thin film coated substrate, underneath the hollow pillar, was evident at the bottom of the holes, confirming that the interior of the hollow pillar was empty and no *S. aureus* cells reside within these pillars (figure 5(d)).
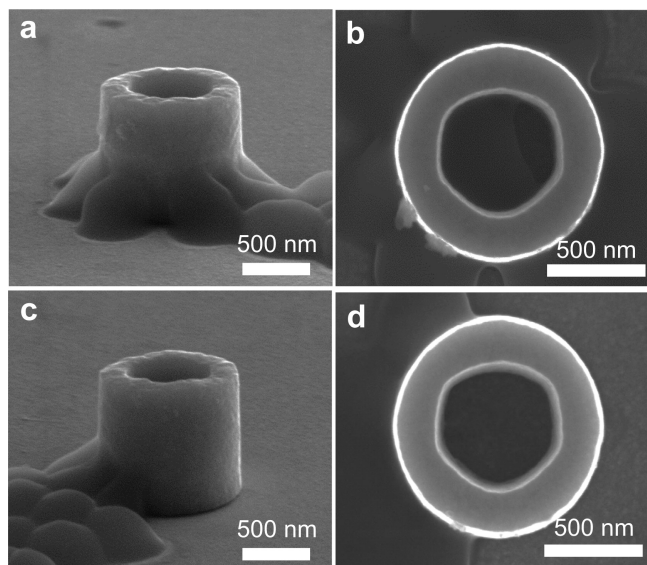
Figure 5. 70° tilted and top-down SEM micrograph revealing two pillars - one with a cell confined within (a) and (b); and another structure without a cell (c) and (d).

The affinity of *S. aureus* cell attachment on x-shaped pillars was also studied. SEM micrographs of two pillars with the microorganism adhered to the top surface of these complex geometric nanostructures are shown in Figure 6 (a) and (b). These small nickel pillars have wall thicknesses of approximately 300 nm. The images suggest that individual cells are likely to firmly adhere to x-shaped pillars; however, these cells have a lower success rate when compared with c-shaped pillars (see Figure 3). Out of the eighteen x-shaped pillars inspected, only three demonstrated bacteria adhesion at the top of the pillar (see Figure 6 (c)). One of the possible explanations is that most cells that were initially attached on these nanostructures are detached due to stresses incurred by turbulent flow of DI water during the rinsing process. In contrast, cells that were partially or completely embedded below the surfaces, such as those on the hollow and c-shaped pillars experience smaller turbulent flow stresses during the DI water rinse process.

A few *S. aureus* cells also survived on top of solid core pillars after the DI water rinse as shown in Figures 7 (a) and (b). Depending on the sizes of these cells relative to the pillar diameters, multiple cells may have attached to these pillars (Figure 7(b)). However, inspections of the eighteen pillars shown in Figure 7 (c) revealed that the probability of single microorganisms to successfully attach and survive at the top surface is closer to the x-shaped pillars but significantly lower than the c-shaped pillars. There are only five columns in the figure that show bacterial cells survived on the top of solid core nickel pillars. Finally, for all columnar shapes, the edge interface between the nanostructures and the gold substrate underneath were highly susceptible to bacteria adhesion, and endured the DI rinse. As shown in Figures 3-7, small colonies of bacteria concentrate at the outer interface between the pillars and the substrate, maximizing surface contact with two contact points, one on the horizontal gold substrate, and another on the pillar sidewall creating strong adhesions.
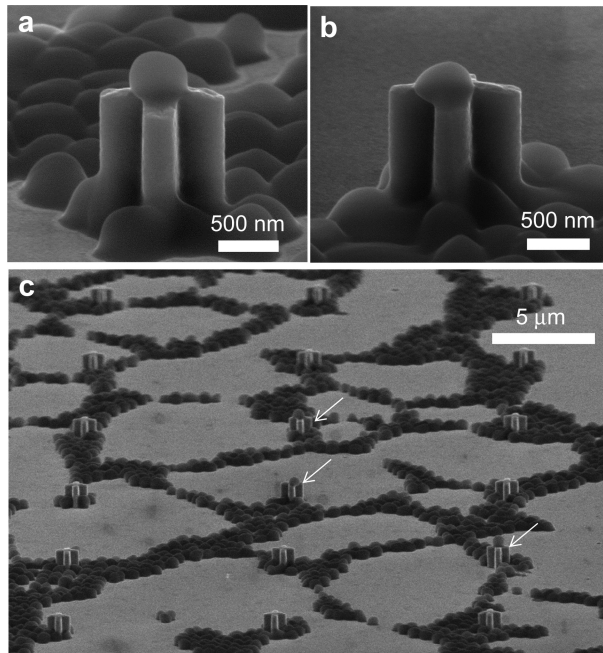
Figure 6. (a)-(b) 70° tilted SEM micrographs revealing two x-shaped columns with cells adhered on top. Far view of pillar arrays that show only 3 pillars contain cells at their top surfaces.
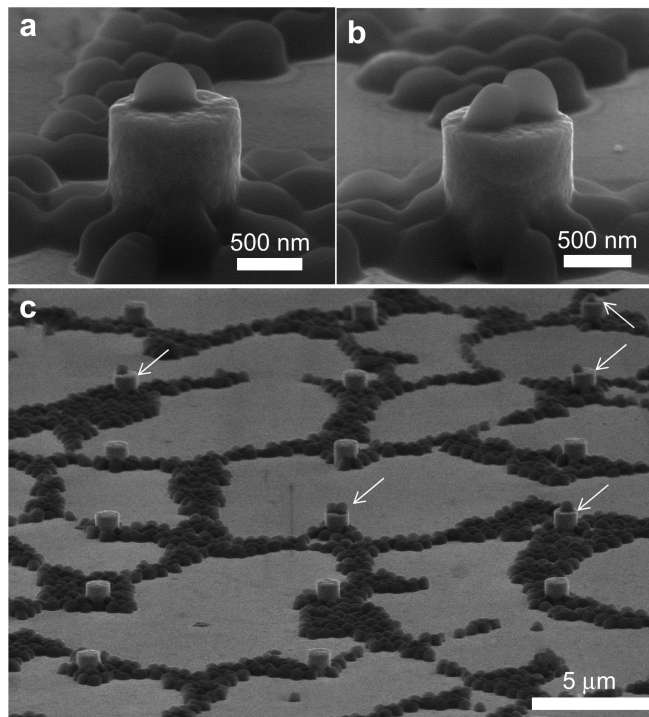
Figure 7. (a)-(b) 70° tilted SEM micrographs revealing two solid pillars with cells adhered on top. (c) Far view of pillar arrays that show only 4 pillars covered with cells on the top surface.

S. aureus cells were also exposed to nanostructures with overhanging topographic features. Figure 8(a) - (d) presents typical mushroom-shaped nickel nanostructures that have been

38

exposed to saline solution with bacterial cells. The micrographs (see Figures 8(b) and 8(c)) confirmed that the bottom surface of the mushroom cap is very smooth like the stem sidewalls. The mushroom and stem diameters of these nanostructures are ~1400 nm and ~220 nm, respectively. It is interesting to observe that these cells were not only able to attach to the stems of these features but also adhered very well at the base of the mushroom caps or the overhangs. This suggests that the adhesion behaviors of *S. aureus* cells are not constrained by the direction of the gravitational force. Similar to the pillars, the interface between the mushroom caps and the stems, and between the stem and horizontal gold substrate contained a higher density of bacteria. This is conceivably due to the two contact points created at these edges, maximizing bacteria adhesion resulting in stronger adhesions at these locations. Furthermore, *S. aureus* cells adhered to larger mushroom shaped structures with 5µm diameter stems fabricated on the same substrate, together with ~220nm mushroom shaped pillars. Significantly more *S. aureus* cells are clustered at the stems of these large structures than the field area (figure 9).
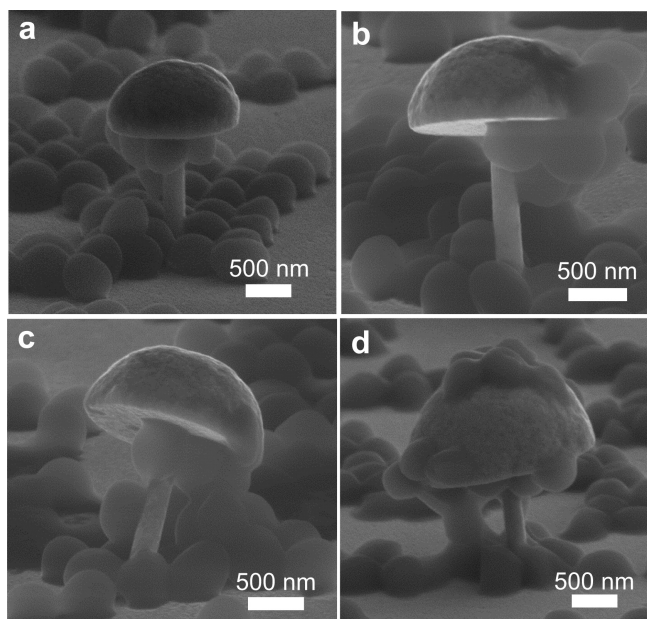
Figure 8. 70º tilted SEM micrograph revealing four different pillars that have been exposed to *S. aureus* bacterial cells.

Another interesting characteristic observed in Figures 8 (c) – (d) indicates some of the *S. aureus* cells attached to the bottom of the mushroom form links with cells on the horizontal gold substrate through an intermediate chain of cells. Pillars with cells that exhibit these behaviors also appear to be bent. However, it is unclear if these bending are driven by the shrinkage of the biological components during the drying process. However, the ability for these intermediate cells to maintain the connectivity even after the DI water rinse represents their high adhesion strengths to neighboring bacteria.

Overall, our results demonstrate the sensitivity of bacterial adhesion to nanometer scale topographical features, and mechanical cues of the surface it interacts with. Our observations suggest that bacteria not only maximize their surface area, but also show high resistance to deformation or spreading, hence freestanding on top of hollow cross sections,

with a circular adhesion contact area, rather than penetrating inside, or adhering to pillar edges and interfaces forming strong 3D adhesion. One explanation for such behavior is the high protein adsorption on metallic surfaces (Nakanishi et al. 2001) which allow the adhesion of bacteria to a substrate with no prior modification with extracellular matrix proteins, through ligand/receptor mediated adhesions. A larger contact area will therefore allow a higher number of ligand and receptor to bind per cell, resulting in the formation of a stronger adhesion. Mohamed et al. (Mohamed et al. 2000) showed the withstanding of higher shear forces by attached *S. aureus* bacteria as a function of higher receptors expressed per cell.
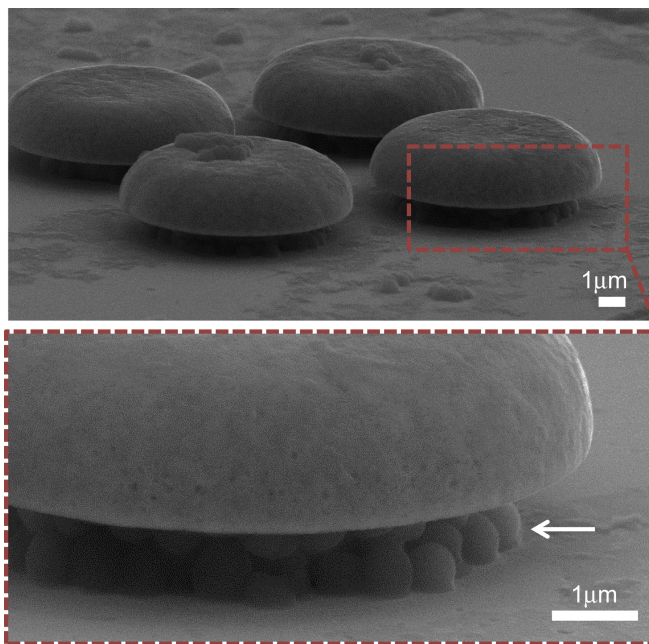
Figure 9. 70° tilted SEM micrograph revealing mushroom shaped structures with 5 μm diameter stems. Several *S. aureus* cells were clustered at the stem of these structures (arrow).

Conclusions

S. aureus cells were successfully deposited on substrates that contain nanocrystalline nickel nanopillars with different cross-sectional geometries and inspected by using high-resolution scanning electron micrographs. The results reveal these cells are able to attach to various small nickel nanostructures and endure DI water rinse but with different survival rates. Nanostructures with via holes that allow cells to embed themselves partially or fully within show a greater probability of success in adhesion to the pillars. In contrast, nickel columns with no holes have the lowest survival rates. Scanning electron micrographs also revealed that *S. aureus* cells are able to attach themselves at the bottom of overhang nanostructures. Finally, using the presented methods, and by varying the geometry, size and spacing of the nanostructures in this study, the effect of nanotopography on *S. aureus* adhesion can further be investigated at the single bacterium level.

2.2 BACTERIAL NETWORKS ON HYDROPHOBIC MICROPILLARS

Introduction

The ability of bacterial cells to form microcolonies and biofilms depends on a variety of factors in the cell environment including but not limited to their initial densities and spatial distributions (Hutchison et al. 2014; Díaz et al. 2009; Kastrup et al. 2008; Feng et al. 2009; Boedicker et al. 2009; Hansen et al. 2016; Pande et al. 2015; Bassler & Losick 2006), and the material and topography of the surface they are attached to (Zeinab Jahed, Lin, et al. 2014; Wu et al. 2011; Truong et al. 2010; Hochbaum & Aizenberg 2010). Probing colony dynamics in a controlled manner is of great importance and requires the design of *in-vitro* model systems of reduced but relevant complexity to study highly complicated phenomena involved in colony formation. Examples of such phenomena include the formation of short range direct cell-cell connections for metabolic cross-feeding, protein exchange or horizontal gene transfer (Pande et al. 2015; Madsen et al. 2012; Remis et al. 2014; Nudleman et al. 2005; Chiura et al. 2011; Yaron et al. 2000), or long range communications between spatially separated microcolonies through quorum sensing (Kastrup et al. 2008; Miller & Bassler 2001). In addition, these complex communications methods between bacterial cells have allowed them to rapidly acquire resistance to antibiotics and thus pose a major threat to public health. The emergence of antibiotic resistant bacteria further amplifies the need for developing technologies that can aid us in understanding colony dynamics in these types of bacteria. Specifically, methicillin-resistant *Staphylococcus aureus* (*S. aureus*) remains one of the most dangerous and prevalent causes of infection which can occur both in health care settings such as medical devices or joint implants, or in the wider community causing complications such as food born illnesses (Chiu et al. 2012; Holden et al. 2004; Cosgrove et al. 2003; Foster et al. 2014). *S. aureus* is a gram-positive, immobile, spherical (coccus) bacterium with a diameter of ~500nm which forms grape-like clusters on solid surfaces. Furthermore, *S. aureus* is a facultative anaerobe meaning that it can grow with or without oxygen.

Several methods have been employed to immobilize and pattern bacteria onto surfaces including dip-pen nanolithography (J. Kim et al. 2012), microcontact printing (Weibel et al. 2005; Xu et al. 2007; Weibel et al. 2007), laser trapping(Hutchison et al. 2014), antibody functionalization of abiotic surfaces (Suo et al. 2008), periodic nanostructure arrays(Hochbaum & Aizenberg 2010), and photolithographic approaches (Palacios-Cuesta et al. 2015). Although such studies have successfully controlled the spatial organization of surface attached bacterial cells at initial stages of biofilm formation (Xu et al. 2007; Hochbaum & Aizenberg 2010; Palacios-Cuesta et al. 2015; Epstein et al. 2011; Zeinab Jahed, Lin, et al. 2014; Suo et al. 2008), even with single cell resolution, to the best of our knowledge no study has truly controlled the three-dimensional architecture of growing microcolonies or biofilms. Also, most of these methods require rigorous and expensive multiple-step processes to pattern bacterial colonies. Moreover, these methods only allow the control of microcolony formation at the solid-liquid interface. However, microcolonies and biofilms can grow at other phase interfaces including liquid-air interfaces (also known as pellicles)(Nait Chabane et al. 2014; Zara et al. 2005; Mielich-S??ss & Lopez 2015) .The

mechanisms of the formation of these microcolonies are particularly understudied. In this study, we propose a simple and low-cost physiochemical method, pertaining to both physiology and chemistry, for patterning *S. aureus* cells, and controlling the architecture of microcolonies of *S. aureus* cells on poly-dimethyl-siloxane (PDMS) hydrophobic micropillars. Due to their exceptional wetting properties, micro-patterned hydrophobic surfaces have been used for a variety of applications including macroscopic fabrication of one-dimensional nanostructures such as aligned DNA or micellar nanowire arrays (Glazer et al. 2014; Guan et al. 2007; Miele et al. 2015; Lin et al. 2010; Charlot et al. 2014; Guan & Lee 2005). Our method takes advantage of the wetting properties of PDMS micropillars as well the adhesion and biofilm formation of *S. aureus* cells on surfaces, to produce nano-strings and rods of *S. aureus* cells.

Results and discussion

Wetting properties of PDMS micropillars by bacteria culture media. Hexagonally arranged arrays of PDMS micropillar were fabricated using a soft-lithography technique as shown in Figure 1A. The fabricated structures were inspected using scanning electron microscopy (SEM) (Figure 1B). The liquid repellent properties of these platforms were evident from the displacement of saline solution from areas in the center of the platforms that contained micropillars when the platform was immersed into the solution (Figure 1C). To gauge the wettability of the PDMS platform by saline and nutrient broth solutions which are commonly used for *S. aureus* culture or storage, the shape and contact angles of droplets of saline and nutrient broth were measured on a control flat PDMS as well as micro-patterned PDMS samples as shown in Figure 1D. The contact angle of broth on the flat PDMS sample (107°±4°) was considerably lower than that of saline (115°±3°) (Figure 1D), indicating more repellence between the saline solution and the flat PDMS surface. Micropattering of the PDMS lead to an increase in contact angle of both liquid probes. The contact angle of the nutrient broth on the micropillar arrays with the highest and lowest surface coverage is 148°±1.5° and 150°±1.5°, respectively. The contact angle of the saline on the micropillar arrays with the highest and lowest surface density is 147°±1° and 150°±1°, respectively. The increment of contact angles on rough surfaces is a well-known effect, which can be explained by two distinct hypotheses. On the one hand, increase of the roughness can result in the increment of the solid-liquid contact area and consequently hydrophobicity (Wenzel 1936). This is known and formulated as Wenzel regime of liquid-solid contact as shown below:

$$\cos \theta^W = r \cos \theta$$

On the other hand, the liquid can partially sit on air pockets trapped between the solid surface asperities leading to superhyrdrophobic condition (Cassie & Baxter 1944). This regime is known as Cassie-Baxter regime and is formulated as:

$$\cos \theta^C = -1 + f(1 + \cos \theta)$$

q is the Young's contact angle on a flat surface, q^c and q^w are the Cassie-Baxter and Wenzel contact angles, respectively, while, r and f represent roughness factor and the area fraction of the liquid-solid interface. Equating these two formulas defines a threshold contact angle q* which indicates the transition between Cassie-Baxter and Wenzel states.

$$\cos \theta^* = (f - 1)/(r - f)$$

According to this equation, presence of air pockets at the interface and accordingly Cassie regime is favorable only if q ≥ q* (Lafuma & Quéré 2003). To obtain more insight about our system, theoretical Cassie-Baxter and Wenzel state contact angles were calculated similar to the method described in a previous work (Shahsavan et al. 2012). Roughness factor, r, and area fraction of the liquid/solid interface, f, were determined using following equations for a hexagonal array of cylindrical micropillars:

$$r = \frac{4\pi dh}{2\sqrt{3}i^2} + 1$$

$$f = \frac{2\pi d^2}{4\sqrt{3}i^2}$$

Where h, d, and i denote the pillars' height, diameter, and center-to-center spacing, respectively. We measured contact angle values for saline and nutrient broth solutions on PDMS platforms with various surface coverage percentages of micropillars and calculated the theoretical values for r, f, q, and q* as tabulated in Table 1. The contact angle for the saline solution on the control flat sample is consistently greater than q* for all micropillar samples. Thus, Cassie-Baxter regime may be more favorable suggesting the presence of air pockets between micropillar arrays and the liquid surface. Accordingly, when the platform was submerged into a saline solution, the liquid contact line was pinned at the interface between the micropillars and flat PDMS surface (Figure 1E). On the other hand, except the micropillar sample with the maximum surface coverage of 33%, q* is higher than the contact angle of the nutrient broth solution on the control flat sample for all other micropillar surfaces, indicating that the presence of air pockets underneath the droplet is less favorable for the nutrient broth solution. In fact, although closer to Cassie-Baxter regime, the drop of nutrient broth on the micropillars may be in the metastable state, thus, more inclined to transit between Wenzel and Cassie regimes (Lafuma & Quéré 2003). Indeed, we observed the transition to Wenzel state when our sample was immersed in the nutrient broth solution where the solution gradually started penetrating into the surface incisions after 1hr (Figure 1E).

Table 1. Summary of measured contact angle values for saline and nutrient broth solutions on PDMS platforms with surface coverage percentages ranging from 19% to 33%, and calculated theoretical values for r, f, q, and q*. Where q is the Young's contact angle on a flat surface, q^c and q^w are the Cassie-Baxter and Wenzel contact angles, respectively, r is the roughness factor, and f represents the area fraction of the liquid-solid interface.

	Geometrical Parameters			Nutrient broth			Saline		
Surface coverage%	r	f	q*	q	q^c	q^w	q	q^c	q^w
33%	2.96	0.33	105^0	$107^0\pm4$	140^0	150^0	$115^0\pm3$	144^0	-
27%	2.62	0.27	108^0	$107^0\pm4$	144^0	140^0	$115^0\pm3$	148^0	-
23%	2.36	0.23	111^0	$107^0\pm4$	147^0	133^0	$115^0\pm3$	150^0	174^0
19%	2.16	0.19	114^0	$107^0\pm4$	150^0	129^0	$115^0\pm3$	153^0	156^0
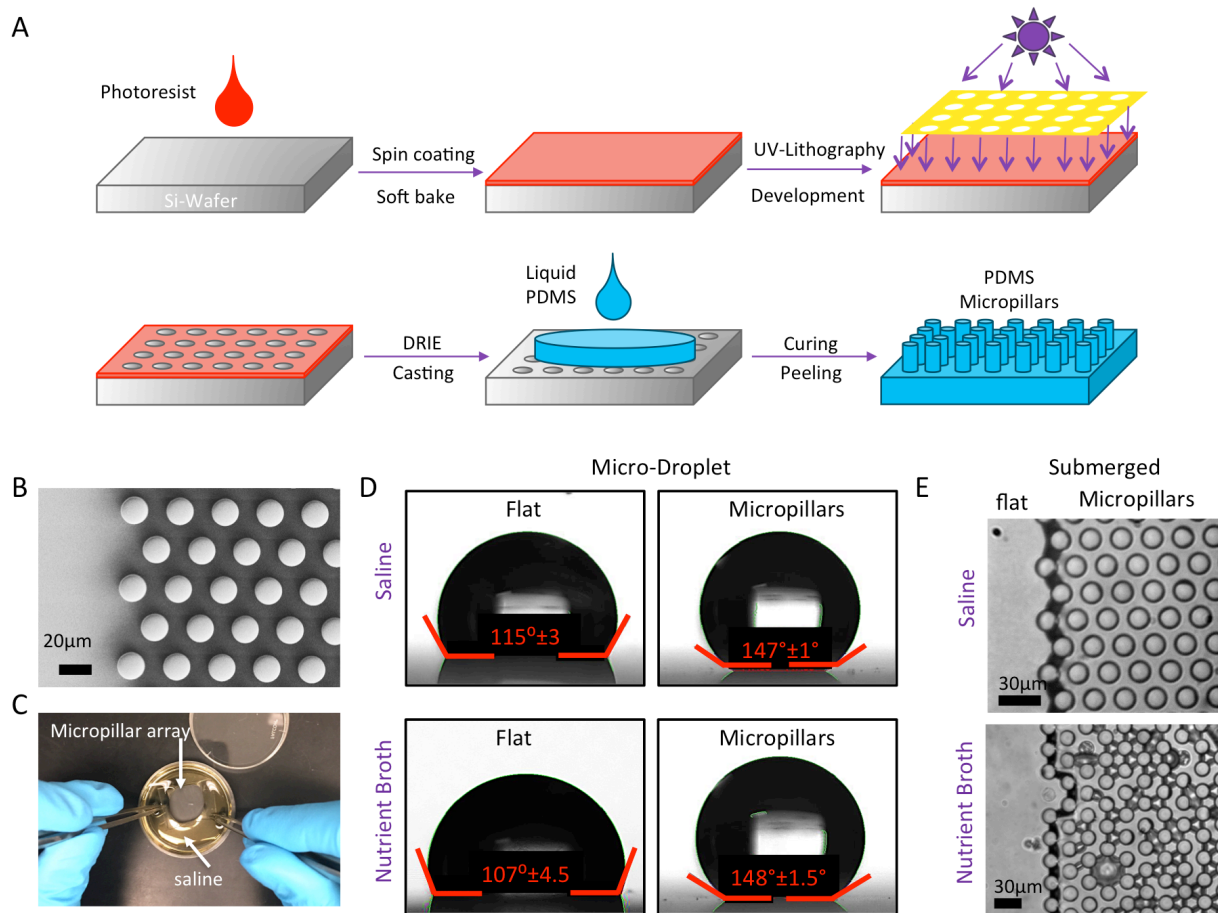
Figure 1. PDMS micropillar platform: fabrication and characterization. A) Schematic representation of the fabrication process of PDMS micropillar arrays B) Top view SEM image of the interface between flat PDMS surface and fabricated hexagonally arranged PDMS micropillars arrays C) Digital camera image showing the hydrophobic nature of the PDMS platform as solution is repelled from the areas containing micropillars while the platform is pressed down into saline solution. D) Side view of the dispensed saline and nutrient broth solutions droplets for measurements of contact angle on flat and micropatterned PDMS surfaces. E) Optical image of PDMS micropillars submerged in saline solution (top) and nutrient broth solution (bottom) after 1 hour of incubation; the solution is pinned at the interface between the micropillars and the flat PDMS surface in saline which indicates the presence of air-gaps formed between the micropillars (top); Alternatively after 1 hour the nutrient broth solution begins to penetrate in between micropillars (bottom).

Adhesion characteristics of S. aureus bacterial cells on PDMS micropillars. *S. aureus* cells in a saline solution were plated on the PDMS platform as shown in Figure 2A, and incubated for 1, 4 or 24 hours. As predicted by wetting studies, adhered bacterial cells only remained on the tops surfaces of micropillars when aspirating the sample after a 1-4 hour incubation time (Figure 2B), as the saline solution likely did not penetrate in between micropillars during this time frame. Both side-view and top-view SEM images, and top view optical images indicated the adhesion of bacteria to the pillar tops as well as the flat PDMS surfaces at 1 and 4 hour incubation times, with a higher density of adhered cells for longer incubation times of 4 hours as expected (Figure 2B). However, after 24 hours of incubation bacterial cells fully covered the PDMS platform indicating that the solution penetrated into the surface asperities after 24 hours and created a fully wetted condition. The cracking of the layer of bacterial cells (for 4 and 24 hr incubation times) and clustering of micropillars

(for 24 hr incubation time) as seen in Figure 2B is a result of the drying process for SEM preparation. Using the remarkable saline-solution repelling properties of these PDMS micropillars, through a single-step aspiration technique, we were able pattern small isolated microcolonies of bacterial cells on top of PDMS micropillars. By changing bacteria incubation times, the size of microcolonies of S. aureus cells can be controlled. Furthermore, using PDMS micropillar arrays of different surface coverage areas (*i.e.* different distance between micropillars) colonies with varying separation distances can be patterned (Table 1, Figure S1).

Figure 2. Formation of *S. aureus* colonies on hydrophobic PDMS micropillars.
A) Representative scanning electron micrograph and optical images of *S. aureus* cells at the interface between PDMS micropillars and their adjacent smooth surfaces. The top row shows a side view SEM image of PDMS micropillars after 1hr, 4hr, and 24hr bacteria incubation times at a 70 degree SEM stage tilt. The second row represents top view SEM images of PDMS micropillar arrays. Note that the side and top views are not from the same PDMS micropillar arrays. These images indicate that bacterial cells adhere preferentially to the smooth surface as well as pillar tops after 1-4hr incubation times but penetrate in between micropillars and cover the platforms fully after 24 hours. Low magnification top view optical microscope images on the third row also show the absence of bacterial cells in between micropillars after 1-4hr incubation times but a full coverage of the platform after 24 hours of incubation. The white dotted lines indicate the interface between micropillars arrays and the adjacent smooth surfaces. Cracking of the bacteria film and clustering of micropillars seen for 24hr incubations times are likely caused while drying the samples for imaging. **B)** Schematic representation of the interfaces between the micropillar platform and the solution containing *S. aureus* bacterial cells. The air pockets trapped in between PDMS micropillars inhibit the *S. aureus* solution from penetrating in between the micropillars. After 24 hours the solution penetrates in between micropillars resulting in cell attachment to the micropillar sidewalls as well as the smooth surface in between micropillars. Scale bars shown on SEM images represent 20 μm.

Fabrication of biostrings of S. aureus cells between PDMS micropillars through physiochemical processes. Detailed SEM inspections of the PDMS micropillar platforms that were aspirated after 1 hour of bacteria incubation revealed several nanometer-scale string-like structures suspended between two (Figure 3A-C) or three (Figure 3D) bacteria microcolonies on adjacent micropillars. These high aspect ratio "biostrings" consisted of one or several round ~500nm diameter *S. aureus* cells aligned side by side between micropillars as shown in Figure 3. Note that we name these microcolonies "biostrings" instead of "biofilms" since the bacterial cells are embedded into strings rather than films. In order to assess whether the dehyrdration step for SEM analysis was resulting in the formation of these biostrings, we imaged our PDMS platforms using optical microscopy directly after aspirating the bacteria solution and before sample dehydration. We observed similar nanostrings forming between microposts (Figure S1). Furthermore, such nanostrings were observed on PDMS micropillar arrays of various surface coverages (27-33%), however a higher number of nanostrings were obtainable on platforms with higher surface area coverage of micropillars (Figure S1).
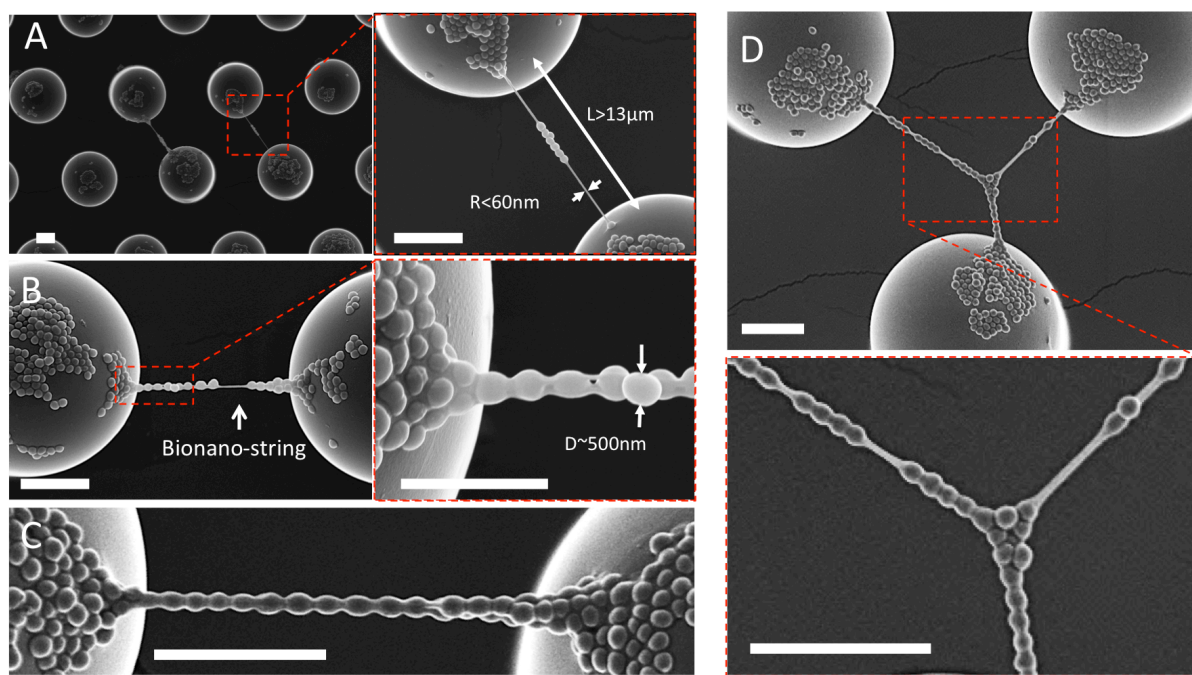
Figure 3. Formation of nano-networks of *S. aureus* cells between neighboring micropillars. A) Low (left) and high (right) magnification SEM images of Nano-strings with nm-scale radii (r<60 nm) and micron-scale lengths (L>13 µm) connecting two bacterical colonies on top of PDMS micropillars. B) *S. aureus* cells with ~500nm diameters embedded inside biostrings and suspended between two adjacent micropillars. C) A string of *S. aureus* cells connecting two adjacent bacterial colonies. D) Biostrings of *S. aureus* cells connecting three adjacent micropillars and forming a network of *S. aureus* cells. All scale bars represent 5 µm.

Next, we examined whether the formation of biostrings of *S. aureus* was due to active adhesion and activity of *S. aureus* cells, or purely a physicochemical phenomenon resulting in a mere deposition of cells during the de-wetting process by mechanisms similar to some previous studies. These studies used wetting/dewetting characteristics of PDMS micropillars to deposit and suspend highly ordered arrays of DNA nanowires on top of micropillars(Guan et al. 2007; Glazer et al. 2014; Miele et al. 2015; Charlot et al. 2014; Lin

et al. 2010; Guan & Lee 2005). To test this, we fixed *S. aureus* cells in solution and plated these dead cells onto PDMS micropillar platforms and aspirated the samples after 1hr incubation. Careful inspections showed no *S. aureus* cell deposition on PDMS micropillars and no network formation (Figure S2). We concluded that in addition to the wetting properties of hydrophobic PDMS micropillars, the formation of networks depended on biological processes, namely the active adhesion of bacteria on pillar tops and the formation of thin biofilms at the bottom surface of the solution, which was not achievable with inactive bacteria.

The proposed mechanisms of biostring formation is depicted in Figure 4A. During the 1hr incubation of bacterial solution on PDMS micropillars, *S. aureus* cells adhere to the solid surfaces that are available to them, specifically the flat PDMS surface and the tops surfaces of micropillars. A thin biofilm or pellicle then begins to form at the bottom of the *S. aureus*-containing saline solution (on top of micropillars). During the sample aspiration and washing process, all *S. aureus* cells that are not strongly attached to any solid surfaces are removed. As the bacteria solution is extracted from the PDMS platform, the thin biofilm collapses into nanostrings suspended between micropillars. Furthermore, during this dewetting process, *S. aureus* cells in the solution that may be sitting on top of air gaps between micropillars get captured in the collapsing biofilm and form a string of bacterial cells embedded within a collapsed biofilm, which we refer to as "biostrings" (Figure 3, Figure 4). The direction of biostring formation depends on the local direction of liquid retraction from the micropillars (Figure 4B). Indeed Lin *et al.* modeled the dewetting mechanisms of hexagonally arranged PDMS micropillar arrays and showed that the alignment of DNA nanowires on top of micropillars is highly dependent on the direction of dewetting as well as the arrangement of the micropillars.
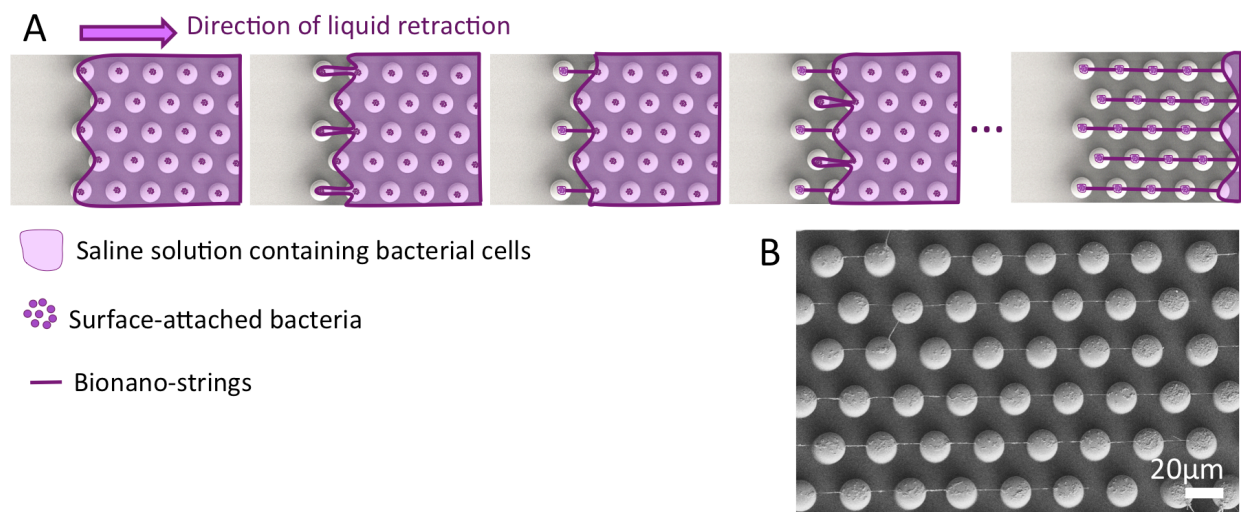
Figure 4. Schematic representation of mechanisms of biostring formation. A) For short incubation times, the solution containing *S. aureus* bacterial cells sits on top of the hydrophobic PDMS micropillars and does not penetrate in between micropillars. A thin biofilm or pellicle then forms on top of these micropillars (at the bottom of the *S. aureus* solution), while several bacterial cells actively adhere to the top surfaces of these micropillars. During the dewetting process, this biofilm collapses into thin biostrings which form between bacterial colonies adhered on adjacent micropillar. These biostrings align in the direction of liquid retention in that location. B) locally aligned biostrings of *S. Aureus* cells on top of PDMS micropillars.

Additionally, increasing either the incubation time (Figure 5A), or the initial concentration of *S. aureus* cells in the saline solution before plating cells (Figure 5B), allowed the control of the number of *S. aureus* cells attached to the top surfaces of micropillars and embedded within biostrings suspended between micropillars as shown in Figure 5. Using this simple technique, we were able to pattern bacterial colonies of varying sizes at the liquid-solid (bacteria solution and PDMS micropillars) and liquid-air (bacteria solution and air-pockets) interfaces. As we show in the next section, these microcolonies can later grow in a controlled manner, into biofilm-like structures with distinct architectures.
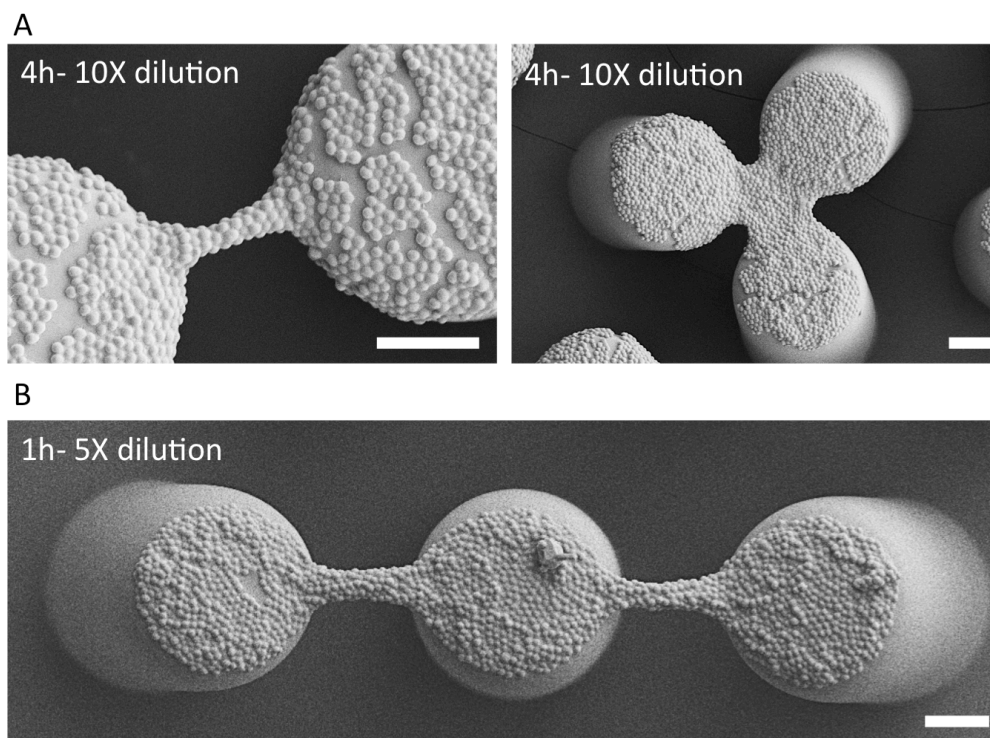
Figure 5. Control of biostring sizes by increasing bacteria incubation times or increasing cell densities. A) SEM images of bacterial cells attached to and suspended between PDMS micropillars with a 1X cell density and 4hour incubation times. B) SEM image of cells attached to and suspended between PDMS micropillars for 5X cell density and 1hr incubation times. All scale bars represent 5 μm.

Biorods of S. aureus cells formed between PDMS micropillars. We next asked whether the *S. aureus* cells that were exposed to the dewetting process for biostring fabrication were able to grow into larger colonies. To test this, directly after aspirating the samples, we submerged the platform in a nutrient broth environment that induces *S. aureus* cell growth and incubated the sample for 24 hours. As opposed to the conventional heterogeneous growth of bacterial colonies (biofilms) on flat surfaces (Garrett et al. 2008), the bacterial cells embedded in the biostrings suspended in between micropillars developed into organized micron-thick rod shaped structures which we refer to as "biorods" as shown in Figure 6A and 6B. As previously mentioned, air pockets are less likely to form between micropillars in the nutrient broth solution compared with the saline solution (Figure 1E, S3). Therefore, the nutrient broth solution reaches a Wenzel state and creates a fully wetted condition on the submerged PDMS platform consisting of biostrings, allowing their access to nutrients, and subsequently, their growth into biorods after 24 hours as shown in

Figure 6C. In order to ensure that the biorods were in fact growing from the biostrings and not arbitrarily, in this step, we only fabricated biostrings in the center of the micropillar platform. Accordingly, we incubated a drop of bacteria-containing saline solution in the center of the platform, instead of submerging the entire PDMS platform in bacteria solution. After aspirating the drop, biostrings only formed in the areas covered by the drop. Consequently, after submersion into a nutrient broth solution for 24 hours, biorods were only observed in the central regions of the PDMS platforms. The
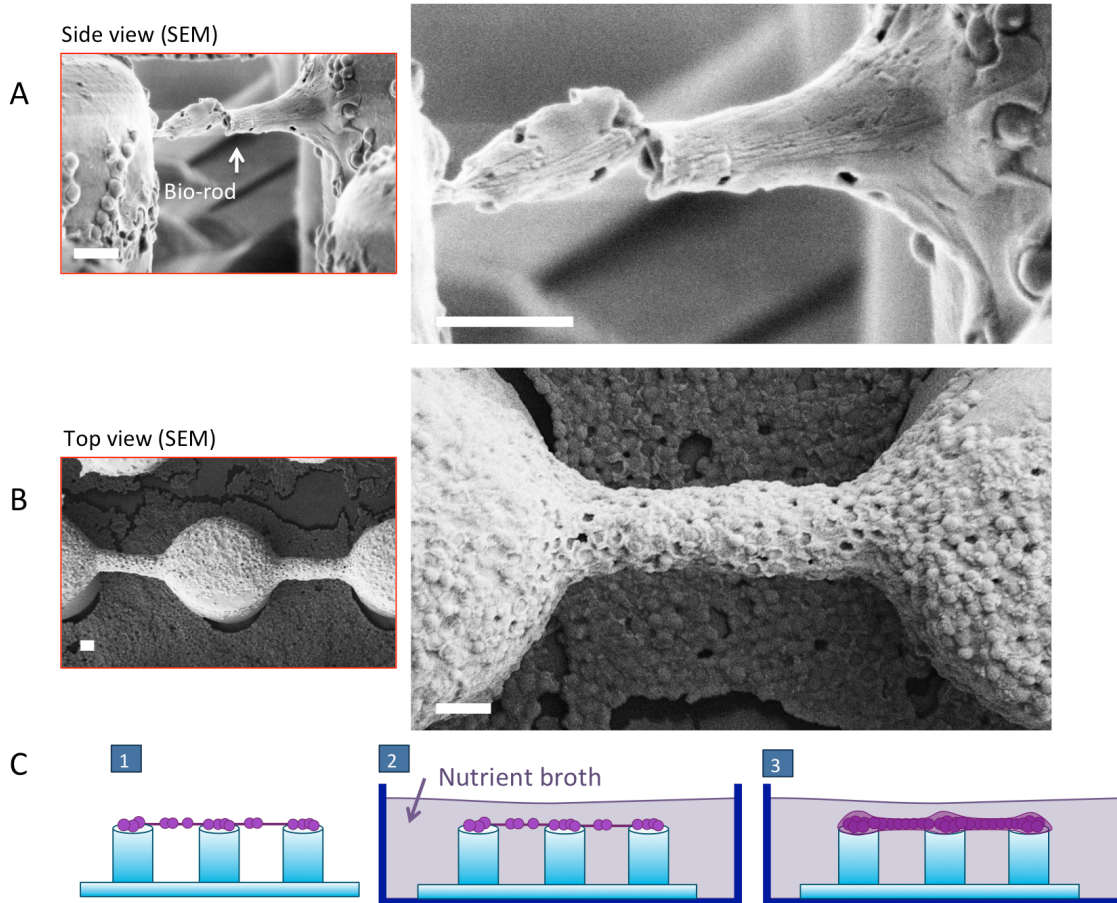
Figure 6. Growth of micron-thick rod shaped bacterial colonies (biorods) from biostrings. A) Top and B) side view SEM images of biorods formed between two adjacent micropillars. C) schematic representation of biorod formation: 1) Biostrings were fabricated by dewetting PDMS micropillar arrays after 1 hr of *S. aureus* incubation 2) platforms were immediately placed into a solution of nutrient broth for 24hrs 3) strings of cells connecting adjacent micropillars grew into rod shaped biofilms or "biorods".

The communications between cells in a bacterial colony depends on several factors including their density and spatial distribution, as well as their surrounding environment; however, the various factors affecting bacterial communication are difficult to differentiate. Using our method, the activities of microcolonies attached to pillar tops can be compared with cells embedded in a thin matrix (the biostrings) and characterized side-by-side (Fig 7A). For example, future live-cell studies on bacterial cells on top of PDMS micropillars, compared with their neighboring biostrings can reveal phenotypical differences between solid-surface-associated and matrix-associated cell colonies in a highly controlled

environment (Figure 7A). Generally, surface-anchored *S. aureus* cells grow into porous nonhomogeneous shaped biofilms on flat surfaces (Figure 7B). The suspended *S. aureus* cells on our PDMS platform showed a more homogeneous radial growth from nanostring structures into micron-thick rod-shaped structures. All previous studies of bacteria patterning have focused on patterning cells on solid surfaces with the goal of characterizing biofilm formation at the solid-liquid interface(Palacios-Cuesta et al. 2015; J. Kim et al. 2012; Suo et al. 2008; Hochbaum & Aizenberg 2010; Epstein et al. 2011), while bacterial colonies can also grow at a liquid air interface. Using closely spaced micropillars with surface coverage of 33% or more (Table 1), the nutrient broth solution also enters the Cassie-Baxter regime meaning that air pockets will form between the PDMS micropillars and so biostrings can grow controllably at the liquid-air interface mimicking the environment of pellicle formation (Figure 7C). Using this method the anaerobic *vs.* aerobic *S. aureus* colony growth could be characterized.

Finally, as shown in computational models by Lin *et al.*, controlling the direction and speed of liquid extraction can precisely control the dewetting patterns of PDMS micropillars (Lin et al. 2010) and hence efficiently generate large arrays of highly ordered and interconnected colonies of bacteria.
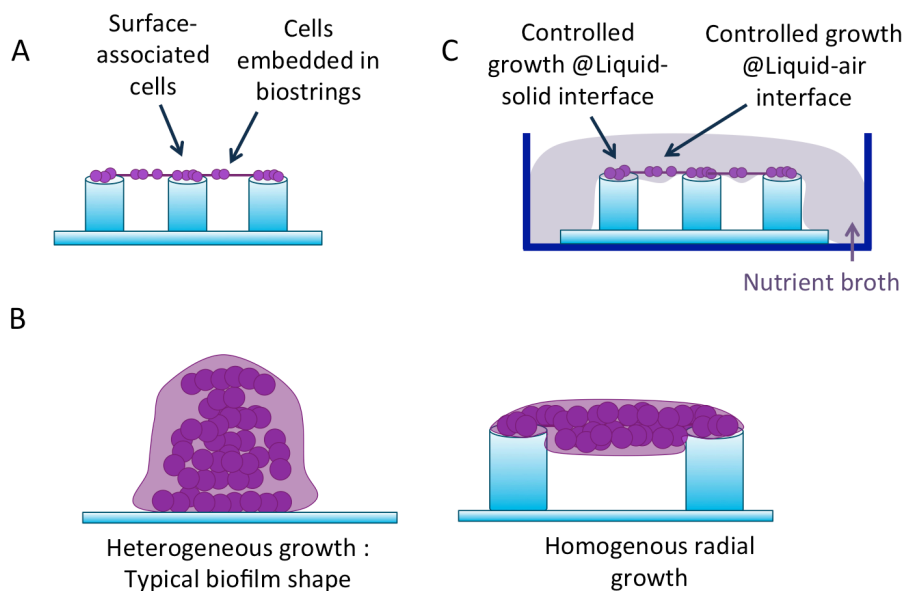
Figure 7. Potential applications for the developed cell patterning method. A) Characterization of intercellular communications and colony growth in surface associated bacteria *vs.* bacterial cells embedded within a thin biostring and suspended between micropillars. B) Controlling a homogeneous radial growth of *S. aureus* colonies as opposed to typical heterogeneous biofilms on solid surfaces. C) Control and comparison of colony growth at the liquid-solid or liquid-air interface by taking advantage of the wetting properties of PDMS micropillars

Conclusions

Bacterial cells have extraordinary communication skills and the capacity to colonize and form social networks in which they develop distinct phenotypes that drastically increase their chances of survival. Understanding the mechanisms of colony formation is therefore of great practical and clinical significance and requires the design of tools that can precisely control the initial organization and subsequent growth of bacterial colonies.

In this study, we developed a low-cost and simple method that utilizes surface dewetting properties of PDMS micropillars together with bacterial physiology to pattern nano and micron scale colonies of methicillin-resistant *S. aureus*. Furthermore, we controlled colony growth architecture and showed that when provided with a nutrient rich environment, the patterned cells can grow into rod-shaped structures.

We believe our developed method can serve as a platform for studying the aerobic and anaerobic growth of bacterial colonies with a significant impact on understanding cell-cell communications such as quorum sensing, horizontal gene transfer and metabolic cross-feeding specially during initial stages of colony formation. Our future studies will be directed at elucidating the effect of spatial control of *S. aureus* colonies on cell-cell communications, and extracting the properties of the generated biorods and comparing them with conventional biofilms grown on flat solid surfaces.

Methods

Fabrication of micropillars. Hexagonally arranged arrays of micropillars were replicated from a negative silicon master mold through casting of liquid PolyDiMethylSiloxane (Sylgard 184, Dow Corning) containing 10%wt cross-linking agent and curing for 1hr at 120^0C. Diameter and the height of the micropillars were fixed at 15mm and 22.5mm, respectively. Center-to-center spacing was varied between 25mm to 32.5mm yielding 33% to 19% micropillars surface coverage (*f*). To avoid any defect to the pillars during the peeling, surface of the master mold was treated with self-assembled monolayers (SAM) of heptadecafluoro-1,1,2,2, tetrahydrodecyltrichlorosilane (Gelest Inc. MA, USA) using the methods described elsewhere (Shahsavan & Zhao 2011).

Contact angle measurement. Sessile drop technique was used for static contact angle measurements using a custom made apparatus. Droplets of saline solution and nutrient broth with volumes of about 5 μL were dispensed on the samples with the rate of 100 mL/hr. At least 10 images of the liquid droplets on the surfaces were analyzed to extract the contact angle at the three-phase contact line.

S aureus culture and plating. *S. aureus* (ATCC 6538) was purchased from Cedarlane Labs (Burlington, ON, Canada). *S. aureus* was inoculated on Trypticase Soy Agar (TSA) plates and incubated at 37 °C for 24 hours. Bacterial cells were harvested using alginate swabs and suspended in 5 mL of sterile saline (2.55%) with nutrient broth (~0.006%) in a 15 mL centrifuge tube. A 2.55% saline solution was prepared and sterilized by using Nalgene filters. In order to preserve S. aureus cells during experiments, 0.006% of nutrient broth was added to the saline solution. *S. aureus* cells were then transferred to the saline solution by adding 5 mL of saline to the TSA plate. *S. aureus* cells were washed with saline solution seven times by centrifugation at 4000 rpm for 10 min. The stock solution of S. aureus cells was diluted 10-fold or 5-fold in saline for low or high-density cell patterning, respectively.

For each experiment, the PDMS platforms were placed inside a petri dish and 4.5 mL of the diluted *S. aureus* solution was added until the solution covered the entire platform (Figure 2A). The platforms were then incubated at 37 °C for 1,4, or 24 hours. Subsequently, the samples were aspirated to remove bacterial solution and either imaged immediately using optical microscopy or prepared for SEM analysis. Alternatively for biorod fabrication,

aspirated samples were placed into a petri dish containing BD BBL™ Prepared Nutrient Broth and incubated at 37 °C for 24 hours before fixation and imaging. As a control for this experiment, an identical sample was fixed and dried directly after aspiration and observed under the SEM.

SEM preparation and imaging. S. aureus cells were fixed using 2.5% glutaraldehyde for 2 h and air-dried in a fume hood for 12 h. The PDMS samples were then coated with a 10nm layer of gold and inspected using a field emission scanning electron microscope (Zeiss LEO 1550).

Chapter 3

MOLECULAR MECHANISMS OF FORCE TRANSMISSION TO THE NUCLEUS

The work presented in this chapter was adapted from the following published manuscripts:

Z Jahed, MRK Mofrad, "*Mechanical LINCs of the nuclear envelope: Where SUN meets KASH*", Extreme Mechanics Letters (special issue on Mechanobiology), (2018)

Z Jahed, M Soheilypour, M Peyro, MRK Mofrad. "*The LINC and NPC relationship–it's complicated!*" Journal of Cell Science, 2016

Z Jahed, H Shams, MRK Mofrad. "*A disulfide bond is required for the transmission of forces through SUN-KASH complexes.*" Biophysical Journal, (2015)

Z Jahed, D Fadavi, U Vu, E Asgari, G.W. G. Luxton, MRK Mofrad, "*Molecular Insights into Mechanism of SUN1 oligomerization in the Nuclear Envelope*", Biophysical Journal, In Press (2018)

Z Jahed, UT. Vu, D Fadavi, H Ke, A Rathish, S Kim, W Feng, Mohammad RK Mofrad, "*A Molecular Model for LINC complex regulation: activation of SUN2 for KASH binding*", Submitted. (2018)

3.1 LINC AND NPC FUNCTIONS AT THE NUCLEAR ENVELOPE

Introduction

The genomic information in eukaryotic cells is protected by a double-layer nuclear membrane, which compartmentalizes the cell into two regions, the nucleus and the cytoplasm. Despite the spatial separation of the cytoplasm and the nucleus, their functions are tightly coupled and regulate various cellular functionalities. This coupling is achieved through two different protein complexes: (i) nuclear pore complexes (NPCs), as the biochemical gateway for nucleocytoplasmic traffic, and (ii) the linkers of the nucleoskeleton and cytoskeleton (LINC) complexes, which act a physical linkage (Fig. 1A). Although NPCs and LINCs are often considered as separate entities that link the nucleus and the cytoplasm, various studies have shown that some functions of NPCs and LINC complexes are intimately associated.

NPCs are the unique gateways for the bidirectional transport of cargo between the nucleus and cytoplasm. As the largest macromolecular complexes in the nuclear envelope (NE), NPCs are responsible for translocation of vital cargos, ranging from different types of RNAs to various proteins (Raices and D'Angelo 2012). NPCs are made up of almost 30 different types of proteins called nucleoporins (Nups) (Fig, 1B), which can be generally categorized into two major groups, FG Nups (Nups rich in Phenylalanine-Glycine repeats) and non-FG Nups (Jamali et al. 2011a). FG Nups possess disordered regions (lacking secondary structure), which are responsible for the transport of cargos through the NPC. In addition to the overall structure of the NPC that has been conserved through evolution, recent bioinformatics studies have identified specific, evolutionary-conserved features in the disordered regions of the sequences of Nups, which are believed to regulate cargo transportation (Ando et al. 2013; M Peyro et al. 2015). Other Nups primarily constitute the building blocks of the NPC scaffold, which is tightly connected to transmembrane proteins and the NE. Beside controlling the nucleocytoplasmic traffic processes, NPCs are involved in many other vital processes in the cell, such as DNA repair, gene expression, aging, apoptosis, determination of cell differentiation (Nagai et al. 2008), and nucleo-cytoskeltal coupling and mechanobiology (Soheilypour et al. 2016a) . However, the underlying mechanism of transport is still under much debate, despite the fact that a multitude of computational and experimental studies have been performed with the aim to shed light on how exactly different cargos are transported through the NPC (Yamada et al. 2010; Moussavi-Baygi et al. 2011; Labokha et al. 2013; Ghavami et al. 2014; Mohaddeseh Peyro et al. 2015; Hough et al. 2015; Milles et al. 2015; Ma et al. 2016).

Aside from the NPC, another type of protein complex provides a physical linkage between cytoskeletal and nucleoskeletal elements and so allows a direct transmission of mechanical signals through the NE. In 2006, two independent studies presented components of these complexes, which are now known as LINC complexes (Crisp et al. 2006a; Padmakumar et al. 2005; McGee et al. 2006). In metazoans and fission yeast, the main components of LINC complexes include proteins of the KASH (Klarsicht, ANC1 and Syne Homology), and the SUN (Sad1p/UNC (uncoordinated)-84) families, which interact in the perinuclear space (PNS) (Fig, 1C). SUN proteins contain a SUN domain that resides in the PNS and is preceded by a coiled coil region that spans the remaining space up to the inner nuclear membrane.

Finally, the transmembrane and a nucleoplasmic domains of SUN proteins link the interior of the nucleus to the PNS (Sosa et al. 2013) . SUN 1 and SUN 2 interact with elements of the nucleoskeleton and bind to Lamin A at their nucleoplasmic domains (Qian Liu et al. 2007) as shown in Fig. 1. The SUN protein UNC-84 is also known to bind to the *Caenorhabditis elegans* lamin LMN-1 (Bone et al. 2014). The nuclear anchors for SUN proteins are not limited to lamins. In yeast, which lack lamins, LINC complexes are anchored to chromosomes and promote chromosome movements (Morimoto et al. 2012). Furthermore, the nucleoplasmic domain of SUN directly binds to chromatin in mammalian cells (Xiong et al. 2008).

KASH domain-containing proteins consist of a short KASH peptide that resides in the PNS where it binds the SUN domain of SUN proteins (Fig. 1C). *In vitro* structural and biochemical characterization of the SUN-KASH complexes show that three KASH proteins can simultaneously bind to a SUN trimer (Z. Zhou et al. 2012a; Sosa et al. 2012a; Nie et al. 2016) (Fig. 1C). To date, six mammalian KASH domain proteins have been identified, including a family of four nuclear envelope spectrin repeat proteins (Nesprins), KASH 5 and lymphocyte-restricted membrane protein (LRMP) (Lindeman and Pelegri 2012; Morimoto et al. 2012; Horn et al. 2013; Rajgor and Shanahan 2013; Luxton and Starr 2014; Padmakumar et al. 2005) (Fig 1C). Nesprin 1 and 2 are the largest isoforms of the nesprin family and the only two that are known to directly interact with actin through their calponin homology actin-binding domain (Crisp et al. 2006b; Sosa et al. 2013; Lombardi, Jaalouk, Shanahan, Burke, Roux, et al. 2011) (Fig. 1A). LINC complexes are also attached to the microtubule network; this is indirect and mediated through motor proteins. Nesprin 1 and 2, as well as Nesprin 4 and KASH5 interact with microtubules through kinesins and dynein (Roux et al. 2009; Horn et al. 2013; Fan and Beck 2004; Morimoto et al. 2012) (Fig. 1A), whereas Nesprin 3 associates with intermediate filaments through plectin (Wilhelmsen 2005). LINC complexes are also present in budding yeast and plants, however the luminal peptide of the outer nuclear membrane (ONM) component of these complexes lacks the conserved KASH domain found in metazoans (Fig. 1C). For a full list of LINC interacting partners please refer to (Rothballer and Kutay 2013b).

The composition of the nuclear envelope is highly tissue specific and more than 215 NE transmembrane proteins have been identified to date (for a complete review see (Wilson and Berk 2010)). In this chapter, we focus specifically on the roles and functions of the NPC and LINC complexes that are associated with the nuclear envelope, as the structural integrity of the NE depends on both complexes. As LINC complexes directly interact with various cytoskeletal elements, we argue that they may play an important role in the association of NPCs with the cytoskeleton. Furthermore, the association of both these complexes with the nucleoskeleton is likely to be codependent. Although early studies showed no significant role of LINC complexes in nuclear transport of proteins through NPCs (Qian Liu et al. 2007), more recent studies discussed here have drawn connections between nucleocytoplasmic transport through NPCs and LINC complexes, further highlighting the importance of better understanding the functional and structural links between these two essential components of the NE.
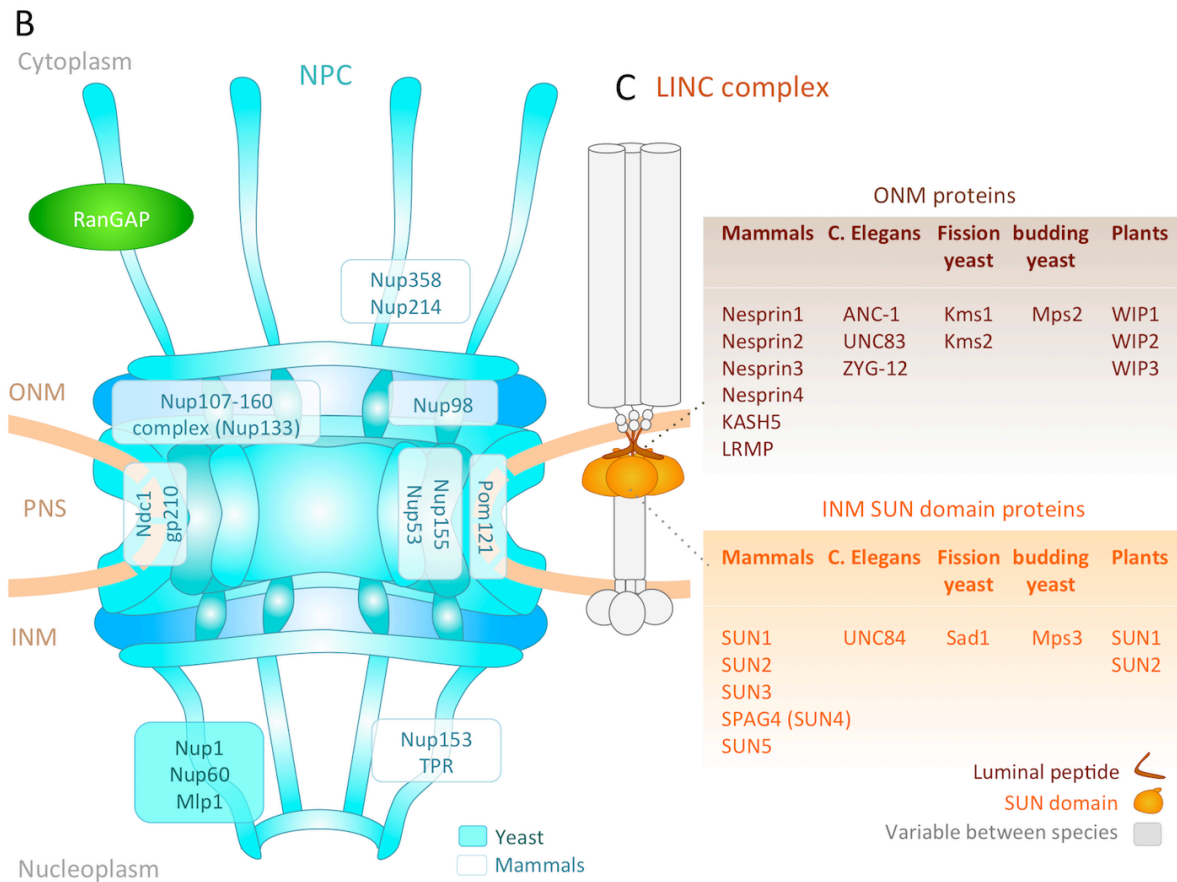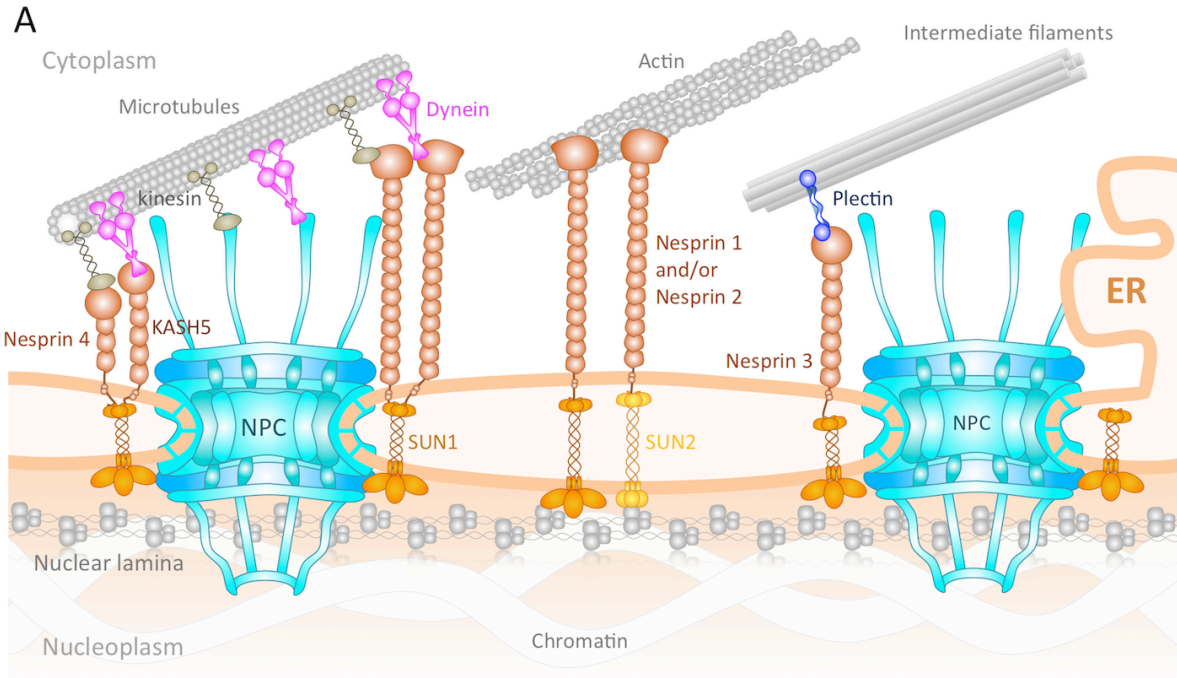
Figure 1: Schematic representation of LINC complexes, and NPCs and their associations at the nuclear envelope.
A) Illustrated here are interactions of LINC complexes and NPCs with the cytoskeleton, nuclear membranes, the nucleoskeleton, as well as each other, at the nuclear envelope (NE). In the cytoplasm, both NPCs and LINC complexes

associate with microtubules through kinesin and dynein motor proteins. LINC complexes also interact directly with the actin cytoskeleton, and with intermediate filaments (IFs) through plectins. In the nucleoplasm, both NPCs and LINC complexes interact with nuclear lamina and chromatin. LINC complexes and NPCs also associate directly or indirectly with each other through interactions between Nup153 and the nucleoplasmic domain of SUN proteins. SUN1, but not SUN2, is directly associated with NPCs. B) Schematic representation of the NPC architecture based on recent X-ray crystallographic analyses of the NPC structure (Lin et al. 2016) . The location of nucleoporins (Nups) that are involved in interactions of the NPC with either the cytoskeleton, the nucleoskeleton, the NE or LINC complexes are indicated. Nup358 and Nup214 are localized to the cytoplasmic filaments of NPCs of vertebrates. Ndc1, gp210, and Pom121 are transmembrane proteins that are mainly involved in integration of the NPC into the NE. Nup153 (Nup1 and Nup60 are yeast homologues) and TPR (Mlp1 is yeast homologue) are nuclear basket Nups. The Nup107-160 complex is one of the building blocks of the NPC scaffold. (Please note that only the Nups discussed in this review are labeled. Moreover, some nucleoporins such as Nup98, appear both at the cytoplasmic and the nucleoplasmic sides and are symmetric in the NPC structure; however, only one occurrence of each nucleoporin is depicted in the figure.)

C) LINC complexes are formed by the interaction of SUN (Sad1p/UNC (uncoordinated)-84)-domain proteins located at the inner nuclear membrane (INM) and a short luminal peptide of a number of outer nuclear membrane (ONM) proteins in the perinuclear space (PNS). The inset provides a list of LINC components in various species, In metazoans and fission yeast, the ONM component of LINC consist of KASH domain (Klarsicht, ANC1 and Syne Homology) proteins that reside mostly in the cytoplasm; these have a short KASH domain that extends into the perinuclear space (PNS) where it interacts with SUN-domain proteins. In yeast and plants, ONM-residing LINC constituents do not contain the conserved KASH domain, but perform a similar biological role. SUN proteins are shown as trimers based on structural studies of the human SUN2 in complex with the KASH domain of Nesprin 2 (pdb IDs 4FI9 and 4DXS) (Z. Zhou et al. 2012a; Sosa et al. 2012a). However, the oligomer state of other SUN proteins has not yet been determined. It should also be noted that it is not yet known whether two different KASH proteins can bind to the same SUN trimer, or whether KASH proteins bound to a SUN protein can associate with different cytoskeletal elements.

Role of the LINC complex in the assembly of NPCs

The first observation of a functional association between LINC and NPCs came from a study in 2007 in Hela cells (Qian Liu et al. 2007); here, the authors showed that both the luminal and nucleoplasmic domains of SUN1 were involved and required for its association with NPCs. Interestingly, many studies have shown partially redundant roles for SUN1 and SUN2 in several cellular functions, including anchoring of nuclei (Lei et al. 2009), DNA damage response (Lei et al. 2012) and centrosome-nucleus coupling (Zhang et al. 2009a), and the development of the retina outer nuclear layer (Yu et al. 2011). However, SUN1 and SUN2 have independent roles at NPCs. Liu et al. showed that only SUN1 and not SUN2 colocalized with Nup153. Furthermore, the distribution of NPCs across the nuclear envelope was altered only upon disruption of SUN1 (Qian Liu et al. 2007). The authors also showed that SUN1 proteins affect the distribution of NPCs independent of KASH-domain nesprin proteins, which couple SUNs to the cytoskeleton (Liu et al., 2007). A later study also showed that NPCs co-localize with SUN1, but not with SUN2 (Lu, Gotzmann, Sironi, V.-M. Jaeger, et al. 2008), suggesting that not all SUN proteins co-localize with NPCs. This was confirmed later on when it was reported that SUN1 only associates with NPCs that are formed during interphase, and not with postmitotic NPCs (Talamas and Hetzer 2011).

Interphase NPCs assemble through different mechanisms than postmitotic NPCs. In the initial postmitotic phase, some NPCs reassemble before the nuclear envelope is completely formed; however, later on during interphase, NPCs assemble *de novo* into a highly organized nuclear envelope and thus are limited by the spacing between the inner nuclear membrane (INM) and ONM (D'Angelo et al. 2006).. Thus, an early step in NPC assembly during interphase is the local fusion of the INM and ONM at sites of NPC assembly; a step SUN1 is likely involved in (shown in Fig 2). By such a *de novo* NPC assembly into the site of membrane expansion when the nucleus grows after mitosis, the density of NPCs on the NE remains constant (Fig, 2). SUN1 associates with the transmembrane Nup Pom121 to reduce

membrane spacing, which may promote membrane fusion (Talamas and Hetzer 2011; Jaspersen and Ghosh 2012) (Fig. 2). In agreement with previous work (Qian Liu et al. 2007), these studies also showed that both the nucleoplasmic and transmembrane domains of SUN1 are required for the localization and association of SUN1 with the NPC. This suggests that the interaction between the nucleoplasmic domain of SUN1 and the NPC is indirect or transient, as any biochemical interaction between SUN1 and NPCs has not been formally proven yet. The effect of SUN1 on the distribution of NPCs is likely due to an inhibition of *de novo* NPC assembly, which reduces the total number of NPCs on the NE, thus explaining the apparent clustering of NPCs (Fig. 2). Furthermore, although SUN1 is essential, its interaction with KASH proteins does not have a significant role in NPC assembly (Talamas and Hetzer 2011).

Lamins also have a vital role in maintaining the mechanical integrity of the NE and positioning the NPCs by acting as their anchoring points; indeed, both Nup53 and Nup153 associate with lamin type A and B, and Nup153 has multiple binding sites for lamins type A and B (for a full review see (Fiserova and Goldberg 2010)). Interestingly, both the N- and C-terminal domains of Nup153 directly interact with lamin; however, some studies suggest that this interaction is partially dependent on SUN1 (Liu et al. 2007; Fiserova and Goldberg 2010). Furthermore, owing to the strong association between Nup153 and lamins, Nup153 might have a role in laminopathies (Al-Haboubi et al. 2011), a set of diseases that have been highly correlated with disruptions of the nucleo-cytoskeletal coupling that is mediated through LINC complexes (Hale et al. 2008; Yang et al. 2013; Méjat and Misteli 2010). Furthermore, lamins are required for the even distribution of NPCs; in their absence, cytoskeletal forces exerted by dynein can pull NPCs toward the centrosome, resulting in their clustering (Guo and Zheng 2015).
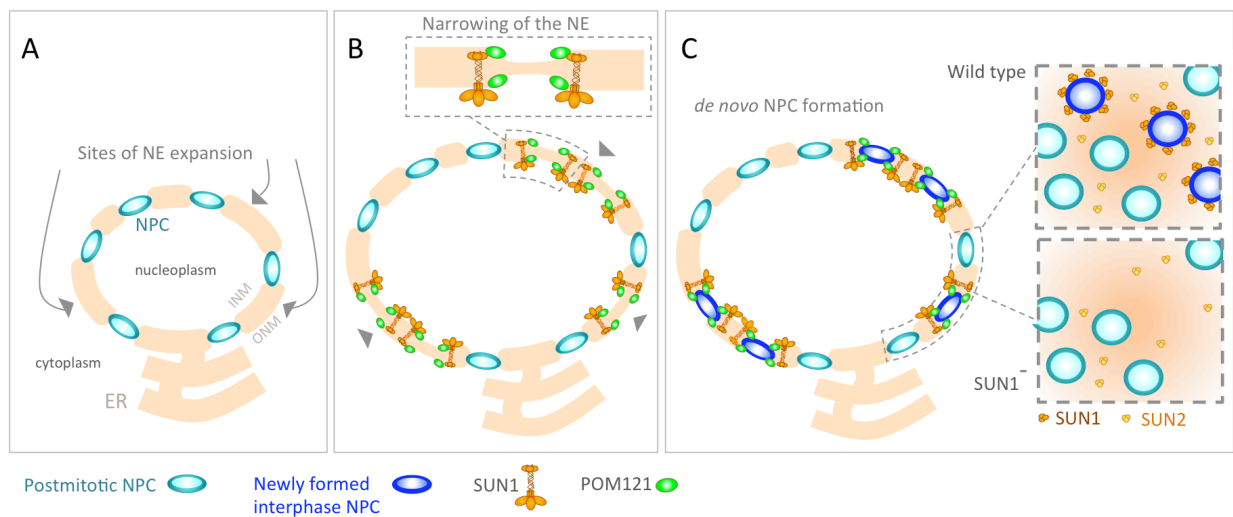
Figure. 2: SUN1-mediated *de novo* NPC assembly. A) During interphase, the nucleus grows and the NE expands at specific locations (gray arrows); however, the density of NPCs remains constant. B) The width of the NE is reduced at sites of NE expansion; here, the interaction of SUN1 with nucleoporin POM121 helps to narrow the NE and so promotes *de novo* NPC assembly. C) Assembly of NPCs at sites of reduced NE width; these newly-formed NPCs remain associated with SUN proteins. In the absence of SUN1, there is no *de novo* NPC assembly resulting in an overall reduction on the total numbers of nuclear pores; therefore, NPCs appear clustered in SUN1-depleted cells (lower inset). Note that SUN1 and SUN2 are both shown as timers however SUN1 and SUN2 oligomeric states during various cellular processes have yet to be validated *in vivo.*

Trafficking of SUN proteins across the NPC for INM localization

The first step in LINC complex formation is the transport of SUN domain proteins from their site of synthesis in the ER to their final destination in the INM. This process is NPC-dependent and involves three major steps (Fig. 3). First SUN-domain proteins, which are inserted into the ER membrane must be translocated from the ER to the ONM where NPCs reside (Fig. 3A Step 1). Next, these proteins must move across the NPC to reach the INM (Fig. 3A Step 2), and finally be retained in the INM where they can bind to KASH domain proteins (Fig. 3A Step 3). The mechanisms of the nuclear import of soluble proteins are well known. Small molecules and ions (<~9nm or 40kDa) can freely diffuse through NPCs, however larger molecules (up to ~40 nm or 25 MDa) contain a nuclear localization signal or sequence (NLS), which is recognized by transporter proteins called importins (Pante and Kann 2002; Jamali et al. 2011). Importins then mediate the transport of cargo through the central pore of the NPC.

SUN domain proteins traverse the NPC through mechanisms that are similar to that of large soluble molecules. With the exception of UNC-84, the nucleoplasmic domains of most SUN proteins are within the 40kDa free diffusion range (see Fig. 3B); however, these proteins are unlikely to freely diffuse through the NPC, due to their anchorage to the membrane and their large luminal domains. Indeed, several SUN proteins have experimentally been proven to contain nuclear-targeting sequences that play roles in their INM localization (Fig. 3B) (Daryabeigi et al. 2016; Tapley et al. 2011; Hasan et al. 2006; Graumann et al. 2010; Chen et al. 2014). Human SUN2, UNC-84, and plant SUN1 and SUN2 all contain nuclear localization signals (NLS) (Turgay et al. 2010; Graumann et al. 2010; Tapley et al. 2011). The NLS of human SUN2 has shown to directly bind to the importinα-importinβ hetrodimer (Impα/Impβ), which may mediate its transport through the NPC (Fig. 3B and C) (Turgay et al. 2010). SUN1 and UNC-84 contain a SUN-specific NE localization sequence named SUN-NELS; however, the importin which recognizes this signal has yet to be determined (Hasan et al. 2006). Another nuclear- targeting sequence found in several INM proteins including the SUN-domain protein UNC-84 is a short positively charged sequence adjacent to the transmembrane domain called the INM-sorting motif (INM-SM). As INM proteins are inserted into the ER, their INM-SM is recognized by a small membrane-associated isoform of importin α, Impα-16, which remains associated with these proteins and potentially mediates their transport across the NPC (Braunagel et al. 2007; Tapley et al. 2011). Finally, the budding yeast SUN protein Mps3 contains a nuclear-targeting domain (Mps3-NTD) that directly binds to yeast histone variant Htz1 (H2A.Z), which contains an NLS-like sequence recognized by several yeast importins including kap123 (Gardner et al. 2011) (Fig. 3C). We did not find any information on the nuclear targeting mechanisms of the fission yeast SUN protein Ndc1, or human SUN3, SUN4, or SUN5.
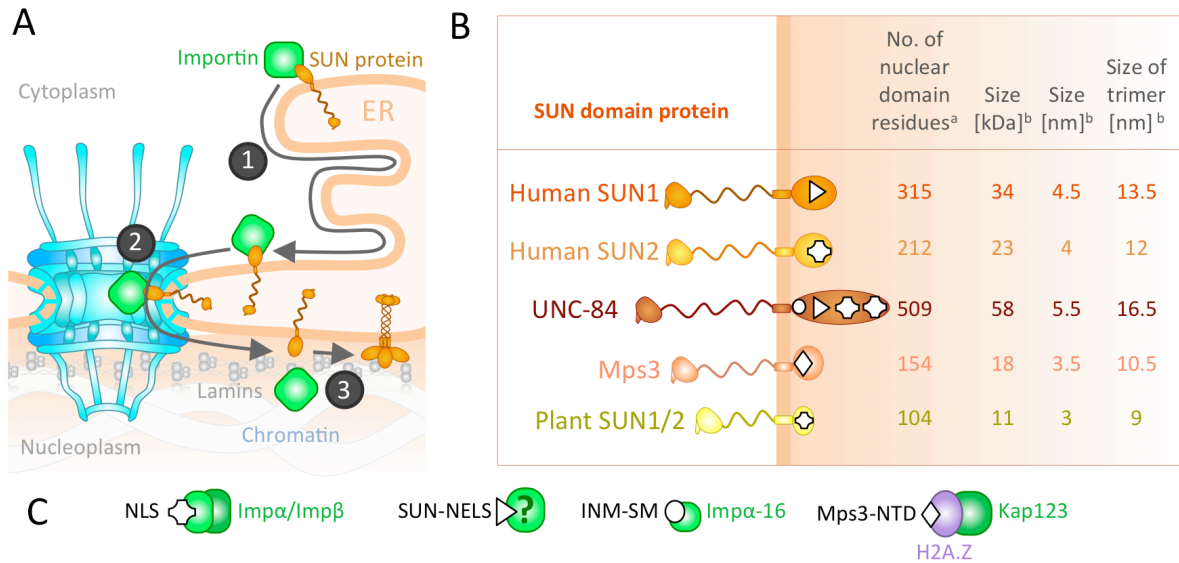
Figure 3: Transport mechanisms of SUN-domain proteins across the NPC for INM localization A) SUN domain proteins are translocated from their site of synthesis in the ER, to the ONM (1) and across the NPC to the INM (2), where they are retained and perform most of their known functions (3). SUN-domain proteins are likely transported across the NPC by transporters (importins) that recognize nuclear-targeting sequences on the nucleoplasmic domains of SUN proteins. B) The size of the nucleoplasmic domains of SUN domain proteins including the number of residues, molecular weights (size kDa) and diameters (size nm). Sizes of the nucleoplasmic domains of SUN trimers are also estimated. Each SUN protein contains a nuclear-targeting sequence on its nucleoplasmic domain as shown. NLS: Nuclear localization signal (cross) (Turgay et al. 2010; Tapley et al. 2011; Graumann et al. 2010), SUN-NELS: SUN-specific nuclear envelope localization signal (triangle) (Tapley et al. 2011; Hasan et al. 2006), INM-SM: inner nuclear membrane sorting motif (circle) (Tapley et al. 2011), Mps3-NTD: budding yeast SUN domain protein Mps3 nuclear targeting domain (diamond) (Gardner et al. 2011). Note that we found no information on the nuclear-targeting mechanisms of fission yeast SUN domain protein Sad1 and hence did not include it. C) Importin proteins recognize the nuclear targeting sequences on SUN proteins and mediate their transport across the nuclear pore. NLSs can bind the importinα-importinβ hetrodimer (Impα/Impβ) (Turgay et al. 2010). The transporter protein that recognizes SUN-NELS is unknown (Tapley et al. 2011; Hasan et al. 2006). The INM-SM is recognized by a small isoform of importin α, Impα-16. Mps3-NTD binds directly to yeast histone variant Htz1 (H2A.Z); H2A.Z contains a nuclear localization signal recognized by yeast importins kap123 (Gardner et al. 2011). Footnotes: [a.] The number of nucleoplasmic residues for each SUN domain protein was extracted from uniprot.org. [b.] All molecular weights were estimated using the Compute pI/Mw tool (Gasteiger E., Hoogland C., Gattiker A., Duvaud S., Wilkins M.R., Appel R.D. 2005). Sizes in nm were calculated using Protein size from MWt tool (http://www.calctool.org/).

Although the role of nuclear targeting sequences of SUN proteins in INM localization is evident, the mechanisms of SUN protein trafficking across the NPC are poorly understood (Fig. 3A Step 2). Recent structural models of the NPC reveal that a considerable disruption of the NPC structure is required for these relatively large proteins of the INM to diffuse across the NPC (Lin et al. 2016). Specifically, the luminal domains of SUN proteins must overcome the POM layer of NPCs (see Text Box 1). One hypothesis is the existence of ~10nm peripheral channels within each spoke of the NPC through which INM proteins may be transported (Maimon et al. 2012; Katta et al. 2014). Conversely, a more recent structural analysis of the NPC showed that Nups are tightly packed within each spoke of the NPC, and no such channels were observable (Lin et al. 2016). However, the authors observed small gaps between the spokes in the central channel, which they suggest as a potential uninterrupted path for INM transport. Future studies are needed to investigate the Nups involved in the trafficking of SUN domain proteins through the NPC.

The upper limit for the size of the nucleoplasmic domains of INM proteins for their successful transport through the NPC has been suggested to be 10 nm (Lin et al. 2016; Turgay et al. 2010). We estimated the size of the nucleoplasmic domains of SUN proteins (Fig. 3B) to be less than 10nm. We also estimated the size of SUN trimers to see whether transport of the trimer would be feasible, as it is not yet known whether SUN proteins form trimers in the ER or ONM, or only after they are targeted to the INM. Based on these estimates, SUN proteins are more likely to be transported as monomers and form higher order oligomers later on inside the INM as shown in Fig. 3A.

Roles of NPCs and LINC complexes in NE architecture

Cells maintain an even spacing between the INM and ONM, which typically ranges from 30 to 50 mn, through mechanisms that are not fully understood. The only known structures through which the INM and ONM are connected are NPCs and the LINC complexes, and it is thus not surprising that both are involved in the architecture of the NE (see Text Box 1). The first structural insights into SUN-KASH complexes predicted that the luminal coiled-coil regions of SUN proteins, which span the NE, may act as a ruler that adapts to, or determines, the width of the PNS (Sosa et al. 2013). The predicted length of SUN1 and SUN2 proteins in the PNS matches the typically observed PNS width of 30 to 50 nm (Sosa et al. 2013), and, according to this hypothesis, the width of the PNS may be reduced in cells that express SUN proteins with shorter luminal domains, such as testis-specific SUN3, SUN4 and SUN5 (Sosa et al. 2013) (see Fig. 4A). However there is currently no evidence that sperm cells or other cells types with shorter SUN proteins have a reduced PNS spacing. Furthermore, shortening of the SUN protein UNC-84 in *C.elegans* did not result in any observable narrowing of the PNS, and interestingly also did not disrupt nucleo-cytoskeletal coupling (Cain et al. 2014; Cain and Starr 2015). The mechanisms by which shorter SUN proteins overcome the PNS gap to bind KASH-domain proteins and mediate nucleo-cytoskeletal coupling remains unclear. Currently, two potential mechanisms are being proposed: (i) LINC complexes composed of shorter SUN proteins either locally pinch the nuclear envelope (Fig. 4A) or (ii) SUN proteins adapt to an existing PNS width by extending their luminal domains (Cain and Starr 2015) (Fig. 4B). In agreement with the second proposed mechanism, our recent molecular dynamics simulations suggested that tensile cytoskeletal forces acting on KASH proteins can be directly transmitted to the luminal domain of SUN proteins without disrupting the SUN-KASH domain interactions, and thus might represent a possible mechanism underlying this extension (Jahed, Shams & Mohammad R K Mofrad 2015). However, cytoskeletal forces can only be transmitted after the LINC complex is formed, so even if these complexes can extend in response to force, it remains unclear how shorter, INM-anchored SUN proteins are able to interact with the KASH domain at the ONM to initiate complex formation.

As discussed above, both the LINC complexes and NPCs are anchored to and span the NE, and are therefore likely to be involved in maintaining an even distance between the INM and ONM, even if they do not determine the exact distance. In fact electron microscopy images of the nuclear envelopes of Hela cells that have been depleted of SUN1 and SUN2 revealed frequent and discrete expansions of the PNS (Crisp et al. 2006a) (Fig. 4C). In regions where these expansions were not observed, the integrity of the NE may have been maintained by NPCs (see Fig. 4C). In *C. elegans*, a similar increase in NE thickness was

observed in UNC-84 mutant cells; this, however, was limited to muscle cells from the body wall, suggesting that SUN proteins only determine NE thickness in force-bearing cells (Cain et al. 2014). The increases in NE spacing due to LINC disruptions observed in these two studies are, however, distinct. In Hela cells lacking SUN1 and SUN2, frequent increases in the PNS spacing of up to ~100nm are seen, whereas the membrane around the NPCs remained intact (Fig. 4B). In contrast, in the UNC-84-mutant *C. elegans* muscle wall cells, large local distortions of up to ~520nm were observed, but only in regions that are assumed to be under high mechanical stress, i.e. the two ends of each of the nuclei. This difference is possibly owing to the different magnitude of forces that are exerted on the ONM of Hela cells compared to the forces that act on the end of each muscle wall nuclei in *C. elegans*. In either case, the nature of the forces that act on the nuclear envelope remain unclear, as the disrupted LINC complexes should no longer be able to transmit forces from the cytoskeleton to the PNS. Forces may be exerted onto the ONM through the dynamic rough endoplasmic reticulum (ER), which expands into the cytoplasm, as the ONM is continuous with and connected to the ER in several areas (English and Voeltz 2013). Furthermore, in the absence of LINC complexes, the INM remains intact and connected to the nuclear lamina and chromatin through NPCs and other INM proteins (see Fig. 4D). This could result in a separation and thus increased distance between the INM and ONM in the absence of LINC complexes (Fig. 4C and D).
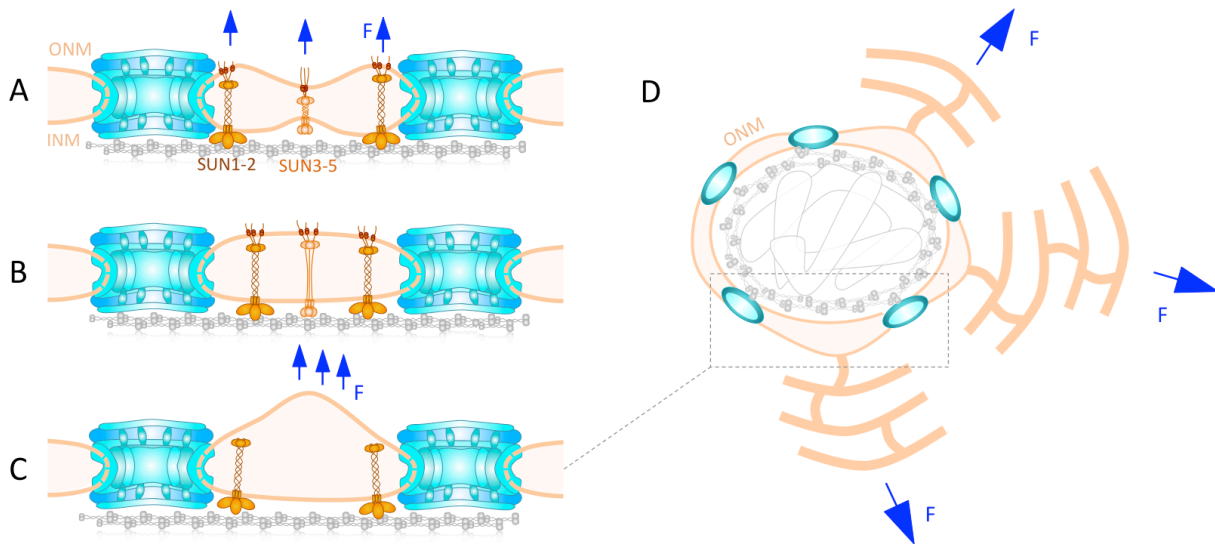
Figure. 4: Possible models for maintenance of NE width by LINC complexes. A) First model: LINC complexes entirely determine the width of the NE. Therefore a locally reduced NE width should be observed for shorter SUN proteins such as testis-specific SUN3, SUN4, or SUN5 compared with SUN1 and SUN2, although this may not be resolvable by current microscopy techniques (Sosa et al. 2013; Cain and Starr 2015; Cain et al. 2014). The integrity of the NE is maintained despite the cytoskeletal forces (blue arrows) that act on LINC complexes B) Second model: LINC complexes adapt to the pre-determined width of the NE by extending their luminal regions so they span the entire NE thickness (Cain and Starr 2015; Cain et al. 2014) C) An increased NE spacing is observed upon disruption of LINC complexes, while the NE remains intact around NPCs (Crisp et al. 2006a; Cain et al. 2014). Mechanical forces (blue arrows) may separate the ONM from the INM in cells where LINC complexes are not able to form and therefore also not able to maintain the connection between the ONM and INM. These forces may be exerted onto the ONM through the dynamic rough reticulum (ER) as shown in Panel D. D) A potential mechanisms of NE separation upon SUN depletion is depicted. Here, the ONM, which is continuous with the rough ER is pulled away from the INM, which remains associated with the nuclear lamina and chromatin in LINC disrupted cells.

Box 1: Structure of NPC and LINC and their anchorage to the nuclear membranes

NPC

The NPC features an eight fold symmetric structure, which is conserved across different species and is suggested to maximize the bending stiffness of the NPC (Wolf and Mofrad 2008). Although the detailed molecular architecture of the NPC is yet to be understood, recent studies have provided us with a more comprehensive architectural model of the NPC (von Appen et al. 2015; Lin et al. 2016). The eight spokes form three distinct parts of the NPC structure, namely the central channel, the cytoplasmic filaments, which emanate into the cytoplasm, and the nuclear basket . A specific complex of Nups, referred to as the coat Nup complex (CNC), forms an outer

ring that is symmetrically located on the cytoplasmic and nuclear faces (Lin et al. 2016). Two distinct layers of Nups, namely central channel Nups (also referred to as the FG layer) and adapter proteins (also referred to as the scaffold layer) form concentric cylinders in the central channel (Jamali et al. 2011; Lin et al. 2016). A third layer of Nups, i.e. POMs (also referred to as the membrane layer), is composed of transmembrane proteins and play a significant role in anchorage of the NPC scaffold into the NE.

The NPC is fused to the nuclear envelope through different types of nucleoporins (Jamali et al. 2011). Various proteins interact with each other and with the NE at different stages of NPC formation and assembly. For example, the transmembrane NPC proteins gp210 and POM121 have a role in anchoring the NPC to the membrane in vertebrates (Rothballer and Kutay 2013a). Other nucleoporins such as Nup53 and Nup155 are also involved in NPC assembly into the NE. Nup53, for instance, directly interacts with the nuclear envelope both in yeast and Xenopus (Marelli et al. 2001; Vollmer et al. 2012). In addition, several studies have identified interactions between Nup53 and transmembrane protein Ndc1 (Mansfeld et al. 2006; Onischenko et al. 2009; Eisenhardt et al. 2014; Hawryluk-Gara et al. 2008). Furthermore, recent experiments have revealed that the nuclear basket Nups Nup1 and Nup60 (as well as the mammalian homologue Nup153) might also be involved in integrating NPCs into the NE (Mészáros et al. 2015; Vollmer et al. 2015). However; these are only examples of the interactions with the NE that are required for NPC assembly; for more comprehensive papers on NPC structure see (Jamali et al. 2011; Alber et al. 2007; Kabachinski and Schwartz 2015).
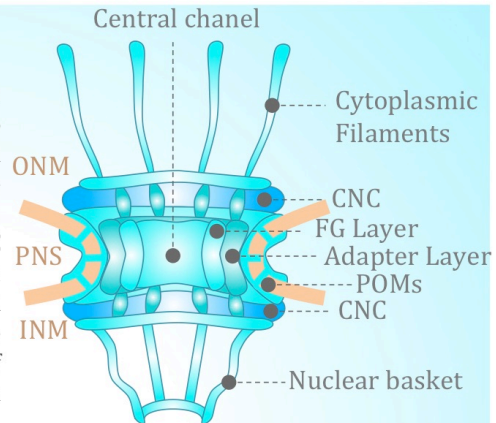
LINC complexes

The crystal structure of,the SUN domains of SUN2 in complex with the luminal KASH peptide of Nesprin 2 has recently been identified in two independent studies (pdb IDs 4FI9 and 4DXS, respectively) (Z. Zhou et al. 2012; Sosa et al. 2012). Both structures revealed a trimeric SUN2 that simultaneously forms strong interactions with three KASH peptides in the PNS. The second, more complete structure (4DXS) also identified a covalent disulfide interaction between two highly conserved cysteine residues of SUN2 and KASH2; this strongly stabilizes the interaction and is potentially crucial for the transmission of cytoskeletal forces to the nucleus (Jahed et al. 2015). LINC complexes interact directly with the NE. First, KASH-domain-containing proteins are anchored to the ONM through their short 21aa transmembrane domain as shown in Fig. 1.   Secondly, trimers formed by SUN proteins contain hydrophobic transmembrane domains that span the INM. This transmembrane domain is variable between various SUN isoforms and can contain one to three loops. Both SUN1 and SUN2 contain a single 21 aa transmembrane domain that interacts directly with the INM. However, some studies predict that three additional hydrophobic sequences within SUN1 may also interact with the INM or ONM

NPCs are also likely to be involved in determining and maintaining NE architecture as the INM and ONM are fused at the periphery of each NPC. Indeed, Nup153 depletion leads to a plasticity of the NE and structural defects, such as membrane invaginations that span through the nucleus (Zhou and Panté 2010). Furthermore, some yeast nuclear basket Nups, such as Nup1 and Nup60, have been found to interact with the INM and induce curvature (Mészáros et al. 2015). Here, bipartite motifs consisting of an amphipathic helix (residues 16-27 in Nup1 and residues 31-40 in Nup60) accompanied by an alpha-helical region (residues 85-123 in Nup1 and residues 91-162 in Nup60) have been suggested to facilitate induction of curvature through a combination of both hydrophobic insertion and scaffolding (Mészáros et al. 2015). Such a mechanism is supported by various observations, including the *in vitro* bending of membranes by Nup1 and Nup60 and *in vivo* reshaping of the nuclear membrane when Nup1 is overexpressed (Mészáros et al. 2015). In addition, it had been shown previously that Nup60 has some affinity to phospholipid bilayers, providing additional support for a role of Nup60 in inducing membrane curvature (Patel and Rexach 2008). Similarly, the mammalian homologue, Nup153, directly binds to the inner nuclear membrane via an N-terminal amphipathic helix (Vollmer et al. 2015).

The effect of LINC complexes on NPC-mediated nucleocytoplasmic transport

A few recent studies have proposed an interesting and direct connection between LINC complexes and transport through the NPC. Transport of biomolecules through the NPC is dependent on the gradient of the small GTPase Ran between the nucleus and the cytoplasm. Two proteins, RanGTPase-activating protein 1 (RanGAP1) in the cytoplasm and RCC1 in the nucleus, maintain this gradient in mammals (Grossman et al. 2012; Schmidt and Görlich 2016). In mammals, NPCs are responsible for anchorage of RanGap1 at the NE. Specifically, RanGap1 is modified by SUMO, which activates it for binding to cytoplasmic Nup538 (Matunis et al. 1998; Kalab and Heald 2008) (Fig 5A). In plants, however, RanGAP1 has a WPP domain that interacts with the WPP-interacting tail-anchored proteins WIT1 and WIT2 at the ONM (Zhao et al. 2008). WPP-domain-interacting proteins (WIPs), in turn, interact with WITs and anchor RanGAP1 to the NE. Recently, WIPs have been suggested to be plant-specific KASH-like proteins that interact with SUN proteins (Zhou et al. 2012). Therefore, in plants, the LINC complex is responsible for anchoring of RanGAP1 to the ONM, which facilitates an efficient regulation of Ran-dependent transport through the NPC. Therefore, plant LINCs are likely responsible for positioning RanGAP1 at the periphery of the NPC as they are able to rapidly capture shuttling RanGTPs and induce their hydrolysis to RanGDP (Fig 5B). No such roles have yet been identified for mammalian LINC complexes. However, a more recent study has explored a direct role for SUN1 in mRNA export through the NPC in mammalian cells (Li and Noegel 2015) Prior to export, mRNA transcripts bind to a multitude of factors and cofactors and form a messenger ribonucleoprotein particle (mRNP) that is then exported. By using co-immunoprecipitation and pulldown experiments, Li and Noegel now showed that both SUN1 and SUN2 directly interact with some mRNP components *in vitro* (Li and Noegel 2015). Moreover, the N-terminus of SUN1 (residues 1-239) directly interact *in vitro* with nuclear export factor 1 (NXF1), the main transporter for the export of the bulk of mRNA, and, accordingly, knockdown of SUN1 results in an accumulation of mRNAs in the nucleus. As SUN1 also interacts with Nup153, the authors proposed a regulatory mechanism for mRNP export, whereby mRNPs associate

with SUN1 and then are handed over to Nup153 for export through the NPC (Li and Noegel 2015). Taken together, these observations not only point to an intriguing connection between LINC complexes and nucleocytoplasmic transport through the NPC, but also lend further support for the existence of physical and functional links between the mechanical and biochemical pathways connecting the nucleus and the cytoplasm.
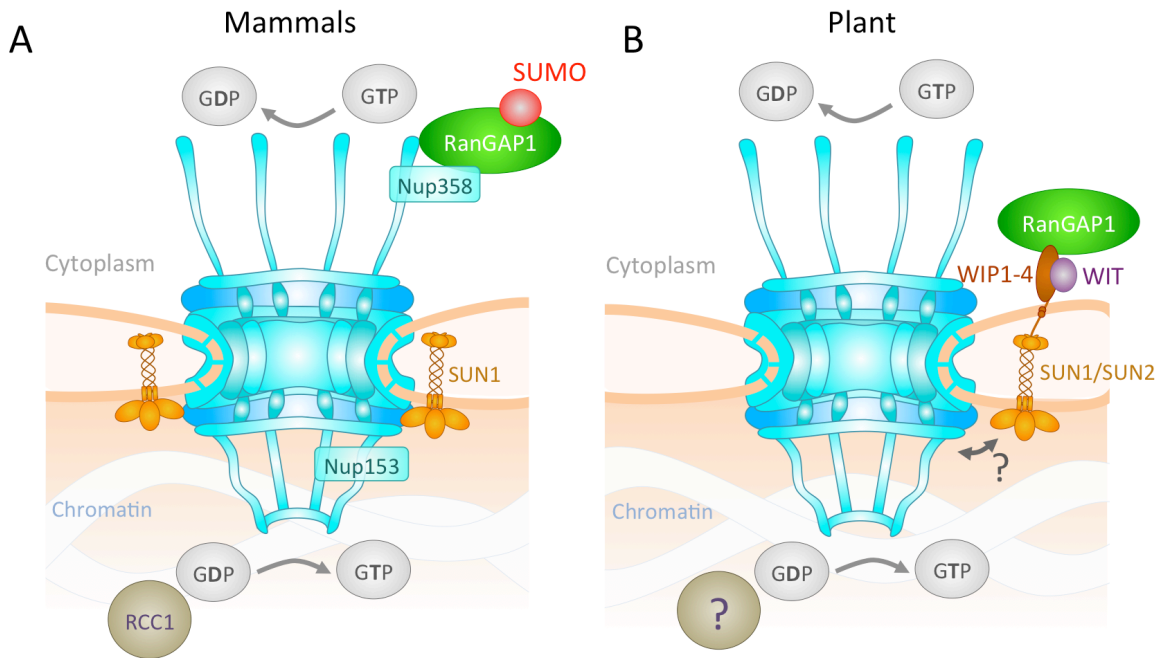
Figure. 5: Role of mammalian and plant LINC complexes in the transport of biomolecules through the NPC. A) In mammals, the concentration gradient of Ran between the cytoplasm and nucleus is maintained by the localization of RanGAP1 and RCC1 at the NPC periphery in the cytoplasm and nucleus respectively. Mammalian RanGap1 is modified by SUMO, which activates it for binding to Nup538 (Matunis et al. 1998). No roles for mammalian SUN1 have been identified in this process thus far, although SUN1 is known to associate with the NPC in mammals. B) In plants, LINC complexes recruit RanGAP1 to the ONM to maintain the gradient of the small GTPase Ran between the nucleus and the cytoplasm. The plant RanGAP1 proteins lack a SUMO-binding domain and are instead anchored to the ONM through WIPs (WIP1 to WIP4) and WIT proteins. Although WIP proteins lack a KASH domain, they are suggested to perform a similar biological function as KASH proteins and bind to plant SUN1 and SUN2 to link the nucleoskeleton and cytoskeleton (Zhou et al. 2012). Plant RanGAP1 has shown to localize to the NPC, which may be mediated by an interaction between plant SUN proteins and Nups in the nuclear basket; similar to the association of Nup153 and SUN1 in mammals. No Homolog of RCC1 in plants has yet been identified.

Cooperation between NPCs and LINCs during mitosis

During open mitosis, the NE breaks down to allow spindle microtubules to access mitotic chromosomes (for a full review on NE breakdown see Güttinger et al. 2009). This process includes the dissociation of the NE and NPCs from lamins and chromatin (Güttinger et al. 2009). NPCs have a primary role in the mitotic process. Through selective transport, nuclear pores mediate the proper localization of the different kinases that participate in mitosis (Alvarez-Fernández and Malumbres 2014). For instance, cyclin-dependent kinase 1 (Cdk1), which interacts with cyclin B, is involved in disassembly of NE through phosphorylation of Nup98 and lamin (Laurell et al. 2011). Cdk1 is transported bidirectionaly through the NPC during the interphase; however, from the beginning of

prophase, Cdk1 is only transported from the cytoplasm into the nucleus (Gavet and Pines 2010).

SUN1 and SUN2 also have critical but redundant roles in the dissociation of chromatin from the INM as a co-depletion of these two proteins delayed membrane removal in Hela cells during NE breakdown (Turgay et al. 2014). The phosphorylation of SUN1 at three residues within its nucleoplasmic domain in early mitosis loosens its interactions with lamins; this facilitates the dissociation of lamins from the INM to prepare for NE breakdown (Patel et al. 2014). At the same time, the interactions between SUN proteins and dynein-linked KASH proteins are maintained, which allows for tearing of the NE through forces that are exerted by molecular motors such as dynein (Patel et al. 2014). NE disassembly is dependent on the recruitment of dynein to mediate spindle assembly, and both LINC complexes and NPCs have been shown indispensible for this process. Two distinct pathways have been observed for dynein recruitment. Nucleoporins Nup133 (Bolhy et al. 2011) and Nup358 (Splinter et al. 2010) recruit dynein through direct interaction with BICD2, the mammalian homologue of the Drosophila Bicaudal D, which acts as an adapter protein between dynein and its cargos in G2/prophase human cells (Splinter et al. 2010). Although mammalian LINC complexes are important in recruiting dynein during cell migration (Zhang et al. 2009a), NPC components appear to be responsible for G2-specific dynein interactions with the NE (Splinter et al. 2010). However, recent studies show that dynein-mediated NE breakdown continues even after NPCs are fully dissociated, suggesting that there is a second, nucleoporin-independent pathway in Hela cells that might involve LINC complexes (Turgay et al. 2014). Indeed, components of LINC complexes interact with dynein during cell division in various species: the *C. elegans* KASH protein ZYG-12 in complex with SUN1 directly binds to dynein and recruits it to the membrane during cell division (Malone et al. 2003). Similarly, *Schizosaccharomyces pombe* KASH proteins Kms1 and Kms2, in complex with the SUN protein Sad1 associate with dynein (Anon 1995; Miki et al. 2004). Finally, the mammalian meiosis-specific KASH5 interacts with the microtubule associated dynein-dynactin complex (Morimoto et al. 2012).

In a closed mitotic system such as in yeast, the factors responsible for chromosome segregation (i.e. the spindle pole body) must be inserted into the NE in order to access the DNA. The yeast nucleoporin Ndc1 is required for the insertion of the spindle pole, and of NPCs, in the NE (Winey 1993; Chen et al. 2014). In addition, yeast SUN protein Mps3 forms a complex with nucleoporin Ndc1 in areas away from NPCs and the spindle pole and partitions it between the two (Chen et al. 2014). The duplication of the spindle pole, a process critical for chromosome segregation, also depends on the interactions between Mps3 with nucleoporin Ndc1(Chen et al. 2014).

As discussed above, the relationship between NPCs and LINC complexes at the NE is highly complex and only a limited number of studies have directly addressed any direct functional interactions between these two integral members of the NE. However, as we have summarized in this chapter, it is clear that the only two known linkages between the interior of the nucleus and the cytoplasm, namely NPCs and LINC complexes, cooperate in various cellular processes. Nevertheless, the molecular details underlying this association and the implications for their cellular functions remain largely unexplored.

Conclusions and open questions

Here, we have examined recent support for the physical and functional connections between the NPC and LINC complexes that contribute to the regulation of various cellular functions. However, despite the ample evidence for associations between these two molecular complexes, several important outstanding questions in the field remain as outlined here.

Most importantly, the direct binding partners that link NPCs and LINC complexes have yet to be identified. Furthermore, it is not known whether the SUN domain proteins that are associated with NPCs are distinguishable from those associated with KASH-domain proteins of LINC complexes and whether SUN-domain proteins could simultaneously interact with NPCs, KASH proteins and the cytoskeleton. Is the subset of NPCs that is associated to LINC complexes through SUN domains functionally or structurally different from other NPCs? Further studies on the distribution of LINC complexes on the NE may shed light into some of these questions. The density and distribution of NPCs on the NE during the cell cycle has been studied in several cell types; however, not much is known with regard to that of the LINC complexes. Furthermore, only few studies thus far have directly addressed the functional and structural relationship between NPCs and LINC complexes. As highlighted here, in order to fully understand the function of these two integral NE assemblies, it will be important to examining their roles in greater detail and in context of different cellular processes. Some unanswered questions to be addressed based on the functional relations of LINC complexes and NPCs in context of the cellular processes discussed in this review are as follows: what is the mechanistic role of SUN1 in the fusion of the INM and ONM during *de novo* NPC assembly? How are membrane anchored SUN proteins transported across the NPC without large disruptions in the NPC structure? What are the mechanistic roles of LINC complexes and NPCs in maintaining the NE spacing?

An association between LINC complexes and NPCs would provide an indirect coupling between the NPC and elements of the cytoskeleton, resulting in the exposure of NPCs to cytoskeletal forces. However, implications of such coupling are only speculative at this point. The complex architecture of the NPC may allow the NPC to change its diameter in response to the transport of differently sized cargos (Solmaz et al. 2011; Solmaz et al. 2013; Koh and Blobel 2015; Melcak et al. 2007). It remains to be determined whether any change in the diameter of the NPC is force-regulated and whether components of the LINC complex have a role in NPC dilation and constriction. It should be noted that the dilation and/or constriction of the NPC is still a matter of controversy and has been refuted by some experimental studies and observations (Stuwe et al. 2015; Chug et al. 2015). In addition, it is now well established that distinct structures (e.g. ion channels, NPCs and nucleoli) are mechanically linked throughout the cell such that mechanical stimuli acting on cell-surface receptors elicit the reorganization of molecular assemblies in the cytoplasm and the nucleus. This has led to the notion that regulatory information may be transferred to different cellular structures, such as ion channels and the NPC (Maniotis et al. 1997). With regard to the NPC, this idea is further supported by the fact that NPCs expand and their transport rates increase upon physical extension of cells (Feldherr 1990). Therefore, one could speculate that the size of the NPC and transport through it could be regulated by

cytoskeletal forces, which, in turn, depend on the external forces applied on the cell. These cytoskeletal forces are transmitted to NPCs through the interactions of their cytoplasmic constituents such as Nup358 with microtubules. Forces from the actin cytoskeleton and intermediate filaments may also be transmitted to NPCs through their associations with LINC complexes. As cytoskeletal forces also regulate LINC complex functions, we could hypothesize that some functionalities of NPCs and LINC complexes are coupled. Based on the recent evidence for a direct role of SUN1 in mRNA export through the NPC (Li and Noegel 2015), this idea of force-regulated transport could be further expanded to include a direct role for cytoskeletal forces in nucleocytoplasmic transport, in addition to an indirect role by regulating the size of the NPC. However, further studies will be required to gain insights into the mechanisms of such a pathway.

3.2 MECHANICAL LINCS OF THE NUCLEAR ENVELOPE: WHERE SUN MEETS KASH

Introduction

The skeletal elements in the cytoplasm and nucleus, namely the cytoskeleton and nucleoskeleton, maintain the structural integrity of the cell in these regions. Comparably, the linkers of cytoskeleton and nucleoskeleton (LINC complexes) can be considered as the chief structural elements of the nuclear envelope (NE), elegantly connecting the nucleus to the cytoskeletal network and transmitting mechanical signals across the NE. The nuclear pore complexes that perforate the NE also conceivably contribute to the mechanics of the NE, however their primary function is to control the exchange of biochemical signals between the cytoplasm and nucleus. The LINC complexes are increasingly established as the rivets that transmit mechanical signals across the NE. Fittingly, LINC complexes are structured for load bearing and force transmission and perform central roles in several cellular processes.

Herein we review the roles of LINC complexes in maintaining or disrupting the structural integrity of the NE. We first examine the current crystallographic data on LINC complexes at the nuclear envelope. Next we discuss the various types of mechanical loading that is experienced by the nuclear envelope through LINC complexes during various cellular processes. Finally, we survey available knowledge of the role of LINC in the loss of structural integrity of the nuclear envelope during nuclear rupture.

The nuclear envelope of eukaryotes is double layered and composed of an inner and outer nuclear membrane (INM and ONM). The structural integrity of the NE is essential for the isolation and protection of genomic information from the cytoplasm. With an intact NE, the exchange of material between the nucleus and cytoplasm can be conducted in a controlled manner through macromolecular protein complexes known as nuclear pore complexes. Although NPCs may also contribute to the mechanical integrity of the nucleus (as discussed in (Zeinab Jahed et al. 2016)), the only other protein complex known to span the NE and physically link the INM and ONM are LINC complexes. LINC complexes are responsible for the transmission of forces across the nuclear envelope (Crisp et al. 2006c; Lombardi, Jaalouk, Shanahan, Burke, Kyle, et al. 2011). Force transmission across the nuclear envelope through LINC complexes is essential for several cellular processes reliant on nuclear movement and positioning, and nuclear mechanotransduction (Isermann & Lammerding 2013).

LINC complexes are formed by the interaction of conserved *Sad1/UNC-84 (*SUN) -domain and *Klarsicht/ANC-1/SYNE* homology (KASH) -domain proteins in the perinuclear space (PNS) (Crisp et al. 2006c; Starr & Han 2002; Padmakumar et al. 2005; McGee et al. 2006). At least six KASH proteins (nesprin-1-4, lymphoid-restricted membrane protein, and KASH5) and five SUN proteins (SUN1-5) have been identified in mammals (Nishioka et al. 2016; Rajgor & Shanahan 2013b; Meinke & Schirmer 2015; Duong et al. 2014; Morimoto et al. 2012). KASH proteins are anchored to the outer nuclear membrane (ONM) and contain large cytoplasmic domains, and a short ~10-32 residue C-terminal KASH domain that

protrudes in to the PNS (Figure 1). SUN proteins are anchored to the inner nuclear membrane (INM) and their conserved C-terminal SUN domains reside in the PNS where they bind to KASH. The N-terminal nucleoplasmic domains of SUN interact with nucleoskeletal elements such as A-type lamins and chromatin, as well as other INM proteins such as Emerin (Chang et al. 2015; Crisp et al. 2006c; Qian Liu et al. 2007; Xiong et al. 2008) (Figure 1). Lamins are type V nuclear intermediate filaments that form a filamentous meshwork at the nuclear periphery, and interact with chromatin, SUN proteins, and other INM proteins, to maintain the structural integrity of the nucleus (Ho & Lammerding 2012; Turgay et al. 2017).

The N-terminal cytoplasmic domains of KASH proteins associate with various elements of the cytoskeleton, including direct interactions with the actin cytoskeleton through their actin binding domains, and indirect bindings to microtubules and intermediate filaments through motor proteins such as kinesin, dynein and plectin (Figure 1) (Lombardi, Jaalouk, Shanahan, Burke, Roux, et al. 2011; Crisp et al. 2006c; Sosa et al. 2012b; Qian Liu et al. 2007; Henning F Horn et al. 2013; Fan & Beck 2004b; Morimoto et al. 2012; Wilhelmsen 2005).
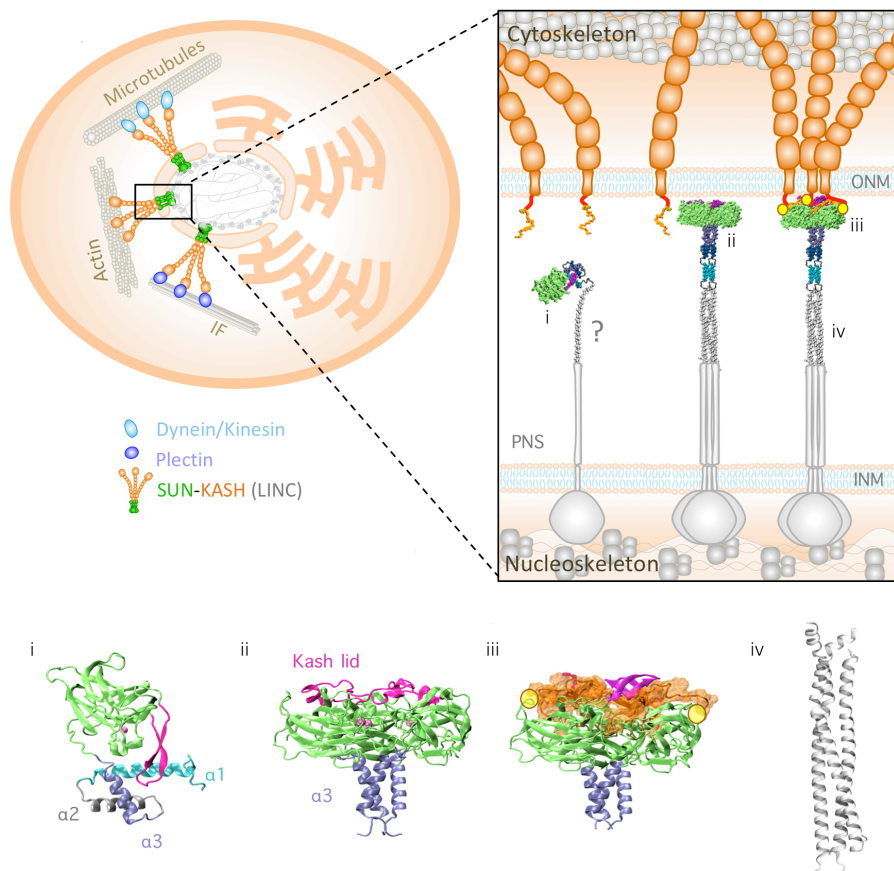
Figure 1: Crystal structure of the LINC complex. Schematic representation of LINC complexes spanning the nuclear envelope and connecting various cytoskeletal elements to the nucleoskeleton (Top). Crystal structures of various fragments of LINC complex proteins SUN2 and KASH2 (bottom): i) Structure of mouse SUN2 monomer (PDB ID: 5ed8), magenta: KASH-lid ii) Human SUN2 trimer (PDB ID: 4DXT) iii) Human SUN2 trimer (green/purple) in complex with KASH2 (orange) forming an overall hexamer, (iv) Coiled coil region of mouse SUN2. Yellow circles: covalent disulfide bonds between SUN and KASH.

LINC is structured for load bearing

Several studies have shown that SUN proteins must oligomerize to bind to KASH proteins and are inactive for KASH binding in a monomeric state (Sosa et al. 2013; Sosa et al. 2012b; Nie et al. 2016; Z. Zhou et al. 2012b). Recent crystallographic data suggest that in a monomeric state, the main KASH binding domain of SUN2 (i.e. the KASH-lid) is inhibited by a three-helix bundle preceding the SUN domain ($\alpha1$-$\alpha3$) (Figure 1-i). Large coiled coil (CC) domains preceding the SUN domain force the SUN domain into a trimeric state, and activate it for KASH binding (Sosa et al. 2013; Sosa et al. 2012b; Nie et al. 2016; Z. Zhou et al. 2012b). Upon trimerization, the minimal region required for KASH binding consists of an alpha helix ($\alpha3$) that forms a trimeric CC, and a beta sandwich core from which the KASH-lid emanates (Figure 1-ii). In this conformation, the SUN trimer can bind to three KASH peptides simultaneously, and form an overall hexameric SUN-KASH complex (Figure 1-iii). Two coiled coil regions are predicted in most SUN domain proteins(Crisp et al. 2006a; Padmakumar et al. 2005), and the recently solved crystal structure of one of the predicted CC regions of SUN2 revealed that it also forms a trimer (Figure 1-iv) (Nie et al. 2016).

Based on the abovementioned crystallographic data, four main attributes of LINC complexes contribute to their suitability as load bearing elements in the nuclear envelope:

(1) The SUN domain is functional in a trimeric state and the higher order oligomerization of these proteins allows for their high stability under force. Additionally, some studies have suggested that SUN proteins can further cluster into even higher order oligomers, which would allow the transmission of even higher forces (Lu, Gotzmann, Sironi, V.-M. Jaeger, et al. 2008; Q. Liu et al. 2007; Jahed et al. 2018).

(2) The interaction between the mammalian SUN2 trimer and the KASH domains of nesprin 1 and nesprin 2 is highly stable, with 24 hydrogen bonds between each KASH peptide and SUN2 trimer, and 1,520 Å^2 of SUN2 trimer buried upon binding to one KASH peptide (Sosa et al. 2012b).

(3) The interaction between mammalian SUN2 and the KASH domains of nesprin 1 and nesprin 2 terminates with a covalent disulfide bond between two highly conserved cysteine residues on each protein. This intermolecular disulfide bond not only further stabilizes the SUN2-KASH2 interaction, but it also allows the transmission of forces to the coiled coil regions of SUN2 (Figure 1-iii)(Jahed, Shams & Mohammad R.K. Mofrad 2015; Sosa et al. 2012b; Sosa et al. 2013).

(4) Most Sun proteins are predicted to contain at least two long coiled coil domains. Coiled coils have been identified as elastic elements in proteins(Schwaiger et al. 2002; Kreuzer & Elber 2013; Sadeghi & Emberly 2009; Wolgemuth & Sun 2006). In some cases like myosin, the CC regions have been characterized and show truly elastic properties where they can reversibly extent more than 2 times their length(Schwaiger et al. 2002). Although the mechanical properties of the CC regions of SUN proteins have yet to be identified, it is likely

that these CCs can also extend reversibly under mechanical forces, and hence contribute to the elasticity of the nuclear envelope.
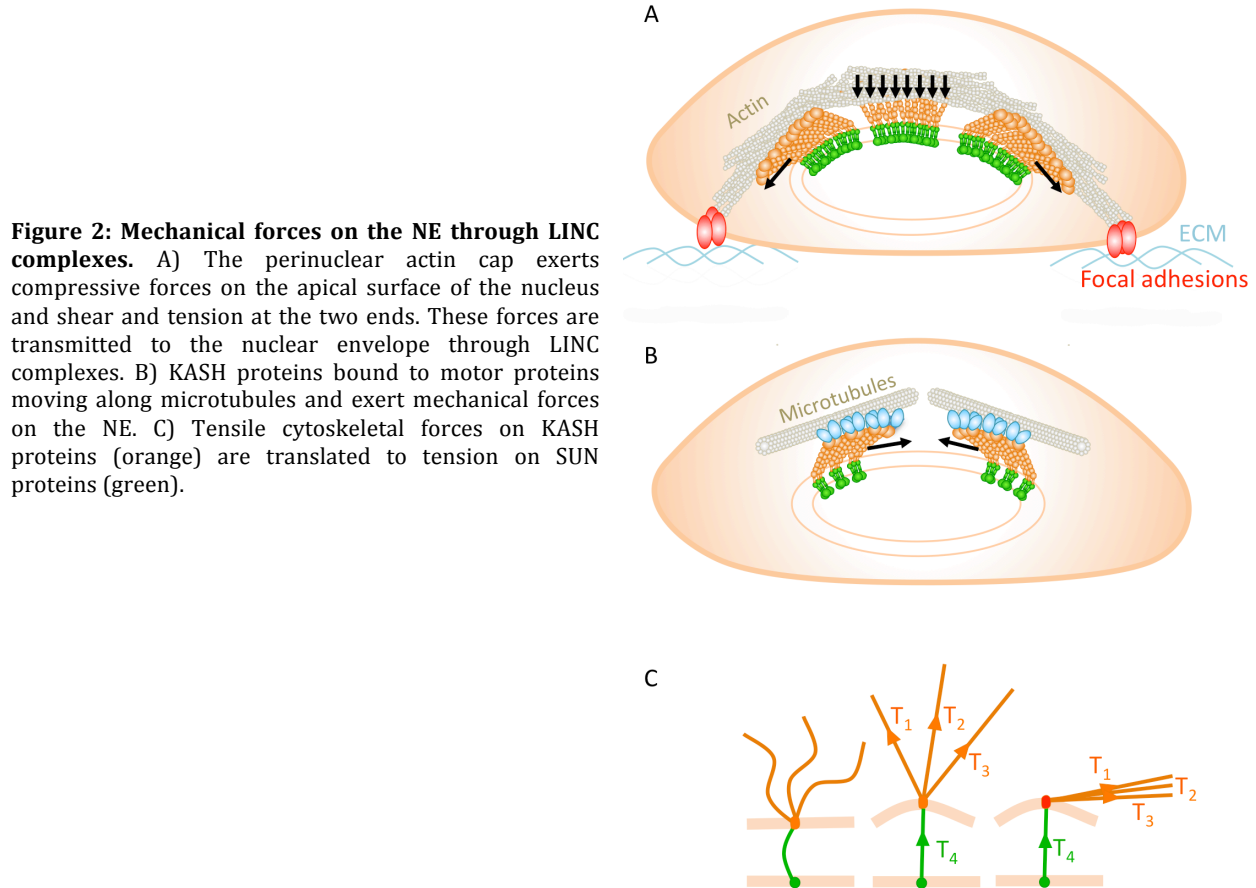
Forces exerted on the nuclear envelope: Tension, compression and shear

The direct binding of nesprin proteins to the actin cytoskeleton through their actin binding domains exposes the SUN-KASH linkage to actomyosin dependent mechanical forces. In 2D cultures, LINC complexes connect the apical surface of the nucleus to a highly ordered and dynamic filamentous actin structure known as the perinuclear actin cap (Figure 2A) (Dong-Hwee Kim et al. 2012; Khatau et al. 2009; Meinke et al. 2014; Gomes et al. 2005; Luxton et al. 2010). The perinuclear actin cap is terminated by focal adhesion molecules that transmit mechanical forces across the cell membrane. The coupling between LINC complexes and focal adhesions through actin filaments induces compressive stresses on the nuclear envelope at the top surface of the nucleus and shear and tensile force at the two ends (Figure 2A). The magnitude and direction of local forces on SUN and KASH proteins is not well known. There are some evidences of tensile forces on elements of the LINC complex. For example, increased separations were observed between the INM and ONM in some regions of SUN1 and SUN2 depleted HeLa cells (Crisp et al. 2006c), as well as at the two ends of force-bearing *C. Elegans* muscle nuclei with disrupted LINC complexes (Cain et al. 2014). These observations suggest that the LINC complex withstands tension at the nuclear envelope, and plays a role in maintaining the even distance between the INM and ONM, at least in load bearing regions (Cain & Starr 2015; Zeinab Jahed et al. 2016; Sosa et al. 2013; Qian Liu et al. 2007; Cain et al. 2014). Furthermore, in mammalian cells, a fluorescence resonance energy transfer (FRET)-based tension biosensor for nesprin 2 showed that nesprin is subject to tension in adherent fibroblast (Arsenovic et al. 2016). Higher levels of tensile force were observed on the apical and equatorial planes of the nucleus. This study suggested that even in compressive regions of the actin cap, nesprins are under tension and orient towards the long axis of the cell (Arsenovic et al. 2016). Since nesprins are anchored to the ONM, when oriented parallel to the NE, tensions on these proteins translates to shear on the ONM.

The indirect interaction of nesprin proteins with microtubules through motor proteins dynein and kinesin also exposes LINC complexes to constant velocity pulling as these motor proteins move along microtubules during several cellular processes reliant on this interaction (Figure 2B) (Ding et al. 2007; Henning F. Horn et al. 2013; McGee et al. 2006). Nesprins are likely under tension in these cellular processes and orient towards the direction of dynein movement, exerting shear and tensile forces on the ONM.

How are these cytoskeletal forces on KASH transmitted to SUN proteins? It has been shown that each SUN protein can interact with three KASH peptides simultaneously *in vitro.* If this is the case *in vivo* and three nesprin proteins can simultaneously bind a SUN trimer, the NE may be subjected to forces in various directions (Figure 2c). However, since the LINC complex is anchored at the INM and ONM, when transmitted across the ONM, these forces likely translate to tensile forces in a direction perpendicular to the INM and ONM on SUN proteins (Figure 2c). One can envision the design of new FRET-based tension sensors inserted into various regions of SUN proteins to better determine the stress state of SUN

proteins in the nuclear envelope and further elucidate the molecular mechanisms of force transmission across the nuclear envelope. Similar approaches can be used to determine stress sates of the nucleoplasmic domains of SUN proteins to understand how forces are ultimately transmitted through SUN proteins to their interacting partners in the nucleus. No crystallographic data is currently available on the nucleoplasmic domains of SUN proteins and their dynamics inside the nucleus remains widely unexplored.

Figure 2: Mechanical forces on the NE through LINC complexes. A) The perinuclear actin cap exerts compressive forces on the apical surface of the nucleus and shear and tension at the two ends. These forces are transmitted to the nuclear envelope through LINC complexes. B) KASH proteins bound to motor proteins moving along microtubules and exert mechanical forces on the NE. C) Tensile cytoskeletal forces on KASH proteins (orange) are translated to tension on SUN proteins (green).

Consequences of forces on the NE through LINC

The mechanical forces exerted on the NE through LINC complexes are essential for several cellular processes reliant on nuclear movement and positioning, and nuclear mechanotransduction (Isermann & Lammerding 2013). These forces are transmitted across the LINC complex to the filamentous lamin meshwork underlying the INM, resulting in nuclear stiffening through the recruitment of more A-type lamin, and hence, a change in the mechanical properties of the nucleus (Guilluy et al. 2014; Isermann & Lammerding 2013). Additionally, these forces can lead to changes in genome organization and gene expression as discussed in a recent review by Uhler and Sivashankar (Uhler & Shivashankar 2017).

On the other hand, recent studies have shown that mechanical stresses exerted on the nuclear envelope can also lead to nuclear rupture both *in vivo* and *in vitro*, compromising the integrity of DNA (Denais et al. 2016). These stresses can be induced on the nucleus by

an external environment as cells migrate through confined spaces, or by intracellular structures such as the perinuclear actin cap (Hatch & Hetzer 2016; Lammerding & Wolf 2016). In the former case, external pressure is applied on the nucleus as the cells "squeeze" through confined spaces and nuclear rupture occurs in a LINC-independent manner. On the other hand, when the actin cap is responsible for nuclear confinement in cultured cells, nuclear rupture is dependent on LINC complexes (Hatch & Hetzer 2016; Lammerding & Wolf 2016). The *in vivo* relevance of LINC complex-dependent nuclear envelope rupture requires further studies.

## 3.3 TRANSMISSION OF FORCES ACROSS THE NUCLEAR ENVELOPE THROUGH LINC COMPLEXES

Introduction

Mechanical linkers of the nucleoskeleton and cytoskeleton (LINC Complexes) play a central role in cellular mechanotransduction(Kaminski et al. 2014) as the mere physical coupling between the interior of the nucleus and the cytoplasm. The tethering of the extracellular matrix (ECM), the cytoskeleton and the nucleoskeleton mediated by these complexes allows for a direct transmission of forces to the nucleus. Transmission of forces through LINC complexes is essential for several biological functions of the cell including polarization, differentiation, division and migration which are dependent on nuclear deformation and positioning (Lombardi, Jaalouk, Shanahan, Burke, Kyle, et al. 2011; Gundersen & Worman 2013; Khatau et al. 2009). Furthermore, LINC complexes are directly connected to focal adhesions through filamentous actin bundles resulting in ultrafast mechanotransduction (Chambliss et al. 2013; Dong-Hwee Kim et al. 2012; Khatau et al. 2009). The distribution of nuclear pore complexes on the surface of the nucleus (Qian Liu et al. 2007; Jamali et al. 2011b) has also been attributed to elements of the LINC complex. Additionally, components of LINC complexes have been implicated in several human diseases including laminopathies and muscular disorders such as Emery–Dreifuss muscular dystrophy and dilated cardiomyopathy (Méjat & Misteli 2010a; Folker & Baylies 2013; Meinke et al. 2011; Meinke et al. 2014; Haque et al. 2010; Isermann & Lammerding 2013; Puckelwartz et al. 2010), and hearing loss (Henning F Horn et al. 2013).

LINC complexes are formed by the interaction of SUN (Sad-1 and Unc), and KASH (Klarsicht, ANC-1, Syne Homology) domain containing proteins in the perinuclear space (PNS)(Zeinab Jahed, Shams, et al. 2014) (Figure 1). In mammalian cells, widely expressed SUN domain containing proteins include SUN1 and SUN2, which interact with various members of KASH domain proteins NESPRINs 1-4 (Nuclear Envelope Spectrin repeat proteins). These complexes are structural and load-bearing elements in the cell and experience both extracellular and intracellular mechanical forces through their linkage to various elements of the cytoskeleton by NESPRIN proteins (Figure 1). Furthermore, they couple the cytoskeleton to the nucleoskeleton through their interaction with nuclear lamina in the nucleoplasm (Figure 1). The increased gap between the inner nuclear membrane (INM) and outer nuclear membrane (ONM) in SUN1, SUN2 mutated cells (Crisp

et al. 2006c) suggests that SUN proteins are subject to tensile forces maintaining the gap between the INM and ONM. Moreover, recent studies showed the initiation of mechanotransduction events such as emerin phosphorylation, through direct application of forces on SUN-KASH complexes in isolated nuclei. (Guilluy et al. 2014) (Figure 1).

The crystal structure of human SUN2 in complex with KASH2 peptide of NESPRIN2 revealed a trimeric SUN2 structure, where three SUN2 protomers interact with three independent ~22 aa KASH2 peptides and form an overall hexameric structure (Sosa et al. 2012b; Wenjia Wang et al. 2012) (Figures 1B,2A,2B). Each SUN2 protomer consists of a SUN domain ($SUN2_{540-717}$) and a minimal helical coiled coil region ($SUN2_{525-540}$) necessary for SUN2 trimerization and KASH binding (Sosa et al. 2012b) (Figure 1B,2A). The SUN domain consists of a beta sandwich core and a ~20 aa beta hairpin extending from this domain, forming the KASH lid ($SUN2_{567-587}$)(Figure 2C) (Sosa et al. 2012b). Each KASH2 peptide interacts with the KASH lid of one SUN2 protomer ($KASH_{6884-6872}$), and the beta sandwich core of the neighboring SUN2 protomers ($KASH_{6872-6862}$) (Figure 1B). A unique feature of this complex is the perfect alignment of two highly conserved cysteine residues, CYS563 of SUN2 and CYS6862 of KASH2 (Sosa et al. 2013) forming a covalent disulfide bond (SS bond) between the two proteins, and highly stabilizing the SUN2-KASH2 interaction (Figure 1B,2C). Although this bond has been shown to be dispensable for SUN-KASH binding in-vitro(Sosa et al. 2012b), the high conservation of both cysteine residues suggests their physiological importance. Herein, we show that under physiologically relevant forces, the stability of the SUN2-KASH2 interaction depends on the inter-molecular SS bond between SUN2 and KASH2. Furthermore, the transmission of forces through these complexes is disrupted upon the disruption of this bond.
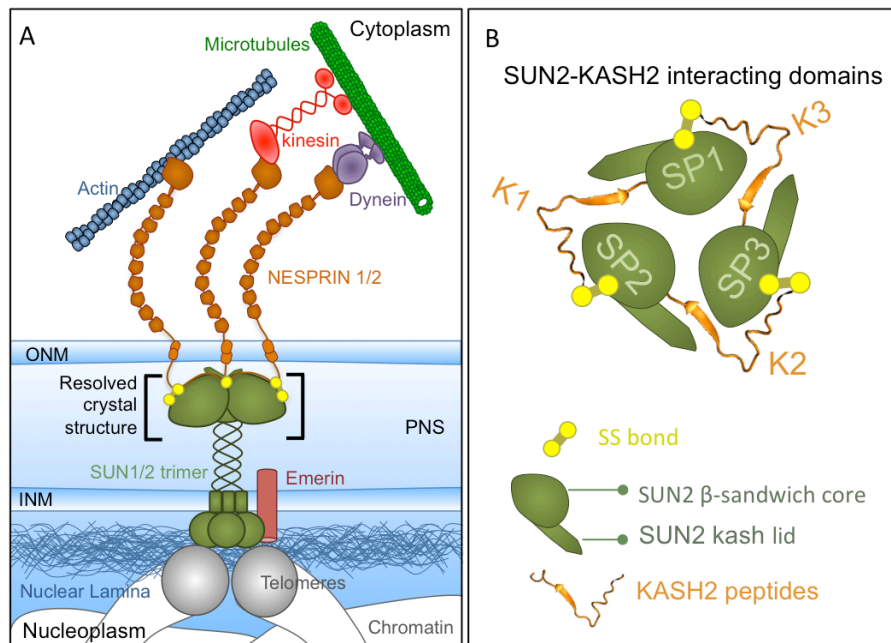
Figure 1: A) A Schematic representation of the SUN1/2-KASH1/2 complex, acting as a bridge between the cytoskeleton and nucleoskeleton. SUN domains of SUN1/2 interact with three KASH peptides of NESPRIN1/2 in the perinuclear space (PNS). The nucleoplasmic domains of SUN1/2 interact with nuclear lamina, and telomeres. In the cytoplasm, NESPRIN1/2

proteins interact with various cytoskeletal components including actin filaments through their actin binding domains, and microtubules through motor proteins, namely kinesin and dynein. Cytoskeletal forces are transmitted through SUN-KASH complexes and result in mechanotransduction events such as Emerin phosphorylation. The crystal structure of a segment of the SUN2-KASH2 complex has been resolved. B) A schematic representation of SUN2-KASH2 interactions: each KASH peptide (orange) interacts with the kash lid of one SUN2 protomer, and the β-sandwich core of the neighboring SUN2 protomer (green).

Figure 2: Crystal structure of the wild type human SUN2-KASH2 hexamer (pdb ID: 4DXS). A) side view of SUN2 trimer (green) containing a SUN domain and a helical coiled coil region, in complex with three KASH2 peptides (orange), B) top view of SUN2-KASH2 hexamer. C) The SUN2-KASH2 interactions, including several nonbonded interactions, terminated with an interaction between CYS563 of SUN2 and CYS6862 of KASH2 which form a disulfide bond (SS bond) (yellow). Each KASH peptide (orange) interacts with the kash lid of one SUN2 protomer, and the β-sandwich core of the neighboring SUN2 protomer (green). Steered molecular dynßamics (SMD) simulations were carried out by applying 25pN tensile forces on CYS6862 of each KASH2 peptide in the SUN2-KASH2 hexamer (site of force application is represented as a pink triangle)
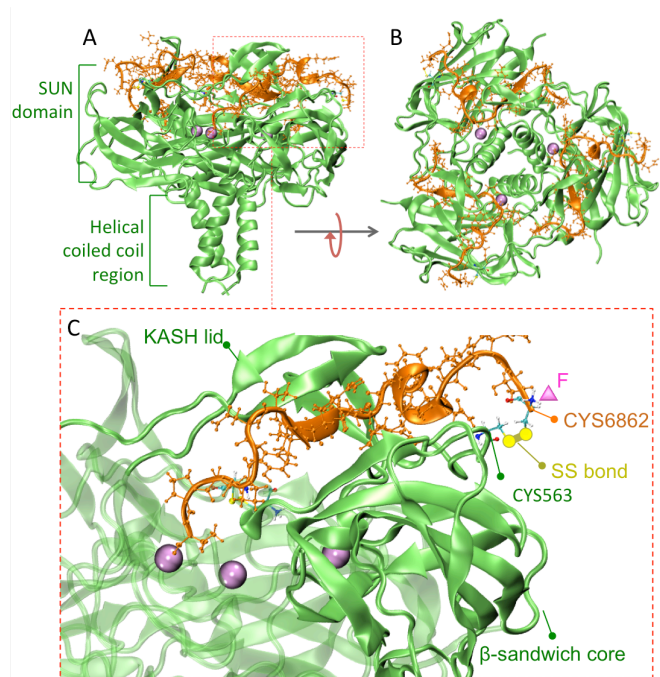
Methods

Modeled system. The crystal structure of SUN2-KASH2 complex was obtained from the protein data bank (PDB ID: 4DXS (Sosa et al. 2012b)) and visualized using VMD software. The structure was trimerized using *MakeMultimer.py* online software. The system was solvated in water, neutralized with counter ions and subsequently ionized with an ion concentration of 150mM KCl, and 50μM of $CaCl^2$. The concentration of Ca^{2+} in the nuclear envelope is estimated to be similar to that of the ER lumen which is known to be in the μM range (Petersen et al. 1998; Grygorczyk & Grygorczyk 1998; Matzke et al. 2010).

Steered molecular dynamics simulations. Steered molecular dynamics (SMD) simulations were conducted using NAMD scalable molecular dynamics (Phillips et al. 2005) with the CHARMM27 force field. In order to simulate tensile cytoskeletal forces applied on KASH domain containing proteins, a constant 25pN force was applied directly to the end residue of each KASH2 peptide (CYS6862) in the direction parallel to the central symmetry axis of the SUN2 trimer (perpendicular to the INM and ONM) (see Figure 3). The 25pN direct tensile forces on groups of SUN-KASH complexes resulted in stiffening of the nuclei (Guilluy et al. 2014). In order to observe changes using steered molecular dynamics simulations in ns timescales, we applied the same 25pN force to a single SUN2-KASH2 complex. Furthermore, the Cα carbons of GLY522 on the helical coiled coil of the SUN2 trimer were fixed in all simulations (see Figure 3). This was rationalized by the fact that that the SUN2 protein interacts with KASH domain containing proteins at its C-terminus, and at the other end, it is tethered to INM through its transmembrane domain, and interacts with nuclear lamins and chromatin in the nucleus at its N-terminus (Farhana Haque et al. 2006; Stewart-Hutchinson et al. 2008; Crisp et al. 2006c). The covalent disulfide bond between CYS6862 and CYS563 was simulated using a patch command in NAMD. To study the role of this bond in force transmission and endurance, we mutated CYS563 of SUN2 to alanine (this structure is referred to as C563A in the text). Additionally, in order to isolate and study the role of the disulfide bond without any potential local changes in the complex due to the alanine substitution, we also conducted SMD on a model

where the patch between the two cysteines was not created (i.e. CYS563 and CYS6862 were included but not covalently bound with an SS bond). A total of three SMD simulation runs were conducted on the wild type structure, which are referred in the text as wild type (WT) simulations. Each simulation contained three KASH peptides interacting with three SUN protomers resulting in a total of 9 interacting pairs. Similarly, four simulation runs were performed for both the mutated structure (C563A), and the structure with a disrupted SS bond (denoted as SS$^-$) resulting in 12 SUN-KASH interacting pairs in each case. An independent equilibration run was performed for each simulation run. The system was minimized, at 5000 steps, and equilibrated for ~2ns with a time step of 2 fs. The temperature and pressure of the system were held constant at 1atm and 310K, using Langevin's piston and Hoover's method during minimization and equilibration (Phillips et al. 2005). A time step of 2fs was used and the cutoff distance for non-bonded interactions was 1.2nm. Periodic boundary conditions were applied in all three directions. SUN2 mutations were modeled using VMD.

RMSF and dynamic cross correlation calculations. The Bio3D R package was used for RMSF and dynamic cross-correlation analyses (Grant et al. 2006). In both cases, the calculations were averaged over the three SUN2 protomers forming the SUN2 trimer in each simulation run, after 100% elongation of the complexes. In total, 9 data sets were averaged in the WT structure, and 12 sets were averaged in the WT and SS$^-$ simulations.

Interaction Energy calculations. The interaction energies were calculated between each SUN protomer, and KASH peptide independently. Each KASH peptide interacted distinctly with only two neighboring SUN protomers and these interaction energies were reported separately. Only the SUN domain of each SUN2 protomer (residues 545-618) was used in the energy calculations, as the helical coiled coil did not interact with the KASH peptide.

Sequence alignment. Sequences of human and mouse SUN and NESPRIN proteins were aligned using Uniprot (Magrane & Consortium 2011).

Results

The disulfide bond between CYS563 of SUN2 and CYS6862 of KASH2 is required for the transmission of forces through the SUN-KASH complex. Conformational changes induced by 25pN tensile forces on the end residue (CYS6862) of each KASH peptide in the WT and C563A complex are shown in Figure 3A. Distinct deformation behaviors are observed between the two complexes. The single C563A mutation, constrained the deformation of the SUN-KASH complex to the SUN domain, and forces on the KASH peptide were no longer able to transmit to the helical coiled coil region as evident from the elongated structures in Figure 3A. The deformation mechanisms of the WT and C563A complexes are compared in Figure 3 where the complex is extended up to 100% its initial length in both cases. The average root mean square fluctuations of all SUN2 residues (SUN2$_{525-718}$) are shown in Figure 3B. In the WT structure, the helical coiled coil region of SUN2 comprising residues SUN2$_{525-540}$ experiences the highest fluctuations. On the contrary, in the C563A structure, the fluctuations peak in the KASH lid region   (SUN2$_{567-587}$), and minimal fluctuations are observed in the helical coiled coil region.
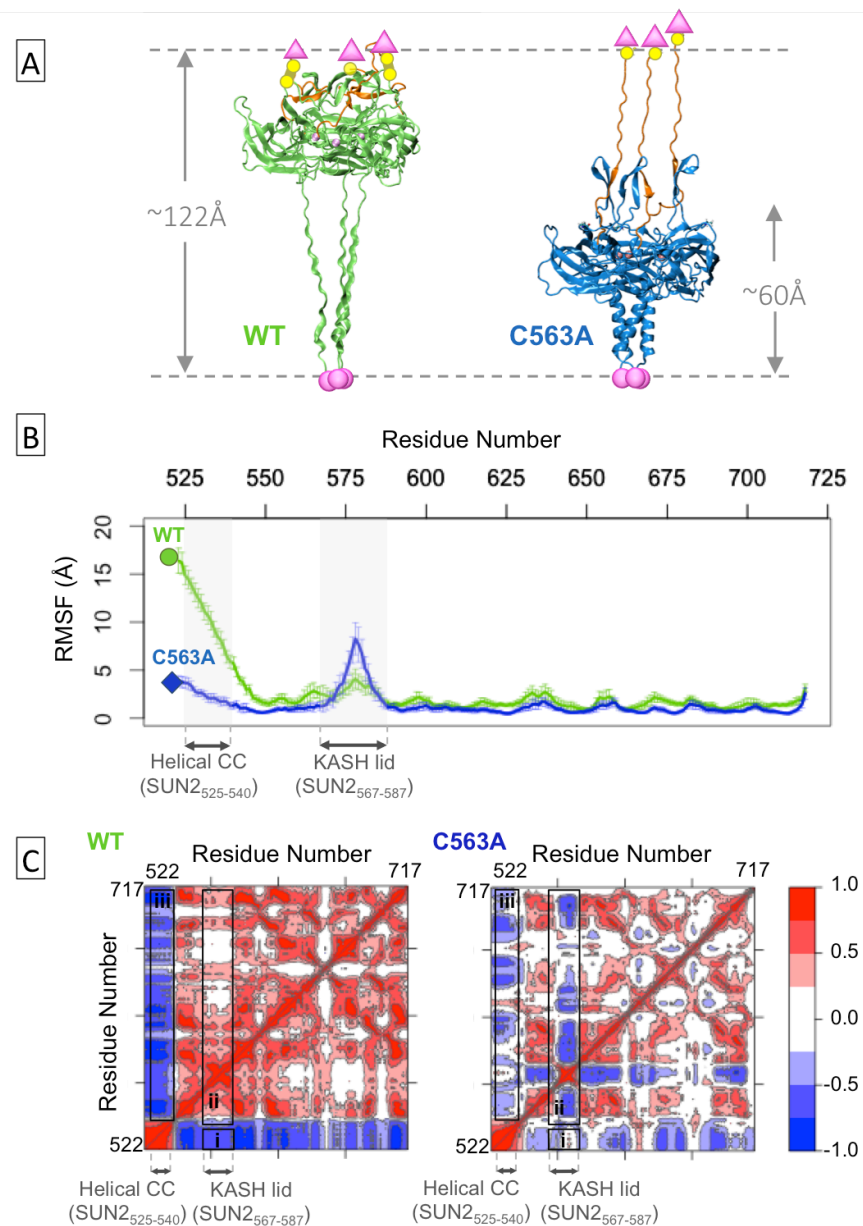
Figure 3: Extension of the SUN2-KASH2 complex (WT, green and C563A blue) to 100% of their initial lengths under 25pN forces. A) CYS6862 of each KASH2 peptide (orange) was pulled with a constant force of 25pN in both cases using steered molecular dynamics resulting in ~100% increase in the length of both structures. Distinct conformational changes were observed in the WT and C563A structures. In the WT complex (right/green), forces on the KASH2 peptide are translated directly to the helical coiled coil region of SUN2 resulting in conformational changes in this region, whereas the SUN domain remains intact. Conversely, the C563A mutated structure experiences minimal conformational changes in its coiled coil region. Pink spheres and triangles represent constraints at the C-terminal ends and the sites of force application, respectively. B) Root Mean Squared Fluctuations (RMSF) of all SUN2 protomer residues (SUN2$_{525-717}$) averaged over all simulations runs (with three protomers in each simulation run) for 100% elongation of the complex. RMSF is highest in the Helical CC (SUN2$_{525-540}$) region of the WT SUN2, whereas the RMSF peaks in the KASH lid (SUN2$_{567-587}$) region of the C563A structure. C) Comparison of the dynamic-cross correlation of all SUN2 protomer residues averaged over all simulation runs (with three protomers in each simulation run) showing i) the negative correlation between the helical CC (SUN2$_{525-540}$) and KASH lid (SUN2$_{567-587}$) is reduced with the C563A mutation, ii) Reduction and change in the dynamic cross-correlation of KASH lid with other SUN2 residues from a positive correlation to a negative correlation as a result of the C563A mutation, iii) Significant reduction in the negative dynamic cross-correlation of the helical CC region with other SUN2 residues in the C563A structure.

To determine how the C563A mutation affects the overall dynamics of SUN2 structure, residue to residue dynamic cross-correlations were evaluated for the three SUN2 protomers forming each SUN2 trimer, and averaged over all simulation runs (Figure 3C). By comparing the dynamic cross-correlation plots for the WT and C563A structures, it is clear that the overall correlations of SUN2 residues are significantly reduced for C563A. Furthermore, the correlation between the KASH lids and the SUN2 helical coiled coil region are notably reduced in the C563A structure (Figure 3C, i). Note that the main SUN-KASH interactions occur in this region, namely the KASH lid of SUN2. Another significant difference in the plots is the change in the cross correlation values of residues in the KASH lid region from a positive correlation with all other SUN2 residues in WT SUN2, to a negative correlation in the C563A structure (Figure 3C, ii). Note that negative cross correlations correspond to movement of the residues in opposite directions (Grant et al. 2006). Finally, the negative cross-correlations between the helical coiled coil region and all other SUN2 residues was remarkably lower in the C563A structure suggesting a decouple between the coiled coil region and the SUN domain.

To further expand on this decoupling, we compared the conformational changes in the helical coiled coil region between the WT and C563A structures. In the wild type SUN2-KASH2 complex, the percent elongation of the helical coiled coil region was linearly correlated with the percent elongation of the entire SUN2-KASH2 complex (Figure 4) where ~100% elongation results in ~176% elongation of the coiled coil region. On the other hand, the SUN domain remains entirely intact throughout the SMD simulation. However with the C563A mutation, the transmission of forces to the helical coiled coil region is interrupted and the coiled coil region remains unstretched upon 100% extension of the complex (Figure 4 B). Furthermore, deformation is confined to the SUN domain, where most prominent changes are seen in the KASH lids (Figure 3A,3B). This is further exemplified by the changes in backbone rotational angles of residues in the coiled coil region of wild type SUN2 (SUN2$_{525-540}$) as shown in the Ramachandran plots in Figure 4B (Lovell et al. 2003). The ψ-ϕ angles of residues in the helical coiled coil region significantly change after 100% elongation of the molecule (Figure 4B). Contrarily, this conformational change is not observed in the C563A structure.

We next explored whether the changes seen in the C563A mutated structure were mainly due to the inhibition of SS bond formation between C563 and C6862. Similar SMD simulations were repeated on the WT structure but with the SS bond between C563A and C6862 inhibited (SS$^-$ structure). We found that the simulations on the SS$^-$ yield similar results as those in the C563A mutations (Figure S1,S2), suggesting that the main contribution of this mutation is the disulfide inhibition. Force transmission to the helical coiled coil region is inhibited and changes are mainly limited to the KASH lids in the absence of the SS bond as evident from the deformed crystal structures ((Figure S1-B), as well as the RMSF values in the SS$^-$ vs. WT structures (Figure S1-B).
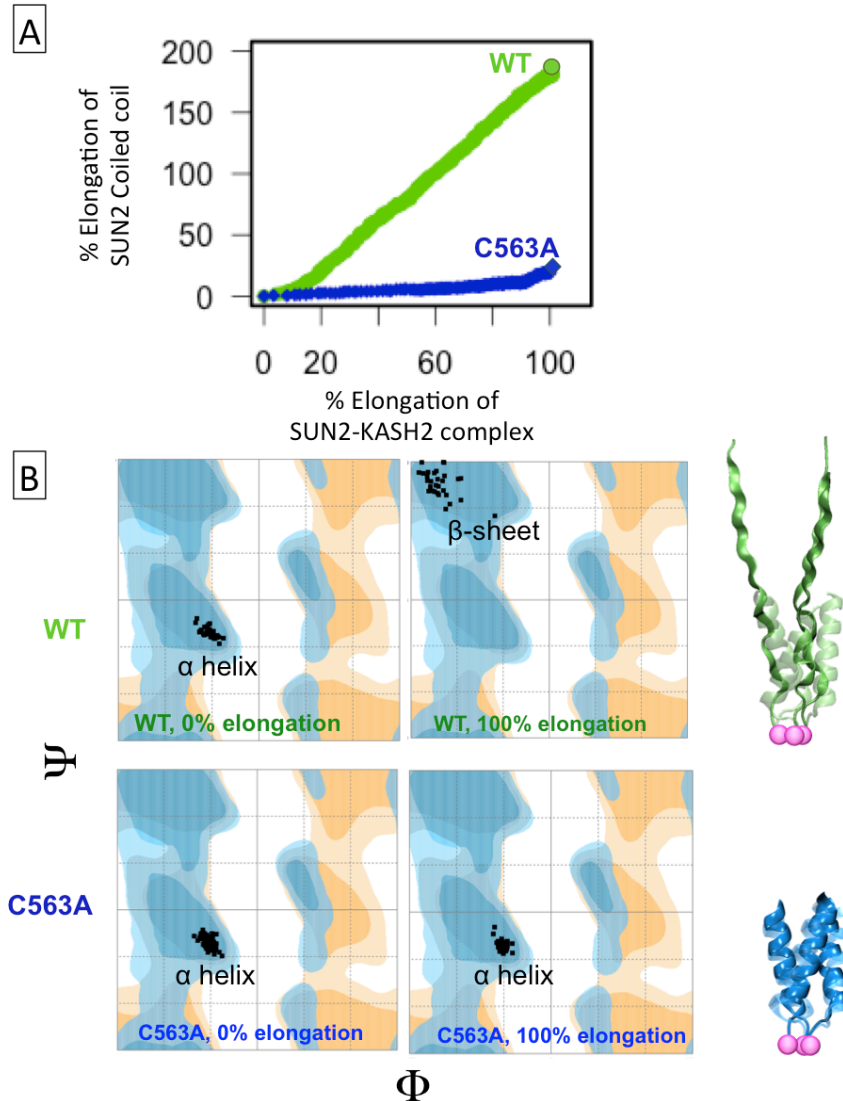
Figure 4: The SS bond between CYS563 of SUN2 and CYS6862 of KASH2 is required for transmission of forces through the SUN2-KASH2 complex. A) Elongation of the minimal helical coiled coil region of SUN2 in response to tensile forces on KASH2 peptide, in the (WT, green) and mutated (C563A, blue) structures; as a function of the % Elongation in the entire SUN2-KASH2 complex. With the C563A mutation, no forces are transmitted to the helical coiled coil region of SUN2, resulting in no elongation in this region; on the other hand, the coiled coil region of SUN2 is elongated to more than 150% of its initial length in the presence of the SS bond. B) Ramachandran plot of residues in the helical coiled coil region before (left) and after (right) elongation of the SUN2-KASH2 complex; changes in the Ψ vs. Φ angles for these residues indicate conformational changes in the helical coiled coil region of WT SUN2 upon the application of tensile forces to the KASH2 peptide. No such changes are seen in the mutated structure (C563A, bottom).

The stability of the SUN2-KASH2 interaction is highly maintained under tensile forces. Next we examined the effect of tensile forces on other non-bonded interaction of SUN2 and KASH2, in the WT, C563A and SS⁻ structures. As noted previously, each KASH2 peptide interacts with the KASH lid of one SUN2 protomer, and the β-sandwich core of the neighboring protomer (Figure 1B,2C). The average total nonbonded (electrostatic and van der Waals) interaction energies between a KASH peptide and each of the two WT SUN protomers it interacts with were evaluated during the application of 25pN tensile forces to the terminal residue of each KASH peptide. The results show minimal fluctuations in the

81

total nonbonded energies indicating that the stability of the interactions are preserved even with an elongation of the complex to 100% of its original length (Figure 5A-B). The KASH peptide maintains a strong ~-145 kcal/mol average nonbonded interaction with SUN2 KASH lid as seen in Figure 4B. The KASH peptide also interacts with SUN β-sandwich core at -122 kcal/mol (Figure 4A). The SUN-KASH complex elongated to 100% of its original length after 28.6 ns of SMD simulations as shown in Figure 2. The head domain of SUN2 remains entirely intact throughout this force-induced elongation of the complex to 100% of its original length maintaining a stable SUN2-KASH2 interaction.

The disulfide bond between CYS 563 of SUN2 and CYS6862 of KASH2 is required for the stability of SUN2-KASH2 interaction under forces. The C563A mutation and the disruption of the SS bond between two interacting cysteine residues of SUN2 and KASH2 in MD simulations both resulted in a full dissociation of the KASH2 peptide from the SUN2 trimer (Figures 5, S3). The average total nonbonded interaction energies between KASH peptides and the β-sandwich core of SUN trimers reduced abruptly after applying 25pN tensile forces (Figures 5, S3). The KASH peptides initially interacted strongly with the β-sandwich core at ~-177 kCal/mol (Figure 5B), however, this interaction showed high instability under forces in the C563A (Figure 5A) and SS⁻ structures (Figure S3-A). A full dissociation of KASH with the β-sandwich core was observed after ~3 ns with a 0 kcal/mol interaction energy after this detachment (Figure 5A). The KASH peptide remained in contact with the KASH lid a few ns longer (Figure 4B) with an initial ~-171 kCal/mol interaction, and a linear decrease in interaction energy, and a full dissociation after ~10ns of SMD simulations.

Figure 5: The disulfide bond between CYS563 of SUN2 and CYS6862 of KASH2 is required for the stability of SUN2-KASH2 complex under forces. Average Non-bonded interaction energies (electrostatic and van der Waals) are shown for KASH peptides with the two neighboring sun promoters it interacts with (inset) in the mutated (C563A, blue) and wild type (WT, green) structures. KASH peptides interact with the KASH lid, (A) and β-sandwich core (B) of two neighboring SUN protomers. The point at which the SUN2-KASH2 complex experiences a 100% elongation is also shown for the WT and C563A structures (stars). The absence of the SS bond results in a 100% elongation of the complex in less than ~3.2 ns of pulling, and a complete dissociated of the KASH2 peptide with the KASH lid (A) and β-sandwich core (B) in the first 10 ns .
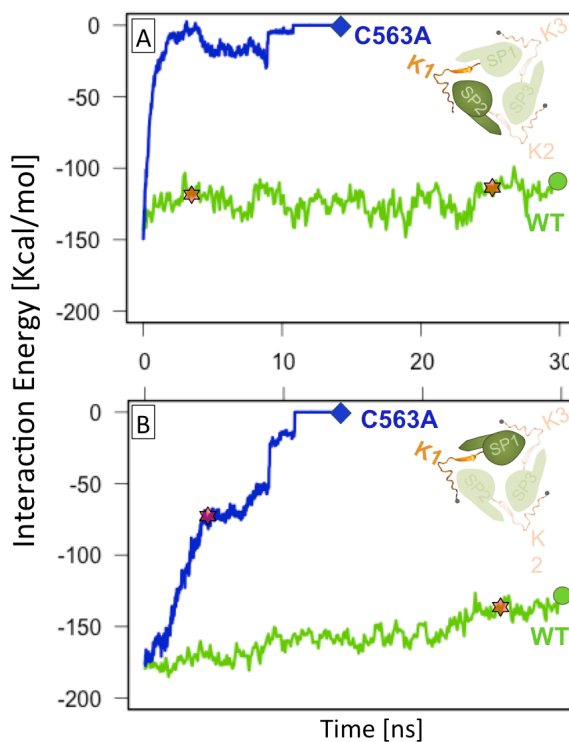
Discussion

LINC complexes are anchored to several elements of the cytoskeleton through their KASH domain containing proteins. For example, NESPRIN1 and NESPRIN2 contain actin-binding domains that directly bind to the actin cytoskeleton(Zhang et al. 2002), and have also been observed to interact and co-localize with dynein and kinesin complexes(Zhang et al. 2009b), connecting the nucleoplasm to the actin filaments as well as microtubules (Figure 1A). Through focal adhesion proteins, the actin cytoskeleton is also linked to the extracellular matrix (ECM) (Zeinab Jahed, Shams, et al. 2014; Mofrad & Kamm 2014). SUN1 and SUN2 proteins interact with lamins type A and B at their nucleoplasmic N-terminal domain (Crisp et al. 2006c; Haque et al. 2010; Farhana Haque et al. 2006), and several members of NESPRIN proteins at their C-terminal in the perinuclear space. Thereby, the nucleoskeleton is coupled with the ECM and extracellular forces can be translated to the nucleus directly through SUN-KASH complexes. Furthermore, all intracellular actomyosin generated contractile forces, and forces generated by other motor proteins, i.e. dynein and kinesin, are also translated to the nucleus through these complexes underscoring their potential role in mechanotransduction through the nuclear envelope.

Our results show that despite a strong ~-801 Kcal/mol average non-bonded interaction between SUN2 and three KASH2 peptides, the covalent disulfide bond between CYS563 of SUN2 and CYS6862 of KASH2 is necessary for the stability of this interaction under tensile forces. The SS bond is not required for the SUN2-KASH2 interaction (Sosa et al. 2012b); however, our results suggest that after the initial anchorage of KASH peptides onto SUN proteins through non-bonded interactions (Figure 6A), the SS bond forms (Figure 6B) to allow the initiation of force transmission in the subsequent linkage of NESPRIN proteins to the cytoskeleton (Figure 6C). Furthermore, upon potential clustering of LINC complexes, forces of magnitudes up to hundreds of pNs can conceivably be endured by these complexes and utilized for nuclear positioning and chromosome organization (Figure 6C).

This stable covalent bond between SUN2 and KASH2, suitably positions the KASH peptide to allow for all other interacting residues to remain aligned during force application to the KASH peptide, and continue their nonbonded interactions. As a result, the SUN domain and KASH peptide complex show minimal fluctuations and conformational changes, and forces are directly translated to the coiled coil region resulting in conformational changes in this region (Figure 3). The full coiled coil region of a full length SUN1/2 protein is predicted to be ~40nm in length (Sosa et al. 2013) and serves as a possible structural component, translating forces between the SUN domain and the nucleoplasm domain of SUN. Coiled coils are also found in several other structural and motor proteins and known to be load bearing structural motifs involved in force transmission between various protein domains (Kreuzer & Elber 2013). Furthermore, coiled coils have highly elastic properties (Wolgemuth & Sun 2006); for example coiled coil regions in Myosin II are shown to be truly elastic structures and to refold against forces up to 30pN in short time scales (Schwaiger et al. 2002). These properties make SUN1 and SUN2 proteins very suitable elastic load bearing components under constant application and release of cytoskeletal forces on the nuclear envelope.
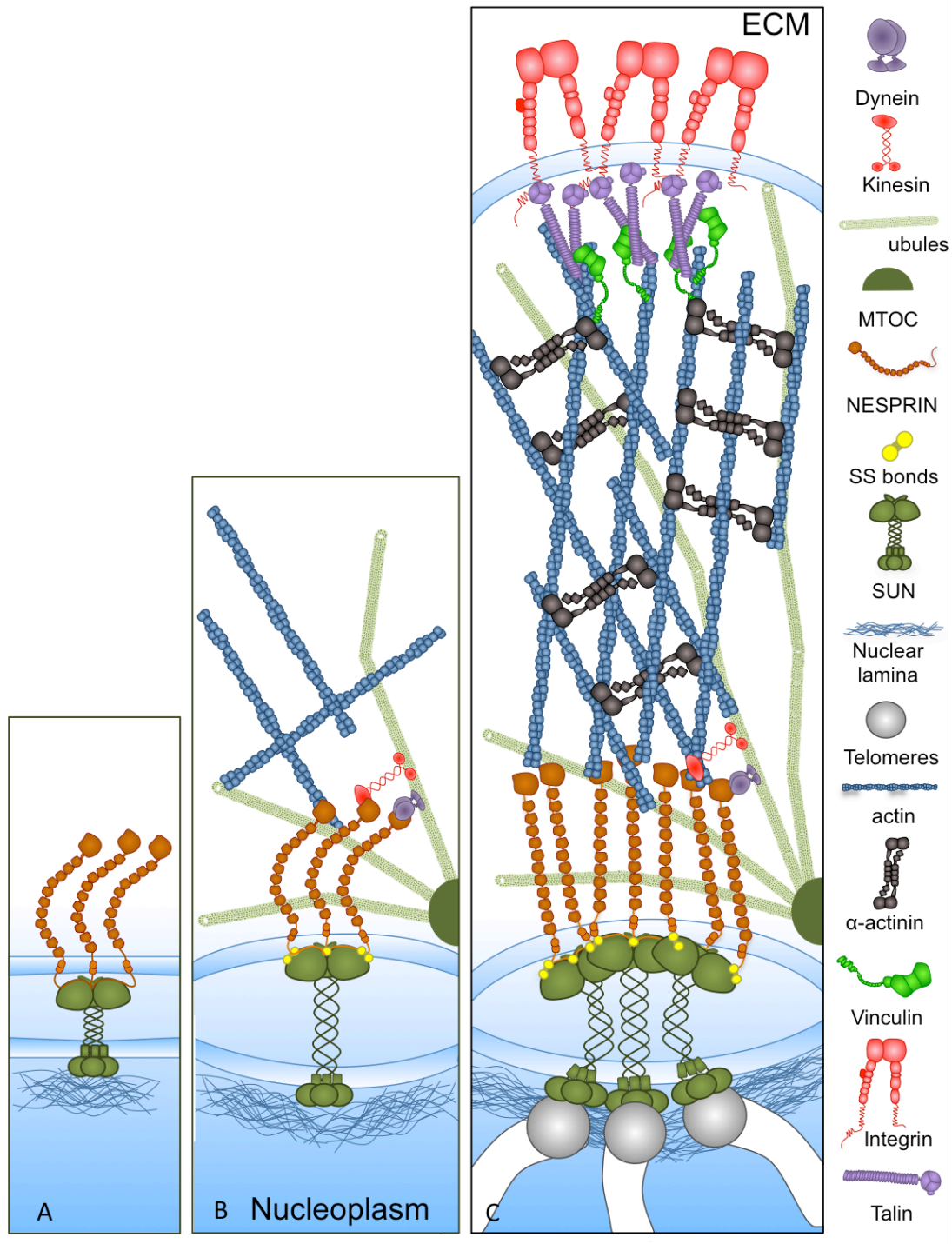
Figure 6: Transmission of forces through LINC complexes: A) a SUN trimer interacts with three KASH peptides from NESPRIN proteins forming several nonbonded interactions. B) The SUN-KASH complex is subject to cytoskeletal forces upon the coupling of NESPRIN proteins with the actin cytoskeleton, inter-protein SS bonds further stabilize the SUN-KASH interaction under mechanical forces, and allow the transmission of cytoskeletal forces to the helical coiled coil region of SUN proteins. C) Potential clustering of SUN-KASH complexes into higher order complexes will allow for the transmission of hundreds of pN forces required for nuclear positioning or the organization of chromatin. Other than intracellular myosin dependent forces, extracellular forces can be transmitted directly to the nucleus through integrins and focal adhesion proteins such as talin and vinculin that also interact with the actin cytoskeleton.

Among human and mouse SUN proteins, SUN1 and SUN2 contain the cysteine residue which can form disulfide bonds with 4 members of the NESPRIN family (NESPRIN 1-4) (Figure 7). However, testis specific SUN3-5 proteins which are small spermiogenesis-specific proteins (Frohnert et al. 2011; Shao et al. 1999; Göb et al. 2010) and are predicted to have shorter coiled coil regions than that of SUN1/2 lack this cysteine residue. Studies have shown that shorter coiled coils unfold under lower forces (Sadeghi & Emberly 2009) which may suggest that LINC complexes with shorter coiled coils are not suitable for bearing and transmission of large forces which can elucidate the absence of the disulfide bond in these complexes. Our results suggest that the nature and strength of the SUN-KASH interaction may determine two distinct roles for LINC complexes: load bearing and transmission *vs.* mere anchorage of the nucleus.

```
SUN DOMAIN PROTEINS

 SUN1_HUMAN   654   STRCSETYETKTALMSLFGIPLWYFSQSPR   684
 SUN2_HUMAN   560   STRCSETYETKTALLSLFGIPLWYHSQSPR   590
 SUN3_HUMAN   198   EAGTSESYKNNKAKLYWHGIGFLNHEMPPD   228
 SUN4_HUMAN   270   LQKTSHDYADRNTAYFWNRFSFWNYARPPT   300
 SUN5_HUMAN   210   FEHTSVTYNHEKAHSYWNWIQLWNYAQPPD   240
 SUN1_MOUSE   756   STRCSETYETKTALLSLFGVPLWYFSQSPR   786
 SUN2_MOUSE   574   STRCSETYETKTALLSLFGIPLWYHSQSPR   604
 SUN3_MOUSE   161   EAGTSESYKNNKAKLYWHGIGFLNYEMPPD   191
 SUN4_MOUSE   272   LEKTSSDYEDQNTAYFWNRLSFWNYARPPS   302
 SUN5_MOUSE   208   FEHTSATYNHDKARSYWNWIRLWNYAQPPD   238


KASH DOMAIN PROTEINS

 Kash1_HUMAN  8768  SEEDYSCALSNNFARSFHPMLRYTNGPPPL  8797
 Kash2_HUMAN  6856  SEEDYSCTQANNFARSFYPMLRYTNGPPPT  6885
 Kash3_HUMAN  977   REEDRSCTLANNFARSFTLMLRY-NGPPPT  975
 Kash4_HUMAN  377   S--GGPCCSHARIPRTPYLVLSYVNGLPPV  404
 Kash1_MOUSE  8770  SEKDYSCALSNNFARSFHPMLRYTNGPPPL  8799
 Kash2_MOUSE  6845  SEDDYSCTQANNFARSFYPMLRYTNGPPPT  6874
 Kash3_MOUSE  977   REEDRSCALANNFARSFALMLRY-NGPPPT  975
 Kash4_MOUSE  361   S--GVSCCSHARLARTPYLVLSYVNGLPPI  388
```

Figure 7: Sequence of human and mouse SUN and KASH domain containing proteins. SUN1 and SUN2 contain a cysteine residue that can form an SS bond with the cysteine of KASH1-4, and assist in load bearing and force transmission to the nucleus. Testis specific SUN3-5 lack the cysteine suggesting a potentially distinct functional role for these SUN proteins.

3.4 MOLECULAR INSIGHTS INTO MECHANISM OF SUN1 OLIGOMERIZATION IN THE NUCLEAR ENVELOPE

Introduction

Linkers of nucleoskeleton and cytoskeleton (LINC) are conserved nuclear envelope (NE)-spanning molecular bridges that provide a direct physical linkage between major cytoskeletal and nucleoskeletal elements(Starr & Han 2002; Padmakumar et al. 2005; Crisp et al. 2006c; F. Haque et al. 2006). The ability of LINC complexes to sense and transmit cytoskeletal forces across the NE is critical for several fundamental cellular processes including meiotic chromosome pairing, mechanotransduction, and nuclear positioning (Lombardi, Jaalouk, Shanahan, Burke, Kyle, et al. 2011; Gundersen & Worman 2013; Khatau et al. 2009). Given the prominent roles of LINC complexes in basic cellular functions, it should not be surprising that mutations in genes encoding their components are associated with a wide range of diseases and disorders including cardiac and skeletal muscular disorders (J Stroud et al. 2014; Yang et al. 2013b; Méjat & Misteli 2010a; Folker & Baylies 2013; Meinke et al. 2011; Meinke et al. 2014; Haque et al. 2010; Isermann & Lammerding 2013; Puckelwartz et al. 2010), cancers (Méjat & Misteli 2010b; Matsumoto et al. 2015), and hearing loss (Henning F Horn et al. 2013).

LINC complexes are composed of the conserved inner nuclear membrane (INM) and outer nuclear membrane (ONM) *Sad1/UNC-84* (SUN) and *Klarsicht/ANC-1/SYNE* homology (KASH) proteins, respectively (Crisp et al. 2006c). Also known as NE spectrin repeat proteins (nesprins), KASH proteins are type II membrane proteins that project their divergent spectrin repeat-containing N-termini into the cytoplasm from the ONM where they interact with the cytoskeleton and other cytoplasmic proteins(Luxton & Starr 2014a). Within the perinuclear space (PNS) of the NE KASH proteins protrude their eponymous ~10-32 residue KASH peptide(Starr & Han 2002). SUN proteins are membrane proteins that are defined by their luminal KASH peptide-binding C-terminal SUN domain (Kim et al. 2016; Malone et al. 1999). The divergent N-termini of SUN proteins reside within the nucleoplasm, where they interact with A-type lamins, chromatin, and other INM proteins(Chang et al. 2015). Mammals encode at least six KASH (nesprin-1-4, lymphoid-restricted membrane protein, and KASH5) and five SUN protein (SUN1-5)-encoding genes, which are expressed in a tissue-specific manner and subject to alternative splicing (Nishioka et al. 2016; Rajgor & Shanahan 2013b; Meinke & Schirmer 2015; Duong et al. 2014).

SUN1 and SUN2 are the most widely expressed mammalian SUN proteins and can interact with the KASH peptides of at least four KASH proteins (nesprin 1-4) (Roux et al. 2009; F. Haque et al. 2006; Zhang et al. 2009a; Wilhelmsen 2005; Yu et al. 2011; Lombardi, Jaalouk, Shanahan, Burke, Kyle, et al. 2011). SUN1 can additionally interact with KASH5 during mammalian meiosis (Morimoto et al. 2012). The promiscuity of SUN1 and SUN2 for KASH proteins is consistent with previous reports of their partial functional redundancy during centrosome-nucleus coupling in neuronal precursors in the developing brain, DNA damage repair, nuclear anchorage in skeletal muscle, and interkinetic nuclear migration in

photoreceptor progenitor cells of the developing retina (Lei et al. 2009; Lei et al. 2012; Zhang et al. 2009a; Yu et al. 2011). However, evidence of specific functions for SUN1- and SUN2-containing LINC complexes also exists in the literature(Nishioka et al. 2016; Lu, Gotzmann, Sironi, V.-M. Jaeger, et al. 2008; Li & Noegel 2015b; Qian Liu et al. 2007). For example, SUN1 is required for DNA double-strand break repair, meiotic chromosome pairing, mRNA export, NPC insertion into and distribution throughout the NE, and nucleolar morphogenesis (Henning F. Horn et al. 2013; Qian Liu et al. 2007; Talamas & Hetzer 2011; Matsumoto et al. 2015; Li & Noegel 2015a; Ding et al. 2007). In addition, linear arrays of SUN2-containing LINC complexes assemble on perinuclear actin cables to form transmembrane actin-associated nuclear (TAN) lines that move the nucleus rearward in migrating fibroblasts and myoblasts (Chang et al. 2015; Luxton et al. 2010). Currently, the molecular mechanisms responsible for these dissimilar SUN1- and SUN2-containing LINC complex functions remain poorly understood.

Early on in the discovery of LINC complexes, structure prediction algorithms detected coiled coil (CC) regions in the luminal domains of SUN1 and SUN2, implying that these proteins oligomerize to perform their functions in the NE (Crisp et al. 2006b; Padmakumar et al. 2005). Subsequently, various experimental techniques were employed to determine the oligomeric state of these proteins and to identify the regions involved in their oligomerization, often yielding contradicting results (Summarized in Table 1). For example, early studies using *in vitro* binding assays and coimmunoprecipitation, found that full length human SUN2 forms homodimers(Wang et al. 2006). Similarly, mouse and human SUN1 were shown to form dimers or tetramers using gel electrophoresis and western blotting, respectively (Lu, Gotzmann, Sironi, V.-M. Jaeger, et al. 2008). Ultimately however, crystal structures of a short fragment of human SUN2 in complex with KASH2 peptides revealed a trimeric SUN domain preceded by an α helix (α3) (Figure 1A) that could simultaneously bind to three KASH peptides (Sosa et al. 2012b; Z. Zhou et al. 2012b; Wenjia Wang et al. 2012). In this structure, each KASH peptide was bound in a groove formed by a highly conserved KASH lid extending from the SUN domain, and the SUN domain of its neighboring protomer (Figure 1A, 1B). Some of these studies suggest that the α3-SUN domain fragment is sufficient for trimerization and KASH binding in SUN2 (Z. Zhou et al. 2012b; Wenjia Wang et al. 2012), while others show that SUN domain trimerization is only enabled by CCs preceding this solved region (Figure 1A) (Sosa et al. 2013; Sosa et al. 2012b; Nie et al. 2016) (Table 1). More recently, Nie et al. solved the structure of a larger fragment of mouse SUN2 containing two additional α helices (α1, α2) (Figure 1C). In this conformation, the KASH lid is bound between a three-helix bundle formed by α1, α2 and α3, keeping the SUN domain monomeric, and inactive for KASH binding(Nie et al. 2016) (Figure1B). Based on the abovementioned structural analyses, the current model of SUN2 oligomerization in the NE proposes an inactive SUN2 in a monomeric form, which is activated by the trimerization of at least the SUN domain and α3 helices (Figure 1D) (Nie et al. 2016). In this model, trimerization is indispensible for KASH binding, however, it remains unclear whether the entire molecule can form trimeric CCs as shown in Figure 1D (Sosa et al. 2013; Nie et al. 2016). It should be noted that the crystal structures of monomeric (α1-SUN) and trimeric (α3-SUN) SUN2 are from different species.

Table 1. Summary of studies on SUN1 and SUN2 protein oligomerization prior to 2017.

Region	Residue range	SUN protein	KASH Binding	Oligomer State	Species	Method/environment	Year/ Reference
Predicted CC2 and SUN domain	336–717	SUN2	-	Dimer[a]	Human	*In vitro* binding assay and coimmunoprecipitation	2006 (Wang et al. 2006)
Predicted CC1-CC2 and SUN domain	433–717	SUN2	-	Dimer[a]	Human	*In vitro* binding assay and coimmunoprecipitation	2006(Wang et al. 2006)
Full length		SUN2	-	Dimer[a]	Human	*In vitro* binding assay and coimmunoprecipitation	2006(Wang et al. 2006)
Full luminal domain without SUN domain	432–737	SUN1	-	Dimer and tetramer	Mouse	Native PAGE	2008 (Lu, Gotzmann, Sironi, V.-M. Jaeger, et al. 2008)
Full length		SUN1	-	Monomer, dimer, and tetramer	Human	Western blot	2008(Lu, Gotzmann, Sironi, V.-M. Jaeger, et al. 2008)
α3-SUN	519-716	SUN2	Yes	Monomer/trimer mix	Human	Size exclusion chromatography, SDS-PAGE gel, and Western blotting	2012(Wenjia Wang et al. 2012; Z. Zhou et al. 2012a)
α3-SUN	519-716	SUN2	Yes	Trimer	Human	Crystallization (pdb ID: 3unp)	2012(Wenjia Wang et al. 2012; Z. Zhou et al. 2012a)
Unrelated trimeric coiled coil (ucc) and α3-SUN	UCC-522-717[b]	SUN2	Yes	Trimer	Human	SDS-PAGE, Crystallization (pdb ID: 4dxt, 4dxs)	2012 (Sosa et al. 2012b)
α3-SUN	522-717	SUN2	No	-	Human	SDS-PAGE	2012(Sosa et al. 2012b)
Almost the entire luminal domain	335-717	SUN2	No	Trimer	Human	Analytical ultracentrifugation (sedimentation equilibrium?)	2012(Sosa et al. 2012b)
CC1	378-450[c]	SUN2	No	Trimer	Mouse	Analytical gel-filtration analysis and chemical cross-linking assay, and size exclusion chromatography Crystallization (pdb ID: 5ed9)	2016(Nie et al. 2016)
CC2-SUN domain	451-699[c]	SUN2	No	Monomer	Mouse	Analytical gel-filtration analysis and chemical cross-linking assay, and size exclusion chromatography Crystallization (pdb ID: 5ed8)	2016(Nie et al. 2016)
CC2 (Includes α1, α2 and α3)	451-523[c]	SUN2	No	Monomer	Mouse		2016(Nie et al. 2016)
CC1-CC2	378-523[c]	SUN2	No	Trimer	Mouse	Analytical gel-filtration analysis and chemical cross-linking assay, and size exclusion chromatography	
SUN	524-699	SUN2	No	Monomer	Mouse		
CC1-CC2-SUN	378-523[c]	SUN2	Yes	Monomer/trimer mix	Mouse		
α3-SUN	~501-699[c]	SUN2	-	Monomer/trimer mix	Mouse	Analytical gel-filtration analysis	2016(Nie et al. 2016)

[a] In their discussion, Wang et al. also suggest that SUN2 protein may form a complex of a dimer or a trimer under certain experimental conditions but this data was not shown in their paper (Wang et al. 2006).

[b] Although residues 522-717 are trimers in the crystalized structure, a non related coiled coil of GCN4 was fused to this fragment for crystallography. The SUN2 522-717 fragment alone is unable to bind KASH and therefore predicted to be a monomer by Sosa et al. without the fusion of this unrelated CC (Sosa et al. 2012b).

[c] These residue numbers correspond to mouse SUN2 Isoform 3, which has a length of 699, and is missing residues 154-185 from the canonical sequence (Nie et al. 2016).
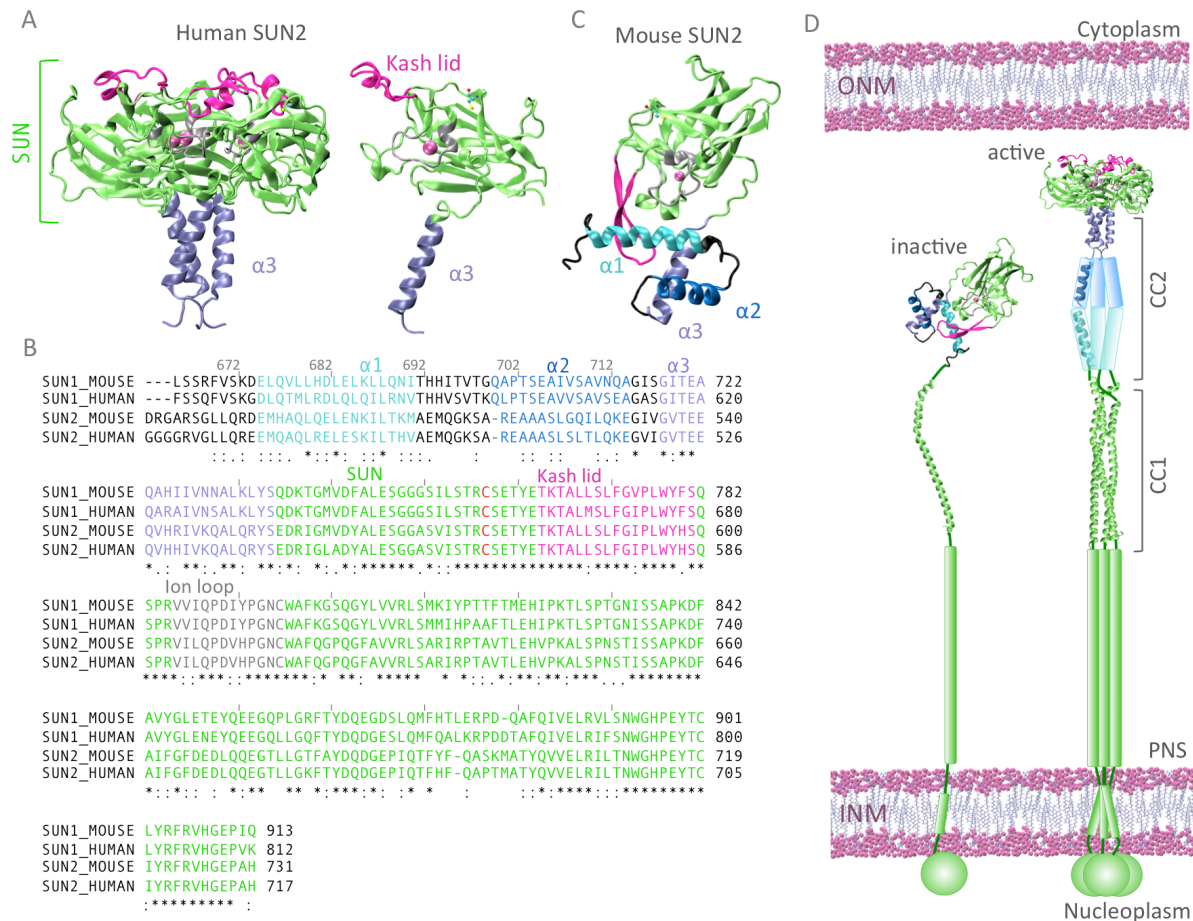
Figure 1. Structures and sequences of SUN domain proteins SUN1 and SUN2. A) Crystal structure of homo-trimeric human SUN2 (Sosa et al. 2012b) (pdb ID: 4dxt) (left) and a representative image of one symmetric unit of this trimer (right). B) Sequence alignment of mouse and human SUN1 and SUN2(Consortium 2017). Important regions identified on the SUN2 crystal structure are colored on the four sequences accordingly. An asterisk (*) indicates positions with fully conserved residues. A colon (:) indicates conservation between groups of strongly similar chemical properties. A period (.) indicates conservation between groups of weakly similar chemical properties (based on Clustal Omega program Formatting) Sequence regions are colored based on aforementioned labels. C) Crystal structure of monomeric mouse SUN2 (Nie et al. 2016) (pdb ID: 5ed8) depicting the autoinhibition of the KASH lid via interaction with the α1-3 helix bundle. Two α helices, α1 (cyan) and α2 (blue), precede the SUN domain and α3. In this conformation the KASH lid (magenta) is hindered by a helix bundle formed by α1, α2 and α3 helices and KASH binding is reportedly inhibited(Nie et al. 2016). D) Working model of SUN2 activation for KASH-binding in the PNS: trimerization of the SUN domain is regulated via CC regions of SUN2 (Nie et al. 2016) and is an essential step for KASH binding and LINC complex formation. INM: inner nuclear membrane, ONM: outer nuclear membrane.

Despite these important mechanistic insights into SUN2 oligomerization and KASH peptide-binding, the lack of similar structural information for SUN1 has limited progress towards understanding the assembly and regulation of SUN1-containing LINC complexes. However, there is evidence in the literature to suggest that SUN1 may assemble a wider range of homo-oligomers than SUN2. For example, native gel electrophoresis and cross-linking studies have demonstrated the existence of SUN1 homo-dimers and -tetramers, which form through a combination of CC interactions and inter-chain disulfide bonds(Lu, Gotzmann, Sironi, V.-M. Jaeger, et al. 2008). Moreover, recent fluorescence fluctuation spectroscopy and brightness analysis conducted in Dr. Joachim Mueller's laboratory at the

University of Minnesota(Hennen et al. n.d.), show that while the luminal domain of SUN2 does homo-trimerize in the nuclear envelope of living cells, the in vivo homooligomerization of the SUN1 luminal domain is not limited to a trimer. Here, we applied a multifunctional computational modeling approach to begin to define the assembly mechanism of SUN1 homo-oligomerization in order to shed light on the functional specification of SUN1- and SUN2-containing LINC complexes.

Methods

Multiple sequence alignments. Sequence alignments were performed using The Basic Local Alignment Search Tool (BLAST) (Consortium 2017). In all shown alignments, Clustal Omega program formatting is used where an asterisk (*) indicates positions with fully conserved residues, a colon (:) indicates conservation between groups of strongly similar properties, and a period (.) indicates conservation between groups of weakly similar properties. Sequence similarities were calculated using BLAST and reported as % identities (i.e. the percentage of residues which are identical between the two sequences) and similarities (the percentage of residues with a positive substitutions). All residue numberings are based on Isoform 1 of the respective SUN protein.

Structural modeling. We generated homology models for mouse SUN1 and SUN2, and human SUN1 trimers using the structure of human SUN2 (pdb ID: 4dxt) as a template. We also modeled the inactive conformation of mouse SUN1 based on the inactive structure of mouse SUN2 (pdb ID: 5ED8). Homology modeling was performed using the SWISS-MODEL servers (Biasini et al. 2014). Swiss model performs an analysis of pairwise interfaces of the template structure to predict the homo-oligomeric structure of the modeled protein. Based on this, all structures made using the 4dxt and 5ed8 templates were predicted to be trimers and monomers respectively. Modeled structures were visualized using VMD software (W. Humphrey et al. 1996). They were next solvated in water, neutralized with counter ions, and ionized with KCl and $CaCl_2$.

Docking. ZDOCK was used for molecular docking of SUN1 or SUN2 trimers (Pierce et al. 2014). ZDOCK uses an energy-based scoring function to rank the top docking solutions among all binding modes in the translational and rotational space between the molecules. We downloaded the top five solutions for SUN1 and SUN2 for further analysis.

MD simulations. All atom MD simulations were performed using NAMD scalable MD with the CHARMM27 force field (Phillips et al. 2005) on a total of 8 systems (summarized in Table S1). All systems were minimized at 5000 steps and equilibrated for ~2 ns with a time step of 2 fs. Simulations were performed under a constant temperature of 310 K, and a constant pressure of 1 atm using Langevin-piston and Hoover's method during minimization and equilibration (Phillips et al. 2005). Additionally, periodic boundary conditions were applied in all three directions. Finally, a total of 3 independent simulation runs were conducted and analyzed for each system (Summarized in the Table S1).

RMSD calculations. Per residue and average RMSD values were computed using RMSD visualizer Tool VMD extension and plotted using R gplot package. All frames of the

trajectory were aligned to a reference frame (frame 0) prior to RMSD computations to eliminate the effect of rotation and translation of the molecule during the simulation. For lateral interaction simulations, we first aligned all frames of the trimer-trimer complex trajectory by using the first frame of one of the trimers as a reference. We then computed the average RMSD of the second trimer with respect to the first trimer.

Energy Calculations. Average nonbonded interaction energies and number of hydrogen bonds between the regions of interest were evaluated in VMD (http://www.ks.uiuc.edu/Research/vmd/vmd-1.9.1/, version 1.9.1), using NAMD energy (Version 1.4) and HBonds (Version 1.2) plugins respectively. The cutoff distance was set to 1.2 nm for all nonbonded interactions, and 3.5Å for hydrogen bonds. An angle cutoff of 20 degrees was used for hydrogen bonds. The structural regions selected for energy calculations were based on various conserved domains identified experimentally for SUN2 as identified in Figure 1B; similar regions were selected on SUN1 based on sequence alignments shown in Figure1B.

For pairwise interaction energy calculations in SUN1 lateral trimer-trimer interactions, we first measured pairwise distances between all residues in trimer 1 and trimer 2. We then identified all residues on trimer 1 that consistently maintained a 4Å distance from trimer 2 over all three simulations trajectories (residues 702, 704, 739, 741, 743, 751, 752, 753, 754, 755, 758, 788, 790, 791 on Human SUN1, Figure S3). Finally, we computed pairwise nonbonded interactions energies between these residues on trimer 1 and trimer 2 and used the R gplot package to create heat maps via the heatmap.2() function. The total energy (VDW and ELEC) fluctuations over MD simulation time are provided in the supplementary figures where relevant (Figure S1, S4).

Angle Calculations. Angles were calculated between various segments of SUN1 or SUN2 (α1, α2, α3 and the KASH lid) by representing each segment as a vector. On each alpha helix, a vector was drawn through two conserved residues near the ends of the helices. Similarly, the KASH lid was represented with a vector passing through two conserved residues on one of its beta strands. The angles were then calculated between the two corresponding vectors representing α1, α2, α3 and the KASH lid segments of SUN1 or SUN2. All residue pairs used in angle calculations are summarized in Table S2).

Results

Homo-trimers are favorable oligomeric states for SUN and α3 domains of SUN1.
Structures of the SUN domains and α3 helices of human and mouse SUN1 (SUN1H, SUN1M) as well as mouse SUN2 (SUN2M), were homology modeled using the crystal structure of human SUN2 (SUN2H, pdb ID: 4dxt) as a template (Biasini et al. 2014). Due to high sequence similarities between the α3-SUN fragments of SUN1 and SUN2 (67% identity and 81% similarity), and particularly high conservation of hydrophobic residues at protomer interfaces, the oligomeric state of all modeled structures were predicted to be homo-trimeric, similar to the SUN2H template (See methods)(Biasini et al. 2014). To further test whether the predicted homo-trimeric state is favorable in SUN1, and to refine our homology models and compare their dynamics, three independent MD simulations were performed on each of the four resulting structural models, namely SUN1M, SUN2M, SUN1H,

and SUN2H. We evaluated the structural stabilities of our models by calculating deviations from their initial states through average, and per-residue RMSD of their backbone atoms over their MD trajectories (Figure 2A). Additionally, we mapped regions with high RMSD values onto each respective modeled structure (Figure 2A). The regions of our models corresponding to loops lacking secondary structure or terminal residues had the highest per-residue RMSD values (RMSD>3Å), as expected (Figure 2A). Despite high per residue RMSD values in these regions, the average RMSD values for all four models reached equilibrium at values below 3Å over the course of three independent 45 ns simulations (Figure 2A).
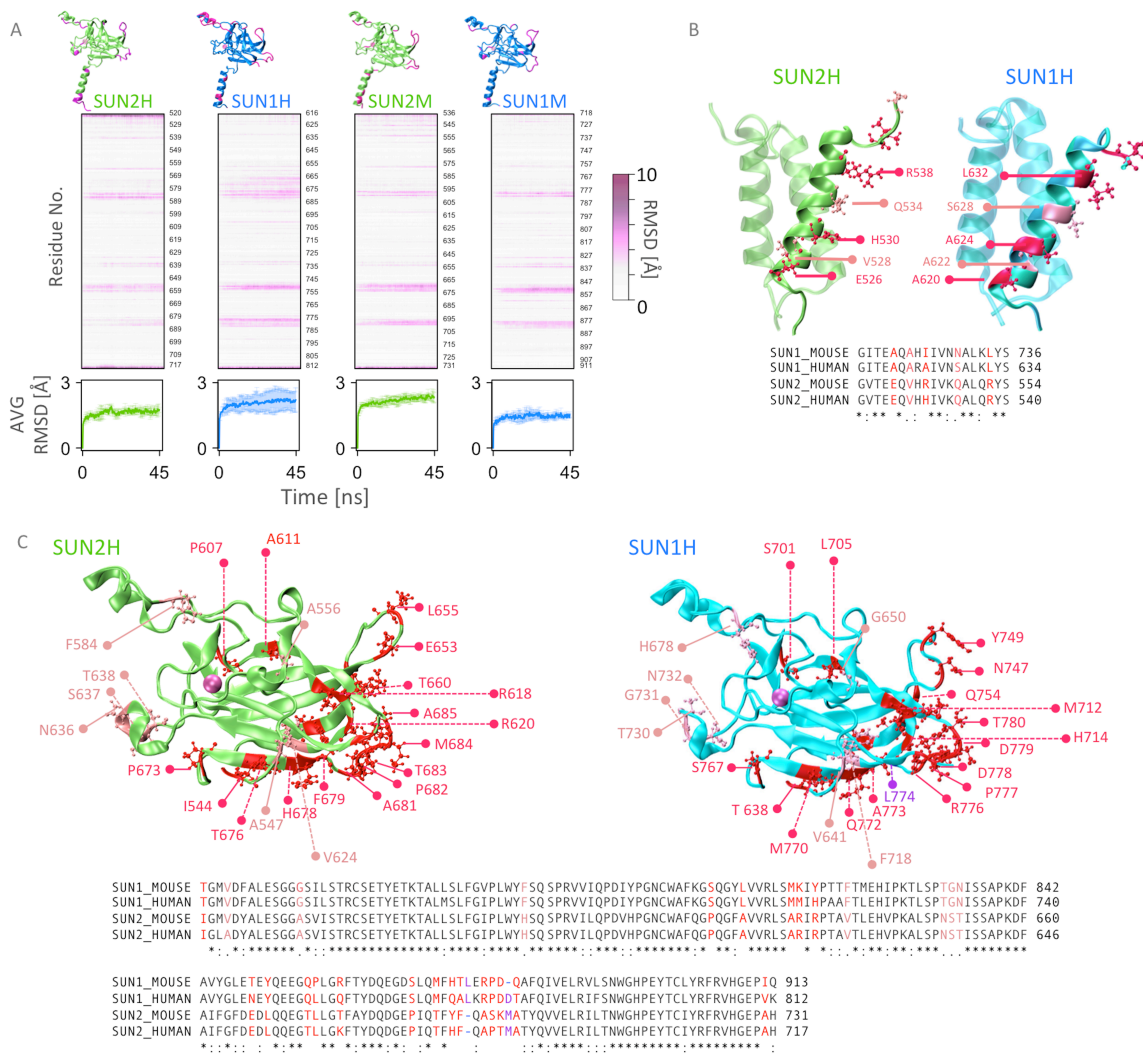
Figure 2. Structural model of SUN1 based on the structure of SUN2. A) RMSD of human and mouse SUN1 (SUN1H, SUN1M), and SUN2 (SUN2H, SUN2M) structural models. Heatmaps show the per-residue Cα atom RMSD over time for SUN2 (green) and SUN1 (blue) relative to the initial minimized modeled structures (top). High RMSD regions are mapped onto the crystal structure of each model and shown above each heatmap. Average Cα atom RMSD for SUN2 (green) and SUN1 (blue) relative to the initial minimized modeled structures (bottom). All frames of the simulation were first aligned to the initial frame before calculating the RMSD. Averages were obtained from three independent simulations runs. B) One-to-one map of non-conserved residue substitutions in the α3 helix between SUN1H and SUN2H. Non-conserved residue substitutions on SUN1 compared with SUN2 are colored in red, semi-conserved residues in pink, and additional residues in purple. C) One-to-one map of non-conserved residue substitutions between the SUN domains of SUN1H and SUN2H.

We next performed a one-to-one map of all non-conserved and semi-conserved substitutions between SUN1H and SUN2H sequences, on their respective refined structural models (Figure 2B, 2C). The hydrophobic residues (V528, V532, L536, Y539) responsible for trimeric CC formation in SUN2H(Zhou et al. 2012), were conserved in the α3 helices of SUN1H (A622, V626, L630, Y633). Interestingly however, charged residues on the solvent-exposed surface of SUN2H α3 helices (R538, Q534, H530, E526) were substituted with hydrophobic or polar residues on the outer layer of SUN1 α3 helices (L632, S628, A624, A620) (Figure 2B). A similar analysis of the SUN domains of SUN1H and SUN2H revealed a highly conserved hydrophobic core at the interface between two SUN protomers (Figure 2C). Most of the non-conserved substitutions were found in solvent-exposed loops in the SUN1H and SUN2H SUN domains (Figure 2C) and corresponded to the regions with high RMSD values shown in Figure 2A.

To compare the potential interactions energies at protomer interfaces between SUN1 and SUN2 trimers, we calculated the total nonbonded interaction energies (VDW and electrostatic) between regions of neighboring SUN protomers that contribute to trimer formation and compared them across MD trajectories of each model (Figures 3A-3B). The total nonbonded protomer-protomer interaction energy is composed of interactions between adjacent SUN domains or α3 helices of neighboring protomers, or between the SUN domain of one protomer and the α3 helix of the neighboring protomer (Figure 3A-3B,S1). These energies were consistent between all our four models (Figure 3A-3B,S1). We further investigated the SUN domain-α3 helix interaction and identified a salt bridge that is formed between the SUN domain and the α3 helix of neighboring protomers that, to the best of our knowledge, was not highlighted in the structure solved by Sosa et al. (Figure 3C, S1)(Sosa et al. 2013; Sosa et al. 2012b). This inter-protomer salt bridge is distinct from the highly conserved intra-protomer salt bridge previously identified between the α3 helix of each protomer and its own SUN domain (D542-R708 pair in SUN2H)(Sosa et al. 2012b). In SUN2H, three of these inter-protomer salt bridges form between K533 residues on each α3 helix, and E672 residues on the SUN domains of adjacent protomers (Figure 3D-3E, S1). Similar inter-protomer salt bridges form between residues K547 and E686 at the same positions on our SUN2M model (Figure 3D-3E, S1). Despite the absence of lysine residues at this position on mouse and SUN1H α3 helices, our models predict that a lysine found in the α3 helix four residues closer to the SUN domain, is positioned perfectly to form a salt bridge with the corresponding residue position on the SUN domains of adjacent protomers (K631-E766 in SUN1H and K733-D868 in SUN1M) (Figure 3D-3E, S1).

To determine the contribution of the identified inter-protomer salt bridges to the overall potential energy of the modeled SUN1 and SUN2 protomer interfaces, we calculated the nonbonded interaction energies between the salt bridge-forming residue pairs (Figure 3C, S1). These energies were equal in value to the interaction energies between the SUN domains and neighboring α3 helices shown in Figure 3B, indicating that the identified inter-protomer salt bridges are the sole inter-protomer interactions between SUN domains and neighboring α3 helices. In addition to nonbonded energies, we quantified the number of hydrogen bonds that form between these residue pairs during a 45 ns MD simulation (Figure 3D, S1). Taken together, these results strongly suggest that like SUN2, the α3-SUN domain fragment of SUN1 favors a trimeric state.
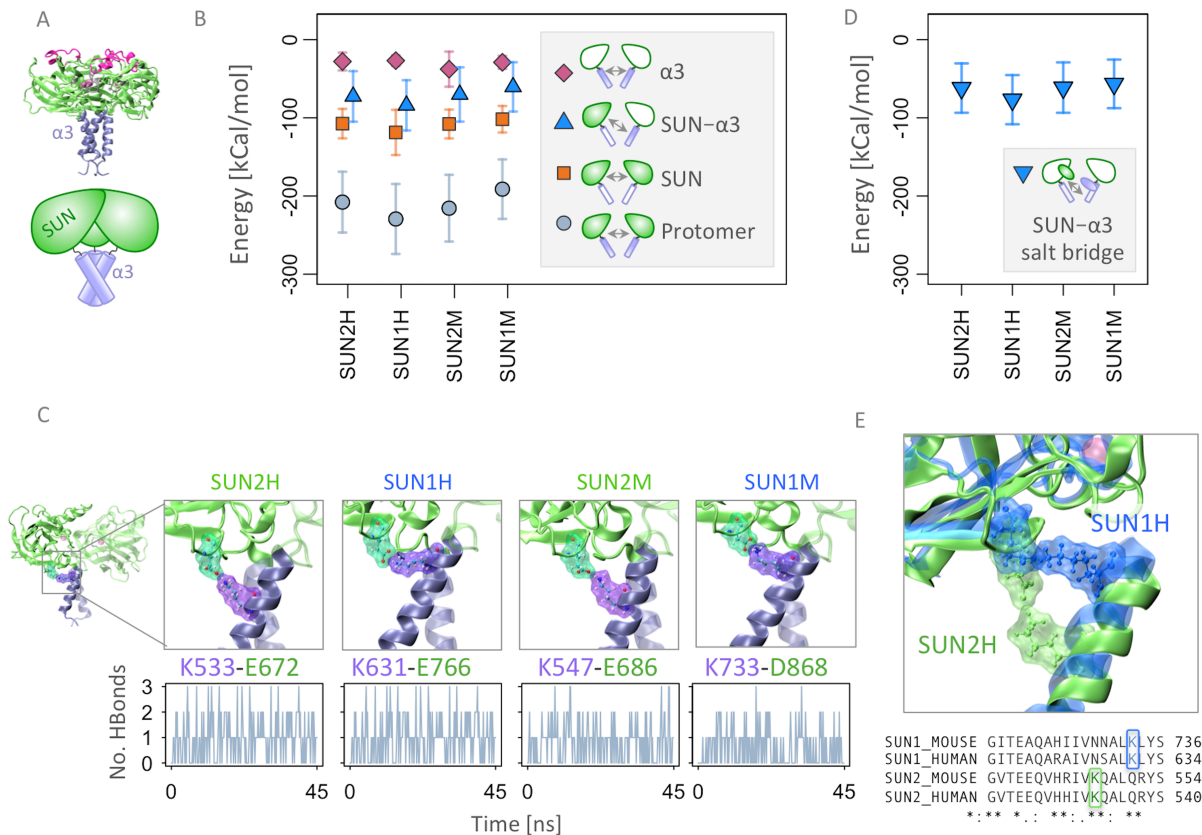
Figure 3: Molecular dynamics of SUN1 and SUN2 homo-trimers. A) Illustration of the human SUN2 trimer domain architecture: the SUN domains are shown in green and CC forming α3 helices in purple. B) Calculated nonbonded interaction energies between the indicated structural regions C) Calculated nonbonded interaction energies between inter-protomer salt bridge-forming residue pairs D) Inter-protomer salt bridges between the SUN domain of each protomer and the α3 helix of an adjacent protomer (top), and number of hydrogen bonds between the inter-protomer salt bridge-forming residue pairs (bottom). Nonbonded interaction energies are averaged over MD simulation time and three independent runs, and error bars correspond to one standard deviation. E) Superimposed structure of one α3 helix and a neighboring SUN domain on SUN1H and SUN2H homo-trimers with the salt bridge-forming residue side chains depicted.

SUN1 forms stable lateral trimer-trimer interactions while SUN2 does not. Our models predict that the α3-SUN domain of SUN1 can homo-trimerize similar to SUN2, so we next sought to investigate how SUN1 homo-trimers might be assembled into higher-order oligomers as observed experimentally (Lu, Gotzmann, Sironi, V. Jaeger, et al. 2008; Hennen et al. n.d.). Previously, SUN proteins were hypothesized to form an extended network in the NE through lateral interactions between the CCs and SUN domains of adjacent homo-trimers (Z. Zhou et al. 2012a; Wenjia Wang et al. 2012). To test this hypothesis, we performed molecular docking on the equilibrated structural models of SUN1 and SUN2 homo-trimers(Pierce et al. 2014).

The results of our initial docking experiments revealed a propensity for SUN protein homo-trimers to interact head-to-head via interactions between their KASH lids (Figure S2). This is unlikely to occur *in vivo* as both SUN trimers are anchored to the inner NE. Hence, we manually blocked the KASH lids from interacting and repeated docking. Four of the top five SUN1 docking solutions (1, 2, 4, and 5) revealed lateral associations between the SUN

domains of adjacent homo-trimers (Figure 4A) (See methods). However, no such docking solutions were observed for SUN2. While three of the five SUN2 docking solutions (1, 3, and 5) involved SUN domain interactions, they did not result in parallel lateral interactions between neighboring homo-trimers. A similar arrangement was observed in the remaining docking solution of SUN1 (3). In addition, the remaining two docking solutions for SUN2 (2 and 4) were mediated by SUN domain-CC interactions, which resulted in an antiparallel homo-trimer arrangement.

Next, to observe the dynamics of such an interaction, we conducted MD simulations on the lateral complex solution obtained from molecular docking of SUN1 trimers. Two SUN2 trimers were also manually positioned into a laterally-interacting complex similar to that of the SUN1 trimers for comparison. The trace of the position (Figure 4B), and RMSD (Figure 4C) of one SUN homo-trimer with respect to the other one over all MD simulations indicated more variability in the position of SUN2 homo-trimers with respect to each other, compared with that of SUN1 homo-trimers (Figure 4C). To begin to determine the mechanism responsible for the lateral SUN domain interactions between adjacent SUN1 homo-trimers, we identified solvent exposed residues at the homo-trimer-homo-trimer interface that maintained a 4Å distance over the course of all three of our MD simulations (Figure S3-A) and calculated their pairwise interaction energies (Figure 4D). Residues with significant VDW or electrostatic interactions among all simulation runs were identified and indicated in Figure 4E. No such interfaces were identified in our SUN2 homo-trimer-homo-trimer simulations (Figure S3-B), however the same interface identified on SUN1 was mapped onto the structure of SUN2 and residues at this interface that were different between SUN1 and SUN2 were highlighted (Figure 4E).

KASH lid inhibition in SUN1 compared with SUN2. Having predicted that the α3-SUN domain of SUN1 is similar to SUN2, we next asked if the KASH lid of a SUN1 monomer might also be autoinhibited by an interaction with the three-helix bundle formed by α1, α2 and α3, as it is in SUN2 (Nie et al. 2016). To do this, we homology modeled mouse SUN1 (SUN1M) monomers using the recently solved monomeric structure of mouse SUN2 (SUN2M, PDB ID: 5ED8) as a template (Figure 5A). Our SUN1M monomer model and the SUN2M monomeric structure were subjected to 90-100 ns MD simulations. Both monomeric SUN1M and SUN2M showed high RMSD values in their α1-3 helix bundle (Figure 5B). However, significantly higher RMSD values were observed in the α2 helix of SUN1M as compared to SUN2M (Figure 5C).

We then performed a one-to-one map of all non-conserved and semi-conserved substitutions between SUN1 and SUN2 sequences, on α1 and α2 domains of the refined modeled structures of monomeric SUN1M and SUN2M (Figure 5D). The α1 regions of SUN1M contained a high level of similar resides with that of SUN2M (35% identity and 53% similarity). And despite a low overall sequence similarity between the α2 regions of SUN1M and SUN2M (0% identity, 33.3% similarity), the main hydrophobic residues on α1 and α2 of SUN2M important for three-helix bundle formation, as identified by Nie et al. (Nie et al. 2016), are either identical or consist of a conservative substitution in SUN1M (with the exception of H513 in the linker region of SUN2M which is substituted with M694 in SUN1M) (Figure 5D).
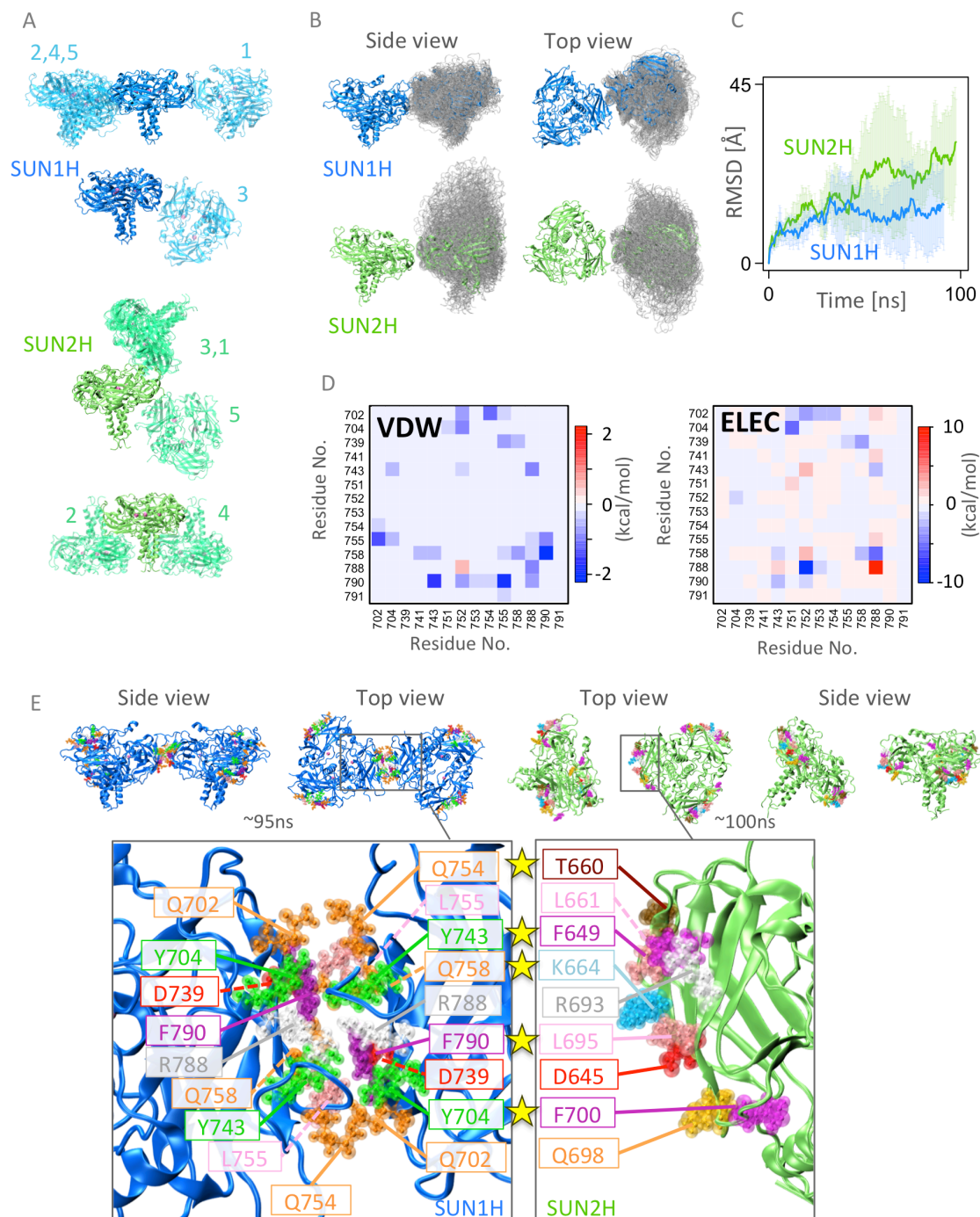
Figure 4: Lateral interaction of SUN1 trimers through their SUN domains. A) Top 5 molecular docking results (zdock server) between two SUN1 or two SUN2 trimers. Similar results are clustered and shown together and each number (1-5) corresponds to the rank of the docking results. B) Visualization of molecular dynamics trajectories of SUN1 and SUN2 homo-trimers with respect to the neighboring trimer, in human SUN1 and human SUN2.C) Average Cα atom RMSD of a human SUN homo-trimer with respect to the neighboring trimer, in human SUN1 and human SUN2. D) Pairwise VDW (left) and ELEC (right) interaction energies between residue pairs within a 4Å distance on two human SUN1 homo-trimers. E) Final frame of MD trajectory of lateral interactions simulations of SUN1 (95ns) or SUN2 (100ns); and close view of interacting residues at the interface of two human SUN1 homo-trimers (blue) and corresponding surface on SUN2 homotrimers (Green). Yellow stars indicate the residues that are different between SUN1 and SUN2 at this interface.
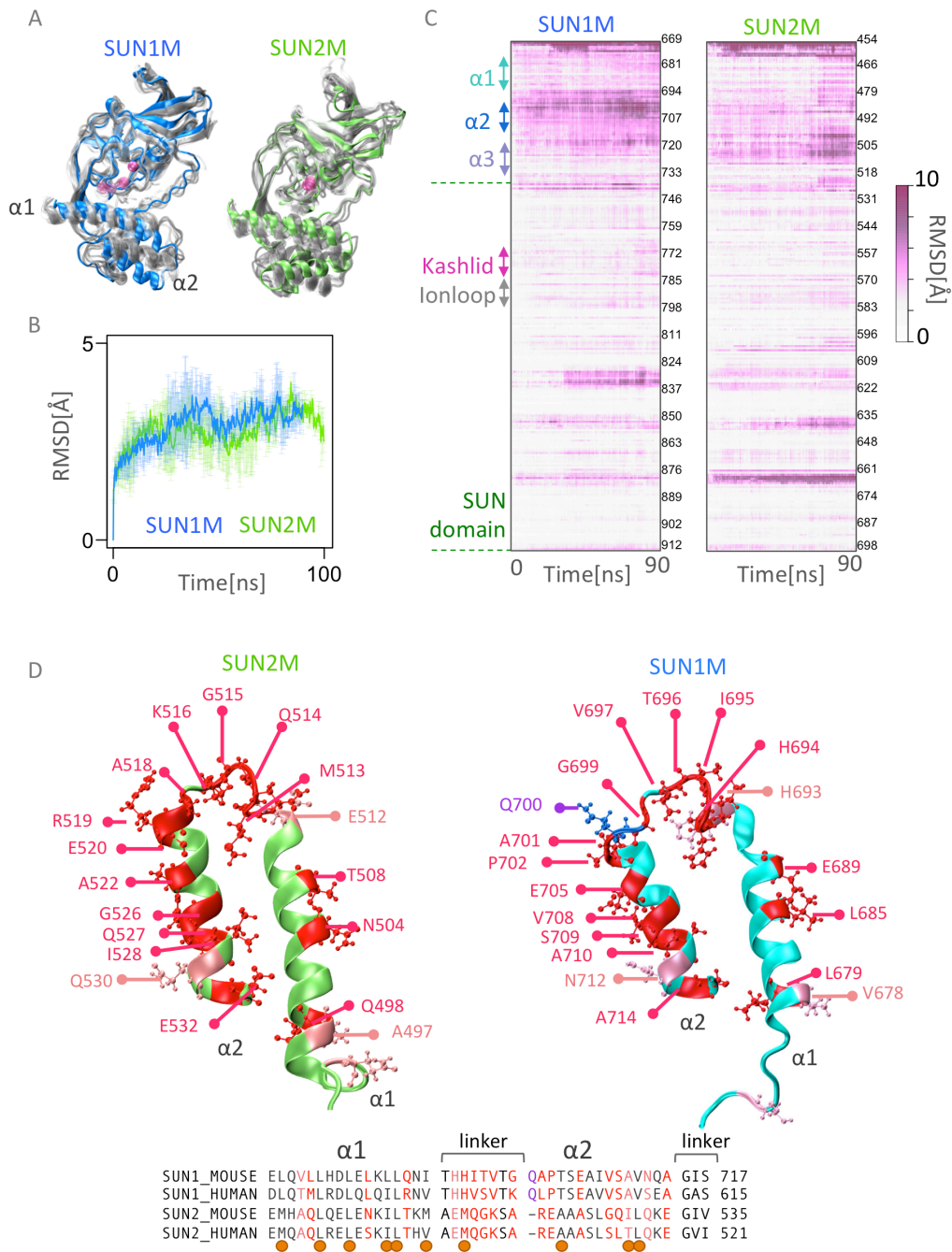
Figure 5: Structural models of monomeric (inactive) mouse SUN1 and SUN2. A) Molecular dynamics trajectory visualization for mouse SUN1 (blue) and SUN2 (green). Traces of the molecular dynamics trajectories of SUN1 and SUN2 trimers over the simulation time are shown in gray. B) Average Cα atom RMSD of mouse SUN1 compared with SUN2. All averages are obtained from three independent runs and error bars correspond to standard deviations. C) Heatmaps of average per-residue Cα atom RMSD over time of mouse SUN1 and SUN2 relative to the initial minimized modeled structures. All averages are obtained from three independent runs. D) One-to-one map of non-conserved residue substitutions between mouse SUN1 and SUN2 on their α1 and α2 regions. Non-conserved residue substitutions on α1 and α2 of SUN1 compared with SUN2 are colored in red, semi-conserved residues in pink, and additional residues in purple. Orange circles represent residues involved in three-helix bundle formation in monomeric mouse SUN2 as identified by Nie et al (Nie et al. 2016).

97

Next, we compared the monomeric SUN1M and SUN2M models by calculating the total nonbonded interaction energies between their KASH lids and α1-3 helix bundle (Figures 6A-6B, S3). The nonbonded interaction energies calculated for the KASH lid-α1 helix interaction were not significantly different between SUN1M and SUN2M. In addition, the α2 helix did not appear to interact with the KASH lid in either SUN protein.
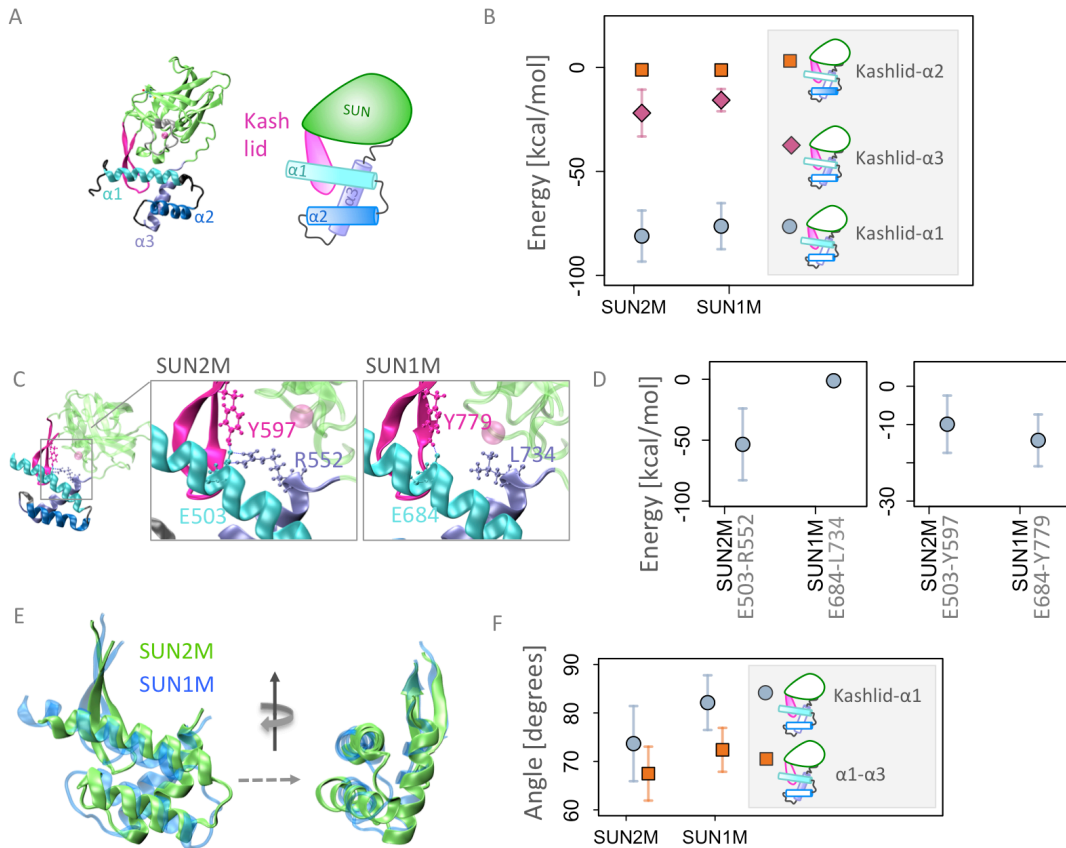
Figure 6: Inhibition of the KASH lid by the α1-3 helix bundle in mouse SUN1 and SUN2. A) Illustration of the inactive mouse SUN2 (SUN2M) domain architecture where the KASH lid (magenta) is bound between a helix bundle formed by α1 (cyan), α2 (blue) and α3 (purple). B) Total nonbonded interaction energies between the KASH lid and α1-3 helices. C) Combined space-filling calotte (CPK) and ribbon representation of the three main residues responsible for bridging α1, α3 and the KASH lid identified in SUN2(Nie et al. 2016), and their corresponding residues on SUN1. D) Interaction energies between the residues indicated in C. E) Superposition of α1-3 and the KASH lid of SUN1 and SUN2 F) Calculated angles between the indicated regions in E. Nonbonded interaction energies and angles are averaged over MD simulation time and three independent runs, and error bars correspond to one standard deviation.

To begin to define the mechanism responsible for the autoinhibition of the SUN1M SUN domain, we sought to identify the residues that contribute to the electrostatic interaction energies between the KASH lid and the α1-3 helix bundle. We first asked if the previously described three-residue network that exists between the KASH lid (Y597), the α1 (E503) helix, and the α3 (R552) helix in SUN2M is also critical for the autoinhibition of SUN1M (Nie et al. 2016). Nie et al. showed that a E503A mutation resulted in the activation of SUN2M for KASH binding *in vitro*(Nie et al. 2016). Additionally, this mutant could marginally increase the localization of KASH2 to the NE *in vivo* demonstrating the importance of the three residue network in SUN2M activation(Nie et al. 2016). In order to

compare with SUN2M, we mapped the corresponding three residues onto the structure of SUN1M (Figure 6C). Indeed, E684 (E503 in SUN2M) is conserved in SUN1M and positioned perfectly to interact with Y779 (Y597 in SUN2M) through electrostatic interactions and hydrogen bonding (Figure 6C-6D, S3). However, the third residue of this network (R552 in SUN2M) is non-conservatively substituted with L734 at the same position on SUN1M, which results in the absence of the salt bridge observed between the α1 and α3 helices of SUN2M.

To further investigate the autoinhibitory role of these three residues in SUN1M and SUN2M, we calculated their pairwise interaction energies (Figure 6D, S3). While the SUN1M α3 helix remained in contact with the KASH lid through electrostatic and hydrogen binding of E684 and Y779, the interaction between the α3 and α1 helices was lost due to the absence of the salt bridge between E684 and L734 (Figure 6D, S3). The lack of this salt bridge also resulted in small shifts in the positions of the α1 and α2 helices relative to the KASH lid in SUN1M as compared to SUN2M (Figure 6E-F, S3). In addition, we measured smaller angels between the α1 and α2 helices as well as between the α1 helix and the KASH lid in SUN1M as opposed to SUN2 (Figure 6E-F, S3). These results suggest that the autoinhibition of the Kash lid maybe be weaker in SUN1M as compared with SUN2M.

Discussion

Here, we provide novel insights into the structure and molecular dynamics of the core LINC complex proteins SUN1 and SUN2. We provide evidence to support that the α3 helix and SUN domain of SUN1 also favors a trimeric state, which is consistent with the homo-trimer being the fundamental functional state for SUN domain proteins(Sosa et al. 2013). In addition, we identify a previously uncharacterized and highly conserved salt bridge that forms between the SUN domain of one protomer and the α3 helix of an adjacent protomer in both SUN1 and SUN2. We also show that like SUN2, the KASH lid of monomeric SUN1 may be kept in an autoinhibited state via interactions with the preceding α1-3 helix bundle. However, the mechanism of autoinhibition appears to differ between SUN1 and SUN2. Finally, we describe a potential mechanism to explain the differential SUN protein homo-oligomerization observed in cells.

SUN1 Oligomerization. The high level of homology between the protomer interfaces of SUN1 and SUN2, specifically in the SUN and α3 domains, and the similarities between SUN1 and SUN2 potential energies in our models over multiple MD simulation runs, provide evidence that like SUN2, the α3-SUN of SUN1 also favors a trimeric state (Figure 2,3). In addition to interactions between adjacent SUN domains and α3 helices, we identified three inter-protomer salt bridges, one between the SUN domain of each protomer and the α3 helix of its neighboring protomer, in the modeled trimers of mouse and human SUN1 and SUN2 (Figure 3C-3E). Judged by its conservation, and it being the only interaction between SUN domains and neighboring α3 helices, we postulate that this salt bridge is important in maintaining the trimer stability. However, it is interesting to see whether disrupting this salt bridge could destabilize the trimers and affect KASH binding *in vivo*. In fact, there are multiple reports of salt bridges contributing to the stability of the active states of proteins

that are capable of adopting various conformations (Wenjian Wang et al. 2012; Wei et al. 2016; Dey et al. 2007; Mehrbod et al. 2013; Barros et al. 2017). We must note that our methods only look at non-bonded potential energy similarities between SUN1 and SUN2 protomer interfaces and provide no information about the entropic costs or the conformational changes required for SUN1 or SUN2 to achieve a trimeric state. In fact, Sosa et al. showed that the SUN domain of SUN2 is insufficient to form a stable trimer and the preceding coiled coil domains of SUN2 enforce this trimerization (Sosa et al. 2012b). However, they also showed that the SUN domain of SUN2 is only functional in a trimeric state (Sosa et al. 2013; Sosa et al. 2012b) Therefore, a similar scenario is imaginable for SUN1 where the SUN domain is functional in a trimeric form, but the coiled coil regions are essential for trimerization and further experiments are required to test this hypothesis.
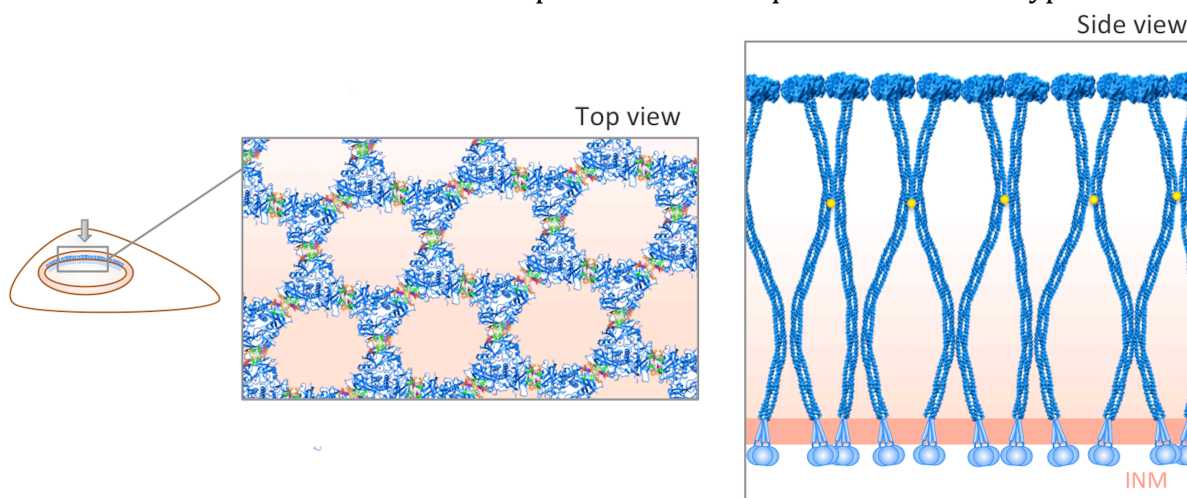
Figure **7: Hypothetical model of higher-order SUN protein oligomer assembly.** Arrays of SUN1 proteins are formed or reinforced at the nuclear envelope by interactions between their SUN domains (Top view). Residues on the surface of SUN1 that reinforce this interaction are colored and match the colors shown in Figure 4E. Additionally, the CC domain of SUN1 can associate through inter-trimer disulfide bonds (Side view). Yellow circles represent disulfide bonds between cysteine residues in the coiled-coil region of SUN1(Lu, Gotzmann, Sironi, V.-M. Jaeger, et al. 2008).

If the SUN domains of SUN1 and SUN2 form trimers, how could one explain the observed assembly of SUN1 into even higher orders in the nuclear envelope of living cells (Lu, Gotzmann, Sironi, V.-M. Jaeger, et al. 2008; Jared Hennen et al. 2017; Hennen et al. n.d.) . Our docking results and molecular dynamics simulations suggest that SUN1 trimers could form higher order clusters by a lateral association of their SUN domains (Figure 4,7). In this model, each SUN1 protomer contains a docking site for a neighboring SUN1 trimer, giving rise to three sites on each trimer (Figure 4E, 7). Additionally, previous studies have shown that the CC-containing regions of the SUN1 luminal domain contains cysteine residues, C526 in SUN1H and C635 in SUN1M, that are capable of forming inter-chain disulfide bonds(Lu, Gotzmann, Sironi, V.-M. Jaeger, et al. 2008). In combination with our proposed SUN-domain docking sites, such disulfides between trimers could lead to clusters of four SUN1 trimers, bound covalently through their CC regions, and interacting through their SUN domains, creating large immobile assemblies in the NE (Figure 7). To understand the functional implications of SUN clustering in the nuclear envelope, we draw a comparison between integrins, which are the transducers of mechanical signals at the cell membrane, and SUN domain proteins, that transmit signals cross the inner nuclear membrane. Integrin

hetero-dimers are able to associate laterally in a process known as integrin clustering, to form focal adhesions, which mediate bi-directional signaling between the ECM and cytoplasm (Roca-Cusachs et al. 2009). Not only is integrin clustering required for the formation of focal adhesions, it is a determining factor in the strength of cell adhesions and the ability to sustain higher forces (Mehrbod & Mofrad 2013; Zeinab Jahed, Shams, et al. 2014; Roca-Cusachs et al. 2009). Likewise, clustering of SUN proteins would enable them to sustain higher forces at the nuclear envelope during various force-dependent processes such as chromosome movement and nuclear positioning(Luxton & Starr 2014b; Jahed, Shams & Mohammad R K Mofrad 2015).

Autoinhibition of the KASH lid in SUN1. We also asked whether SUN1, like SUN2, could adopt an inactive fold in which the SUN domain is bound to its preceding α helical domains. However, our results provide various indications of how molecular mechanisms of SUN1 activation and oligomerization may differ from that of SUN2. First, we identified a string of charged residues on the surface of SUN2 α3 that were all substituted with hydrophobic residues on SUN1 α3 (L632, A624, A620 in SUN1H, and L734, I726, A722 in SUN1M) (Figure 2B). Despite indications of a trimeric α3-SUN domain of SUN1 in our models, we cannot eliminate the possibility of an alternative arrangement of the α3 regions of SUN1 that would bury these residues. It is possible that these residues on SUN1 α3 are involved in the inhibition of the KASH lid in the protein's inactive state.

Secondly, we show that an important three residue cross bridge between α1, α3 and the KASH lid is missing one component in SUN1 (R552 in SUN2M is substituted with L734 in SUN1M as shown in Figure 6C). Thirdly, we showed that the hydrophobic residues on α1, α2 and α3 that are responsible for three-helix bundle formation on SUN2 are highly conserved between SUN1. Therefore, our models predict that α1, α2 and α3 domains are involved in KASH lid inhibition in SUN1, but this inhibition may be weaker than that of SUN2 due to the lack of a conserved substitution of R552 of SUN2M in SUN1 (Figure 6, S3). The differential inhibitory mechanisms of SUN1 SUN domain as compared with SUN2 suggest that SUN1 and SUN2 may also be activated via different mechanisms which could have various implications in the context of their distinct cellular processes. For example, a recent study suggests that SUN1 may inhibit RhoA activation by limiting the activity of SUN2, suggesting that SUN1 and SUN2 may compete for KASH binding (Thakar et al. 2017). The absence of a salt bridge between the KASH lid and SUN1 alpha 3 might suggest that the KASH lid is more readily available for KASH binding in SUN1 and hence would win in competition with SUN2.

Finally, we cannot overlook the possibility of different mechanisms of LINC formation and function across organisms. For example, contrary to all published data on human and mouse LINC complexes, Daryabeigi et al. recently showed that in *C. elegans* the oligomerization of SUN1 is not required for the formation of a functional LINC complex (Daryabeigi et al. 2016). It would be interesting to see how altered oligomerization states could relate to the diverse functions of these highly conserved SUN domain proteins across organisms.

# 3.5 A Molecular Model for LINC complex regulation: Activation of SUN2 for KASH binding

Introduction

The nucleoskeleton and cytoskeleton are physically integrated through linkers of nucleoskeleton and cytoskeleton (LINC) that span the nuclear envelope (NE) (Starr & Han 2002; Padmakumar et al. 2005; Crisp et al. 2006c; F. Haque et al. 2006). LINC complexes are formed by an interaction of inner nuclear membrane (INM) *Sad1/UNC-84* (SUN) and outer nuclear membrane (ONM) *Klarsicht/ANC-1/SYNE* homology (KASH) proteins (Crisp et al. 2006c) in the perinuclear space (PNS) (Fig. 1A). The nucleoplasmic domains of SUN proteins and the cytoplasmic domains of KASH proteins associate with the nucleoskeleton and cytoskeleton, respectively, and provide a crucial means for the bearing and transmission of mechanical forces across the NE (Sosa et al. 2013; Sosa et al. 2012b; Jahed, Shams & Mohammad R.K. Mofrad 2015; Jahed & Mofrad 2018; Zeinab Jahed et al. 2016; Cain & Starr 2015; Soheilypour et al. 2016b). Several fundamental cellular processes are therefore dependent on LINC complex functions, including mechanotransduction, meiotic chromosome pairing, and nuclear positioning (Lombardi, Jaalouk, Shanahan, Burke, Kyle, et al. 2011; Gundersen & Worman 2013; Khatau et al. 2009; Zeinab Jahed, Shams, et al. 2014). Underscoring their significance is a growing list of human diseases associated with mutations in genes coding for LINC complex proteins, including cardiac and skeletal muscular disorders, cancers, and hearing loss (J Stroud et al. 2014; Yang et al. 2013b; Méjat & Misteli 2010a; Folker & Baylies 2013; Meinke et al. 2011; Meinke et al. 2014; Haque et al. 2010; Isermann & Lammerding 2013; Puckelwartz et al. 2010; Matsumoto et al. 2015; Henning F Horn et al. 2013).

Two widely expressed and most extensively studied proteins of the SUN family are mammalian SUN1 and SUN2, which have been shown to interact with the KASH peptides of at least four KASH proteins (nesprin 1-4) (Roux et al. 2009; F. Haque et al. 2006; Zhang et al. 2009a; Wilhelmsen 2005; Yu et al. 2011; Lombardi, Jaalouk, Shanahan, Burke, Kyle, et al. 2011). Although the details of LINC complex regulation remains unknown, recent crystal structures of various fragments of SUN2 have provided invaluable insights into the molecular structure and regulation of SUN2, and its interaction with KASH proteins (Sosa et al. 2012b; Z. Zhou et al. 2012b; Wenjia Wang et al. 2012; Nie et al. 2016; Xu et al. 2018). Based on these studies, there are at least two well-established features of LINC complex regulation.

Firstly, these studies collectively agree that the conserved SUN domain of SUN2 functions as a trimer and must oligomerize to interact with KASH. Sosa et al. showed that in a trimeric state, SUN2 can bind to three KASH peptides simultaneously to form an overall hexameric structure (Fig. 1B-i) (Sosa et al. 2012b). In this structure, an α-helix (α_3) preceding the SUN domain formed a trimeric coiled coil. Additionally, the SUN domain contained a "KASH-lid" region that served as the main binding site for KASH peptides (Fig. 1, B and C). Each KASH peptide was sandwiched between two protomers, and interacted with the KASH-lid of one protomer and the core of the neighboring protomer (Fig 1B-i).

Secondly, these studies suggest that the SUN domain alone is not sufficient for the trimerization of SUN2, and that coiled-coil (CC) domains preceding the SUN domain may regulate its trimerization. In agreement with this, SUN domain proteins are predicted to contain at least two CC domains (CC1 and CC2) preceding the conserved SUN domain (Fig. 1A). Point mutations in the predicted CC domains have been incidentally associated with several diseases, underscoring their prominent role in SUN2 function. For example, a point mutation in E438 in Human (E452 in Mouse), which is on the CC1 domain of SUN2, was observed in muscular dystrophy-associated SUN2 variants (Meinke et al. 2014) .
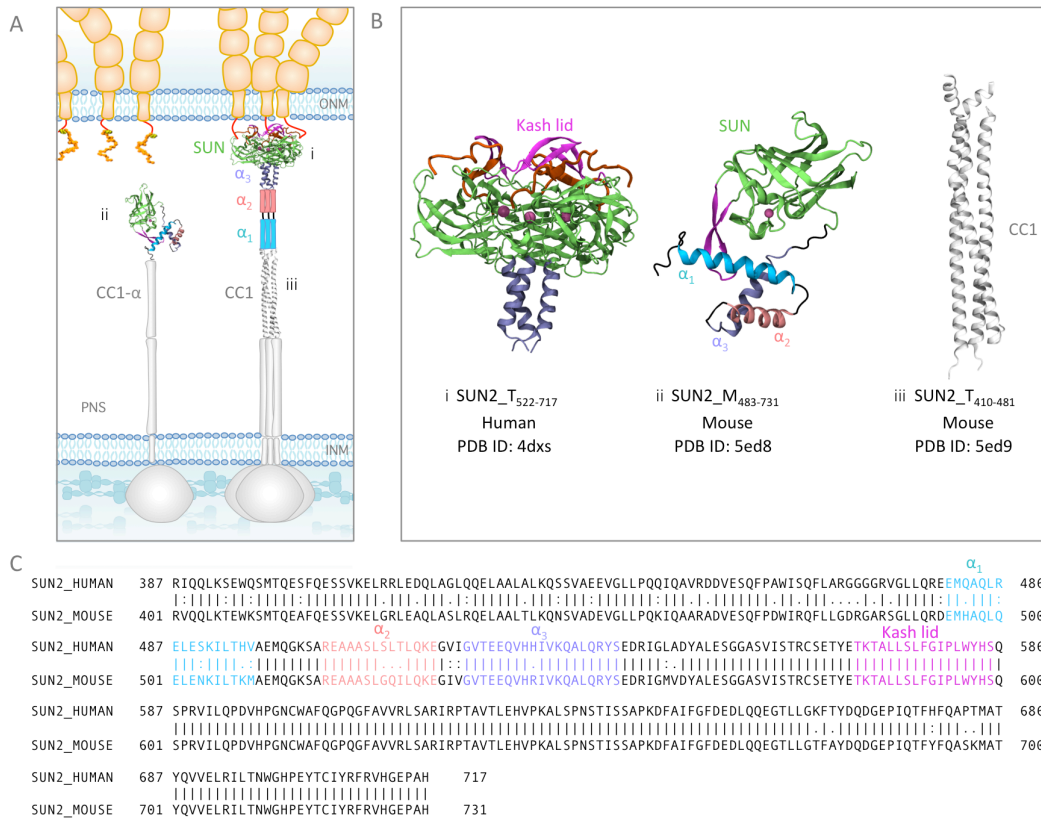
Figure 1: Structures of various fragments of SUN2, in a trimeric or monomeric state in the nuclear envelope. A) Schematic representation of the standing model of SUN2 organization in the nuclear envelope. The *in vitro* crystal structures available from various studies are shown in their respective positions, and all other regions for which no experimental structural information is available are shown with schematic cartoon representations. Note that the organization of α_1 and α_2 in the trimer, as well as CC1-α in the monomer is unknown. B) Available structures of SUN2 fragments: i) Structure of Human $Sun2_{522-717}$ trimer bound to three KASH peptides ii) Structure of mouse $SUN2_{483-731}$ monomer iii) Structure of coiled coil (CC1) of Mouse $SUN2_{420-481}$. (Each structural fragment is represented by its residue range. SUN2_M is used for the monomeric state of each fragment and SUN2_T for a trimeric state). C) Amino acid sequences of human and mouse SUN2. Structural domains on human and mouse Sun2 are shown with the similar colors for comparison (α_3 in purple, α_2 in pink, α_1 in cyan, Sun domain in green and the Kash lid in magenta).

Recent crystal structures of the CC1 and CC2-SUN fragments of mouse SUN2 revealed that CC1 could independently form a trimer, whereas the CC2-SUN2 unexpectedly adopts an inactive monomeric conformation (Fig. 1B, ii, iii). In this inactive conformation the KASH-lid is supposedly auto-inhibited through interactions with a three helix bundle formed by three α helices, α_1, α_2 and α_3 (Fig., B-ii and C) (Nie et al. 2016). Consequently, a point

mutation in α_1 (E471A) could result in the activation and trimerization of the protein. Recently, this auto-inhibitory domain was shown to also be conserved in SUN1 (Xu et al. 2018; Jahed et al. 2018). It is important to note that in these studies the crystal screening of CC1-CC2-SUN was unsuccessful possibly due to its heterogeneous state, and in order to determine the crystal structures each protein fragment (CC1 and CC2-SUN) was expressed separately, therefore any structural changes resulting from interactions between CC1 and CC2-SUN could not be captured.

The reported crystal structures to date have provided a useful foundation for exploring the regulation of LINC complexes at the NE. The molecular mechanisms of LINC complex function, however, remain largely understudied. Specifically, the interplay between CC1 and CC2, and the mechanisms of monomer trimer transition of SUN2 remain unknown. In this study, we constructed structural models of monomeric CC1-CC2-SUN using the available structural fragments of SUN2, and observed the dynamics of these structures using ~1 microsecond molecular dynamics (MD) simulations to provide insights into the potential molecular mechanisms of SUN2 activation.

Results

Structural model of SUN2 monomer

Given that current experimental attempts have failed to screen for larger fragments of SUN2 proteins, we used homology modeling (Phyre2 (Kelley et al. 2015)) and combined structural information obtained from various fragments of SUN2 (SUN2_T$_{410-481}$ and SUN2_M$_{483-731}$) as templates to predict the model of a larger fragment of the monomeric SUN2 protein SUN2_M$_{413-731}$ (Fig. 2A). In the modeled monomeric SUN2 structure, we labeled the α helix of CC1 as CC1$_\alpha$. The region between CC1$_\alpha$ and α_1 (SUN2$_{468-474}$) consists of an unstructured flexible glycine rich loop (GGGGRVG), and so various orientations of the two protein domains, α_1-SUN and CC1$_\alpha$, were obtained from homology modeling (Fig. 2A). Also, because the modeled structures consisted of regions for which structural template information was available, the confidence scores of all models were 100% in all regions, except in the flexible glycine rich loop region, as expected (Fig. 2A). To determine the dynamics of these larger fragments of the modeled SUN2_M$_{413-731}$ structure, we selected two models with distinct orientations between α_1-SUN and CC1$_\alpha$ (SUN2_M1$_{413-731}$ and SUN2_M2$_{413-731}$ identified with stars in Fig. 2). For this selection each modeled structure was aligned to the CC1 trimer (SUN2_T$_{410-481}$) to ensure there would be no physical overlap between residues in the three monomers (SUN2_M$_{413-731}$) once assembled into a trimer (Fig. 2B). We used these selected models with distinct orientations of α_1-SUN and CC1$_\alpha$ (SUN2_M1$_{413-731}$ and SUN2_M2$_{413-731}$ in Fig. 2, B and C) to determine the dynamics of SUN2_M$_{413-731}$, which contains the CC1$_\alpha$-SUN domains, using molecular dynamics simulations.

Molecular dynamics trajectories of SUN2 monomer

To observe the dynamics of the two selected homology models, we conducted molecular dynamics simulations on these models. The molecular dynamics trajectories of both models showed high variability in the position of the α1-SUN domain with respect to CC1$_\alpha$ (Fig. 3A). Notably, both modeled structures bend in the region proceeding residue E452, which is enabled by a flexible G residue at position 454 (Figs., 1C and 3). The angles

between the regions on the two sides of G454 on $CC1_\alpha$ varied between 60-173° over the molecular dynamics simulations (Fig. 3B).

**Molecular dynamics of auto-inhibited α_1-SUN in the presence of $CC1_\alpha$**

In order to gain insights into the dynamics of auto-inhibited α_1-SUN in the presence of $CC1_\alpha$, we compared the dynamics of the α_1-SUN domains in short and long fragments of SUN2 monomer during 1-microsecond MD simulations. These simulations were conducted on three modeled structures namely, $SUN2\_M_{483-731}$, $SUN2\_M1_{413-731}$, $SUN2\_M2_{413-731}$ (Fig. 4). Both $SUN2\_M1_{413-731}$ and $SUN2\_M2_{413-731}$ experienced large conformational changes as evident by the superposition of their initial and final structures over our MD simulation times (Fig. 4, A and B) Moreover, we calculated average root mean square fluctuations (RMSF) of each model (Fig. 4C). Our results show that $CC1_\alpha$ regions of $SUN2\_M1_{413-731}$ and $SUN2\_M2_{413-731}$ highly fluctuate compared with their α_1-SUN domains. In agreement with trajectory visualizations presented in Fig3, both modeled structures show a peak in RMSF value at residue E452, and a kink in the $CC1_\alpha$ region at G454 (Fig. 4, A, B and C). We also compared the RMSF values of $SUN2\_M1_{413-731}$ and $SUN2\_M2_{413-731}$ with that of $SUN2\_M_{483-731}$ (Fig. 4C). Both models of $CC1_\alpha$-SUN showed higher fluctuations in their α_1-SUN domains compared with the isolated model of α_1-SUN ($SUN2\_M_{483-731}$) (Fig. 4C).

Next, to determine the conformational changes in the α_1-SUN domains in the presence of the $CC1_\alpha$ domain, we calculated the RMSD (root mean square deviation) of residues 483-713 (α_3-SUN) from their original structures over our MD simulation times (Fig. 4D) (see methods for details). The RMSD of residues from the original structure (at time=0) were compared between the three modeled structures ($SUN2\_M_{483-731}$, $SUN2\_M1_{413-731}$ and $SUN2\_M2_{413-731}$) in order to determine protein domains that deviate from the original α_1-SUN conformation in the presence of $CC1_\alpha$ (Fig. 4D). RMSD values up to 20 Å were calculated for several residues in the α_1-α_3 helix bundle and the KASH-lid regions for the modeled structure of $SUN2\_M1_{413-731}$ (Fig. 4D), indicating a high variation in these regions compared to the isolated α_1-SUN. High RMSD values were also calculated for α_3 regions of $SUN2\_M2_{413-731}$, however the deviations in the KASH-lid of this modeled structure were lower than that of $SUN2\_M1_{413-731}$.

The KASH-lid is released from its auto-inhibited state in the presence of $CC1_\alpha$

The auto-inhibition of the KASH-lid of SUN2 is mediated by a three-residue cross bridge where Y565 on the KASH-lid interacts with E471 and R520 on α_1 and α_3 respectively (Fig. 5A) (Nie et al. 2016). A mutation E471A is suggested to disrupt this three-residue cross bridge and release the KASH-lid from its proposed auto-inhibited state and promote KASH binding *in vitro* (Nie et al. 2016). We therefore developed a fourth model, $SUN2\_M\_E471A_{483-731}$, which contained the abovementioned mutation. To obtain insights into the auto-inhibitory state of SUN2 in the presence of $CC1_\alpha$, we compared the distances between the center of mass of these three residues during 1µs MD simulations in our four modeled structures (Fig. 5 B and C). Mutation of E471A resulted in a 5.50 +/-1.34 Å increase in the distance between residue Y565 on the KASH-lid and residue R520 on α_3, compared with WT $SUN2\_M_{483-731}$ (Fig. 5 B and C). Interestingly, our two models of $CC1_\alpha$-SUN, $SUN2\_M1_{413-731}$ and $SUN2\_M2_{413-731}$, that contained E at position 471 also showed separation between Y565 and R520 similar to that of the mutated model, $SUN2\_M\_E471A_{483-731}$ (Fig. 5 B and C).

Residue Y565 and R520 showed an increased distanced of 7.07 +/-1.7 Å and 4.25 +/-1.63 Å in models SUN2_M1$_{413-731}$ and SUN2_M2$_{413-731}$, respectively. Note that the first 200ns of simulations were omitted in the calculation of the average changes in residue distances. These results suggest that CC1$_\alpha$ can induce changes in the conformation of α_1-SUN to mediate the release of the KASH-lid from its auto-inhibitory state.
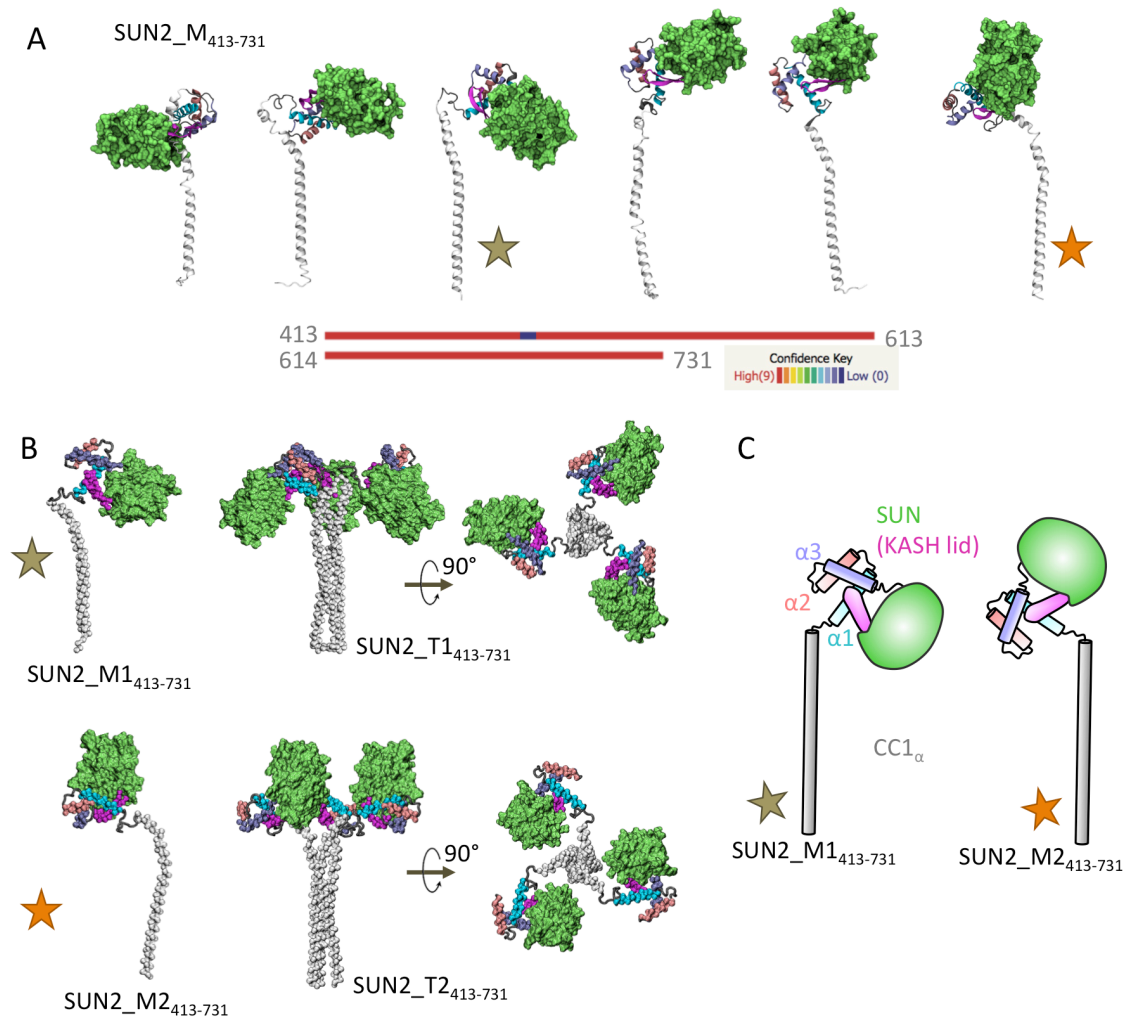
Figure 2: Structural models of SUN2$_{413-731}$ in monomeric and trimeric states. A) Predicted homology models of SUN2 monomer using Phyre2 with various conformations. Confidence of prediction is shown for residues 413 to 731. The stars represent the two conformations that were used in this study B) Selected homology models of SUN2$_{413-731}$ monomers with two distinct conformations (SUN2_M1$_{413-731}$ and SUN2_M2$_{413-731}$ shown with brown and orange stars respectively); these models showed no structural overlap with neighboring monomers when assembled into a trimer. Side and top views of the trimeric models are also shown (SUN2_T1$_{413-731}$ and SUN2_T1$_{413-731}$). C) Schematic representation of structural models of SUN2_M1$_{413-731}$ (brown star) and SUN2_M2$_{413-731}$ (orange star) used in this study, for comparison.
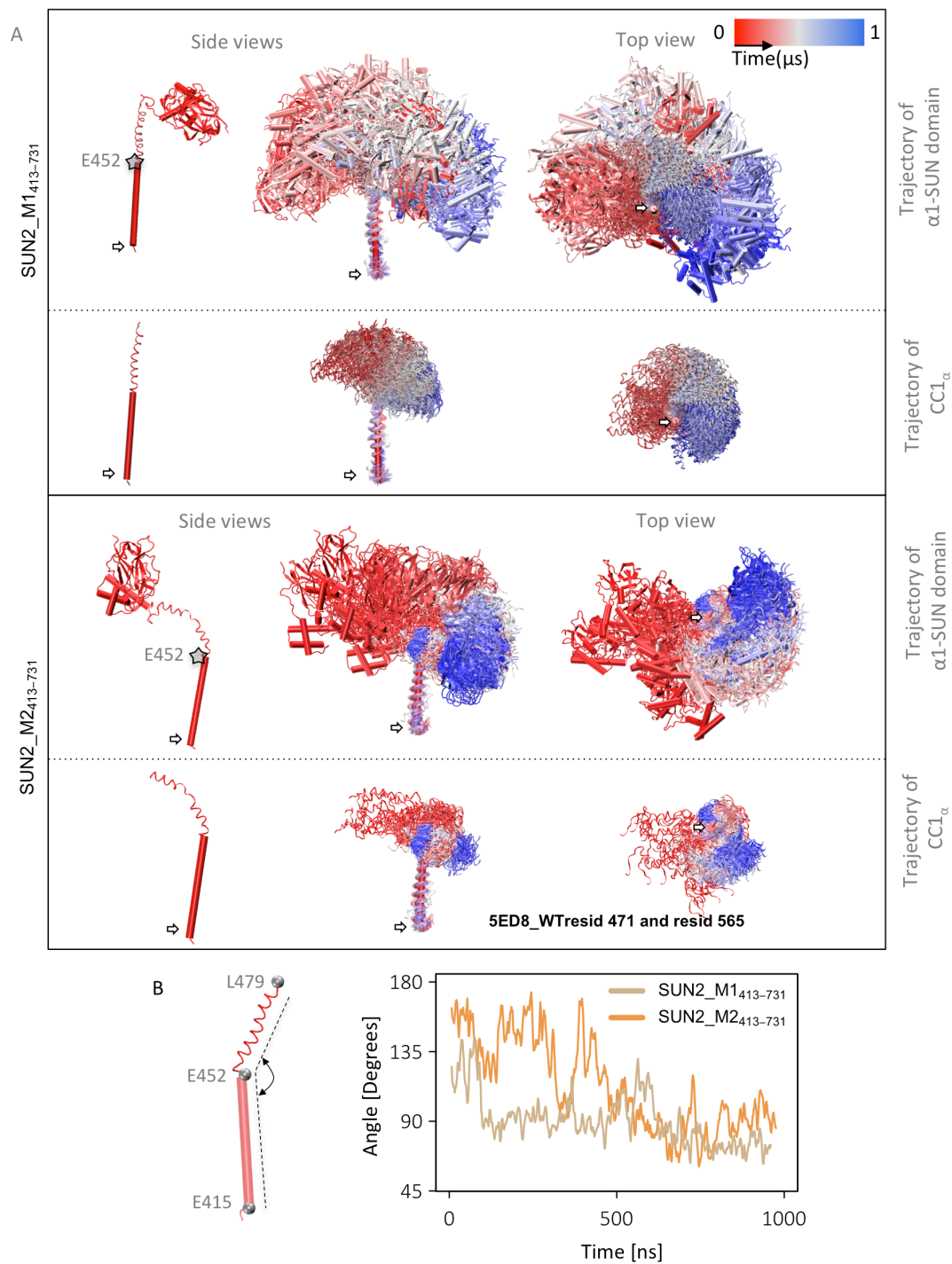
Figure 3: Trajectory of SUN2 monomer during molecular dynamics simulations. A) Side and top views of CC1$_\alpha$ and α_1-SUN domain trajectories (the same trajectories are shown without α_1-SUN domain for better visualization of the trajectory of CC1$_\alpha$ alone), B) Angles between three residues E415, E452 and L479 in CC1$_\alpha$ of SUN2_M1$_{413-731}$ and SUN2_M2$_{413-731}$. (All molecular dynamics simulation frames were aligned to the first time frame using residues E415-E452 for this visualization). White arrows show the position of the terminal residues on CC1$_\alpha$.
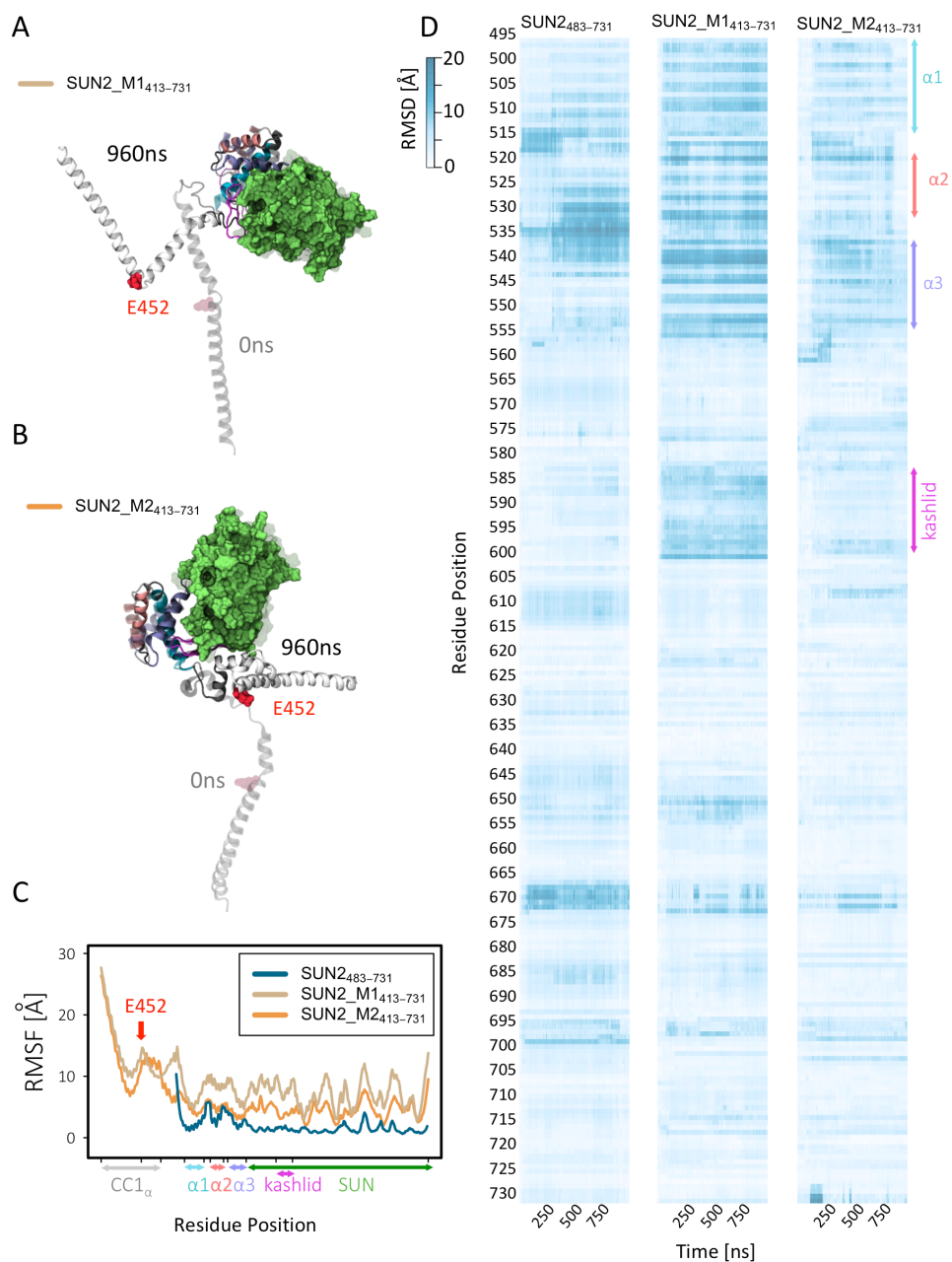
Figure 4: Comparison of the dynamics of SUN2$_{413-731}$ structural models, with wildtype SUN2$_{483-731}$ monomer over 1 microsecond long molecular dynamics simulations. A) First and final frames of structural models of SUN2_M1$_{413-731}$ and after 1 microsecond long MD simulations. B) First and final frames of structural models of SUN2_M2$_{413-731}$ after 1 microsecond long MD simulations. C) Root mean square fluctuations (RMSF) of SUN2_M1$_{413-731}$, SUN2_M2$_{413-731}$ structural models, and wild type SUN2$_{483-731}$. D) Per residue root mean square deviations (RMSD) of SUN2_M1$_{413-731}$, SUN2_M2$_{413-731}$, and SUN2$_{483-731}$ structural models. All simulation trajectories were aligned to the SUN2$_{483-731}$ fragment of the initial frame for each model prior to RMSD calculations.
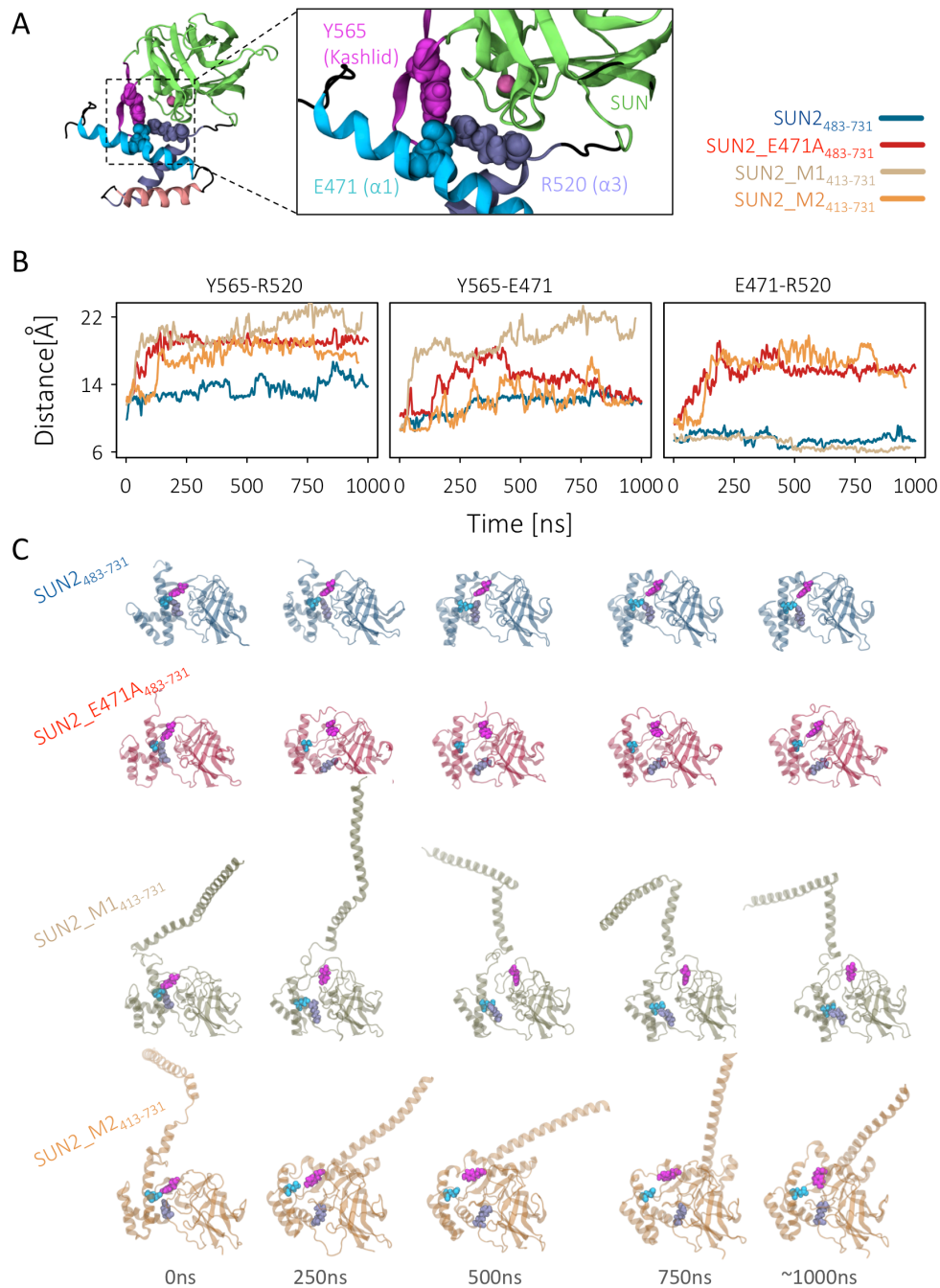
Figure 5: The link between kash lid and α₁- α₃ helix bundle is lost in SUN2₄₁₃₋₇₃₁ structural models. A) The main residue cross-bridge that maintains the kash lid in an autoinhibited state in SUN2₄₈₃₋₇₃₁ monomer. An E471A mutation has been shown to release the kash lid from the α₁- α₃ helix bundle and activate it for kash binding. (Nie et al. 2016). B) Distance between the three residues on SUN2₄₁₃₋₇₃₁ structural models, compared with wild type and E471A mutant SUN2₄₈₃₋₇₃₁ monomers over microsecond long molecular dynamics simulations. Five frames of each simulation trajectory are shown to represent the evolution of the distances of these residues in the four structural models during each simulation run. Residues 413-731 are aligned on the four structures to facilitate visual comparisons.

CC1α-SUN is an unstable trimer *in vitro* and mutations in E471 can change the trimer-monomer ratio

We performed analytical gel-filtration on the CC1α-SUN fragment (SUN2$_{410-731}$) to determine the oligomeric state of this region *in vitro*. Our results show that this fragment is an unstable trimer and forms a monomer-trimer equilibrium *in vitro* (Fig. 6). As previously mentioned, the CC1α region in both modeled structures of CC1α-SUN adopted a kink at the same location near E452 during our MD simulations. In order to determine the importance of the region involved in forming this kink in the activation (trimerization) of SUN2, we deleted the region and tested the oligomer state of a shorter fragment (SUN2$_{458-731}$). Deletion of SUN2$_{410-456}$ completely forced SUN2 into a monomeric state. Next, we examined the role of E452 (E438 in Human) in the oligomer state of the SUN2$_{410-731}$ fragment by introducing point mutations. An E452 mutation changes the ratio between monomer and trimer in solution. Substitution of E452 with a hydrophobic residue (E452A) significantly reduces the monomer concentration, whereas mutation to a positively charged residue (E452R) reduces the trimer concentration and increases the monomeric concentration. Most noteworthy is the conserved substitution with a negatively charged residue (E452D), which has previously been observed in muscular dystrophy-associated SUN2 variants (Meinke et al. 2014). This substitution maintains the WT trimer concentration, but increases the monomer concentration significantly compared with WT. Our analytical gel-filtration results show that E452 plays a significant role in the oligomerization of SUN2.
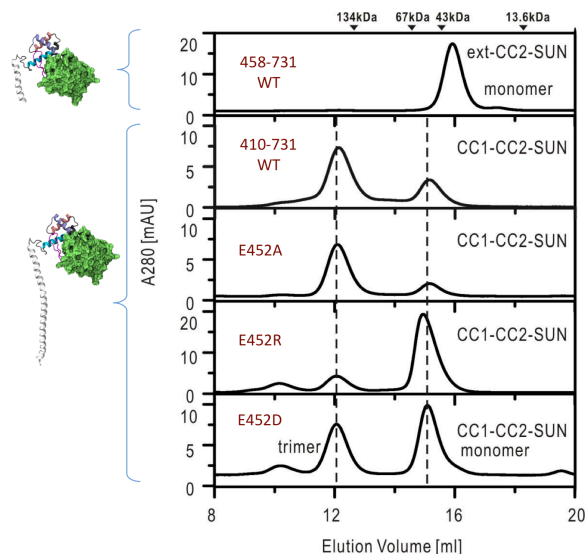
Figure 6: Point mutations in E452 change the monomer-trimer ratio of SUN2: Analytical gel-filtration analysis of CC1-CC2-SUN (residues 410-731) and the mutants. The elution volumes of MW markers are indicated at the top.

Calcium ion binding may regulate activation of SUN2

Finally, to explain a potential mechanism of how E452 may be involved in trimer-monomer transition of SUN2$_{413-731}$, we took a closer look at the dynamics and interactions of this residue in our MD simulations. In model SUN2_M1$_{413-731}$, E452 binds stably to a Ca^{2+} ion in our modeled system within the first ~60ns and maintains this interaction up to 1μs (Fig. 7A). In this model, CC1α kinks, but there are no interactions between the SUN domain and CC1α. In model SUN2_M2$_{413-731}$, E452 also binds to a Ca^{2+} ion at ~370ns. Interestingly, when

not bound to an ion, the $CC1_\alpha$ interacts with the $SUN2_{458-731}$ region through E452, as evident from the electrostatic energies calculated between these regions throughout the simulation time (Fig. 7, A and B). The correlation between ion binding and $SUN2_{458-731}$ binding of E452 was calculated as R=-0.84 indicating a strong negative correlation (Fig. 7A). These results suggest that if E452 is not occupied by a Ca^{2+}, it interacts with other regions of the molecule including the SUN domain.
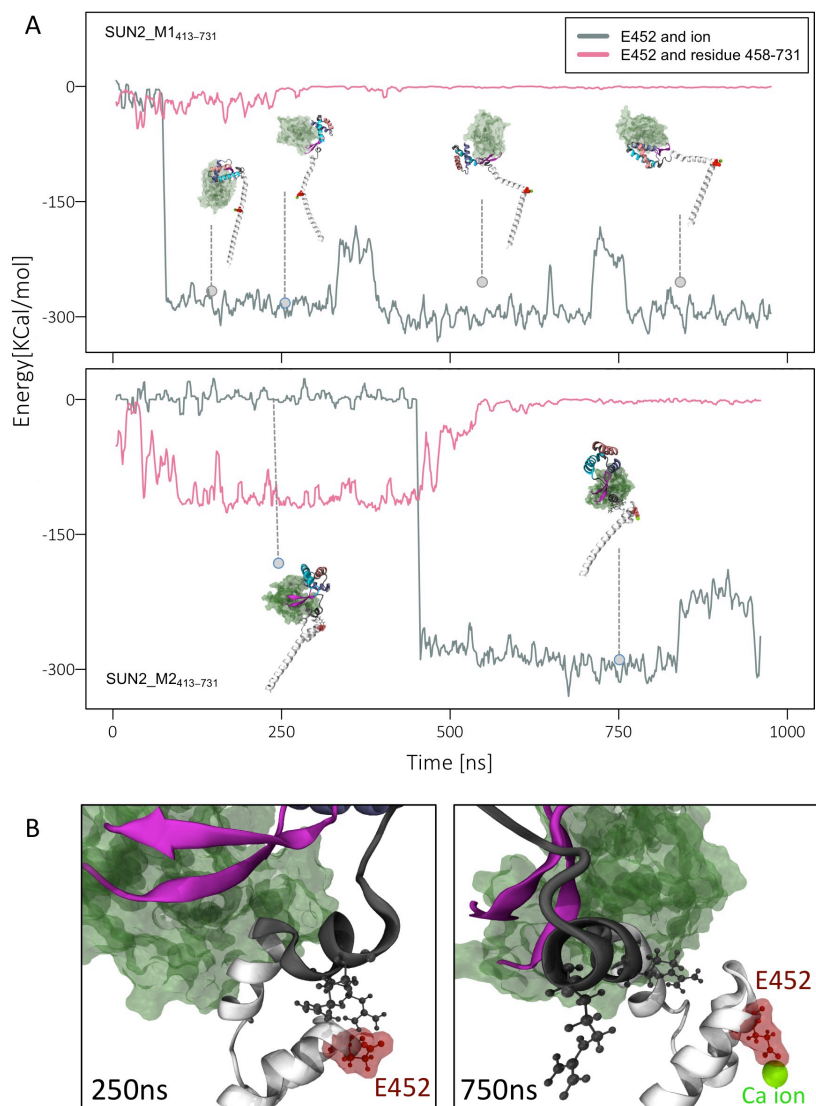
Figure 7: EDMD related residue (E452) binds to Ca^{2+} ion and regulates the conformation of CC1-CC2-SUN domain. A) Electrostatic Interactions between calcium ion and residue E452, compared with nonbonded interactions between E452 and residues 458-731 for $SUN2\_M1_{413-731}$ (top) and $SUN2\_M2_{413-731}$ (bottom) showing a negative correlation between these interactions (R=-0.84) B) Representative image of E452 bound to residues 458-731 in the absence of Ca^{2+} ion (left, 250ns), and representative image of E452 associated with a Ca^{2+} ion and separated from other domains (right, 750ns)

Discussion

*S*tructural information of small fragments of the LINC complex have greatly enhanced our understanding of the interaction of SUN2 and KASH proteins in the nuclear envelope (Sosa et al. 2012b; Nie et al. 2016; Wenjia Wang et al. 2012). Experimental crystal screening of larger fragments of SUN2 proteins have been reported as unsuccessful, however, likely due to SUN2's heterogeneous state, therefore limiting our understanding of the molecular dynamics and regulation of these proteins in the nuclear envelope. In order to determine the crystal structure of SUN2, various fragments of the protein have been expressed separately, and thus any structural changes resulting from associations of various regions of SUN2 have not been able to be captured by current experiments (Sosa et al. 2012b; Nie et al. 2016; Wenjia Wang et al. 2012). For this reason, we used an integrative computational approach incorporating all available structural information to develop a model of a large fragment of SUN2 monomer, which consisted of the $CC1_\alpha$ and the reported auto-inhibited α_1-SUN domain of SUN2.

Through microsecond MD simulations we show that $CC1_\alpha$ is highly flexible as a monomer and adopts a hinge like motion at residue G454 (Figs., 3 and 5), forming a V shaped $CC1_\alpha$ (Fig. 8). This may suggest that $CC1_\alpha$ actually contains two separate α-helices (we name them $CC1_{\alpha1}$ and $CC1_{\alpha2}$) that are linked through a flexible Glycine residue (Fig. 8). Our gel filtration analysis shows that $CC1_{\alpha1}$ is essential for activation, and deleting $CC1_{\alpha1}$ completely disrupts the trimerization of $SUN2_{413\text{-}731}$ (Fig. 6). In fact, although both $CC1_{\alpha1}$ and $CC1_{\alpha2}$ have been reported to be important in the formation of the coiled coil CC1 *in vitro* (Nie et al. 2016), CC predictors all predict a zero probability for $CC1_{\alpha2}$ to form a CC (Fig. S1). In agreement with these predictions, our results suggest that $CC1_{\alpha1}$ and not $CC1_{\alpha2}$, is the main regulator of trimerization. Additionally, since the $SUN2_{413\text{-}731}$ trimer is unstable between a trimer and monomer (Nie et al. 2016), it is plausible that the domains preceding $CC1_{\alpha1}$ stabilize $SUN2_{413\text{-}731}$. In agreement with this hypothesis, CC predictors suggest that regions preceding $CC1_{\alpha1}$ can also form CCs. Gel filtration experiments including regions preceding $CC1_{\alpha1}$ would be required to further test this hypothesis.

Additionally, our results show that the presence of $CC1_\alpha$ alters the dynamics and conformation of α_1-SUN domains (Fig. 4) suggesting that $CC1_\alpha$ may be sufficient to activate the KASH-lid and release it from its supposed auto-inhibitory state (Fig. 5). Based on these results, it is unclear whether full-length SUN2 has the ability to actually adopt an auto-inhibited conformation in the nuclear envelope. We hypothesize that the KASH-lid is free in the full-length molecule and does not adapt an auto-inhibited conformation (Fig. 8).

SUN proteins must overcome the 30-50 nm NE spacing to bind to KASH (Cain & Starr 2015). Hence, taking the anchorage of SUN2 to the INM into consideration, the hinge formed between $CC1_{\alpha1}$ and $CC1_{\alpha2}$ would position the SUN domain closer to the INM and even more inaccessible to short KASH domains at the ONM (Fig. 8B). A monomer-trimer transition could result in the straightening of the molecule and extension of SUN2 across the nuclear envelope where it meets KASH (Fig. 8) (Jahed & Mofrad 2018). Although the requirement for SUN2 trimerization is now widely accepted, the regulators of its monomer-trimer transition are not known. For example, although SUN2 trimerization is required for KASH binding, some predictions suggested that as a trimer, SUN2 proteins may be too large

to be transported through the nuclear pore (Zeinab Jahed et al. 2016). Then how would SUN2 selectively regulate its oligomerization once localized to the INM and ready to bind to KASH? Several experimental studies are required to elucidate these mechanisms, however, we propose a hypothetical model in which residue E471 is highly involved in the monomer-trimer transition of SUN2. Our analytical gel-filtration results show that E452 plays a significant role in the oligomerization of SUN2 *in vitro* (Fig. 6). These results showed that different point mutations in E452 could change the monomer-trimer ratio of CC1-CC2-SUN2 (Fig. 6). Previous crystal screening attempts of CC1-CC2-SUN2 may have been unsuccessful due to the instability of this fragment as a trimer (Fig. 6). Based on present results, CC1-CC2-SUN2_E452A can force the molecule into a monomer state, and CC1-CC2-SUN2_E452R can force the molecule into a trimer complex. It would be interesting to screen for crystals with these mutations to capture the monomer and trimer state of CC1-CC2-SUN2.
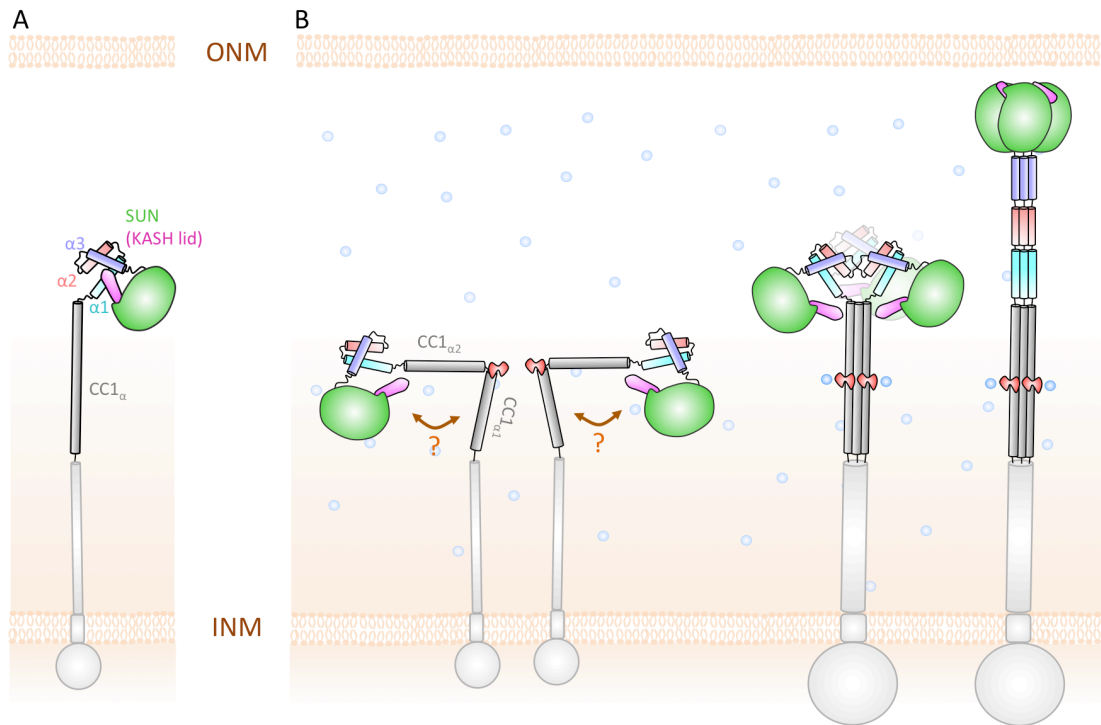
Figure 8: Hypothetical Model of SUN2 arrangement in the nuclear envelope A) Standing model of SUN2 monomer inside the nuclear envelope where the KASH-lid of SUN2 is auto-inhibited by α_1-α_3 helices, B) Our hypothetical model of SUN2 monomer in the nuclear envelope where CC1 bends at residue E452 into two separate α helices CC1$_{\alpha1}$ and CC1$_{\alpha2}$. Additionally, in this model the KASH-lid is not auto-inhibited. In this model, E452 (shown in red) is involved in the monomer-trimer transition and mediates the association of the SUN domain with the CC regions of SUN2 through Ca^{2+} binding.

Finally, how would E452 be involved in SUN2 oligomerization *in vivo*? Based on our MD results, we propose that in the NE, the interactions of Ca^{2+} with E452 of each SUN2 monomer may be a factor in the trimerization of SUN2 (Fig. 7). There is accumulating evidence that Ca^{2+} ion channels in the INM and ONM of mammalian cells can generate and maintain ion gradients in the PNS. Ca^{2+} signaling regulates several cellular processes and it

113

is plausible that it plays a role in the activation of SUN2 for KASH binding and ultimately the formation of LINC complexes (Petersen et al. 1998; Matzke et al. 2010).

Methods

Sequence Alignment.
The amino acid sequence of Mouse and Human SUN2 were obtained from Uniprot (Magrane & Consortium 2011; Consortium 2017) and aligned using The Basic Local Alignment Search Tool (BLAST) (Consortium 2017). Isoform1 of Mouse SUN2 is used for residue numbering throughout the manuscript unless otherwise stated.

Structural Models of SUN2
SUN2_M$_{483-731}$ and SUN2_M_E471A$_{483-731}$: The solved crystal structure of monomeric Mouse SUN2_M$_{483-731}$ was directly downloaded from the protein data bank (PDB: 5ed8). To develop the SUN2_M_E471A$_{483-731}$ model, a point mutation E471A was introduced to SUN2_M$_{483-731}$ using VMD mutator tool.

SUN2_M1$_{483-731}$ and SUN2_M2$_{483-731}$: We used the solved crystal structures of monomeric Mouse SUN2$_{483-731}$ (PDB: 5ed8) and one monomer of the trimeric coiled coil (CC1) of Mouse SUN2$_{420-481}$ (PDB: 5ed9) as templates to generate homology models of monomeric Mouse SUN2$_{413-731}$. Homology modeling was performed using the Phyre2 Protein Fold Recognition Server Intensive mode (Kelley et al. 2015). Phyre2 produced structural models of various conformations of monomeric Mouse SUN2$_{413-731}$ where 316 residues (98%) were modeled at >90% accuracy (Kelley et al. 2015), two of which were chosen for this study, model 1 (SUN2_M1$_{413-731}$) and model 2 (SUN2_M2$_{413-731}$). These two models were chosen because they adapt distinct conformations at the two bounds of conformations obtained with homology modeling, and showed no structural overlap with neighboring monomers when assembled into a trimer. All models produced by Phyre2 were monomeric, and so trimers of model 1 (SUN2_T1$_{413-731}$) and model 2 (SUN2_T2$_{413-731}$) were produced by manual placement of three monomers to check for overlap. Modeled structures were all visualized using VMD (http://www.ks.uiuc.edu/Research/vmd/vmd-1.9.1/, version 1.9.1) (W Humphrey et al. 1996; Phillips et al. 2005). All models were solvated in water using namd solvate package, with a 2.4 Å boundary and 20 Å box padding. The system was subsequently neutralized with counter-ions, and ionized with KCl and CaCl$_2$. Calcium concentrations in the PNS are predicted to be similar to that of the ER. However, due to several limitations in methods of measuring intra-ER Ca^{2+}, various measurements have been reported for the concentration of Ca^{2+} ranging from ~10-1000μM (Gerasimenko et al. 2014). In this study we used a concentration of 500 μM of Ca^{2+}. The final size of the four systems including the proteins, ions and water were 71K, 72K, 165K, and 225K atoms for SUN2_M$_{483-731}$, SUN2_M_E471A$_{483-731}$, SUN2_M1$_{483-731}$ and SUN2_M2$_{483-731}$, respectively.

Molecular Dynamics Simulations
All atom molecular dynamics (MD) simulations for this study were performed using NAMD scalable MD with the CHARMM force field (Phillips et al. 2005). All systems were minimized at 5000 steps and equilibrated for 2 ns with a time step of 2 fs where all linear bonds involving hydrogen and any other atoms were considered to be rigid (non-vibrating). Simulations were performed under a constant temperature of 310 K and a

constant pressure of 1 atm using the Langevin piston method and Hoover's method during minimization and equilibration. Periodic boundary conditions were applied in all three directions and particle mesh Ewald (PME) was used with a 1Å maximum space between grid points, for calculating electrostatic during MD simulations with periodic boundary conditions. All simulations were run for ~1 microsecond.

Electrostatic Interaction Energy Plots

The nonbonded electrostatic interaction energies were calculated using VMD and NAMD energy (Version 1.4) with cutoff for nonbonded interactions set to 12 Å, and using a switching function with a switching distance of 10 Å. (Phillips et al. 2005). All plots were produced using R gplot package. The correlation coefficient between the energies was calculated using the cor() function (http://www.r-tutor.com/elementary-statistics/numerical-measures/correlation-coefficient). Using this function, the correlation coefficient R_{xy} between two variables x and y, with individual standard deviations S_x and S_y, and a covariance of S_{xy} is calculated using the following formula:

$$R_{xy} = \frac{S_{xy}}{S_x S_y}$$

A correlation coefficient of 1 indicates that the variables are positively linearly related, and -1, indicates that the variables are negatively linearly related.

RMSD and RMSF Calculations

The RMSD of residues 483-731 of three structural models SUN2_M$_{483-731}$, SUN2_M1$_{413-731}$, SUN2_M2$_{413-731}$ were computed using RMSD visualizer Tool VMD. In order to eliminate the effect of rotation and translation of the molecules during the simulation, for each model we aligned all frames of the trajectory to a reference frame (frame 0) using only residues 483-731, prior to RMSD computations. Atomic RMS Fluctuations over MD trajectories, were evaluated using the rmsf() function in R Bio3D package (Grant et al. 2006). The RMSF values are often used as measures of conformational variance in MD simulations. All plots were generated using the plot() or heatmap.2() functions of R gplot package.

Protein purification and gel-filtration analysis

DNA sequences of SUN2$_{458-731}$ and SUN2$_{410-731}$ were amplified by PCR from the full-length mouse SUN2 (NM_194342) and then inserted into a modified pET32a vector (with an N-terminal GB1-His$_6$ tag). Point mutations in E452 of SUN2$_{410-731}$ were created using the standard PCR-based mutagenesis method and confirmed by DNA sequencing. Recombinant proteins were expressed in *Escherichia coli* BL21 (DE3) host cells at 16 °C. The GB1-His$_6$-tagged proteins were purified by affinity chromatography (Ni^{2+}-Sepharose 6 Fast Flow, GE Healthcare) followed by size exclusion chromatography (Superdex-200 26/60, GE Healthcare). After cleavage of the tag, the resulting proteins were further purified by another run of size-exclusion chromatography. The oligomeric states of all the protein samples were checked by analytical gel-filtration (Superdex-200 10/300GL, GE Healthcare) in the buffer (50 mM Tris-HCl, pH 8.0, 100 mM NaCl, 1 mM DTT, 1 mM EDTA).

Chapter 4

CONCLUSIONS AND FUTURE WORK

4.1 SUMMARY AND CONCLUSIONS

Both mammalian and bacterial cells are sensitive to mechanical stimulation and their fate is tied to their ability to sense and respond to physical cues of the extracellular environment. The responses of cells to mechanical cues such as topography and stiffness are very complex and involve several hundreds of proteins that cooperate to transduce mechanical signals into biochemical outputs. These cellular responses have led to the design of novel devices for biological applications such as nanowires for drug delivery, intracellular recordings, and isolation and capture of circulating tumor cells (Xie, Alexander M. Xu, et al. 2013; Chiappini et al. 2015; Shalek et al. 2012; Persson et al. 2013; Shalek et al. 2010; VanDersarl et al. 2012; Wang et al. 2014; Wang et al. 2010; Zhang et al. 2016; Nagrath et al. 2007; Xie et al. 2010). The characterization of the cell-nano interface is therefore important for tuning and optimizing nano pattered devices for the biological application of interest. In the work presented in chapters 1-2 of this thesis, we employed a combination of high-resolution electron microscopy and confocal microscopy to characterize cellular responses to 3D vertical nanopillars of various shape, size and arrangements. We showed that all these factors influence the adhesion characteristics of cells on nanopillars.

At the molecular scale, signals are transmitted to the cytoskeleton through integrin-mediated focal adhesions. A percentage of these adhesions are directly linked to the nucleus through bundles of actin filaments and LINC complexes rendering them a likely and important candidate for cell mechanotransduction. Moreover recent studies suggest that mechanotrandsuction on stiff substrates is dominated by focal adhesions that are directly linked to the nucleus (Dong-Hwee Kim et al. 2012). Although the molecular mechanisms of mechanosensing and force transmission across the cell plasma membrane at the sites of cell adhesion have been extensively studied, the mechanisms of mechanotransduction at the nuclear envelope (NE) are largely unknown. The work presented in chapter 3 of this thesis provides insights into the molecular mechanisms of force transmission across the NE through LINC complexes. Using molecular dynamics simulations, we showed that the LINC complex is highly stable under tensile forces and forces on KASH proteins are transmitted to the coiled coil regions of SUN proteins. Furthermore we discussed mechanisms by which SUN protein SUN1 but not SUN2 may form higher order oligomers in the NE of living cells. Finally, we showed that the coiled coil regions of SUN2 can alter the dynamics and conformation of the conserved SUN2 SUN domains, suggesting that the coiled coils may be sufficient to activate the KASH-lid and release it from its supposed auto-inhibitory state.

In combination with recent crystallographic data on the LINC complex, the work presented in this thesis provides key insights into the molecular mechanisms of LINC complex function. However, there remain several questions on the molecular mechanisms of mechanotransduction at the NE, which are discussed in the next section.

4.2 OUTLOOK AND FUTURE WORK

Although our understanding of the role of LINC complexes in the mechanical integrity of the NE has significantly increased in the past decade, several questions remain unanswered. Firstly, it is unknown whether KASH proteins are able to oligomerize like SUN proteins, and if so, how this would influence the magnitude and direction of forces on the NE. Currently, no crystallographic data is available on the structure of cytoplasmic domains of nesprins or other KASH proteins. Such information would greatly enhance our understanding of the structural features of these proteins and their response to mechanical forces. Additionally, no crystallographic data is available on the nucleoplasmic domains of SUN protein where they interact with A-type lamins and chromatin. Unraveling atomic level details of the nucleoplasmic domains of SUN proteins, and the nature of their interaction with the nucleoskeleton, will help better understand how forces may be transmitted to nuclear contents, specially chromatin, and how this may ultimately modulate gene expression(Uhler & Shivashankar 2017; Isermann & Lammerding 2013).

Moreover, the structural data on SUN proteins is limited to the most widely expressed mammalian SUN protein, SUN2. The crystal structures of other mammalian SUN proteins such as SUN1 and SUN3-5 are yet to be solved. Particularly interesting are SUN3-5 which contain much shorter CC regions than SUN1-2 proteins and it is unclear how these shorter proteins are able to overcome the NE spacing and reach across the NE to bind to KASH (Sosa et al. 2013; Cain & Starr 2015; Zeinab Jahed et al. 2016).

Another remaining question that requires further investigation is how forces are transmitted across the nuclear membranes. In Chapter 3.2 we proposed a model in which cytoskeletal forces in all directions on KASH proteins are transferred as tensile forces across the ONM due to the anchorage of these protein at the nuclear membranes. This would need to be investigated further

Finally, most of the current information on the structure and higher order assembly mechanism of LINC complex are based on *in vitro* data. Recent developments of *in vivo* techniques allowing the imaging and quantification of protein-protein interactions inside the NE of living cells promise new developments on the LINC complex assembly at the NE (J. Hennen et al. 2017; Jorgens et al. 2016).

In the next section, we propose future directions and techniques that can be used to gain insights into the abovementioned unknowns of the molecular mechanisms of LINC complex function.

Mathematical models of the nuclear envelope

The mechanical boundary conditions on SUN and KASH, i.e. anchorage to the INM and ONM, undoubtedly affect their structures, mobility, interactions with other proteins, and force transmission to the nucleus. It is important to note that the small-scale mechanics of the lipid bilayers at the INM and ONM, and their ability to rupture, largely influences the forces experienced by and transmitted across the transmembrane domains of SUN and KASH proteins. Limited studies have addressed this topic; however, recent advances in experimental and computational biophysical approaches to study cell membranes (Chabanon et al. 2017) will allow researchers to better characterize local membrane

responses to mechanical force. Computational mathematical models have previously been used to overcome challenges posed by small-scale biological experiments scale (Jamali et al. 2010). Such models can be used to represent components of the NE as elastic or viscoelastic elements (Fig. 1). The mechanical integrity of the NE can then be compared in the presence (Fig.1 A) and absence (Fig.1 B) of nucleo-cytoskeletal coupling through LINC complexes.
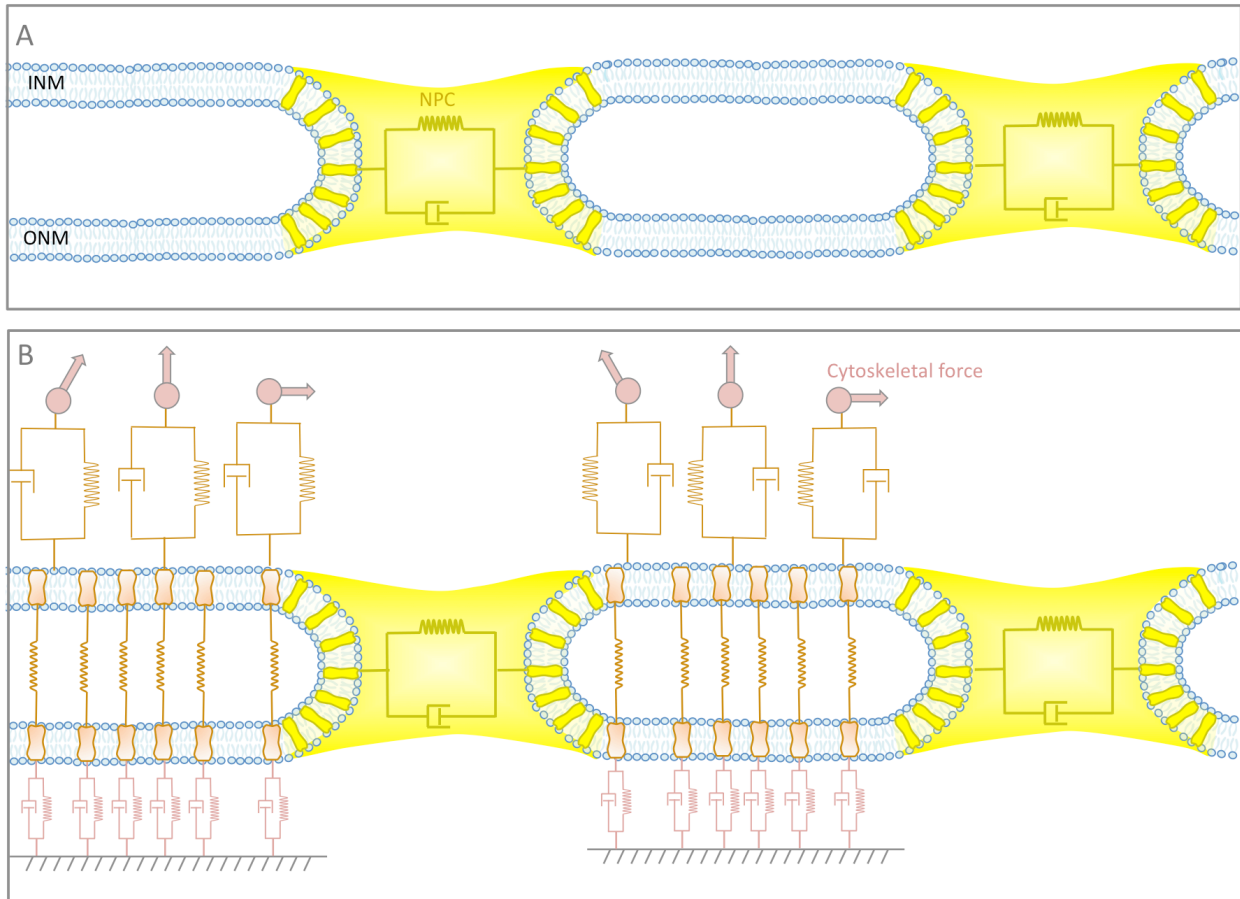
Figure 1: Simplistic mechanical model of the nuclear envelope (NE) A) Model of the NE before LINC complex formation. Several components of the NPC (shown in yellow) insert into the nuclear membranes to fuse the INM and ONM at site of NPC insertion. The pore of the NPC has been suggested to acquire viscoelastic properties by the interactions of disordered nucleoporins (FG Nups) that are anchored to the nuclear membrane (B) Mechanical model of the NE after the nucleoskeleton and cytoskeleton are linked through LINC complexes. SUN domain proteins with long coiled coils are shown as elastic springs that span the NE and are anchored to the INM trough their transmembrane domain, and to the ONM through KASH proteins. Cytoplasmic domains of KASH proteins are represented with a viscoelastic mechanical model. These domains experience cytoskeletal forces in all directions, as KASH proteins associate with actin, microtubules and intermediate filaments in the cytoplasm as discussed in Chapter 3.

Determining the link between SUN protein length and function

The current model describing SUN-KASH interactions in the NE can only explain the KASH binding of two widely expressed proteins SUN1 and SUN2. This model suggests that a short KASH peptide at the ONM binds to the conserved SUN domain of SUN proteins (Fig 2). However, only SUN1 and SUN2 contain large enough coiled coil domains to span the length of the NE, whereas SUN3-5 contain much shorter coiled coil regions and would therefore be

unable to overcome the NE spacing and reach across the NE to bind to KASH with the current model (Sosa et al. 2013; Cain & Starr 2015; Zeinab Jahed et al. 2016).

There is no evidence that the distance between the ONM and INM varies by cell type, or region. However, it is one plausible explanation for the formation of LINC complex that contain shorter SUN proteins such as SUN3-5 (Sosa et al. 2013; Z. Jahed et al. 2016). Careful inspection of electron microscopy images of the NE of cell populations may provide more information on the NE spacing in various regions of cells and across various cell types.
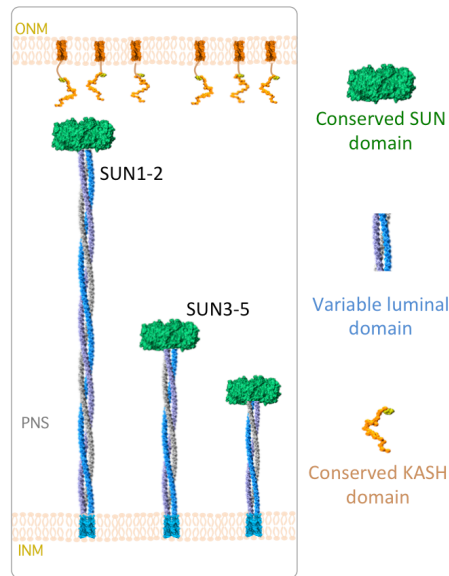
Figure 2: Standing Model of SUN-KASH interaction in the nuclear envelope. SUN1 and SUN2 contain long coiled coil domains that would span the space between the INM and ONM, while SUN3-5 contain shorter coiled coil domains and would not reach across the nuclear envelope in the current model.

Determining the *in vivo* conformation of the LINC complex

Current models of the regulation and conformational dynamics of LINC complex proteins are mostly based on in vitro crystallographic data. Recently Arsenovic et al. used a Fluorescence resonance energy transfer (FRET)-based biosensor to determine the forces on LINC complex proteins inside the NE (Arsenovic et al. 2016). The design of similar FRET-based tension sensors inserted into various regions of SUN proteins will allow a better determination on the stress state of SUN proteins in the nuclear envelope and further elucidate the molecular mechanisms of force transmission across the nuclear envelope. Additionally, the activation mechanisms of LINC complex proteins can be obtained by inserting FRET probes in various regions of SUN proteins (Fig 4.). We propose the insertion of FRET donor and accepter pairs at locations shown in Fig 4 (proceeding the CC1 region, and preceding the KASH lid) to test the two proposed conformational states of SUN proteins *in vivo*. One challenge with FRET sensor design on SUN proteins is

distinguishing changes in FRET due to protein oligomerization from changes due to conformational changes of the monomer.
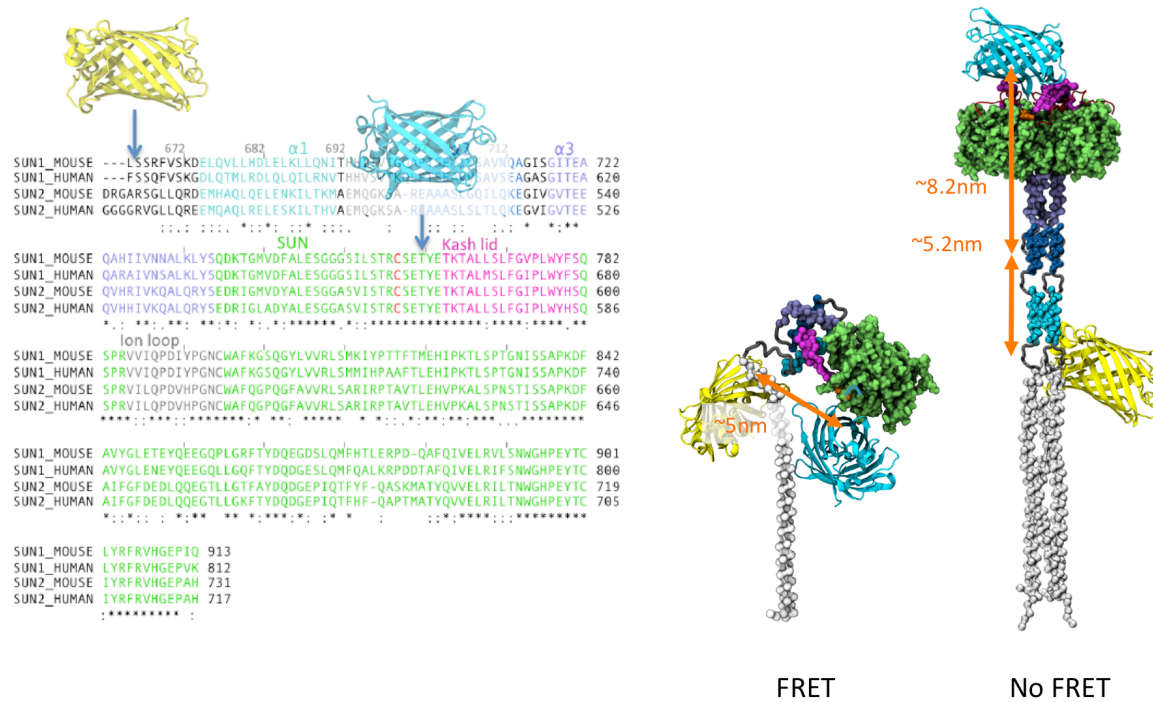
Figure 3: Fluorescent resonance energy transfer (FRET) probes for determining activation mechanisms of LINC complex in the nuclear envelope.

Final remarks

I was introduced to the molecular world of cellular biomechanics in 2013 when I joined Prof. Mofrad's Molecular Cell Biomechanics lab at UC Berkeley. The depth of knowledge that has been obtained in this field in the past few decades has amazed me throughout my PhD. On the other hand, I am flabbergasted by all that we yet do not understand about basic functions of these fundamental units of life. One way of describing the sophistication of cells is by viewing cells as machines based on an idea proposed by Prof. Michael Sheets, a leader in the field of cellular mechanotransduction. He proposes that Darwinian evolution could be compared to the evolution of automobiles. Automobiles have evolved over only a hundred years to contain thousands of parts and features that perform very specific functions, each incrementally improving the overall function of an automobile. For example, if we look at 2018 Mercedes-Benz models, every small detail that goes into the overall shape on its surface makes it more fuel efficient, faster, and maybe merely more aesthetically pleasing than older models, allowing it to survive in the automobile market. On the other hand, cells have evolved over billions of years to reach their level of sophistication and are thereby billions of times more complex than automobiles. It is therefore not surprising that we still know so little. With all the exciting new technologies developed in the past decade from tools to sequence and genetically engineering cells, to computational tools developed to store and analyze increasingly large data sets, there is great promise that we can unravel this complex unit of life.

REFERENCES

Aalipour, A. et al., 2014. Plasma membrane and actin cytoskeleton as synergistic barriers to nanowire cell penetration. *Langmuir : the ACS journal of surfaces and colloids*, 30(41), pp.12362–12367.

Agudelo-Garcia, P. a et al., 2011. Glioma cell migration on three-dimensional nanofiber scaffolds is regulated by substrate topography and abolished by inhibition of STAT3 signaling. *Neoplasia (New York, N.Y.)*, 13(9), pp.831–40. Available at: http://www.pubmedcentral.nih.gov/articlerender.fcgi?artid=3182275&tool=pmcentrez&rendertype=abstract.

Al-Haboubi, T. et al., 2011. Distinct association of the nuclear pore protein Nup153 with A- and B-type lamins. *Nucleus (Austin, Tex.)*, 2(5), pp.500–9. Available at: http://www.tandfonline.com/doi/abs/10.4161/nucl.2.5.17913#.Vgs5zH0RMg4 [Accessed September 25, 2015].

Albuschies, J. & Vogel, V., 2013. The role of filopodia in the recognition of nanotopographies. *Scientific reports*, 3, p.1658. Available at: http://www.pubmedcentral.nih.gov/articlerender.fcgi?artid=3625890&tool=pmcentrez&rendertype=abstract [Accessed December 18, 2013].

Alvarez-Fernández, M. & Malumbres, M., 2014. Preparing a cell for nuclear envelope breakdown: Spatio-temporal control of phosphorylation during mitotic entry. *BioEssays : news and reviews in molecular, cellular and developmental biology*, 36(8), pp.757–65. Available at: http://www.ncbi.nlm.nih.gov/pubmed/24889070 [Accessed October 30, 2015].

Ando, D. et al., 2013. Physical motif clustering within intrinsically disordered nucleoporin sequences reveals universal functional features. *PloS one*, 8(9), p.e73831. Available at: http://journals.plos.org/plosone/article?id=10.1371/journal.pone.0073831 [Accessed March 6, 2016].

Anon, 1995. The Product of the Spindle Formation Gene sadl + Associates with the Fission Yeast Spindle Pole Body and Is Essential for Viability. , 129(4), pp.1033–1047.

Arenas, M. a et al., 2013. Doped TiO2 anodic layers of enhanced antibacterial properties. *Colloids and surfaces. B, Biointerfaces*, 105, pp.106–12. Available at: http://www.ncbi.nlm.nih.gov/pubmed/23357736 [Accessed December 24, 2013].

Arsenovic, P.T. et al., 2016. Nesprin-2G, a Component of the Nuclear LINC Complex, Is Subject to Myosin-Dependent Tension. *Biophysical Journal*, 110(1), pp.34–43.

Avizienyte, E. & Frame, M.C., 2005. Src and FAK signalling controls adhesion fate and the epithelial-to-mesenchymal transition. *Current opinion in cell biology*, 17(5), pp.542–7. Available at: http://www.ncbi.nlm.nih.gov/pubmed/16099634 [Accessed December 11, 2014].

Barros, E.P. et al., 2017. Electrostatic Interactions as Mediators in the Allosteric Activation of Protein Kinase A RI?? *Biochemistry*, 56(10), pp.1536–1545.

Barth, E. et al., 1989. In vitro and in viva comparative colonization of Staphylococcus aureus and Staphylococcus epidermidis on orthopaedic orthopaedic implant materials.

Biomaterials, 10, pp.325–328.

Bassler, B.L. & Losick, R., 2006. Bacterially Speaking. *Cell*, 125(2), pp.237–246.

Bellail, A.C. et al., 2004. Microregional extracellular matrix heterogeneity in brain modulates glioma cell invasion. *International Journal of Biochemistry and Cell Biology*, 36(6), pp.1046–1069.

Beningo, K.A. et al., 2001. Nascent focal adhesions are responsible for the generation of strong propulsive forces in migrating fibroblasts. *The Journal of cell biology*, 153(4), pp.881–8. Available at: http://www.pubmedcentral.nih.gov/articlerender.fcgi?artid=2192381&tool=pmcentr ez&rendertype=abstract.

Berthing, T. et al., 2012. Cell membrane conformation at vertical nanowire array interface revealed by fluorescence imaging. *Nanotechnology*, 23(41), p.415102. Available at: http://www.ncbi.nlm.nih.gov/pubmed/23010859 [Accessed December 19, 2013].

Biasini, M. et al., 2014. SWISS-MODEL: Modelling protein tertiary and quaternary structure using evolutionary information. *Nucleic Acids Research*, 42(W1), pp.252–258.

Boedicker, J.Q., Vincent, M.E. & Ismagilov, R.F., 2009. Microfluidic confinement of single cells of bacteria in small volumes initiates high-density behavior of quorum sensing and growth and reveals its variability. *Angewandte Chemie - International Edition*, 48(32), pp.5908–5911.

Bolhy, S. et al., 2011. A Nup133-dependent NPC-anchored network tethers centrosomes to the nuclear envelope in prophase. *The Journal of cell biology*, 192(5), pp.855–71. Available at: http://jcb.rupress.org/content/192/5/855.short [Accessed July 29, 2015].

Bone, C.R. et al., 2014. The Caenorhabditis elegans SUN protein UNC-84 interacts with lamin to transfer forces from the cytoplasm to the nucleoskeleton during nuclear migration. *Molecular Biology of the Cell*, 25(18), pp.2853–2865. Available at: http://www.molbiolcell.org/cgi/doi/10.1091/mbc.E14-05-0971.

Bornschlögl, T. et al., 2013. Filopodial retraction force is generated by cortical actin dynamics and controlled by reversible tethering at the tip. *Proceedings of the National Academy of Sciences of the United States of America*, 110(47), pp.18928–33. Available at: http://www.ncbi.nlm.nih.gov/pubmed/24198333 [Accessed December 11, 2013].

Braunagel, S.C. et al., 2007. Early sorting of inner nuclear membrane proteins is conserved. *Proceedings of the National Academy of Sciences of the United States of America*, 104(22), pp.9307–12. Available at: http://www.pubmedcentral.nih.gov/articlerender.fcgi?artid=1874229&tool=pmcentr ez&rendertype=abstract [Accessed February 25, 2016].

Burek, M.J. & Greer, J.R., 2010. Fabrication and microstructure control of nanoscale mechanical testing specimens via electron beam lithography and electroplating. *Nano letters*, 10(1), pp.69–76. Available at: http://www.ncbi.nlm.nih.gov/pubmed/19961184 [Accessed December 30, 2013].

Cain, N.E. et al., 2014. The SUN protein UNC-84 is required only in force-bearing cells to

maintain nuclear envelope architecture. *The Journal of cell biology*, 206(2), pp.163–72. Available at: http://www.ncbi.nlm.nih.gov/pubmed/25023515 [Accessed October 12, 2014].

Cain, N.E. & Starr, D.A., 2015. SUN proteins and nuclear envelope spacing. *Nucleus*, 6(1), pp.2–7. Available at: http://www.tandfonline.com/doi/full/10.4161/19491034.2014.990857.

Campoccia, D. et al., 2008. Molecular epidemiology of Staphylococcus aureus from implant orthopaedic infections: ribotypes, agr polymorphism, leukocidal toxins and antibiotic resistance. *Biomaterials*, 29(30), pp.4108–16. Available at: http://www.ncbi.nlm.nih.gov/pubmed/18676012 [Accessed December 24, 2013].

Cassie, B.D. & Baxter, S., 1944. wettability of porous surfaces,. *Transactions of the Faraday Society*, 40(5), pp.546–551.

Chabanon, M., Stachowiak, J.C. & Rangamani, P., 2017. Systems biology of cellular membranes: a convergence with biophysics. *Wiley Interdisciplinary Reviews: Systems Biology and Medicine*, 9(5), pp.20–22.

Chambliss, A.B. et al., 2013. The LINC-anchored actin cap connects the extracellular milieu to the nucleus for ultrafast mechanotransduction. *Scientific reports*, 3, p.1087. Available at: http://www.pubmedcentral.nih.gov/articlerender.fcgi?artid=3548190&tool=pmcentr ez&rendertype=abstract [Accessed May 28, 2014].

Chang, W., Worman, H.J. & Gundersen, G.G., 2015. Accessorizing and anchoring the LINC complex for multifunctionality. *The Journal of Cell Biology*, 208(1), pp.11–22.

Charlot, B. et al., 2014. Elongated unique DNA strand deposition on microstructured substrate by receding meniscus assembly and capillary force. *Biomicrofluidics*, 8(1), p.14103. Available at: http://www.pubmedcentral.nih.gov/articlerender.fcgi?artid=3977786&tool=pmcentr ez&rendertype=abstract.

Chen, J. et al., 2014. The SUN protein Mps3 controls Ndc1 distribution and function on the nuclear membrane. *The Journal of Cell Biology*, 204(4), pp.523–539. Available at: http://www.jcb.org/cgi/doi/10.1083/jcb.201307043.

Chiappini, C. et al., 2015. Biodegradable nanoneedles for localized delivery of nanoparticles in vivo: Exploring the biointerface. *ACS Nano*, 9(5), pp.5500–5509.

Chiu, H.-C. et al., 2012. Development of novel antibacterial agents against methicillin-resistant Staphylococcus aureus. *Bioorganic & medicinal chemistry*, 20(15), pp.4653–60. Available at: http://www.pubmedcentral.nih.gov/articlerender.fcgi?artid=3401364&tool=pmcentr ez&rendertype=abstract [Accessed December 24, 2013].

Chiura, H.X. et al., 2011. Evidence for particle-induced horizontal gene transfer and serial transduction between bacteria. *FEMS Microbiology Ecology*, 76(3), pp.576–591.

Chug, H. et al., 2015. Crystal structure of the metazoan Nup62•Nup58•Nup54 nucleoporin complex. *Science (New York, N.Y.)*, 350(6256), pp.106–10. Available at:

http://science.sciencemag.org/content/350/6256/106.abstract [Accessed February 12, 2016].

Consortium, T.U., 2017. UniProt : the universal protein knowledgebase. , 45(November 2016), pp.158–169.

Cordero, J., Munuera, L. & Folgueira, M.D., 1994. Influence of metal implants on infection. *J. Bone Jt. Surg. [British]*, 76(5).

Cosgrove, S. et al., 2003. Comparison of Mortality Associated with Methicillin Resistant and Methicillin Susceptible Staphylococcus aureus Bacteremia: A Meta-analysis. *Clinical Infectious Diseases*, 36(1), pp.53–59. Available at: http://www.journals.uchicago.edu/doi/abs/10.1086/345476.

Cox, C.D., Bavi, N. & Martinac, B., 2018. Bacterial Mechanosensors. *Annual Review of Physiology*, 80(1), p.17.1-17.23. Available at: http://www.ncbi.nlm.nih.gov/pubmed/29195054%0Ahttp://www.annualreviews.org/doi/10.1146/annurev-physiol-021317-121351.

Crisp, M. et al., 2006a. Coupling of the nucleus and cytoplasm: role of the LINC complex. *The Journal of cell biology*, 172(1), pp.41–53. Available at: http://jcb.rupress.org/content/172/1/41.abstract [Accessed September 1, 2015].

Crisp, M. et al., 2006b. Coupling of the nucleus and cytoplasm: role of the LINC complex. *The Journal of cell biology*, 172(1), pp.41–53. Available at: http://jcb.rupress.org/content/172/1/41 [Accessed September 1, 2015].

Crisp, M. et al., 2006c. Coupling of the nucleus and cytoplasm: role of the LINC complex. *The Journal of cell biology*, 172(1), pp.41–53. Available at: http://www.pubmedcentral.nih.gov/articlerender.fcgi?artid=2063530&tool=pmcentr ez&rendertype=abstract [Accessed August 22, 2014].

D'Angelo, M. a et al., 2006. Supp Data: Nuclear pores form de novo from both sides of the nuclear envelope. *Science (New York, N.Y.)*, 312(5772), pp.440–443.

Dalby, M.J., Gadegaard, N., et al., 2004. Investigating filopodia sensing using arrays of defined nano-pits down to 35 nm diameter in size. *The international journal of biochemistry & cell biology*, 36(10), pp.2005–15. Available at: http://www.ncbi.nlm.nih.gov/pubmed/15203114 [Accessed December 18, 2013].

Dalby, M.J., 2005. Topographically induced direct cell mechanotransduction. *Medical Engineering and Physics*, 27(9), pp.730–742.

Dalby, M.J., Riehle, M.O., et al., 2004. Use of nanotopography to study mechanotransduction in fibroblasts--methods and perspectives. *European journal of cell biology*, 83(4), pp.159–169.

Daryabeigi, A. et al., 2016. Nuclear Envelope Retention of LINC Complexes Is Promoted by SUN-1 Oligomerization in the Caenorhabditis elegans Germ Line. *Genetics*. Available at: http://www.ncbi.nlm.nih.gov/pubmed/27098914.

Denais, C.M. et al., 2016. Nuclear envelope rupture and repair during cancer cell migration. , 7297(March), pp.1–9.

Dey, M. et al., 2007. Conserved intermolecular salt bridge required for activation of protein

kinases PKR, GCN2, and PERK. *Journal of Biological Chemistry*, 282(9), pp.6653–6660.

Díaz, C. et al., 2009. Submicron trenches reduce the Pseudomonas fluorescens colonization rate on solid surfaces. *ACS Applied Materials and Interfaces*, 1(1), pp.136–143.

Ding, X. et al., 2007. SUN1 Is Required for Telomere Attachment to Nuclear Envelope and Gametogenesis in Mice. , (June), pp.863–872.

Duong, N.T. et al., 2014. Nesprins : Tissue-Specific Expression of Epsilon and Other Short Isoforms. , 9(4).

English, A.R. & Voeltz, G.K., 2013. Endoplasmic reticulum structure and interconnections with other organelles. *Cold Spring Harbor Perspectives in Biology*, 5(4), pp.1–16.

Epstein, a K. et al., 2011. Control of bacterial biofilm growth on surfaces by nanostructural mechanics and geometry. *Nanotechnology*, 22(49), p.494007. Available at: http://iopscience.iop.org/0957-4484/22/49/494007.

Fan, J. & Beck, K. a, 2004a. A role for the spectrin superfamily member Syne-1 and kinesin II in cytokinesis. *Journal of cell science*, 117(Pt 4), pp.619–29. Available at: http://www.ncbi.nlm.nih.gov/pubmed/14709720.

Fan, J. & Beck, K. a, 2004b. A role for the spectrin superfamily member Syne-1 and kinesin II in cytokinesis. *Journal of cell science*, 117(Pt 4), pp.619–29.

Feldherr, C.M., 1990. The permeability of the nuclear envelope in dividing and nondividing cell cultures. *The Journal of Cell Biology*, 111(1), pp.1–8. Available at: http://jcb.rupress.org/content/111/1/1.abstract?ijkey=ea8b9ec70e68a8ce53d18493 7161be1a832f1ef6&keytype2=tf_ipsecsha [Accessed October 31, 2015].

Feng, S. et al., 2009. Confinement regulates complex biochemical networks: Initiation of blood clotting by "diffusion acting." *Biophysical Journal*, 97(8), pp.2137–2145. Available at: http://dx.doi.org/10.1016/j.bpj.2009.08.004.

Ferrari, A. et al., 2010. Neuronal polarity selection by topography-induced focal adhesion control. *Biomaterials*, 31(17), pp.4682–4694. Available at: http://dx.doi.org/10.1016/j.biomaterials.2010.02.032.

Fiserova, J. & Goldberg, M.W., 2010. Relationships at the nuclear envelope: lamins and nuclear pore complexes in animals and plants. *Biochemical Society transactions*, 38(3), pp.829–831.

Folker, E.S. & Baylies, M.K., 2013. Nuclear positioning in muscle development and disease. *Frontiers in physiology*, 4(December), p.363. Available at: http://www.pubmedcentral.nih.gov/articlerender.fcgi?artid=3859928&tool=pmcentr ez&rendertype=abstract [Accessed October 17, 2014].

Foster, T.J. et al., 2014. Adhesion, invasion and evasion: the many functions of the surface proteins of _Staphylococcus aureus_. *Nat.Rev.Microbiol.*, 12(1740–1534 (Electronic)), pp.49–62. Available at: http://dx.doi.org/10.1038/nrmicro3161.

Fozdar, D.Y. et al., 2011. Selective axonal growth of embryonic hippocampal neurons according to topographic features of various sizes and shapes. *International Journal of Nanomedicine*, 6(1), pp.45–57.

Francois, P. et al., 2000. Identification of plasma proteins adsorbed on hemodialysis tubing that promote Staphylococcus aureus adhesion. *The Journal of laboratory and clinical medicine*, 135(1), pp.32–42. Available at: http://www.ncbi.nlm.nih.gov/pubmed/10638692.

Frohnert, C., Schweizer, S. & Hoyer-fender, S., 2011. SPAG4L / SPAG4L-2 are testis-specific SUN domain proteins restricted to the apical nuclear envelope of round spermatids facing the acrosome. , 17(4), pp.207–218.

Gardner, J.M. et al., 2011. Targeting of the SUN protein Mps3 to the inner nuclear membrane by the histone variant H2A.Z. *Journal of Cell Biology*, 193(3), pp.489–507.

Garrett, T.R., Bhakoo, M. & Zhang, Z., 2008. Bacterial adhesion and biofilms on surfaces. *Progress in Natural Science*, 18(9), pp.1049–1056.

Gasteiger E., Hoogland C., Gattiker A., Duvaud S., Wilkins M.R., Appel R.D., B.A., 2005. Protein Identification and Analysis Tools on the ExPASy Server. , pp.571–607. Available at: http://web.expasy.org/protparam.

Gavet, O. & Pines, J., 2010. Activation of cyclin B1-Cdk1 synchronizes events in the nucleus and the cytoplasm at mitosis. *The Journal of cell biology*, 189(2), pp.247–59. Available at: http://jcb.rupress.org/content/189/2/247.short [Accessed October 30, 2015].

Gerasimenko, J. V., Petersen, O.H. & Gerasimenko, O. V., 2014. Monitoring of intra-ER free Ca2+. *Wiley Interdisciplinary Reviews: Membrane Transport and Signaling*, 3(3), pp.63–71.

Ghavami, A. et al., 2014. Probing the disordered domain of the nuclear pore complex through coarse-grained molecular dynamics simulations. *Biophysical journal*, 107(6), pp.1393–402. Available at: http://www.ncbi.nlm.nih.gov/pubmed/25229147.

Gittens, R.A. et al., 2012. Differential Responses of Osteoblast Lineage Cells to Nanotopographically-Modified, Microroughened Titanium- Aluminum-Vanadium Alloy Surfaces. *Biomaterials*, 33(35), pp.8986–8994.

Glazer, P.J. et al., 2014. Generating aligned micellar nanowire arrays by dewetting of micropatterned surfaces. *Small*, 10(9), pp.1729–1734.

Göb, E. et al., 2010. Mammalian sperm head formation involves different polarization of two novel LINC complexes. *PloS one*, 5(8), p.e12072. Available at: http://www.pubmedcentral.nih.gov/articlerender.fcgi?artid=2919408&tool=pmcentrez&rendertype=abstract [Accessed May 31, 2013].

Gomes, E.R., Jani, S. & Gundersen, G.G., 2005. Nuclear movement regulated by Cdc42, MRCK, myosin, and actin flow establishes MTOC polarization in migrating cells. *Cell*, 121(3), pp.451–63.

Gomez, N., Lu, Y., et al., 2007. Immobilized nerve growth factor and microtopography have distinct effects on polarization versus axon elongation in hippocampal cells in culture. *Biomaterials*, 28(2), pp.271–284.

Gomez, N., Lee, J.Y., et al., 2007. Micropatterned polypyrrole: A combination of electrical and topographical characteristics for the stimulation of cells. *Advanced Functional Materials*, 17(10), pp.1645–1653.

Gomez, N., Chen, S. & Schmidt, C.E., 2007. Polarization of hippocampal neurons with competitive surface stimuli: contact guidance cues are preferred over chemical ligands. *Journal of the Royal Society, Interface / the Royal Society*, 4(13), pp.223–233.

Grant, B.J. et al., 2006. Bio3d: An R package for the comparative analysis of protein structures. *Bioinformatics*, 22(21), pp.2695–2696.

Graumann, K., Runions, J. & Evans, D.E., 2010. Characterization of SUN-domain proteins at the higher plant nuclear envelope. *Plant Journal*, 61(1), pp.134–144.

Gristina, a G. et al., 1987. Adhesive colonization of biomaterials and antibiotic resistance. *Biomaterials*, 8(6), pp.423–6. Available at: http://www.ncbi.nlm.nih.gov/pubmed/3427140.

Grossman, E., Medalia, O. & Zwerger, M., 2012. Functional architecture of the nuclear pore complex. *Annual review of biophysics*, 41, pp.557–84. Available at: http://www.annualreviews.org/doi/abs/10.1146/annurev-biophys-050511-102328 [Accessed February 4, 2016].

Grygorczyk, C. & Grygorczyk, R., 1998. A Ca 2 ‡ - and voltage-dependent cation channel in the nuclear envelope of red beet. , 1375, pp.117–130.

Guan, J. & Lee, L.J., 2005. Generating highly ordered DNA nanostrand arrays. *Proceedings of the National Academy of Sciences of the United States of America*, 102(51), pp.18321–18325.

Guan, J., Yu, B. & Lee, L.J., 2007. Forming highly ordered arrays of functionalized polymer nanowires by dewetting on micropillars. *Advanced Materials*, 19(9), pp.1212–1217.

Guilluy, C. et al., 2014. Isolated nuclei adapt to force and reveal a mechanotransduction pathway in the nucleus. *Nature cell biology*, (August 2013). Available at: http://www.ncbi.nlm.nih.gov/pubmed/24609268 [Accessed March 19, 2014].

Gundersen, G.G. & Worman, H.J., 2013. Nuclear positioning. *Cell*, 152(6), pp.1376–89. Available at: http://www.pubmedcentral.nih.gov/articlerender.fcgi?artid=3626264&tool=pmcentrez&rendertype=abstract [Accessed March 20, 2014].

Guo, Y. & Zheng, Y., 2015. Lamins position the nuclear pores and centrosomes by modulating dynein. *Molecular biology of the cell*, p.mbc.E15-07-0482-. Available at: http://www.molbiolcell.org/content/early/2015/08/02/mbc.E15-07-0482.abstract [Accessed August 18, 2015].

Güttinger, S., Laurell, E. & Kutay, U., 2009. Orchestrating nuclear envelope disassembly and reassembly during mitosis. *Nature Reviews Molecular Cell Biology*, 10(3), pp.178–191. Available at: http://www.nature.com/doifinder/10.1038/nrm2641.

Hai, A., Shappir, J. & Spira, M.E., 2010. In-cell recordings by extracellular microelectrodes. *Nature Methods*, 7(3), pp.200–202. Available at: http://www.nature.com/doifinder/10.1038/nmeth.1420 [Accessed December 19, 2013].

Hale, C.M. et al., 2008. Dysfunctional connections between the nucleus and the actin and microtubule networks in laminopathic models. *Biophysical journal*, 95(11), pp.5462–

5475. Available at: http://dx.doi.org/10.1529/biophysj.108.139428.

Hansen, R.H. et al., 2016. Stochastic Assembly of Bacteria in Microwell Arrays Reveals the Importance of Confinement in Community Development. *Plos One*, 11(5), p.e0155080. Available at: http://dx.plos.org/10.1371/journal.pone.0155080.

Hanson, L. et al., 2012. Characterization of the cell-nanopillar interface by transmission electron microscopy. *Nano letters*, 12(11), pp.5815–20. Available at: http://www.ncbi.nlm.nih.gov/pubmed/23030066.

Haque, F. et al., 2010. Mammalian SUN protein interaction networks at the inner nuclear membrane and their role in laminopathy disease processes. *The Journal of biological chemistry*, 285(5), pp.3487–98. Available at: http://www.pubmedcentral.nih.gov/articlerender.fcgi?artid=2823409&tool=pmcentrez&rendertype=abstract [Accessed September 18, 2014].

Haque, F. et al., 2006. SUN1 Interacts with Nuclear Lamin A and Cytoplasmic Nesprins To Provide a Physical Connection between the Nuclear Lamina and the Cytoskeleton. *Molecular and cellular biology*, 26(10), pp.3738–3751.

Haque, F. et al., 2006. SUN1 Interacts with Nuclear Lamin A and Cytoplasmic Nesprins To Provide a Physical Connection between the Nuclear Lamina and the Cytoskeleton. *Molecular and Cellular Biology*, 26(10), pp.3738–3751. Available at: http://mcb.asm.org/content/26/10/3738.abstract [Accessed October 19, 2015].

Harris, L.G. et al., 2007. Staphylococcus aureus adhesion to standard micro-rough and electropolished implant materials. *Journal of materials science. Materials in medicine*, 18(6), pp.1151–6. Available at: http://www.ncbi.nlm.nih.gov/pubmed/17268867 [Accessed November 14, 2013].

Harris, L.G., Foster, S.J. & Richards, R.G., 2002. An introduction to Staphylococcus aureus, and techniques for identifying and quantifying S. aureus adhesins in relation to adhesion to biomaterials: review. *European cells & materials*, 4, pp.39–60. Available at: http://www.ncbi.nlm.nih.gov/pubmed/14562246.

Hasan, S. et al., 2006. Nuclear envelope localization of human UNC84A does not require nuclear lamins. *FEBS Letters*, 580(5), pp.1263–1268.

Hatch, E.M. & Hetzer, M.W., 2016. Nuclear envelope rupture is induced by actin-based nucleus confinement. *JCB*.

Hennen, J. et al., 2017. Article Quantitative Brightness Analysis of Protein Oligomerization in the Nuclear Envelope. *Biophysj*, 113(1), pp.138–147. Available at: http://dx.doi.org/10.1016/j.bpj.2017.05.044.

Hennen, J. et al., Fluorescence Fluctuation Spectroscopy Reveals Differential SUN Protein Oligomerization In Living Cells. *Molecular Biology of the Cell*, (Under revision).

Hennen, J. et al., 2017. Quantitative brightness analysis of protein oligomerization in the nuclear envelope. *Mol Biol Cell.*

Ho, C.Y. & Lammerding, J., 2012. Lamins at a glance. *Journal of cell science*, 125(Pt 9), pp.2087–93. Available at: http://jcs.biologists.org/content/125/9/2087.short [Accessed January 15, 2016].

Hochbaum, A.I. & Aizenberg, J., 2010. Bacteria pattern spontaneously on periodic nanostructure arrays. *Nano Letters*, 10(9), pp.3717–3721.

Hoelzle, M.K. & Svitkina, T., 2012. The cytoskeletal mechanisms of cell-cell junction formation in endothelial cells. *Molecular biology of the cell*, 23(2), pp.310–23. Available at: http://www.pubmedcentral.nih.gov/articlerender.fcgi?artid=3258175&tool=pmcentr ez&rendertype=abstract [Accessed December 19, 2013].

Holden, M.T.G. et al., 2004. Complete genomes of two clinical Staphylococcus aureus strains: evidence for the rapid evolution of virulence and drug resistance. *Proceedings of the National Academy of Sciences of the United States of America*, 101(26), pp.9786–91. Available at: http://www.pubmedcentral.nih.gov/articlerender.fcgi?artid=470752&tool=pmcentre z&rendertype=abstract.

Horn, H.F. et al., 2013. A mammalian KASH domain protein coupling meiotic chromosomes to the cytoskeleton. *Journal of Cell Biology*, 202(7), pp.1023–1039.

Horn, H.F. et al., 2013. The LINC complex is essential for hearing. *The Journal of Clinical Investigation*, 123(2), pp.740–750.

Hough, L.E. et al., 2015. The molecular mechanism of nuclear transport revealed by atomic-scale measurements. *eLife*, 4, p.e10027. Available at: http://elifesciences.org/content/4/e10027v3 [Accessed April 12, 2016].

Hu, X. et al., 2010. An in vitro assessment of titanium functionalized with polysaccharides conjugated with vascular endothelial growth factor for enhanced osseointegration and inhibition of bacterial adhesion. *Biomaterials*, 31(34), pp.8854–63. Available at: http://www.ncbi.nlm.nih.gov/pubmed/20800276 [Accessed December 24, 2013].

Humphrey, W., Dalke, A. & Schulten, K., 1996. VMD-visual molecular dynamics. *J. Mol. Graphics*, 14, pp.33–38.

Humphrey, W., Dalke, A. & Schulten, K., 1996. VMD: visual molecular dynamics. *Journal of molecular graphics*, 14(1), pp.33–8, 27–8.

Huo, K. et al., 2013. Osteogenic activity and antibacterial effects on titanium surfaces modified with Zn-incorporated nanotube arrays. *Biomaterials*, 34(13), pp.3467–78. Available at: http://www.ncbi.nlm.nih.gov/pubmed/23439134 [Accessed December 24, 2013].

Hutchison, J.B. et al., 2014. Single-Cell Control of Initial Spatial Structure in Bio fi lm Development Using Laser Trapping.

Isermann, P. & Lammerding, J., 2013. Nuclear mechanics and mechanotransduction in health and disease. *Current biology : CB*, 23(24), pp.R1113-21. Available at: http://www.ncbi.nlm.nih.gov/pubmed/24355792 [Accessed October 1, 2014].

Jahed, Z., Molladavoodi, S., et al., 2014. Cell responses to metallic nanostructure arrays with complex geometries. *Biomaterials*, 35(34), pp.9363–9371. Available at: http://www.ncbi.nlm.nih.gov/pubmed/25123921 [Accessed August 23, 2014].

Jahed, Z., Jin, S., et al., 2012. Fabrication and buckling behavior of polycrystalline palladium,

cobalt, and rhodium nanostructures. *Materials Science and Engineering: A*, 542, pp.40–48. Available at: http://linkinghub.elsevier.com/retrieve/pii/S0921509312002316 [Accessed November 9, 2012].

Jahed, Z., Evans, R.D., et al., 2012. Mechanical properties of columnar submicron cobalt structures with various cross-sectional geometries. *Scripta Materialia*, 67(5), pp.463–466. Available at: http://linkinghub.elsevier.com/retrieve/pii/S1359646212003776 [Accessed November 9, 2012].

Jahed, Z., Shams, H., Mehrbod, M., et al., 2014. *Mechanotransduction pathways linking the extracellular matrix to the nucleus*,

Jahed, Z., Shams, H., et al., 2014. Mechanotransduction pathways linking the extracellular matrix to the nucleus. *International review of cell and molecular biology*, 310, pp.171–220. Available at: http://www.ncbi.nlm.nih.gov/pubmed/24725427 [Accessed July 17, 2014].

Jahed, Z. et al., 2018. Molecular insights into the mechanisms of SUN1 oligomerization in the nuclear envelope. *Biophysical journal*, 114, pp.1190–1203.

Jahed, Z., Lin, P., Seo, B.B., et al., 2014. Responses of Staphylococcus aureus bacterial cells to nanocrystalline nickel nanostructures. *Biomaterials*, 35(14).

Jahed, Z., Lin, P., et al., 2014. Responses of Staphylococcus aureus bacterial cells to nanocrystalline nickel nanostructures. *Biomaterials*, 35(14), pp.4249–54. Available at: http://www.ncbi.nlm.nih.gov/pubmed/24576805 [Accessed June 3, 2014].

Jahed, Z. et al., 2016. The LINC and NPC relationship - it's complicated! *Journal of Cell Science*, 129(17).

Jahed, Z. et al., 2016. The LINC and NPC relationship – it's complicated! *Journal of Cell Science*, 129, pp.3219–3229. Available at: http://jcs.biologists.org/lookup/doi/10.1242/jcs.184184.

Jahed, Z. & Mofrad, M.R.K., 2018. Mechanical LINCs of the nuclear envelope: Where SUN meets KASH. *Extreme Mechanics Letters*, 20, pp.99–103. Available at: http://linkinghub.elsevier.com/retrieve/pii/S2352431617301876.

Jahed, Z., Shams, H. & Mofrad, M.R.K., 2015. A Disulfide Bond Is Required for the Transmission of Forces through SUN-KASH complexes. *Biophysical Journal*, 109(August), pp.1–9. Available at: http://dx.doi.org/10.1016/j.bpj.2015.06.057.

Jahed, Z., Shams, H. & Mofrad, M.R.K., 2015. A Disulfide Bond Is Required for the Transmission of Forces through SUN-KASH Complexes. *Biophysical journal*, 109(3), pp.501–9.

Jamali, T. et al., 2011a. *Nuclear Pore Complex. Biochemistry and Biophysics of Nucleocytoplasmic Transport in Health and Disease* 1st ed., Elsevier Inc.

Jamali, T. et al., 2011b. *Nuclear Pore Complex. Biochemistry and Biophysics of Nucleocytoplasmic Transport in Health and Disease* 1st ed., Elsevier Inc. Available at: http://dx.doi.org/10.1016/B978-0-12-386043-9.00006-2.

Jamali, Y., Azimi, M. & Mofrad, M.R.K., 2010. A sub-cellular viscoelastic model for cell population mechanics. *PloS one*, 5(8). Available at:

http://www.pubmedcentral.nih.gov/articlerender.fcgi?artid=2938372&tool=pmcentr ez&rendertype=abstract [Accessed November 17, 2013].

Jaspersen, S.L. & Ghosh1, S., 2012. Nuclear envelope insertion of spindle pole bodies and nuclear pore complexes. *Nucleus*, 3(3), pp.226–236.

J Stroud, M. et al., 2014. LINC complex proteins in cardiac structure, function, and disease. *Circulation research*, 114(3), pp.538–548.

Jiang, X. et al., 2005. Directing cell migration with asymmetric micropatterns. *Proceedings of the National Academy of Sciences of the United States of America*, 102(4), pp.975–978.

Jin, S., Burek, M.J., et al., 2012. Fabrication, microstructure, and mechanical properties of high strength cobalt sub-micron structures. *Materials Science and Engineering: A*, 552, pp.104–111. Available at: http://linkinghub.elsevier.com/retrieve/pii/S0921509312007071 [Accessed November 9, 2012].

Jin, S., Xie, S., et al., 2012. Microstructure and mechanical properties of sub-micron zinc structures. *Journal of Materials Research*, 27(16), pp.2140–2147. Available at: http://www.journals.cambridge.org/abstract_S088429141200146X [Accessed November 12, 2012].

Jorgens, D.M. et al., 2016. Deep nuclear invaginations linked to cytoskeletal filaments: Integrated Bioimaging of epithelial cells in 3D culture Danielle. *Journal of cell science*, 94720(August).

Kalab, P. & Heald, R., 2008. The RanGTP gradient - a GPS for the mitotic spindle. *Journal of cell science*, 121(Pt 10), pp.1577–86. Available at: http://www.ncbi.nlm.nih.gov/pubmed/18469014.

Kaminski, A., Fedorchak, G.R. & Lammerding, J., 2014. *The cellular mastermind(?)-mechanotransduction and the nucleus.* 1st ed., Elsevier Inc. Available at: http://www.ncbi.nlm.nih.gov/pubmed/25081618 [Accessed November 21, 2014].

Karska-Wysocki, B., Bazo, M. & Smoragiewicz, W., 2010. Antibacterial activity of Lactobacillus acidophilus and Lactobacillus casei against methicillin-resistant Staphylococcus aureus (MRSA). *Microbiological research*, 165(8), pp.674–86. Available at: http://www.ncbi.nlm.nih.gov/pubmed/20116228 [Accessed December 24, 2013].

Kastrup, C.J. et al., 2008. Spatial localization of bacteria controls coagulation of human blood by "quorum acting". *Nature chemical biology*, 4(12), pp.742–750. Available at: http://eutils.ncbi.nlm.nih.gov/entrez/eutils/elink.fcgi?dbfrom=pubmed&id=1903153 1&retmode=ref&cmd=prlinks%5Cnpapers3://publication/uuid/A5A17102-78DB-4490-8D8C-26380149B986.

Katta, S.S., Smoyer, C.J. & Jaspersen, S.L., 2014. Destination: Inner nuclear membrane. *Trends in Cell Biology*, 24(4), pp.221–229. Available at: http://dx.doi.org/10.1016/j.tcb.2013.10.006.

Kelley, L.A. et al., 2015. The Phyre2 web portal for protein modelling , prediction and analysis. *Nat Protoc*, 10(6), pp.845–858.

Khatau, S.B. et al., 2009. A perinuclear actin cap regulates nuclear shape. *Proceedings of the*

National Academy of Sciences of the United States of America, 106(45), pp.19017–22. Available at: http://www.pubmedcentral.nih.gov/articlerender.fcgi?artid=2776434&tool=pmcentr ez&rendertype=abstract.

Kilian, K.A. et al., 2010. Geometric cues for directing the differentiation of mesenchymal stem cells. *Proceedings of the National Academy of Sciences*, 107(11), pp.4872–4877. Available at: http://www.pnas.org/cgi/doi/10.1073/pnas.0903269107.

Kim, D.-H. et al., 2012. Actin cap associated focal adhesions and their distinct role in cellular mechanosensing. *Scientific reports*, 2, p.555. Available at: http://www.pubmedcentral.nih.gov/articlerender.fcgi?artid=3412326&tool=pmcentr ez&rendertype=abstract [Accessed June 2, 2014].

Kim, D.-H. et al., 2012. Matrix nanotopography as a regulator of cell function. *The Journal of cell biology*, 197(3), pp.351–60. Available at: http://www.pubmedcentral.nih.gov/articlerender.fcgi?artid=3341161&tool=pmcentr ez&rendertype=abstract [Accessed November 18, 2014].

Kim, D.H. et al., 2012. Matrix nanotopography as a regulator of cell function. *Journal of Cell Biology*, 197(3), pp.351–360.

Kim, D.I. et al., 2016. Making the LINC: SUN and KASH protein interactions. , 396(4), pp.295–310.

Kim, J. et al., 2012. DPN104-Direct-write patterning of bacterial cells by dip-pen nanolithography. *Journal of the American Chemical Society*, 134(40), pp.16500–16503.

Kim, W. et al., 2007. Interfacing silicon nanowires with mammalian cells. *Journal of the American Chemical Society*, 129(23), pp.7228–9. Available at: http://www.ncbi.nlm.nih.gov/pubmed/24140651.

Koh, J. & Blobel, G., 2015. Allosteric Regulation in Gating the Central Channel of the Nuclear Pore Complex. *Cell*, 161(6), pp.1361–1373.

Kreuzer, S.M. & Elber, R., 2013. Coiled-coil response to mechanical force: global stability and local cracking. *Biophysical journal*, 105(4), pp.951–61. Available at: http://www.pubmedcentral.nih.gov/articlerender.fcgi?artid=3752098&tool=pmcentr ez&rendertype=abstract [Accessed October 30, 2014].

Labokha, A.A. et al., 2013. Systematic analysis of barrier-forming FG hydrogels from Xenopus nuclear pore complexes. *The EMBO journal*, 32(2), pp.204–18.

Ladoux, B. & Mège, R.M., 2017. Mechanobiology of collective cell behaviours. *Nature Reviews Molecular Cell Biology*, 18(12), pp.743–757. Available at: http://dx.doi.org/10.1038/nrm.2017.98.

Lafuma, A. & Quéré, D., 2003. Superhydrophobic states. *Nature materials*, 2(7), pp.457–60. Available at: http://www.ncbi.nlm.nih.gov/pubmed/12819775.

Lammerding, J. & Wolf, K., 2016. Nuclear envelope rupture : Actin fibers are putting the squeeze on the nucleus. , pp.1–4.

Laurell, E. et al., 2011. Phosphorylation of Nup98 by multiple kinases is crucial for NPC disassembly during mitotic entry. *Cell*, 144(4), pp.539–50. Available at:

http://www.sciencedirect.com/science/article/pii/S0092867411000134 [Accessed October 30, 2015].

Lei, K. et al., 2012. Inner nuclear envelope proteins SUN1 and SUN2 play a prominent role in the DNA damage response. *Current biology : CB*, 22(17), pp.1609–15.

Lei, K. et al., 2009. SUN1 and SUN2 play critical but partially redundant roles in anchoring nuclei in skeletal muscle cells in mice. *Proceedings of the National Academy of Sciences of the United States of America*, 106(25), pp.10207–10212.

Li, P. & Noegel, A.A., 2015a. Inner nuclear envelope protein SUN1 plays a prominent role in mammalian mRNA export. *Nucleic acids research*.

Li, P. & Noegel, A.A., 2015b. Inner nuclear envelope protein SUN1 plays a prominent role in mammalian mRNA export. *Nucleic acids research*. Available at: http://nar.oxfordjournals.org/content/early/2015/10/15/nar.gkv1058.abstract [Accessed October 20, 2015].

Lin, C.H. et al., 2010. Patterning nanowire and micro-/nanoparticle array on micropillar-structured surface: Experiment and modeling. *Biomicrofluidics*, 4(3), pp.1–15.

Lin, D.H. et al., 2016. Architecture of the symmetric core of the nuclear pore. *Science*, 352(6283), p.aaf1015-aaf1015. Available at: http://science.sciencemag.org/content/352/6283/aaf1015.abstract [Accessed April 15, 2016].

Lindeman, R.E. & Pelegri, F., 2012. Localized products of futile cycle/lrmp promote centrosome-nucleus attachment in the zebrafish zygote. *Current Biology*, 22(10), pp.843–851. Available at: http://dx.doi.org/10.1016/j.cub.2012.03.058.

Liu, Q. et al., 2007. Functional association of Sun1 with nuclear pore complexes. *The Journal of Cell Biology*, 178(5), pp.785–798. Available at: http://www.jcb.org/cgi/doi/10.1083/jcb.200704108.

Liu, Q. et al., 2007. Functional association of Sun1 with nuclear pore complexes. *The Journal of cell biology*, 178(5), pp.785–98. Available at: http://www.pubmedcentral.nih.gov/articlerender.fcgi?artid=2064544&tool=pmcentrez&rendertype=abstract [Accessed October 24, 2014].

Lombardi, M.L., Jaalouk, D.E., Shanahan, C.M., Burke, B., Kyle, J., et al., 2011. The interaction between nesprins and sun proteins at the nuclear envelope is critical for force transmission between the nucleus and cytoskeleton. *The Journal of biological chemistry*, 286(30), pp.26743–53.

Lombardi, M.L., Jaalouk, D.E., Shanahan, C.M., Burke, B., Roux, K.J., et al., 2011. The interaction between nesprins and sun proteins at the nuclear envelope is critical for force transmission between the nucleus and cytoskeleton. *The Journal of biological chemistry*, 286(30), pp.26743–53.

Louis, D.N., 2006. Molecular pathology of malignant gliomas. *Annual review of pathology*, 1, pp.97–117.

Lovell, S.C. et al., 2003. Structure validation by C alpha geometry: phi,psi and C beta deviation. *Proteins-Structure Function and Genetics*, 50(August 2002), pp.437–450.

Available at: http://onlinelibrary.wiley.com/store/10.1002/prot.10286/asset/10286_ftp.pdf?v=1&t=gwhx9jy0&s=b3b0f129a5acf7f4513aea04d22aad7ee4f4a89d.

Lu, W., Gotzmann, J., Sironi, L., Jaeger, V.-M., et al., 2008. Sun1 forms immobile macromolecular assemblies at the nuclear envelope. *Biochimica et Biophysica Acta (BBA) - Molecular Cell Research*, 1783(12), pp.2415–2426. Available at: http://linkinghub.elsevier.com/retrieve/pii/S0167488908003078.

Lu, W., Gotzmann, J., Sironi, L., Jaeger, V., et al., 2008. Sun1 forms immobile macromolecular assemblies at the nuclear envelope. *Biochimica et Biophysica Acta journal*, 1783(12), pp.2415–2426. Available at: http://dx.doi.org/10.1016/j.bbamcr.2008.09.001.

Luxton, G.G. & Starr, D.A., 2014a. KASHing up with the nucleus: Novel functional roles of KASH proteins at the cytoplasmic surface of the nucleus. *Current Opinion in Cell Biology*, 28(1), pp.69–75. Available at: http://dx.doi.org/10.1016/j.ceb.2014.03.002.

Luxton, G.G. & Starr, D.A., 2014b. KASHing up with the nucleus: Novel functional roles of KASH proteins at the cytoplasmic surface of the nucleus. *Current Opinion in Cell Biology*, 28(1), pp.69–75.

Luxton, G.W.G. et al., 2010. Linear arrays of nuclear envelope proteins harness retrograde actin flow for nuclear movement. *Science (New York, N.Y.)*, 329(5994), pp.956–9.

Ma, J., Goryaynov, A. & Yang, W., 2016. Super-resolution 3D tomography of interactions and competition in the nuclear pore complex. *Nature structural & molecular biology*, 23(3), pp.239–47. Available at: http://dx.doi.org/10.1038/nsmb.3174 [Accessed April 12, 2016].

Madsen, J.S. et al., 2012. The interconnection between biofilm formation and horizontal gene transfer. *FEMS Immunology and Medical Microbiology*, 65(2), pp.183–195.

Magrane, M. & Consortium, U., 2011. UniProt Knowledgebase: a hub of integrated protein data. *Database : the journal of biological databases and curation*, 2011, p.bar009. Available at: http://www.pubmedcentral.nih.gov/articlerender.fcgi?artid=3070428&tool=pmcentrez&rendertype=abstract [Accessed October 29, 2014].

Mahmud, G. et al., 2009. Directing cell motions on micropatterned ratchets. *Nature Physics*, 5(8), pp.606–612. Available at: http://dx.doi.org/10.1038/nphys1306.

Maimon, T. et al., 2012. The human nuclear pore complex as revealed by cryo-electron tomography. *Structure*, 20(6), pp.998–1006. Available at: http://dx.doi.org/10.1016/j.str.2012.03.025.

Malone, C.J. et al., 2003. The C. elegans Hook Protein, ZYG-12, Mediates the Essential Attachment between the Centrosome and Nucleus. *Cell*, 115(7), pp.825–836.

Malone, C.J. et al., 1999. UNC-84 localizes to the nuclear envelope and is required for nuclear migration and anchoring during C . elegans development. , 3181, pp.3171–3181.

Maniotis, A.J., Chen, C.S. & Ingber, D.E., 1997. Demonstration of mechanical connections between integrins, cytoskeletal filaments, and nucleoplasm that stabilize nuclear

structure. *Proceedings of the National Academy of Sciences*, 94(3), pp.849–854. Available at: http://www.pnas.org/content/94/3/849.full#ref-38 [Accessed October 30, 2015].

Matsumoto, A. et al., 2015. Global loss of a nuclear lamina component, lamin A/C, and LINC complex components SUN1, SUN2, and nesprin-2 in breast cancer. *Cancer Medicine*, 4(10), pp.1547–1557.

Matunis, M.J., Wu, J. & Blobel, G., 1998. SUMO-1 modification and its role in targeting the Ran GTPase-activating protein, RanGAP1, to the nuclear pore complex. *Journal of Cell Biology*, 140(3), pp.499–509.

Matzke, A.J.M., Weiger, T.M. & Matzke, M., 2010. Ion channels at the nucleus: electrophysiology meets the genome. *Molecular plant*, 3(4), pp.642–52. Available at: http://www.pubmedcentral.nih.gov/articlerender.fcgi?artid=2910552&tool=pmcentr ez&rendertype=abstract [Accessed October 21, 2014].

McBeath, R. et al., 2004. Cell shape, cytoskeletal tension, and RhoA regulate stem cell lineage commitment. *Developmental Cell*, 6(4), pp.483–495.

McGee, M.D. et al., 2006. UNC-83 Is a KASH Protein Required for Nuclear Migration and Is Recruited to the Outer Nuclear Membrane by a Physical Interaction with the SUN Protein UNC-84. *Molecular Biology of the Cell*, 17, pp.1790–1801.

Mcguire, A.F., Santoro, F. & Cui, B., 2018. Interfacing Cells with Vertical Nanoscale Devices: Applications and Characterization. *Annual Review of Analytical Chemistry Annu. Rev. Anal. Chem*, 111226(1), pp.1–12. Available at: https://doi.org/10.1146/annurev-anchem-061417-125705.

McNamara, L.E. et al., 2012. The role of microtopography in cellular mechanotransduction. *Biomaterials*, 33(10), pp.2835–2847. Available at: http://dx.doi.org/10.1016/j.biomaterials.2011.11.047.

Mehrbod, M. & Mofrad, M.R.K., 2013. Localized Lipid Packing of Transmembrane Domains Impedes Integrin Clustering A. D. McCulloch, ed. *PLoS Computational Biology*, 9(3), p.e1002948.

Mehrbod, M., Trisno, S. & Mofrad, M.R.K., 2013. On the activation of integrin αIIbβ3: outside-in and inside-out pathways. *Biophysical journal*, 105(6), pp.1304–15.

Meinke, P. et al., 2014. Muscular dystrophy-associated SUN1 and SUN2 variants disrupt nuclear-cytoskeletal connections and myonuclear organization. *PLoS genetics*, 10(9), p.e1004605. Available at: http://www.pubmedcentral.nih.gov/articlerender.fcgi?artid=4161305&tool=pmcentr ez&rendertype=abstract [Accessed October 24, 2014].

Meinke, P., Nguyen, T.D. & Wehnert, M.S., 2011. The LINC complex and human disease. *Biochemical Society transactions*, 39(6), pp.1693–7. Available at: http://www.ncbi.nlm.nih.gov/pubmed/22103509 [Accessed October 24, 2014].

Meinke, P. & Schirmer, E.C., 2015. LINC ' ing form and function at the nuclear envelope. , 589, pp.2514–2521.

Méjat, A. & Misteli, T., 2010a. LINC complexes in health and disease. *Nucleus (Austin, Tex.)*,

1(1), pp.40–52. Available at:
http://www.pubmedcentral.nih.gov/articlerender.fcgi?artid=3035119&tool=pmcentr
ez&rendertype=abstract.

Méjat, A. & Misteli, T., 2010b. LINC complexes in health and disease. *Nucleus (Austin, Tex.)*, 1(1), pp.40–52.

Melcak, I., Hoelz, A. & Blobel, G., 2007. Structure of Nup58/45 Suggests Flexible Nuclear Pore Diameter by Intermolecular Sliding. *Science*, 315(5819), pp.1729–1732.

Melcher, G.A. et al., 1994. Influence of type of medullary nail on the development of local infection. *J Bone Joint Surg*, 76(6).

Mészáros, N. et al., 2015. Nuclear Pore Basket Proteins Are Tethered to the Nuclear Envelope and Can Regulate Membrane Curvature. *Developmental Cell*.

Miele, E. et al., 2015. Writing and functionalisation of suspended DNA nanowires on superhydrophobic pillar arrays. *Small*, 11(1), pp.134–140.

Mielich-S??ss, B. & Lopez, D., 2015. Molecular mechanisms involved in Bacillus subtilis biofilm formation. *Environmental Microbiology*, 17(3), pp.555–565.

Miki, F. et al., 2004. Two-hybrid search for proteins that interact with Sad1 and Kms1, two membrane-bound components of the spindle pole body in fission yeast. *Molecular Genetics and Genomics*, 270(6), pp.449–461.

Miller, M.B. & Bassler, B.L., 2001. QUORUM SENSING IN BACTERIA. *Annual Review of Microbiology*, pp.165–189.

Milles, S. et al., 2015. Plasticity of an ultrafast interaction between nucleoporins and nuclear transport receptors. *Cell*, 163(3), pp.734–45. Available at: http://www.sciencedirect.com/science/article/pii/S0092867415012647 [Accessed March 28, 2016].

Mofrad, M.R.K. & Kamm, R.D., 2014. *Cellular Mechanotransduction Diverse Perspectives from Molecules to Tissues*, Cambridge University Press.

Mohamed, N., Rainier, T.R. & Ross, J.M., 2000. Novel experimental study of receptor-mediated bacterial adhesion under the influence of fluid shear. *Biotechnology and bioengineering*, 68(6), pp.628–36. Available at: http://www.ncbi.nlm.nih.gov/pubmed/10799987.

Moran, E., Byren, I. & Atkins, B.L., 2010. The diagnosis and management of prosthetic joint infections. *The Journal of antimicrobial chemotherapy*, 65 Suppl 3, p.iii45-54. Available at: http://www.ncbi.nlm.nih.gov/pubmed/20876628 [Accessed December 24, 2013].

Morimoto, A. et al., 2012. A conserved KASH domain protein associates with telomeres, SUN1, and dynactin during mammalian meiosis. *Journal of Cell Biology*, 198(2), pp.165–172.

Moussavi-Baygi, R. et al., 2011. Brownian dynamics simulation of nucleocytoplasmic transport: a coarse-grained model for the functional state of the nuclear pore complex. *PLoS computational biology*, 7(6), p.e1002049.

Nagai, S. et al., 2008. Functional targeting of DNA damage to a nuclear pore-associated

SUMO-dependent ubiquitin ligase. *Science (New York, N.Y.)*, 322(5901), pp.597–602.

Nagrath, S. et al., 2007. Isolation of rare circulating tumour cells in cancer patients by microchip technology. *Nature*, 450(7173), pp.1235–9.

Nait Chabane, Y. et al., 2014. Characterisation of pellicles formed by Acinetobacter baumannii at the air-liquid interface. *PloS one*, 9(10), p.e111660.

Nakanishi, K., Sakiyama, T. & Imamura, K., 2001. On the adsorption of proteins on solid surfaces, a common but very complicated phenomenon. *Journal of bioscience and bioengineering*, 91(3), pp.233–44. Available at: http://www.ncbi.nlm.nih.gov/pubmed/16232982.

Nie, S. et al., 2016. Coiled-Coil Domains of SUN Proteins as Intrinsic Dynamic Regulators. *Structure*, 24(1), pp.80–91. Available at: http://linkinghub.elsevier.com/retrieve/pii/S0969212615004645.

Nishioka, Y. et al., 2016. SUN1 splice variants, SUN1_888, SUN1_785, and predominant SUN1_916, variably function in directional cell migration. *Nucleus*, 7(6), pp.00–00. Available at: https://www.tandfonline.com/doi/full/10.1080/19491034.2016.1260802.

Nudleman, E., Wall, D. & Kaiser, D., 2005. Cell-to-cell transfer of bacterial outer membrane lipoproteins. *Science (New York, N.Y.)*, 309(5731), pp.125–127.

Oga, M. et al., 1988. Surgical biomaterials and differential colonization by Staphylococcus epidermidis. *Biomaterials*, 9(3), pp.285–9. Available at: http://www.ncbi.nlm.nih.gov/pubmed/3408804.

Padmakumar, V.C. et al., 2005. The inner nuclear membrane protein Sun1 mediates the anchorage of Nesprin-2 to the nuclear envelope. *Journal of cell science*, 118(Pt 15), pp.3419–30.

Palacios-Cuesta, M. et al., 2015. Patterning of individual Staphylococcus aureus bacteria onto photogenerated polymeric surface structures. *Polymer Chemistry*, 6, pp.2677–2684. Available at: http://dx.doi.org/10.1039/C4PY01629G.

Panciera, T. et al., 2017. Mechanobiology of YAP and TAZ in physiology and disease. *Nature Reviews Molecular Cell Biology*, 18(12), pp.758–770. Available at: http://dx.doi.org/10.1038/nrm.2017.87.

Pande, S. et al., 2015. Metabolic cross-feeding via intercellular nanotubes among bacteria. *Nature Communications*, 6, p.6238. Available at: http://dx.doi.org/10.1038/ncomms7238%5Cnhttp://www.nature.com/doifinder/10.1038/ncomms7238.

Pante, N. & Kann, M., 2002. Nuclear Pore Complex Is Able to Transport Macromolecules with Diameters of 39 nm. *Molecular biology of the cell*, 13(February), pp.425–434.

Papa, R. et al., 2013. A new anti-infective strategy to reduce the spreading of antibiotic resistance by the action on adhesion-mediated virulence factors in Staphylococcus aureus. *Microbial pathogenesis*, 63, pp.44–53. Available at: http://www.ncbi.nlm.nih.gov/pubmed/23811076 [Accessed December 17, 2013].

Patel, J.T. et al., 2014. Mitotic phosphorylation of SUN1 loosens its connection with the

nuclear lamina while the LINC complex remains intact. *Nucleus (Austin, Tex.)*, 5(5), pp.462–473. Available at: http://www.ncbi.nlm.nih.gov/pubmed/25157413.

Patel, S.S. & Rexach, M.F., 2008. Discovering novel interactions at the nuclear pore complex using bead halo: a rapid method for detecting molecular interactions of high and low affinity at equilibrium. *Molecular & cellular proteomics : MCP*, 7(1), pp.121–31. Available at: http://www.mcponline.org/content/7/1/121.full [Accessed June 25, 2015].

Persat, A. et al., 2015. The mechanical world of bacteria. *Cell*, 161(5), pp.988–997. Available at: http://dx.doi.org/10.1016/j.cell.2015.05.005.

Persson, H. et al., 2013. Fibroblasts cultured on nanowires exhibit low motility, impaired cell division, and DNA damage. *Small*, 9(23), pp.4006–4016.

Persson, H. et al., 2015. From immobilized cells to motile cells on a bed-of-nails: effects of vertical nanowire array density on cell behaviour. *Scientific reports*, 5(November), p.18535. Available at: http://www.pubmedcentral.nih.gov/articlerender.fcgi?artid=4686997&tool=pmcentrez&rendertype=abstract.

Petersen, O.H. et al., 1998. The calcium store nuclear envelope in the. , 23, pp.87–90.

Peyro, M. et al., 2015. Evolutionary conserved features regulate the formation of the FG network at the center of the nuclear pore complex. *Scientific Reports*.

Peyro, M. et al., 2015. Nucleoporin's Like Charge Regions Are Major Regulators of FG Coverage and Dynamics Inside the Nuclear Pore Complex. *PloS one*, 10(12), p.e0143745.

Phillips, J.C. et al., 2005. Scalable molecular dynamics with NAMD. *Journal of computational chemistry*, 26(16), pp.1781–802. Available at: http://www.pubmedcentral.nih.gov/articlerender.fcgi?artid=2486339&tool=pmcentrez&rendertype=abstract [Accessed October 18, 2013].

Pierce, B.G. et al., 2014. Structural bioinformatics ZDOCK server : interactive docking prediction of protein – protein complexes and symmetric multimers. , 30(12), pp.1771–1773.

Popat, K., Chatvanichkul, K.-I. & L. Branes, G., 2007. Osteogenic differentiation of marrow stromal cells cultured on nanoporous alumni surfaces. *Journal of biomedical materials research. Part A*, 81(4), pp.771–780.

Puckelwartz, M.J. et al., 2010. Nesprin-1 mutations in human and murine cardiomyopathy. *Journal of molecular and cellular cardiology*, 48(4), pp.600–8. Available at: http://www.pubmedcentral.nih.gov/articlerender.fcgi?artid=2837775&tool=pmcentrez&rendertype=abstract [Accessed October 24, 2014].

Puckett, S.D. et al., 2010. The relationship between the nanostructure of titanium surfaces and bacterial attachment. *Biomaterials*, 31(4), pp.706–13. Available at: http://www.ncbi.nlm.nih.gov/pubmed/19879645 [Accessed December 24, 2013].

Raices, M. & D'Angelo, M.A., 2012. Nuclear pore complex composition: a new regulator of tissue-specific and developmental functions. *Nature reviews. Molecular cell biology*,

13(11), pp.687–99. Available at: http://dx.doi.org/10.1038/nrm3461 [Accessed November 20, 2015].

Rajgor, D. & Shanahan, C.M., 2013a. Nesprins: from the nuclear envelope and beyond. *Expert reviews in molecular medicine*, 15(July), p.e5. Available at: http://www.pubmedcentral.nih.gov/articlerender.fcgi?artid=3733404&tool=pmcentr ez&rendertype=abstract.

Rajgor, D. & Shanahan, C.M., 2013b. Nesprins: from the nuclear envelope and beyond. *Expert reviews in molecular medicine*, 15(July), p.e5.

Rajnicek, a, Britland, S. & McCaig, C., 1997. Contact guidance of CNS neurites on grooved quartz: influence of groove dimensions, neuronal age and cell type. *Journal of cell science*, 110 (Pt 2, pp.2905–2913.

Rashidi, A. & Amadeh, A., 2010. Effect of electroplating parameters on microstructure of nanocrystalline nickel coatings. *Journal of Materials Science & Technology*, 26(1), pp.82–86. Available at: http://linkinghub.elsevier.com/retrieve/pii/S1005030210600138.

Remis, J.P. et al., 2014. Bacterial social networks: Structure and composition of Myxococcus xanthus outer membrane vesicle chains. *Environmental Microbiology*, 16(2), pp.598–610.

Renzulli, A. et al., 2000. Mitral and Aortic Valve Endocarditis. *Tex Heart Inst J.*, pp.67–69.

Robinson, J.T. et al., 2012. Vertical nanowire electrode arrays as a scalable platform for intracellular interfacing to neuronal circuits. *Nature nanotechnology*, 7(3), pp.180–4. Available at: http://www.ncbi.nlm.nih.gov/pubmed/22231664 [Accessed December 16, 2013].

Robinson, J.T., Jorgolli, M. & Park, H., 2013. Nanowire electrodes for high-density stimulation and measurement of neural circuits. *Frontiers in neural circuits*, 7(March), p.38. Available at: http://www.pubmedcentral.nih.gov/articlerender.fcgi?artid=3594763&tool=pmcentr ez&rendertype=abstract [Accessed December 17, 2013].

Roca-Cusachs, P. et al., 2009. Clustering of alpha(5)beta(1) integrins determines adhesion strength whereas alpha(v)beta(3) and talin enable mechanotransduction. *Proceedings of the National Academy of Sciences of the United States of America*, 106(38), pp.16245–16250.

Rochford, E.T.J. et al., 2013. Bacterial adhesion to orthopaedic implant materials and a novel oxygen plasma modified PEEK surface. *Colloids and surfaces. B, Biointerfaces*, 113C, pp.213–222. Available at: http://www.ncbi.nlm.nih.gov/pubmed/24103502 [Accessed December 24, 2013].

Rothballer, A. & Kutay, U., 2013. The diverse functional LINCs of the nuclear envelope to the cytoskeleton and chromatin. *Chromosoma*, 122(5), pp.415–429.

Roux, K.J. et al., 2009. Nesprin 4 is an outer nuclear membrane protein that can induce kinesin-mediated cell polarization. *Proceedings of the National Academy of Sciences of the United States of America*, 106(7), pp.2194–9. Available at:

http://www.pubmedcentral.nih.gov/articlerender.fcgi?artid=2650131&tool=pmcentrez&rendertype=abstract.

Sadeghi, S. & Emberly, E., 2009. Length-dependent force characteristics of coiled coils. *Physical Review E*, 80(6), p.61909. Available at: http://link.aps.org/doi/10.1103/PhysRevE.80.061909 [Accessed October 28, 2014].

Safi, M. et al., 2011. Interactions between magnetic nanowires and living cells: uptake, toxicity, and degradation. *ACS nano*, 5(7), pp.5354–64. Available at: http://www.ncbi.nlm.nih.gov/pubmed/21699198.

Schmidt, H.B. & Görlich, D., 2016. Transport Selectivity of Nuclear Pores, Phase Separation, and Membraneless Organelles. *Trends in biochemical sciences*, 41(1), pp.46–61. Available at: http://www.sciencedirect.com/science/article/pii/S0968000415002091 [Accessed March 4, 2016].

Schwaiger, I. et al., 2002. The myosin coiled-coil is a truly elastic protein structure. *Nature materials*, 1(4), pp.232–5. Available at: http://www.ncbi.nlm.nih.gov/pubmed/12618784 [Accessed October 30, 2014].

Seo, B.B. et al., 2013. Influence of grain size on the strength size dependence exhibited by sub-micron scale nickel structures with complex cross-sectional geometries. *Materials Science and Engineering: A*, 596, pp.275–284. Available at: http://linkinghub.elsevier.com/retrieve/pii/S0921509313014093 [Accessed January 9, 2014].

Seo, B.B. et al., 2016. Trapping polystyrene and latex nanospheres inside hollow nanostructures using Staphylococcus aureus cells. *Journal of Experimental Nanoscience*, 11(4).

Shahsavan, H., Arunbabu, D. & Zhao, B., 2012. Biomimetic modification of polymeric surfaces: A promising pathway for tuning of wetting and adhesion. *Macromolecular Materials and Engineering*, 297(8), pp.743–760.

Shahsavan, H. & Zhao, B., 2011. Conformal adhesion enhancement on biomimetic microstructured surfaces. *Langmuir*, 27, pp.7732–7742.

Shalek, A.K. et al., 2012. Nanowire-Mediated Delivery Enables Functional Interrogation of Primary Immune Cells: Application to the Analysis of Chronic Lymphocytic Leukemia. *Nano Letters*, 12, pp.6498–6504.

Shalek, A.K. et al., 2010. Vertical silicon nanowires as a universal platform for delivering biomolecules into living cells. *Proceedings of the National Academy of Sciences of the United States of America*, 107(5), pp.1870–5. Available at: http://www.pubmedcentral.nih.gov/articlerender.fcgi?artid=2836617&tool=pmcentrez&rendertype=abstract [Accessed November 8, 2013].

Shao, X. et al., 1999. Spag4 , a Novel Sperm Protein , Binds Outer Dense- Fiber Protein Odf1 and Localizes to Microtubules of Manchette and Axoneme. , 123, pp.109–123.

da Silva Meira, Q.G. et al., 2012. Influence of temperature and surface kind on biofilm formation by Staphylococcus aureus from food-contact surfaces and sensitivity to sanitizers. *Food Control*, 25(2), pp.469–475. Available at:

http://linkinghub.elsevier.com/retrieve/pii/S0956713511005123 [Accessed December 24, 2013].

Soheilypour, M. et al., 2016a. On the nuclear pore complex and its roles in nucleo-cytoskeletal coupling and mechanobiology. *Cellular and Molecular Bioengineering*.

Soheilypour, M. et al., 2016b. On the nuclear pore complex and its roles in nucleo-cytoskeletal coupling and mechanobiology. *Cellular and Molecular Bioengineering*, 9(2), pp.217–226.

Solmaz, S.R. et al., 2011. Molecular Architecture of the Transport Channel of the Nuclear Pore Complex. *Cell*, 147(3), pp.590–602.

Solmaz, S.R., Blobel, G. & Melcák, I., 2013. Ring cycle for dilating and constricting the nuclear pore. *Proceedings of the National Academy of Sciences of the United States of America*, 110(15), pp.5858–63.

Song, M.M. et al., 2010. Cytotoxicity and cellular uptake of iron nanowires. *Biomaterials*, 31(7), pp.1509–17. Available at: http://www.ncbi.nlm.nih.gov/pubmed/19945156 [Accessed December 19, 2013].

Sosa, B. a et al., 2012a. LINC complexes form by binding of three KASH peptides to domain interfaces of trimeric SUN proteins. *Cell*, 149(5), pp.1035–47.

Sosa, B. a et al., 2012b. LINC complexes form by binding of three KASH peptides to domain interfaces of trimeric SUN proteins. *Cell*, 149(5), pp.1035–47. Available at: http://www.pubmedcentral.nih.gov/articlerender.fcgi?artid=3383001&tool=pmcentr ez&rendertype=abstract [Accessed May 29, 2013].

Sosa, B. a, Kutay, U. & Schwartz, T.U., 2013. Structural insights into LINC complexes. *Current opinion in structural biology*, 23(2), pp.285–91. Available at: http://www.pubmedcentral.nih.gov/articlerender.fcgi?artid=4077334&tool=pmcentr ez&rendertype=abstract [Accessed October 22, 2014].

Splinter, D. et al., 2010. Bicaudal D2, dynein, and kinesin-1 associate with nuclear pore complexes and regulate centrosome and nuclear positioning during mitotic entry. *PLoS biology*, 8(4), p.e1000350. Available at: http://journals.plos.org/plosbiology/article?id=10.1371/journal.pbio.1000350 [Accessed September 15, 2015].

Starr, D.A. & Han, M., 2002. Role of ANC-1 in Tethering Nuclei to the Actin Cytoskeleton. , 298(October), pp.2000–2003.

Stewart-Hutchinson, P.J. et al., 2008. Structural requirements for the assembly of LINC complexes and their function in cellular mechanical stiffness. *Experimental Cell Research*, 314(8), pp.1892–1905.

Stuwe, T. et al., 2015. Architecture of the fungal nuclear pore inner ring complex. *Science (New York, N.Y.)*, 350(6256), pp.56–64. Available at: http://science.sciencemag.org/content/350/6256/56.abstract [Accessed March 4, 2016].

Suo, Z. et al., 2008. Efficient immobilization and patterning of live bacterial cells. *Langmuir*, 24(8), pp.4161–4167.

Talamas, J.A. & Hetzer, M.W., 2011. POM121 and Sun1 play a role in early steps of interphase NPC assembly. *The Journal of Cell Biology*, 194(1), pp.27–37. Available at: http://jcb.rupress.org/content/194/1/27.full [Accessed June 26, 2015].

Tan, J.L. et al., 2003. Cells lying on a bed of microneedles: An approach to isolate mechanical force. *Proceedings of the National Academy of Sciences of the United States of America*, 100(4), pp.1484–1489. Available at: http://www.pubmedcentral.nih.gov/articlerender.fcgi?artid=149857&tool=pmcentre z&rendertype=abstract.

Tapley, E.C., Ly, N. & Starr, D.A., 2011. Multiple mechanisms actively target the SUN protein UNC-84 to the inner nuclear membrane. *Molecular biology of the cell*, 22(10), pp.1739–52. Available at: http://www.molbiolcell.org/content/22/10/1739.full#ref-24 [Accessed January 30, 2016].

Teterycz, D. et al., 2010. Outcome of orthopedic implant infections due to different staphylococci. *International journal of infectious diseases : IJID : official publication of the International Society for Infectious Diseases*, 14(10), pp.e913-8. Available at: http://www.ncbi.nlm.nih.gov/pubmed/20729115 [Accessed December 24, 2013].

Thakar, K. et al., 2017. Opposing roles for distinct LINC complexes in regulation of the small GTPase RhoA. , 28(1), pp.182–191.

Truong, V.K. et al., 2010. The influence of nano-scale surface roughness on bacterial adhesion to ultrafine-grained titanium. *Biomaterials*, 31(13), pp.3674–83. Available at: http://www.ncbi.nlm.nih.gov/pubmed/20163851 [Accessed November 14, 2013].

Turgay, Y. et al., 2010. A classical NLS and the SUN domain contribute to the targeting of SUN2 to the inner nuclear membrane. *The EMBO journal*, 29(14), pp.2262–75.

Turgay, Y. et al., 2014. SUN proteins facilitate the removal of membranes from chromatin during nuclear envelope breakdown. *The Journal of Cell Biology*, 204(7), pp.1099–1109. Available at: http://www.jcb.org/cgi/doi/10.1083/jcb.201310116.

Turgay, Y. et al., 2017. The molecular architecture of lamins in somatic cells.

Uhler, C. & Shivashankar, G. V., 2017. Regulation of genome organization and gene expression by nuclear mechanotransduction. *Nature Reviews Molecular Cell Biology*, 18(12), pp.717–727. Available at: http://dx.doi.org/10.1038/nrm.2017.101.

Ulrich, T., de Juan Pardo, E.M. & Kumar, S., 2009. The mechanical rigidity of the extracellular matrix regulates the srtucture, motility, and proliferation of glioma cells. *Cancer Res.*, 69(10), pp.4167–4174.

Umesh, V. et al., 2014. Microenvironmental stiffness enhances glioma cell proliferation by stimulating epidermal growth factor receptor signaling. *PLoS ONE*, 9(7), pp.1–8.

VanDersarl, J.J., Xu, A.M. & Melosh, N., 2012. Nanostraws for direct fluidic intracellular access. *Nano letters*, 12(8), pp.3881–6. Available at: http://www.ncbi.nlm.nih.gov/pubmed/22166016.

Vining, K.H. & Mooney, D.J., 2017. Mechanical forces direct stem cell behaviour in development and regeneration. *Nature Reviews Molecular Cell Biology*, 18(12), pp.728–742. Available at: http://dx.doi.org/10.1038/nrm.2017.108.

Vollmer, B. et al., 2015. Nup153 Recruits the Nup107-160 Complex to the Inner Nuclear Membrane for Interphasic Nuclear Pore Complex Assembly. *Developmental cell*, 33(6), pp.717–28. Available at: http://www.sciencedirect.com/science/article/pii/S1534580715003159 [Accessed January 13, 2016].

Wang, J.H. & Lin, J.S., 2007. Cell traction force and measurement methods. *Biomechanics and modeling in mechanobiology*, 6(6), pp.361–71. Available at: http://www.ncbi.nlm.nih.gov/pubmed/17203315 [Accessed October 26, 2012].

Wang, Q. et al., 2006. Characterization of the Structures Involved in Localization of the SUN Proteins to the Nuclear Envelope and the Centrosome. *DNA and Cell Biology*, 25(10), pp.554–562. Available at: http://www.liebertonline.com/doi/abs/10.1089/dna.2006.25.554.

Wang, S. et al., 2009. Three-dimensional nanostructured substrates toward efficient capture of circulating tumor cells. *Angewandte Chemie - International Edition*, 48(47), pp.8970–8973.

Wang, S. et al., 2010. Three-Dimensional Nanostructured Substrates toward Efficient Capture of Circulating Tumor Cells. , 48(47), pp.8970–8973.

Wang, S., Wan, Y. & Liu, Y., 2014. Effects of nanopillar array diameter and spacing on cancer Cell Capture and Cell Behaviors. *Nanoscale*, 0(21), pp.1–8. Available at: http://dx.doi.org/10.1039/C4NR02854F.

Wang, W. et al., 2012. Salt bridges regulate both dimer formation and monomeric flexibility in HdeB and may have a role in periplasmic chaperone function. *Journal of Molecular Biology*, 415(3), pp.538–546. Available at: http://dx.doi.org/10.1016/j.jmb.2011.11.026.

Wang, W. et al., 2012. Structural insights into SUN-KASH complexes across the nuclear envelope. *Cell research*, 22(10), pp.1440–52. Available at: http://www.pubmedcentral.nih.gov/articlerender.fcgi?artid=3463262&tool=pmcentrez&rendertype=abstract [Accessed October 22, 2014].

Wang, X. et al., 2009. Staphylococcus aureus adhesion to different implant surface coatings: An in vitro study. *Surface and Coatings Technology*, 203(22), pp.3454–3458. Available at: http://linkinghub.elsevier.com/retrieve/pii/S0257897209004368 [Accessed December 24, 2013].

Wei, Q. et al., 2016. A new autoinhibited kinase conformation reveals a salt-bridge switch in kinase activation. *Scientific Reports*, 6(1), p.28437. Available at: http://www.nature.com/articles/srep28437.

Weibel, D.B. et al., 2005. Supporting Information for A Bacterial Printing Press that Regenerates its Ink : Contact Printing Bacteria Using. , (11), pp.1–2.

Weibel, D.B., Diluzio, W.R. & Whitesides, G.M., 2007. Microfabrication meets microbiology. *Nature reviews. Microbiology*, 5(3), pp.209–18. Available at: http://www.ncbi.nlm.nih.gov/pubmed/17304250.

Wenzel, R.N., 1936. Resistance of solid surfaces to wetting by water. *Ind. Eng. Chem.*, 28,

pp.988–994.

Wierzbicki, R. et al., 2013. Mapping the complex morphology of cell interactions with nanowire substrates using FIB-SEM. *PloS one*, 8(1), p.e53307. Available at: http://www.pubmedcentral.nih.gov/articlerender.fcgi?artid=3541134&tool=pmcentr ez&rendertype=abstract [Accessed December 16, 2013].

Wilhelmsen, K., 2005. Nesprin-3, a novel outer nuclear membrane protein, associates with the cytoskeletal linker protein plectin. *The Journal of Cell Biology*, 171(5), pp.799–810. Available at: http://www.jcb.org/cgi/doi/10.1083/jcb.200506083.

Williamson, J.C. et al., 2000. Oxacillin-resistant Staphylococcus aureus endophthalmitis after ganciclovir intraocular implant. *American journal of ophthalmology*, 129(4), pp.554–5. Available at: http://www.ncbi.nlm.nih.gov/pubmed/10764879.

Wilson, K.L. & Berk, J.M., 2010. The nuclear envelope at a glance. *Journal of Cell Science*, 123(12), pp.1973–1978. Available at: http://jcs.biologists.org/cgi/doi/10.1242/jcs.019042.

Winey, M., 1993. NDC1: a nuclear periphery component required for yeast spindle pole body duplication. *The Journal of Cell Biology*, 122(4), pp.743–751. Available at: http://jcb.rupress.org/content/122/4/743.abstract?ijkey=4e25722580daaf5afd1f324 171b2e5e97fa25a61&keytype2=tf_ipsecsha [Accessed April 12, 2016].

Wolgemuth, C. & Sun, S., 2006. Elasticity of α-Helical Coiled Coils. *Physical Review Letters*, 97(24), p.248101. Available at: http://link.aps.org/doi/10.1103/PhysRevLett.97.248101 [Accessed October 22, 2014].

Wong, S.Y. et al., 2015. Constitutive Activation of Myosin-Dependent Contractility Sensitizes Glioma Tumor-Initiating Cells to Mechanical Inputs and Reduces Tissue Invasion. *Cancer Research*, 75(6), pp.1113–1122. Available at: http://cancerres.aacrjournals.org/cgi/doi/10.1158/0008-5472.CAN-13-3426.

Wu, Y. et al., 2011. Differential response of Staphylococci and osteoblasts to varying titanium surface roughness. *Biomaterials*, 32(4), pp.951–60. Available at: http://www.ncbi.nlm.nih.gov/pubmed/20974493 [Accessed November 14, 2013].

Xie, C. et al., 2010. Noninvasive neuron pinning with nanopillar arrays. *Nano letters*, 10(10), pp.4020–4. Available at: http://www.pubmedcentral.nih.gov/articlerender.fcgi?artid=2955158&tool=pmcentr ez&rendertype=abstract [Accessed October 27, 2012].

Xie, C. et al., 2011. Vertical nanopillars for highly localized fluorescence imaging. *Proceedings of the National Academy of Sciences of the United States of America*, 108(10), pp.3894–9. Available at: http://www.pubmedcentral.nih.gov/articlerender.fcgi?artid=3054026&tool=pmcentr ez&rendertype=abstract [Accessed December 16, 2013].

Xie, X. et al., 2015. Determining the Time Window for Dynamic Nanowire Cell Penetration Processes. *ACS Nano*, 9(12), pp.11667–11677.

Xie, X., Xu, A.M., et al., 2013. Mechanical model of vertical nanowire cell penetration. *Nano*

letters, 13(12), pp.6002–8. Available at:
http://www.ncbi.nlm.nih.gov/pubmed/24237230.

Xie, X., Xu, A.M., et al., 2013. Nanostraw-electroporation system for highly efficient
intracellular delivery and transfection. *ACS Nano*, 7(5), pp.4351–4358.

Xiong, H. et al., 2008. Dictyostelium Sun-1 Connects the Centrosome to Chromatin and
Ensures Genome Stability. *Traffic*, 9(5), pp.708–724. Available at:
http://doi.wiley.com/10.1111/j.1600-0854.2008.00721.x.

Xu, L. et al., 2007. Microcontact printing of living bacteria arrays with cellular resolution.
Nano Letters, 7(7), pp.2068–2072.

Xu, Y. et al., 2018. Structural conservation of the autoinhibitory domain in SUN proteins.
Biochemical and Biophysical Research Communications, 496(4), pp.1337–1343.
Available at:
http://www.ncbi.nlm.nih.gov/pubmed/29408528%0Ahttp://linkinghub.elsevier.com
/retrieve/pii/S0006291X18302389.

Yamada, J. et al., 2010. A bimodal distribution of two distinct categories of intrinsically
disordered structures with separate functions in FG nucleoporins. *Molecular & cellular
proteomics : MCP*, 9(10), pp.2205–2224.

Yang, L. et al., 2013a. Mutations in LMNA Modulate the Lamin A - Nesprin-2 Interaction and
Cause LINC Complex Alterations. *PLoS ONE*, 8(8).

Yang, L. et al., 2013b. Mutations in LMNA Modulate the Lamin A - Nesprin-2 Interaction and
Cause LINC Complex Alterations. *PLoS ONE*, 8(8), p.e71850.

Yaron, S. et al., 2000. Vesicle-mediated transfer of virulence genes from Escherichia coli
O157:H7 to other enteric bacteria. *Applied and environmental microbiology*, 66(10),
pp.4414–20. Available at:
http://www.pubmedcentral.nih.gov/articlerender.fcgi?artid=92318&tool=pmcentrez
&rendertype=abstract.

Yu, J. et al., 2011. KASH protein Syne-2/Nesprin-2 and SUN proteins SUN1/2 mediate
nuclear migration during mammalian retinal development. *Human Molecular Genetics*,
20(6), pp.1061–1073.

Zara, S. et al., 2005. FLO11 -Based Model for Air-Liquid Interfacial Biofilm Formation by
Saccharomyces cerevisiae FLO11 -Based Model for Air-Liquid Interfacial Biofilm
Formation by Saccharomyces cerevisiae. *Applied and Environmental Microbiology*,
71(6), pp.2934–2939.

Zhang, F. et al., 2016. Hierarchical Nanowire Arrays as Three-Dimensional Fractal
Nanobiointerfaces for High Efficient Capture of Cancer Cells. *Nano Letters*, 16(1),
pp.766–772.

Zhang, Q. et al., 2002. The Nesprins Are Giant Actin-Binding Proteins, Orthologous to
Drosophila melanogaster Muscle Protein MSP-300. *Genomics*, 80(5), pp.473–481.
Available at: http://linkinghub.elsevier.com/retrieve/pii/S088875430296859X
[Accessed November 25, 2014].

Zhang, X. et al., 2009a. SUN1/2 and Syne/Nesprin-1/2 Complexes Connect Centrosome to

the Nucleus during Neurogenesis and Neuronal Migration in Mice. *Neuron*, 64(2), pp.173–187. Available at: http://dx.doi.org/10.1016/j.neuron.2009.08.018.

Zhang, X. et al., 2009b. SUN1/2 and Syne/Nesprin-1/2 complexes connect centrosome to the nucleus during neurogenesis and neuronal migration in mice. *Neuron*, 64(2), pp.173–87. Available at: http://www.pubmedcentral.nih.gov/articlerender.fcgi?artid=2788510&tool=pmcentrez&rendertype=abstract.

Zhao, Q., Brkljacic, J. & Meier, I., 2008. Two Distinct Interacting Classes of Nuclear Envelope-Associated Coiled-Coil Proteins Are Required for the Tissue-Specific Nuclear Envelope Targeting of Arabidopsis RanGAP. *THE PLANT CELL ONLINE*, 20(6), pp.1639–1651.

Zhou, L. & Panté, N., 2010. The nucleoporin Nup153 maintains nuclear envelope architecture and is required for cell migration in tumor cells. *FEBS letters*, 584(14), pp.3013–20. Available at: http://www.sciencedirect.com/science/article/pii/S001457931000431X [Accessed June 2, 2015].

Zhou, X. et al., 2012. Novel plant SUN-KASH bridges are involved in RanGAP anchoring and nuclear shape determination. *The Journal of Cell Biology*, 196(2), pp.203–211.

Zhou, X. et al., 2012. Novel plant SUN-KASH bridges are involved in RanGAP anchoring and nuclear shape determination. *The Journal of cell biology*, 196(2), pp.203–11. Available at: http://www.pubmedcentral.nih.gov/articlerender.fcgi?artid=3265956&tool=pmcentrez&rendertype=abstract [Accessed November 20, 2014].

Zhou, Z. et al., 2012a. Structure of Sad1-UNC84 homology (SUN) domain defines features of molecular bridge in nuclear envelope. *The Journal of biological chemistry*, 287(8), pp.5317–26.

Zhou, Z. et al., 2012b. Structure of Sad1-UNC84 homology (SUN) domain defines features of molecular bridge in nuclear envelope. *The Journal of biological chemistry*, 287(8), pp.5317–26. Available at: http://www.pubmedcentral.nih.gov/articlerender.fcgi?artid=3285312&tool=pmcentrez&rendertype=abstract [Accessed January 5, 2015].